



marum

Regulation of oxygen dynamics in sandy sediments

Dissertation

Autor: Soeren Ahmerkamp
Max Planck Institut für Marine Mikrobiologie
Fachbereich Geowissenschaften der Universität Bremen

1. Prüfer: Prof. Dr. Marcel Kuypers
Universität Bremen
Max Planck Institut für Marine Mikrobiologie, Biogeochemie

2. Prüfer: PD. Dr. Christian Winter
Universität Bremen
Marum - Zentrum für Marine Umweltwissenschaften

Diese Arbeit ist im Rahmen des Marum Cross-Cutting-Project 5 unter der Leitung von Moritz Holtappels entstanden.

Diese Dissertation wurde in der Zeit von Oktober 2012 bis September 2016 im Rahmen des Programms "The International Max Planck Research School of Marine Microbiology" (MarMic) am Max Planck Institut für Marine Mikrobiologie Bremen angefertigt. Datum des Promotionskolloquiums: 28.09.2016.



Soeren Ahmerkamp

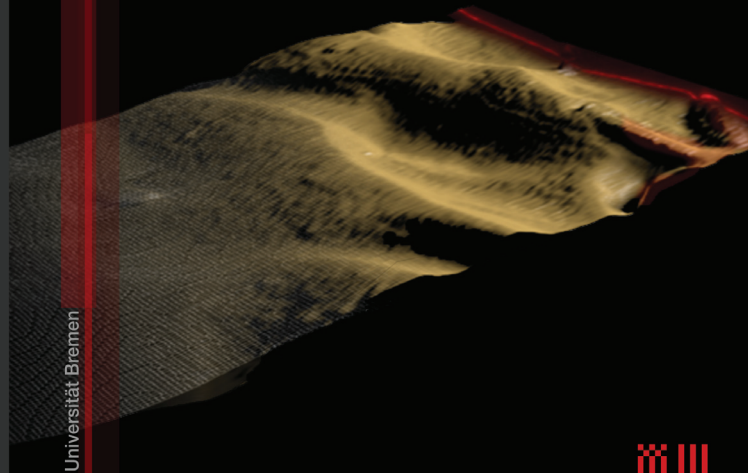
Regulation of oxygen dynamics in sandy sediments



Dissertation zur Erlangung des Grades eines Doktors der Naturwissenschaften Dr. rer. nat.
im Fachbereich Geowissenschaften

Regulation of oxygen dynamics in sandy sediments

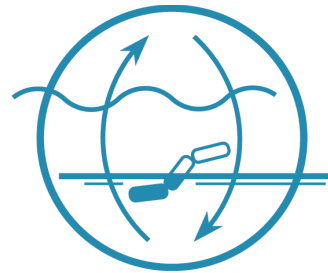
Soeren Ahmerkamp



Universität Bremen



Regulation of oxygen dynamics by transport processes and microbial respiration in sandy sediments



Dissertation

zur Erlangung des Grades eines Doktors der Naturwissenschaften

- Dr. rer. nat. -

im Fachbereich Geowissenschaften
der Universität Bremen

Soeren Ahmerkamp

Bremen, Mai 2016

Diese Arbeit wurde in der Zeit vom Oktober 2012 bis Mai 2016 im Rahmen des Programms “The International Max Planck Research School of Marine Microbiology” (MarMic) angefertigt. Die Ergebnisse dieser Arbeit wurden am Max Planck Institut für Marine Mikrobiologie (Biogeochemie) erarbeitet.

Datum des Promotionskolloquiums: 28.9.2016

Diese Arbeit ist im Rahmen des Marum Cross-Cutting-Project 5 unter der Leitung von Moritz Holtappels entstanden.

Autor: **Soeren Ahmerkamp**

Universität Bremen

Max Planck Institut für Marine Mikrobiologie

Gutachter: **Prof. Dr. Marcel MM Kuypers**

Universität Bremen

Max Planck Institut für Marine Mikrobiologie

Zweitgutachter: **PD Dr. Christian Winter**

Universität Bremen

Marum - Zentrum für Marine Umweltwissenschaften

| | | |
|------------|---|------------|
| I | Introduction | |
| 1 | Introduction | 17 |
| 1.1 | Continental Shelves | 17 |
| 1.2 | Transport Processes | 20 |
| 1.2.1 | Diffusion | 21 |
| 1.2.2 | Advection | 21 |
| 1.2.3 | Sediment Transport | 24 |
| 1.2.4 | Reactions | 25 |
| 1.3 | Benthic Biogeochemical Cycling | 27 |
| 1.4 | Aim and Outline of the Thesis | 30 |
| 1.5 | North Sea | 33 |
| 1.6 | Bibliography | 35 |
| II | Manuscripts | |
| 2 | Bedform migration and benthic oxygen fluxes | 47 |
| 3 | Oxygen dynamics in subtidal sands | 81 |
| 4 | Regulation of microbial respiration in sands | 123 |
| 5 | Coupled nitrification-denitrification in sands | 147 |
| 6 | Aerobic denitrification in sands | 185 |
| III | Implications for the Environment | |
| 7 | Implications for the Environment | 221 |
| 7.1 | Discussion & Outlook | 221 |
| 7.2 | Quantification | 227 |
| 7.3 | Bibliography | 229 |
| 8 | Acknowledgements | 233 |

Manuscripts not included in the thesis 236

Summary

More than 50% of the continental shelves are covered by sandy sediments that are permeable and allow for advective porewater flow. The interaction of small scale bedforms and bottom water currents creates pressure gradients, which pump reactive solutes and organic matter from bottom waters into the sediment pore space where they stimulate the benthic microbial community. This stimulation accelerates benthic carbon remineralization and nutrient turnover. So far, permeable sediment studies have generally assumed that the sediment is immobile, even though the continental shelves are a high energy environment. Strong tidal currents and wind-waves regularly mobilize the sea floor leading to changes in its morphology (morphodynamics). Little is known about the regulation of solute and particle fluxes within sandy sediments when they are exposed to such variable morpho- and hydrodynamics. The presented thesis aims to improve our understanding of transport processes in sandy sediments and to identify physical and biological parameters that control benthic biogeochemical cycling.

The thesis integrates benthic biogeochemistry with the research field of sediment transport to relate the knowledge of transport-reaction dynamics in the porespace with the transport dynamics of the sediment itself. The interdisciplinary approach combines mathematical modelling, field measurements and laboratory experiments.

In the first study, a numerical model was developed that relates porewater transport of oxygen and microbial respiration with bedform migration - the most ubiquitous form of sediment transport. Both, porewater advection and bedform migration are forced by the same hydrodynamic regime and their combined impact on oxygen fluxes was assessed along increasing bottom water currents. The study revealed that the oxygen distribution changes significantly in and underneath migrating bedforms. At the same time, bedform migration significantly reduces porewater advection. These observations lead to the counter intuitive finding that oxygen fluxes decrease with increasing bottom water velocities as soon as bedforms start to migrate.

Second, the benthic observatory 'LanceALot' was developed to validate the results

of the modelling study and to investigate benthic oxygen dynamics under strong tidal currents and wave forcing. The multiple instruments of 'LanceALot' allowed to monitor concurrent measurements of bottom water currents, surface topographies and oxygen penetration depths, as well as their temporal variability. Thereby, the response of benthic oxygen penetration and net uptake to strong tidal currents and waves could be described and quantified for various sediment types, bottom water velocities, and respiration rates within the subtidal areas of the German Bight. Confirming the modelling study, the oxygen distribution in the sediment was found to respond to the movement of the upper sediment layer. Underneath the bedforms, the hydro- and morphodynamics along a tidal cycle promoted a distinct layer of highly variable redox conditions. These conditions present a challenge to microorganisms, because it exposes them to a variety of different electron acceptors on rapid temporal scales. Further, the study revealed that migration of bedforms leads to a reduction of respiration rates due to the washout of organic particles, which also prevents clogging of the pore space and maintains the advective porewater flow. Despite the variability of the hydrodynamic forcing, it was possible to predict the broad range of oxygen fluxes by a simple mechanistic model on the basis of measured grain size, bottom water velocity and respiration rates.

Fast porewater advection enhances the transport of organic carbon and electron acceptors to the microbial community. In layers with sufficient supply of reactants other factors may limit the microbial growth. In permeable sands, bacteria colonize the surface area of sand grains, and especially depressions in these surfaces that prevent the abrasion of cells when the grains are moved. In a third study, the microbial respiration was measured for different grain size fractions of a sandy sediment station in the North Sea to evaluate the available surface area as a limiting factor. In a novel approach, bacterial cell counts and microbial reaction rate measurements were combined with measurements of sediment grain size and surface area. The results demonstrate that bacterial cells colonize sediment grains at constant areal cell densities and thus, reaction rates correlated with sediment surface area. Furthermore, confocal microscopy data revealed that microbes preferably colonize cracks and depressions. In such microenvironments the bacteria could be stimulated by increasing porewater advection, most likely as a result of increased supply of labile organic carbon.

Besides the oxygen dynamics the potential alleviation of eutrophication by benthic nitrogen-loss was investigated in two additional studies. The results of transport modelling in combination with rate measurements revealed a high potential for benthic nitrogen-loss within the German Bight. These losses were mainly driven by denitrification and coupled nitrification-denitrification. Further, the highly variable redox conditions described in the

previous study promote specific metabolic adaptations such as aerobic denitrification. To demonstrate such adaption, variable redox conditions were simulated in flow-through-reactors. The data show that such redox treatments can indeed stimulate the capacity of aerobic denitrification. Under consideration of the large oxygen penetration depths that were measured, aerobic denitrification might strongly enhance nitrogen-loss in sandy sediments.

The presented findings on transport- and morphodynamics and bacterial colonization behavior enhance our understanding of microbial respiration in sandy sediments that control benthic biogeochemical cycling.

Zusammenfassung

Gegenstand der vorliegenden Doktorarbeit sind die Sauerstoffdynamiken in sandigen Sedimenten, mit dem Schwerpunkt auf der Interaktion von Transportprozessen und mikrobiologischen Reaktionsprozessen. Über 50% der Kontinentalschelfe werden von sandigen Sedimenten bedeckt, die permeabel sind und somit einen advektiven Porenwasserstrom zulassen. Dieser Porenwasseradvektion wird eine zentrale biogeochemische Bedeutung zugesprochen. Durch die Porenwasseradvektion wird das Benthos mit reaktiven gelösten Substanzen und organischem Kohlenstoff aus der Wassersäule versorgt. Hierdurch werden Kohlenstoffremineralisierung und Nährstoffkreisläufe beschleunigt. Kennzeichnend für Kontinentalschelfe sind starke Tidenströmungen und ein intensiver Wellengang welche zu regelmäßiger Mobilisierung der sandigen Sedimente führen (Morphodynamik). Wie die Strömungs- und Morphodynamiken die benthischen Stoffflüsse beeinflussen ist bisher nicht vollständig verstanden. Das Ziel der vorliegenden Arbeit besteht darin, ein besseres mechanistisches Verständnis über die Regulierung der Stoffflüsse durch Transportprozesse und mikrobielle Respiration in sandigen Sedimenten zu erlangen und somit Vorhersagen mit Hilfe von Transportmodellen zu ermöglichen.

Im Rahmen der vorliegenden Arbeit wurde das Forschungsgebiet der benthischen Biogeochemie mit dem Forschungsgebiet des Sedimenttransportes kombiniert, um die Transport- und Reaktionsdynamiken im Porenraum mit den Transportdynamiken des Sedimentes zu verknüpfen.

Hierfür wurden in einer ersten Modellierungsstudie die Transport- und Reaktionsgleichungen durch den Effekt von migrierenden Bodenformen, die dominierende Form des Sedimenttransportes, erweitert. Diese Gleichungen wurden numerisch für typische Nordsee Randbedingungen gelöst. Die Ergebnisse zeigen, dass die Sauerstoffverteilung unter den migrierenden Bodenformen deutlich von bekannteren stationären Bodenformen abweicht. Durch die direkte Kopplung der Porenwasseradvektion und Bodenformmigration mit den Strömungsgeschwindigkeiten konnte gezeigt werden, dass Bodenformmigration die Porenwasseradvektion negativ beeinflusst, wodurch Sauerstoffflüsse reduziert werden,

trotz steigender Strömungsgeschwindigkeiten.

Um die Modellierungsstudie zu bestätigen wurde die Regulierung von Sauerstoffdynamiken unter *in situ* Bedingungen untersucht. Ein eigens entwickeltes autonomes benthisches Observatorium, genannt 'LanceALot', wurde innerhalb der Deutschen Bucht eingesetzt, wodurch erstmals hochaufgelöste Strömungsgeschwindigkeiten, Oberflächentopographien und Sauerstoffeindringtiefen, sowie deren zeitliche Variabilität gemessen werden konnten. Die Sauerstoffverteilungen stimmten mit der Modellierungsstudie überein und zeigten die charakteristischen Muster für stationäre, als auch migrierende Bodenformen. Die variierenden Morpho- und Hydrodynamiken entlang eines Tidenzyklus erzeugten eine Sedimentzone, die stetig zwischen oxischen und anoxischen Bedingungen wechselte und damit eine große Herausforderung für mikrobielle Lebensgemeinschaften darstellt. Es konnte gezeigt werden, dass die benthischen Respirationsraten stark von migrierenden Bodenformen reduziert werden. Dies wurde auf mechanische Reibung und Auswaschung von organischem Kohlenstoff zurückgeführt, wodurch aber auch die Permeabilität der sandigen Sedimente gewahrt blieb. Trotz der großen hydrodynamischen Variabilität konnten die Sauerstoffflüsse innerhalb der Deutschen Bucht durch ein einfaches Modell beschrieben werden, welches lediglich auf der Strömungsgeschwindigkeit, Korngröße und Respirationsrate basiert.

Die starke Porenwasseradvektion in sandigen Sedimenten beschleunigt den Transport von organischem Kohlenstoff und Elektronenakzeptoren aus dem Bodenwasser zu den benthischen mikrobiellen Gemeinschaften. In Habitaten mit genügend Reaktanten ist das mikrobielle Wachstum von anderen Faktoren limitiert. Bakterien besiedeln die Oberfläche von Sandkörnern, insbesondere Mulden in denen sie, im Falle von Sedimentbewegung, vor mechanischer Reibung geschützt sind. Um die verfügbare Oberfläche als limitierenden Faktor zu testen, wurden in einer dritten Studie Nordseesedimente beprobt und in verschiedene Sedimentfraktionen aufgetrennt. In einem neuartigen Ansatz wurden bakterielle Zellzahlen mit Messungen von Sedimenteigenschaften und mikrobiellen Reaktionsraten kombiniert. Die Ergebnisse zeigen, dass Sandkörner von Bakterien mit einer konstanten Flächendichte besiedelt werden. Die Respirationsraten stellen somit indirekt eine Funktion der Sedimentoberfläche dar. Mithilfe von Konfokalmikroskopie konnte die Besiedlung der Bakterien zudem visualisiert werden. Bakterien wurden vorwiegend in Mulden und Mikrorissen identifiziert. In den Mikrorissen konnten starke Porenwasserströmungen die bakterielle Aktivität stimulieren. Dieses Phänomen lässt sich auf die erhöhte Verfügbarkeit von labilem organischem Kohlenstoff zurückführen.

In zwei weiteren Untersuchungen wurden Stickstoffverluste innerhalb der sandigen Sedimente der Deutschen Bucht untersucht. In der vierten Studie wurde das entwickelte

Stoffflussmodell genutzt, um aus den gemessenen Reaktionsraten potentielle Stickstoffverluste zu bestimmen. Die Ergebnisse dieser Modellierung zeigten, dass sandige Sedimente in der Nordsee eine wichtige Senke für Stickstoff sind und damit potentiell der anthropogenen Eutrophierung entgegenwirken. Der Stickstoffverlust wird vorwiegend durch Denitrifizierung und der Kopplung von Nitrifizierung und Denitrifizierung geleistet. In der fünften Studie, wurde der aerobe Denitrifizierungsprozess untersucht. Mit Hilfe der Kopplung von experimentellen Daten und Transportmodellierungen von Durchflussinkubatoren konnte gezeigt werden, dass die Denitrifizierung unter aeroben Bedingungen stattfindet und kein Resultat von anoxischen Mikronischen darstellt. Unter Berücksichtigung der hohen gemessenen Sauerstoffeindringtiefen kann die aerobe Denitrifizierung deutlich zu dem Stickstoffverlust beitragen.

Die Ergebnisse der vorliegenden Arbeit über Transport- und Morphodynamiken und der spezifischen Kolonisierung von Sandkörnern erweitern unser Verständnis der mikrobiellen Respiration und der damit verbundenen biogeochemischen Kreisläufen in sandigen Sedimenten.



Introduction

| | | |
|----------|--------------------------------|-----------|
| 1 | Introduction | 17 |
| 1.1 | Continental Shelves | |
| 1.2 | Transport Processes | |
| 1.3 | Benthic Biogeochemical Cycling | |
| 1.4 | Aim and Outline of the Thesis | |
| 1.5 | North Sea | |
| 1.6 | Bibliography | |



1. Introduction

1.1 Continental Shelves

“Why is it that scuba divers and surfers are some of the strongest advocates of ocean conservation? Because they’ve spent time in and around the ocean, and they’ve personally seen the beauty, the fragility, and even the degradation of our planet’s blue heart. ”

– Sylvia Earle

As part of the ocean, continental shelves represent highly productive ecosystems teeming with life and as such deserve our protection. However, successful protection of the oceans requires a better understanding of their ecosystem functioning.

Continental shelves are submarine terraces linking the continents to the open oceans. Extending on average 65 km from shore, continental shelves occupy a total area of $30 \cdot 10^6 \text{ km}^2$, representing 7.5% of the total ocean area (Jahnke, 2010; Sverdrup et al., 1942). Starting from the coastline, the continental shelves slope gently (0.1°) towards the shelf break from where the steep continental slope (4°) connects the shelves to the ocean basins. The average water depths range between 130 m and 350 m resulting in a strong hydrodynamic forcing.

At the outer continental shelves, hydrodynamic forcing is mainly induced by wind- and density-driven currents. Trade winds in equatorial regions and convective winds along the continents initialise movement of watermasses. As a result of the rotation of the earth, i.e. Coriolis force, the depth integrated transport of the watermasses is shifted by 90° compared to the wind direction. These, so called Ekman currents create upwelling along

the equator and western margins of the continents (Fasham, 2003). Additionally, the small water volume of the continental shelves in comparison to the open oceans leads to a reduced thermal capacity promoting density-driven currents (Huthnance, 1981). The reduced thermal capacity leads to changes in horizontal stratification creating salinity and temperature gradients on short timescales. These spatial and temporal gradients drive currents and promote internal waves. While wind- and density-driven currents are important for water mass exchange and nutrient supply their energetic contribution to the total physical forcing is minor compared to the processes that occur at the inner continental shelves (Huthnance, 1981).

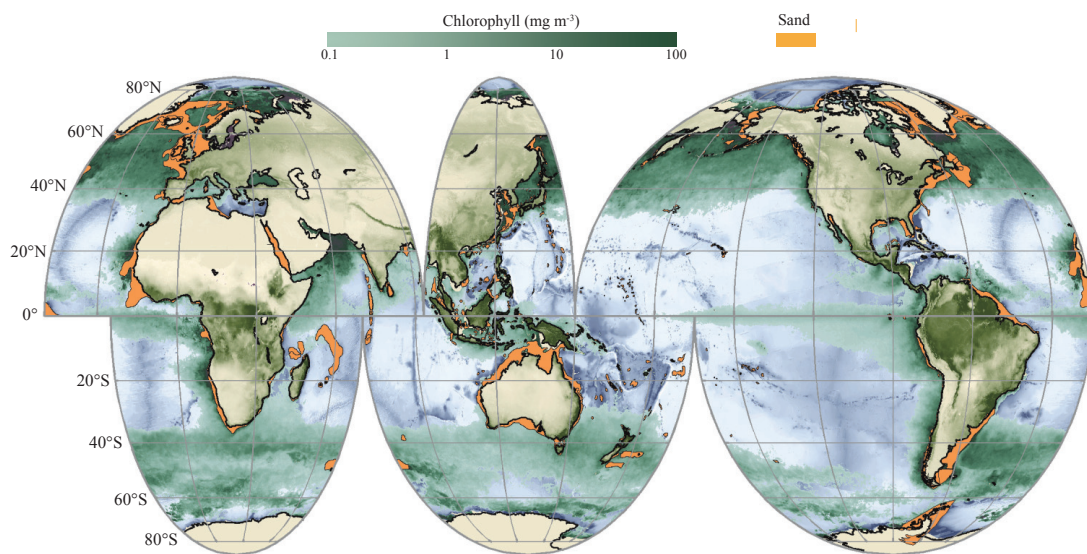


Figure 1.1: The world-map shows the chlorophyll concentration in green and sandy sediments in orange. Additionally the bathymetry is shown schematically in light blue. Data provided by Emodnet (Sediment), Naval Office of Oceanography (Sediment), NASA (Chlorophyll, average 2014-2015)

Towards the inner continental shelves, hydrodynamic forcing is dominated by surface gravity waves such as tidal and wind-generated waves (Nittrouer and Wright, 1994). Tidal waves have their maximum amplitude where they interact with continental margins. Here, the large amplitude leads to pressure gradients which create strong currents (Schwidierski, 1980). These currents are further enhanced by wind-generated waves that transport energy from the open ocean towards the inner continental shelf. In the shallow inner continental shelf waters surface waves interact with the seafloor leading to wave breaking and creation of turbulence which enhances mixing. As a result, the surface layer of the seafloor is regularly mobilized (George and Hill, 2008) leading to a sediment sorting and distribution that is fairly similar on all continental shelves (e.g. Hayes, 1967).

Most of the continental shelves were dry land during the last Ice Age, 21,000 years before present, when water level was 120 m lower than today (Fleming et al., 1998). The rising sea level eroded the outer parts of the continental shelves leaving behind mostly terrigenous sediment, composed of relict silica sand (Emery, 1968; Pinet, 2011). The relative amount of sands ranges from 42% in tropical and polaric latitudes with a maximum of 60% in temperate climate zones (compare Figure 1.1). In average, sands on continental shelves constitute approximately 50% of all sediments. The remaining fraction is mostly composed of rock and gravel, and to a much smaller extent silt and clay (Hayes, 1967).

The shallow water depths on continental shelves tie the sediment distribution to the hydrodynamic forcing. Observations of surface waves have shown that 40% of the shelf sediments are potentially eroded and reworked (George and Hill, 2008). This is enhanced by tidal currents which alone have the potential to mobilize the coastal seafloor (McCave, 2002; Berg, 1987). The mobilization of sediments leads to a re-suspension of fine material leaving behind coarse grained sands. These finer sediments are redeposited in regions of weaker hydrodynamic forcing, i.e. the outer continental shelves. Therefore, the fraction of fine sediment increases towards the outer shelves and the continental slopes (Gross, 1977). Deposition of mud on the inner continental shelf is limited to river runoff zones, such as river deltas, and regions of weaker hydrodynamic forcing such as canyons or enclosed seas (McCave, 2002).

Continental shelves play a disproportionately large role relative to their surface area for the ocean biosphere as highly productive ecosystems (Walsh, 1991). River runoff, aeolian input, groundwater discharge and upwelling provide nutrients that fuel a primary production which is 15-21% of the global production (Jahnke, 2010; Behrenfeld and Falkowski, 1997) (compare Figure 1.1). Light often penetrates the surface layer down the seafloor especially in coastal waters stimulating additional benthic primary production which significantly contributes to the total production (Nelson et al., 1999). Therefore, continental shelves play a crucial role in the global cycling of nutrients and carbon.

The recycling of organic carbon can be separated into water column processes and benthic processes. In the water column, zooplankton might consume a substantial portion of the fixed carbon (Ducklow et al., 2001), though, in shelf waters the consumption was shown to be minor (Wollast, 1998). Large amounts of the remaining biomass accumulate in marine aggregates (Marine Snow), and start to sink towards the seafloor (Alldredge and Silver, 1988). During the descent, heterotrophic organisms degrade the aggregates (Kiørboe, 2001). In relatively shallow waters gravitational settling is limited to timescales of hours to days, and remineralization in the water column is consequently reduced (Malone et al., 1983). In deeper regions, settling might be accelerated by oscillating internal waves

which lead to a downwelling of organic material (Mann and Lazier, 2013). Thus, in total 20% to 60% of the fixed carbon reaches the ocean seafloor (Gattuso et al., 1998).

The large amounts of organic carbon that reach the seafloor suggest that the continental shelves are a sink for atmospheric carbon. Indeed, such observations were made for outer continental shelves (Thomas et al., 2004). At the inner continental shelf, sandy sediments were found to be non-accumulating in terms of organic carbon (de Haas et al., 2002). However, by tracing ^{210}Pb it has been shown that a large portion of the organic carbon is worked into the sandy sediments (Bacon et al., 1994) whereas only 5% is transported laterally to the outer shelves (de Haas et al., 2002). This implies that a large portion must be remineralized within the sediment. In contrast, as a result of low organic carbon concentrations - compared to muddy sediments - sandy sediments have been ignored as deserts of biogeochemical cycling (Boudreau et al., 2001). By coupling the biogeochemical reactions to the advective porewater flow in sandy sediments, Huettel et al. (2014) established a framework to explain the high remineralization rates in sandy sediments and their important role for the nutrient cycling.

1.2 Transport Processes

Transport phenomena on continental shelves play a vital role for the global biogeochemical cycling by stimulating reaction rates. These transport phenomena vary over many scales ranging from rivers and ocean currents of kilometer scale down to the microbial cells in which the solutes react. This thesis focuses on the transport processes that take place in marine sediments of continental shelves.

Mathematically, transport on all scales can be described by the continuity equation:

$$\frac{\partial C}{\partial t} = -\nabla \cdot \vec{J} - R_c \quad (1.1)$$

where ∇ is the nabla operator, i.e. partial derivative in each spatial dimension, C is the concentration of a solute, t the time variable, \vec{J} the total flux and R the reaction rate of the solute. Simply speaking, the equation states that the temporal concentration change depends on the fluxes into and out of the system and reacts at a rate R . The total flux is composed by the diffusive flux (J_{diff}) and advective flux (J_{adv}).

In biogeochemistry, fluxes are typically discussed in terms of net fluxes through a surface. This represents the difference of outflow and inflow fluxes into a system such as in marine sediments at their equilibration state ($\frac{\partial C}{\partial t} = 0$). These net fluxes differ from the fluxes described above as they do not only depend on the physical transport but also

biotic and abiotic reaction rates. Understanding net fluxes, therefore, requires a good understanding of the biological reactions, but also the physical transport induced by diffusion and advection.

1.2.1 Diffusion

When observing particles on a micrometer scale they move randomly and undirected. The magnitude of this motion is a function of temperature, which represents the energy saved in the motion of atoms and molecules (Einstein, 1905). The movement of a single particle is undirected but the interaction of several particles leads to an increase of the entropy state, i.e. equilibration of concentration gradients. By statistically averaging particle interactions, the flux was found to be proportional to the concentration gradient related by the temperature dependent diffusion constant D (Fick, 1855):

$$\vec{J}_{diff} = -D\nabla C \quad (1.2)$$

On the macroscopic scale, sediment can be separated into volumes of voids and volumes of solids. The porosity θ represents the proportion void volume to total volume. The solute concentration in the sediment can, therefore, be represented as a concentration in the porewater (C) or concentration per bulk volume sediment (θC). Unless specific, concentrations will be henceforth represented as porewater concentrations. The porosity itself prolongs the path solutes take through the pore space. Apparent diffusion is thus reduced by the tortuosity, which represents the squared ratio of effective length to the layer thickness of the porous medium (Boudreau, 1996).

In marine systems, diffusion transport dominates on micrometer to millimeter scales, e.g. transport of solutes into microbial cells, or where advection is prevented, such as marine aggregates and cohesive sediments. However, the majority of the inner continental shelves is covered by sandy sediments. In these sediments the large pore space allow for advective transport at timescales that are much faster than pure diffusion (Thibodeaux and Boyle, 1987).

1.2.2 Advection

On larger scales, the transport of solutes is dominated by the bulk motion of the surrounding fluid which can mathematically be described by a vector field \vec{u} . The advective flux is then defined as:

$$\vec{J}_{adv} = \vec{u}C \quad (1.3)$$

Substituting the diffusive (Equation 1.2) and advective flux (Equation 1.3) into the continuity Equation 1.1 the scalar-transport-reaction equation reads:

Scalar Transport Reaction Equation

$$\frac{\partial C}{\partial t} = -\nabla \cdot \vec{J} - R_c = \underbrace{D\nabla^2 C}_{\text{Diffusion}} - \underbrace{\vec{u} \cdot \nabla C}_{\text{Advection}} - \underbrace{R_c}_{\text{Reaction}} \quad (1.4)$$

In most systems, the variables in Equation 1.4 can be measured. The biggest challenge is measuring the velocity vector field \vec{u} , which strongly differs between systems, for example in the water column and the sediment.

In sandy sediments the relatively large pore spaces allow for an interstitial flow which is referred to as porewater advection (Huettel et al., 2014). Porewater advection is driven by pressure gradients (∇p). However, the sediment matrix causes a resistance, leading to a pressure drop within the sediment. Assuming that the resistance scales linearly with the velocity, porewater advection can be directly related to the pressure gradient following Darcy's law:

Darcy's law

$$\vec{u} = -\frac{k}{\mu\theta} \nabla p \quad (1.5)$$

where k is the permeability, μ the dynamic viscosity.

The pressure gradients in marine sediments can originate from many different processes including bioirrigation, gas seeps, density-driven convection, tidal pumping, etc. All these listed processes contribute to interfacial solute fluxes, but, most of the processes are only of local relevance such as intertidal systems and have a minor contribution by considering the area of relevance. The largest portion of interfacial fluxes within the subtidal zone of continental shelves is induced by bedform topographies of centimeter scales (Santos et al., 2012).

Bedforms, ubiquitous on the seafloor, act as an obstacle for overlying currents. At the stoss side of the bedform water flow accelerates (Thibodeaux and Boyle, 1987). This acceleration leads to an increase of the dynamic pressure at the sediment-water interface (Figure 1.2 a). Following Bernoulli's principle (Bernoulli, 1738) the total energy of a system remains constant, therefore, at the lee side of the bedform - where the currents deaccelerate - the dynamic pressure drops to values below zero. The resulting pressure gradient has been subject to different studies based on laboratory experiments (e.g. Janssen et al., 2012). It was found that the pressure gradient generally scales with the square of the

current velocity but also varying ratios of bedform height to water level (Fehlman, 1985). For bedforms of centimeter scales, the amplitude of the pressure variation was found to range in between 1 – 10 Pa. This is equivalent to a water head of 0.1 mm – 1 mm. Therefore, in situ measurement are difficult and little is known about the controlling mechanisms of the pressure gradients (Huettel et al., 1996).

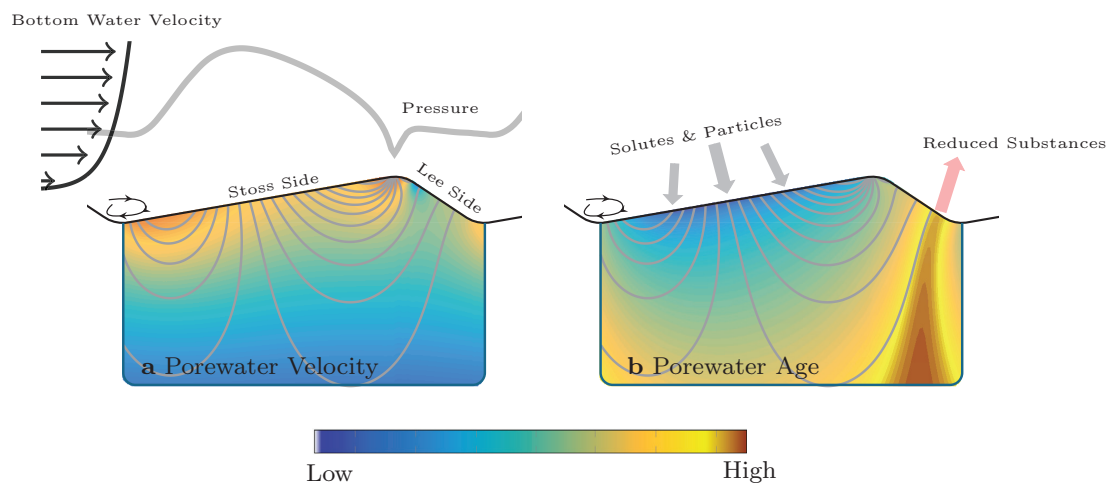


Figure 1.2: Schematic illustrations to emphasize the processes within sandy sediments. **a** shows the magnitude of the porewater velocity together with the pressure distribution above the sediment-water interface. **b** shows the porewater age; at the lee side a narrow outlet becomes apparent, which releases reduced substances to the water column (illustration based on Janssen et al., 2012; Cardenas and Wilson, 2007; Precht et al., 2004, and many more).

The pressure gradient induced by the bedform and bottom water interaction drives an advective porewater flow through the sediment as expressed in equation 1.5 (Thibodeaux and Boyle, 1987). The streamlines that have their origin at the stoss side of the bedform penetrate deeply into the bedform before turning towards the outflow at the lee side of the bedform (Figure 1.2 **a**). From modelling studies it was inferred that the porewater velocities close to the sediment-water interface range between 0.1 cm h^{-1} to 100 cm h^{-1} (e.g. Cardenas and Wilson, 2007). These porewater velocities decrease strongly with increasing depth (Elliott and Brooks, 1997*b*). In situ porewater velocities along bedforms were found to range between 54 cm h^{-1} in the upper sediment layers and 6 cm h^{-1} at a few centimeter depth below the sediment surface (Reimers et al., 2004).

Though advective processes largely dominate in sands, diffusion also takes place. Therefore, it is interesting to calculate the relative importance of advection to diffusion which can be summarized by the non-dimensional Péclet number:

Péclet Number

$$Pe = \frac{U\eta}{D} \quad (1.6)$$

By substituting Equation 1.5 into Equation 1.6 it can be calculated for which permeabilities advection timescales dominate ($Pe > 10$). For typical pressure gradients of around 2 Pa and bedforms with wavelengths of $\lambda = 0.2$ m and heights of $\eta = 0.02$ m (Janssen et al., 2012) and a typical diffusion coefficient of around $10^{-9} \text{ m}^2 \text{ s}^{-1}$ a permeability of $5 \cdot 10^{-12} \text{ m}^2$ denotes the limit where advection starts to dominate the system. These permeabilities are characteristic for sandy sediments with grain size distributions of medians larger than $150 \mu\text{m}$ (Krumbein et al., 1943).

Advected porewater interacts with sand grains leading to preferential pathways which promote a smearing of solutes along the pathway through the porous media referred to as dispersion (Matyka et al., 2008). On a larger scale the sum of microscale processes behave like diffusion and can be summarized by an additional dispersion coefficient which is a function of the porewater velocity. The dispersion coefficient typically exceeds diffusion by three orders of magnitude (Bear and Buchlin, 1978).

1.2.3 Sediment Transport

The presence of bedforms in shallow waters is evidence of a regularly mobilized seabed. Sediment transport is either induced by biological processes, such as bioturbation (Meysman et al., 2006), or physical transport, such as sediment re-suspension and re-deposition during storm events and bedform migration (Traykovski et al., 1999). Both process types lead to a reworking of sediment in which overlying bottom water is trapped and porewater is released.

Bioturbation is very heterogenous and induced by many different organisms ranging from polychaetes (Kristensen and Blackburn, 1987) to walruses (Oliver et al., 1985). Mathematically, bioturbation is difficult to grasp as the reworking of sediment induces a transformation of the sediment matrix itself. Quantitatively, bioturbation by infauna constitutes the largest portion sediment reworking. Infaunal bioturbation is incorporated into models by assuming an enhanced diffusion based on experimental determinations. But, this requires detailed information about the organisms that induce the turbation, which is generally tedious to assess. However, based on laboratory experiments and tracking of tracers it was shown that bioturbation contributes substantially to benthic remineralization processes (D'Andrea et al., 2004; Aller, 1994; Kristensen and Blackburn, 1987).

Sediment re-suspension and re-deposition events are difficult to quantify and can rework

large amounts of sediment (Gagan et al., 1988). This also applies to commercial bottom trawling which does not only rework sediment but might impact benthic communities (De Groot, 1984).

Migrating bedforms are omnipresent in the intertidal (deVries Klein, 1970) and subtidal of continental shelves (Knaapen et al., 2005; Traykovski, 2007) as well as rivers (Berg, 1987). The importance in terms of sediment transport has been recognized for a long time (Einstein, 1950), but their impact on interfacial solute fluxes is not well understood. The length and height of bedforms is mainly a function of the sediment grain size and only varies slightly with bottom water velocities (Yalin, 1985) which leads to specific morphodynamics. As soon as the bottom water reaches the critical bed shear stress, sediment is constantly eroded at the stoss side of the bedform and deposited at the lee side leading to a train-like movement (Yalin, 1972). At the same time, porewater is released where sediment is eroded and bottom water is trapped at the lee side of the bedforms (Elliott and Brooks, 1997*b*; Pilditch and Miller, 2006). This turnover was quantified based on simple analytical models and was shown to contribute significantly to interfacial fluxes (Rutherford et al., 1993; Santos et al., 2012). These models assumed a simple turnover of the bedforms without considering the interaction with the pressure gradient pumping bottom water from the opposite direction into the bedform. Therefore, the interfacial fluxes induced by bedform migration might be largely overestimated. Indeed it was shown in early studies, that the migrating bedform counteracts the pressure-driven advective porewater flow consequently reducing penetration depths of solutes (Elliott and Brooks, 1997*a,b*). Furthermore, the inclusion of dispersion into the same model showed that fast porewater oscillations, in combination with dispersion, enhance solute fluxes (Bottacin-Busolin and Marion, 2010). However, these processes have not been studied under in situ conditions. The models have thus far only considered the behavior of non-reactive solutes and the impact on reactive solutes has not been investigated. Therefore, it is yet unknown how bedform migration is involved in the biogeochemical cycling.

1.2.4 Reactions

Heterotrophic microbial communities gain energy from the oxidation of organic carbon compounds. As oxidizing agents a variety of electron acceptors exist in nature and in the classical perception they are used in order of decreasing energy yield, i.e. energy that is released during the redox processes. Thermodynamically most favorable is oxygen, followed by nitrate, iron (III), manganese (IV), sulfate and carbon dioxide (Canfield et al., 2005). This thesis focuses on oxygen and the various chemical forms of inorganic nitrogen, such as nitrate, nitrite and ammonium. Oxygen is the first electron acceptor in the redox

cascade and, therefore, inhibits the subsequent redox processes. Additionally, reduced reactants of anoxic reactions are re-oxidized in the presence of oxygen (Glud, 2008). Thus, oxygen is a good indicator for the total carbon remineralization.

Inner continental shelves are exposed to large river runoffs leading to inorganic nitrogen emissions (Erisman et al., 2007). In biological systems inorganic nitrogen compounds are important as nutrients and electron acceptor at once. In high concentrations inorganic nitrogen fuels plankton blooms which can have severe impacts on ecosystems. But, the nitrogen pollution is potentially alleviated by biologically mediated redox reactions, such as denitrification (Gao et al., 2010; Marchant et al., 2014). In denitrification reactions nitrate is reduced to dinitrogen gas via nitrite. While these reactions remove excess inorganic nitrogen from a system, they may also produce nitrous oxide, a potent greenhouse gas (Codispoti and Christensen, 1985). The transformations of inorganic-nitrogen are subject of this study because of their important ecological impacts.

The electron acceptors and donors are consumed at specific volumetric consumption rates, which depend on the bacterial cell numbers and cell specific activity. Even though, electron acceptors and electron donors can both be limiting, the focus is generally on the terminal electron acceptor as it is easier to monitor and only little is known about the uptake of the complex and diverse organic molecules. The volumetric consumption rates are assumed to be constant along decreasing concentrations. Only at very low concentrations the enzyme speed is limited. This kinetic is typically covered by assuming first-order kinetic, i.e. Monod-curve: (Boudreau, 1997):

Monod-Kinetic

$$R_c = \frac{RC}{K_m + C} \quad (1.7)$$

Here R is the maximum reaction rate in the porewater and K_m the half saturation coefficient. If just considering the enzyme speed, values of K_m are typically in the nano-molar range. But in sediments, irrespective of the domination of diffusion or advection, values are typically found in the micro-molar range (Kessler et al., 2013; Thamdrup et al., 1998). Despite these observations only little is known about the regulation of the reaction rate, but it emphasizes the strong coupling to transport processes. Many processes have been found to be limited by diffusive supply. In sandy sediments, where advection is present, it is an interesting question what limits the reaction rate as very high fluxes of electron acceptors are present especially close to the sediment-water interface.

1.3 Benthic Biogeochemical Cycling

Benthic biogeochemical cycling on continental shelves strongly depends on the interaction of the above-described transport processes and volumetric reaction rates. The type of transport process that dominates (advection vs diffusion) depends on the physical characteristics of the sediment which strongly differ between muds and sands.

So far, most investigations have focused on muddy sediments (Viollier et al., 2003). Muddy sediments are mostly composed of silt, clay and fine sand grains in which strong cohesion prevents advection. Interfacial fluxes through the sediment-water interface are, therefore, limited to diffusion. As muddy sediments are mostly located in regions of weak hydrodynamic forcing, electron donors are supplied by the settling of particulate organic matter. The electron acceptors are solely supplied by diffusion. Therefore, the concentration gradient between the water column and the sediment controls the total supply of solutes, i.e. net fluxes, into the sediment. The strength of the concentration gradient is controlled by the microbial reaction rate in the sediment (Equation 1.4). In this way the activity of the microbial community affects its own supply of electron acceptors. This creates a vertical stratification of microbial communities (Ravenschlag et al., 2001) and a distribution of the electron acceptors along their electron affinity with only vertical gradients (Jørgensen, 2000; Böttcher et al., 2000).

At the inner continental shelf the bacterial abundances in muddy sediments are extremely high ($> 1 \cdot 10^9 \text{ cells cm}^{-3}$) (Llobet-Brossa et al., 1998, 2002), implying that volumetric reaction rates are also high. However, aerobic remineralization takes place in a few millimeter-thick layer close to the sediment-water interface because diffusive transport is limited (Jørgensen, 2000). Despite proximity to the water column, direct coupling to overlying currents is only induced by a diffusive boundary layer (Pope, 2000). This sub-layer connects the sediment-water interface to the turbulent flow and is diffusion-controlled. The thickness of the diffusive boundary layer varies depending on the current strength, which leads to slight variation of solute fluxes (Rasmussen and Jørgensen, 1992; Lorke et al., 2003; Kelly-Gerreyn et al., 2005; Glud et al., 2007). Overall the temporal and spatial variability is small which simplifies quantifications because net fluxes of oxygen and reaction rates can be estimated from single oxygen profiles (Berg et al., 1998; Lettmann et al., 2012). Additionally, modelling approaches require only a limited set of boundary conditions, i.e. diffusion coefficient, oxygen concentration and oxygen respiration which can easily be deduced from oxygen profiles or be determined empirically (Glud et al., 2007; Middelburg et al., 1996).

The microbial environment and biogeochemical setting of sandy sediments strongly

differs from that of cohesive sediments (Huettel et al., 2014). As a result of the lower organic carbon content and smaller bacterial cell numbers (DeFlaun and Mayer, 1983), the volumetric reaction rates in sands are an order of magnitude below those of muddy sediments. Considering the theories that apply to diffusion-controlled systems, i.e. fluxes are only a function of concentration gradients controlled by reaction rates, sandy sediments would indeed play a minor role in the biogeochemical cycling on continental shelves. However, in the last quarter-century it was shown that the permeability of sandy sediments allows for advection through the pore space and thus may sustain large fluxes despite low reaction rates.

It was inferred from flume experiments and modelling studies that the interfacial advective porewater transport separates the sediment-water interface into an inflow zone, at the stoss side of the bedform, and an outflow zone, at the lee side of the bedform (Figure 1.2 b). At the inflow zone, the sediment biota are supplied with oxygen and other electron acceptors from the bottom water. These solutes are consumed along streamlines towards the outflow. In contrast to diffusion, the advection increases the penetration depth and, therefore, the area available to microbial reactions which increases solute fluxes significantly. At the outflow zone reaction products such as ammonium, phosphate and silicate, are released back to the water column in narrow 'chimney-like' outlets (Figure 1.2 b). This specific zonation leads to a heterogeneous 2-dimensional distribution of the biological reactive solutes (Ziebis et al., 1996). The concurrent inflow of bottom water and outflow of porewater accelerates the benthic pelagic coupling.

Advection also transports particulate organic matter into the sediment and makes it available to benthic microbial communities (Huettel et al., 1996). As sandy sediments are generally located in regions of strong hydrodynamic forcing, gravitational settling of organic matter is limited. Therefore, the advection through the sediment-water interface is an important mechanism supplying electron donors from the water column to the microbes in the sandy sediment (Ehrenhauss and Huettel, 2004). This intensifies the metabolic activity in terms of volumetric reaction rates (Huettel and Rusch, 2000). However, as the porewater velocity decreases vertically, the organic particles are likely to be filtered out within the first few centimeter. This leads to partially suppressed porewater advection as the pore space becomes clogged (Huettel et al., 2014). Permeability is then reduced and the supply of solutes is hindered. Clogging might be attenuated by the migration of bedforms which has been shown to expose particulate organic matter to the sediment surface which is then re-suspended (Pilditch and Miller, 2006).

Despite the fact that bedforms are mobile features of the seafloor the relevance of this specific sediment transport for the biogeochemical cycling is not known. From modelling

studies it was proposed that the migration of bedforms leads to a release of porewater at the stoss side where sediment gets eroded, and trapping at the lee side, where sediment deposits (Elliott and Brooks, 1997*b*; Rutherford et al., 1993). This leads to another mode in which electron acceptors and donors are supplied to benthic communities (Santos et al., 2012). From flume experiments it was proposed that with the migrating bedform, i.e. moving pressure gradient, the zone of advection changes dynamically which promotes changes of the redox conditions. Additionally, when bedform migration exceeds the transport timescales of porewater advection a redox seal forms (Precht et al., 2004). However, the hypotheses are based on qualitative insights and were not quantified. Mechanistically the interaction of porewater advection, bedform migration and reactions rates is not understood.

The tight coupling between water column and benthic processes leads to a highly variable environment providing a high diversity of redox conditions within sandy sediments (Huettel et al., 2003; Hunter et al., 2006). The vast majority of the microbial communities live attached to sand grains (Rusch et al., 2003; Gobet et al., 2012), but frequent mobilization of sandy sediments leads to mechanical abrasion and forces the microbes into cracks and depressions (Weise and Rheinheimer, 1977; Miller, 1989). In these microenvironments the microbes are subject to varying chemical gradients which were found to promote metabolic adaptations on a community level (Gobet et al., 2012) and specific metabolic pathways (Gao et al., 2010). The variations are triggered on time scales of minutes to hours, i.e. tidal fluctuations, and on time scales of weeks to month such as seasonal variations, i.e. primary production in the water column. The fluctuations on short timescale have been shown to promote metabolic pathways that are not strictly coupled to the availability of the electron acceptor with the highest electron affinity. Such an example is denitrification under aerobic conditions as found in intertidal sandy sediments (Gao et al., 2010). On longer timescales, the largest proportion of the community structure adapts to the seasonal fluctuations related to the primary productivity. Community structures were found to be highly diverse and not adapted to certain electron acceptors (Gobet et al., 2012).

In situ evidence of the solute distributions in permeable sediments are rare. However, recent technical improvements, including benthic chamber incubations (Janssen, Faerber, Huettel, Meyer and Witte, 2005) and eddy covariance measurements (Berg et al., 2003) allowed for quantification of net oxygen fluxes. The systems support the proposed high remineralization rates within sandy sediments (Huettel et al., 2014) and the coupling to physical parameters including bottom water velocities and permeability (McGinnis et al., 2014; Janssen, Huettel and Witte, 2005). Nevertheless, the instruments do not allow for a mechanistic understanding of transport processes including estimation of carbon

rem mineralization and nutrient turnover. Further, by using a simplified upscaling of measured reaction rates it has been estimated that denitrification in sandy sediments substantially contributes to n-loss in intertidal systems (Gao et al., 2012; Marchant et al., 2014). But, the estimates are very rough and models are needed that simplify quantifications.

Due to rapid pore water exchange and intensified transport of oxidized and reduced reactants, sandy sediments function as a biocatalytic filter which is highly efficient in organic matter remineralization and nutrient turnover. However, investigations thus far have mostly focused on flume experiments and modelling studies for a very confined range of stationary boundary conditions. Therefore, only little is known about the redox conditions that occur under a transient forcing, induced by tides and wind-driven waves, as found on continental shelves. Transient forcing induces changing bottom water velocities but also leads to regular events of sediment mobilization, i.e. bedform migration. The interaction of migrating bedforms with transport processes and microbial reactions is not understood. The highly variable hydrodynamics and morphodynamics on the inner continental shelf complicate the assessment of the dynamic habitat and, for this reason, the development of instruments and models that are capable of resolving the high temporal and spatial variation of the solute distributions are needed.

1.4 Aim and Outline of the Thesis

The introduction provided a short outline of benthic remineralization and nutrient turnover on continental shelves with special emphasis on the transport processes that stimulate the biogeochemical reactions. The focus was on sandy sediments as they cover the largest portion of the shelf area. The high permeability of sand allows for advection through the pore space which leads to an intensified benthic-pelagic coupling and accelerated benthic biogeochemical cycling. As mentioned, sands are typically situated in regions of strong hydrodynamic forcing and are regularly mobilized. Our knowledge about how biogeochemical processes are regulated under such dynamic conditions is limited since subtidal measurements are lacking and models cover only a confined range of boundary conditions.

This doctoral thesis work investigates the regulation of benthic oxygen fluxes by transport processes and microbial respiration in sandy sediments. In an integrated approach, state-of-the-art methods were developed combining numerical models, in situ measurements and ex situ experiments. Within the last 3.5 years, six cruises were conducted in the German Bight to apply these methods. A substantial part of the work was dedicated to the development of appropriate methods including programming, mathematics and

experiments, in order to answer the scientific questions. The results are presented and discussed in five manuscripts.

Though we know that large areas of the seafloor are regularly mobilized, the impact of sediment transport on solute fluxes is not well understood. In a first study bedform migration, the most prominent type of sediment transport, was introduced into the transport-reaction equations. A large variety of bottom water velocities and sediment characteristics were tested in a numerical model. More than a thousand model runs were performed in order to systematically describe and quantify oxygen distributions with a special focus on net oxygen fluxes.

Only a few published studies include oxygen profiles from subtidal sandy sediments. These profiles are spatially and temporally limited and are not correlated with surface topographies nor the hydrodynamic forcing. In consequence, our knowledge about regulation mechanisms of oxygen transport under in situ conditions is limited. Therefore, the benthic observatory 'LanceALot' was developed that allows for simultaneous acquisition of oxygen profiles, topography scans and current velocities over a tidal cycle. The results from four cruises and 16 deployments are presented in the second manuscript, covering most of the sediment types and current velocities as found in the German Bight. The in situ measurements were supplemented by ex situ rate measurements which allowed, in combination with the oxygen penetration depth, for oxygen flux estimations. Within the second manuscript the controlling mechanisms of oxygen fluxes are intensively discussed and the mechanistic model derived in the first manuscript is tested to investigate the predictability of oxygen fluxes.

Microbial reaction rates largely contribute to biogeochemical fluxes. These rates are typically measured, but little is known about their regulation, thus complicating their parameterization in models. The aim of the third manuscript was to identify the regulatory mechanisms for oxygen respiration within sandy sediments. Therefore, manipulative experiments were conducted in flow-through-reactors. Measurements of sediment characteristics such as surface to volume ratio, permeability, dispersion and porosity were supplemented by microbial rate measurements and bacterial cell counts. Additionally, the specific colonization of sand grains was investigated.

Sandy sediments on continental shelves are an important sink for nitrogen. The aim of two additional manuscripts was to improve our understanding of nitrogen cycling within sandy sediments. In the first of the two additional manuscripts the aim was to determine the contribution of the various nitrogen transformations to the total nitrogen-loss in the German Bight. Therefore, a model which was derived in the first and second manuscript was applied to determine nitrogen-fluxes based on measured microbial reaction rates.

The second of the two additional manuscripts focuses on denitrification under aerobic conditions. In the second manuscript the variable redox zone was identified, in which regular changes of oxic and anoxic conditions occur. These conditions were hypothesized to promote metabolic adaptations such as aerobic denitrification. In order to investigate these metabolic adaptations the variable redox conditions were simulated in manipulative experiments and denitrification rates were determined.

The overarching aims of this thesis were to improve our mechanistic understanding of oxygen fluxes and to identify the regulatory mechanisms of transport and respiration in sandy sediments. These are discussed in the final chapter with special focus on the environmental implications. The discussion is supplemented by a quantification of benthic remineralization and nitrogen-loss within the German Bight.

1.5 North Sea

Investigations were carried out in the subtidal of the German Bight which is the southeastern part of the North Sea. With 575000 km² the North Sea constitutes the largest portion of the European Shelf representing 2% of global shelf area. As a marginal shelf the North Sea is encompassed by France, Belgium, Netherlands, Germany, Scandinavia and Great Britain (Otto et al., 1990). The average water depth of 90 m leads to a strong hydrodynamic forcing which is mainly induced by semi-diurnal tides rotating anti-clockwise around three amphidromic points (compare Figure 1.3) (Pugh, 1996). The tidal amplitude in coastal regions varies from 0.12 m off the Norwegian coast to 3.8 m off Eastern England (Otto et al., 1990). The pressure gradients induced by the tidal waves generate surface currents in between 0.2 m s⁻¹ in deep regions and 1 m s⁻¹ in coastal waters. Wind-driven surface gravity waves contribute substantially to the current velocities especially in the southern North Sea where wind-waves interact with the seafloor (Coelingh et al., 1996; Grashorn et al., 2015).

The seafloor is mostly composed of relict silica and silt sediments (Figure 1.3) transported during the last glacial period. Exposed to the strong hydrodynamic forcing the sediments undergo frequent re-distribution and sorting, which leaves behind coarser grained sediments and forces finer sediments into regions with reduced hydrodynamic forcing (De Jonge and Van Beusekom, 1995; Guillen and Hoekstra, 1997; Guillén and Hoekstra, 1996). This is typically in proximity of the amphidromic points and deeper waters such as the Skagerrak in between Denmark and Norway, where the North Sea reaches down to more than 700 m.

Water mass exchange takes mainly place through the English Channel and northern opening of the North Sea. Based on the origin, the water masses can be loosely separated into two main types: German Bight water (or English Channel water) and North Atlantic water (Kempe and Pegler, 1991; Reid et al., 1993). The water masses are subject to a different nutrient loading and differ considerably in their characteristics in terms of carbon fixation and carbon remineralization. The water masses in the northern North Sea - above 56° N - are characterized by strong exchanges with the North Atlantic. Therefore, nutrient concentrations are relatively low as riverine discharges have a minor contribution (Ducrottoy et al., 2000). Additionally, the large water depths of more than 80 m strongly dilute the water fraction that arrives in the central and northern North Sea. This leads to carbon fixation rates that cover the lower end of the North Sea (10 mol m⁻² y⁻¹) (van Beusekom and Diel-Christiansen, 1994; Moll, 1998). However, despite low carbon fixation rates the carbon dioxide export is high (1.5 mol m⁻² y⁻¹) (Thomas et al., 2004).

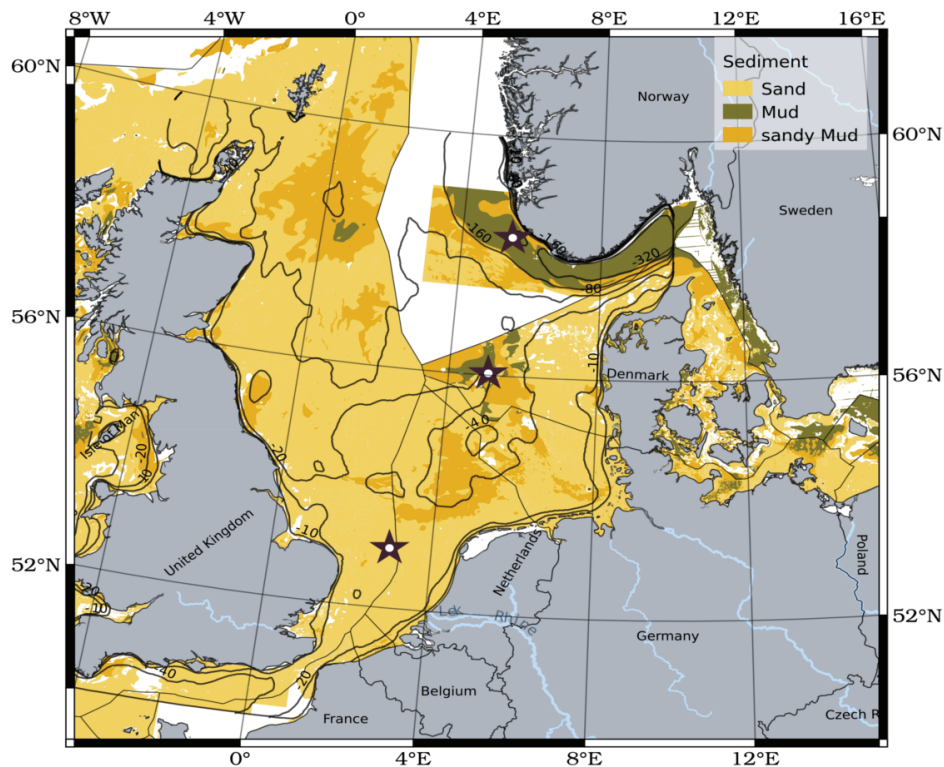


Figure 1.3: The North Sea sediment is depicted in colors while the bathymetry is indicated as black lines where numbers denote the depth in meters. The stars represent the amphidromic points of the North Sea. The gray line indicates the exclusive economic zone of Germany. The map reveals that the seafloor of the North Sea, including the German Bight, is mostly covered by sandy sediment and to a lower extent by muddy sand and mud (after Folk (2000), Data provided by Emodnet Network).

The southern part - below 56° N - of the North Sea is mostly composed of German Bight water. As a result of the low water depth the German Bight water is characterized by strong riverine discharges mainly induced by Rhine ($2900 \text{ m}^3 \text{ s}^{-1}$), Elbe ($870 \text{ m}^3 \text{ s}^{-1}$) and Meuse ($350 \text{ m}^3 \text{ s}^{-1}$) leading to anthropogenic nutrient enrichment fueling high productivity (Lenhart and Pohlmann, 1997). In terms of inorganic nitrogen the total export into the North Sea by rivers equals in average 300 kt y^{-1} but is also highly variable as estimates range from $127 - 1100 \text{ kt y}^{-1}$ (Ducrottoy et al., 2000; Radach and Pättsch, 2007; Johannsen et al., 2008). These riverine runoffs coincide with strong primary productivity with an estimated annual carbon fixation rate of $31 \text{ mol m}^{-2} \text{ y}^{-1}$ (Wollast, 1991). The high primary production within coastal waters reduces nutrients from coastal waters towards the open seas (Gerlach, 1981). As a result of the low average water depths (mostly below 50 m) water column remineralization is limited and a large portion of the organic carbon reaches the seafloor. However, despite intense plankton blooms and large export the carbon burial is relatively low and was found to range in between $0 - 0.5 \text{ mol m}^{-2} \text{ y}^{-1}$. In the English

Channel the North Sea was even identified as a source for carbon dioxide (Thomas et al., 2004). This indicates that a large portion of the organic carbon is remineralized within the sediments.

1.6 Bibliography

Allredge, A. L. and Silver, M. W. (1988), 'Characteristics, dynamics and significance of marine snow', *Progress in oceanography* **20**(1), 41–82.

Aller, R. C. (1994), 'Bioturbation and remineralization of sedimentary organic matter: effects of redox oscillation', *Chemical Geology* **114**(3), 331–345.

Bacon, M., Belastock, R. A. and Bothner, M. H. (1994), '210 pb balance and implications for particle transport on the continental shelf, us middle atlantic bight', *Deep Sea Research Part II: Topical Studies in Oceanography* **41**(2), 511–535.

Bear, J. and Buchlin, J.-M. (1978), 'Modelling and applications of transport phenomena in porous media', **5**.

Behrenfeld, M. J. and Falkowski, P. G. (1997), 'Photosynthetic rates derived from satellite-based chlorophyll concentration', *Limnology and oceanography* **42**(1), 1–20.

Berg, J. H. (1987), 'Bedform migration and bed-load transport in some rivers and tidal environments', *Sedimentology* **34**(4), 681–698.

Berg, P., Risgaard-Petersen, N. and Rysgaard, S. (1998), 'Interpretation of measured concentration profiles in sediment pore water', *Limnology and Oceanography* **43**(7), 1500–1510.

Berg, P., Røy, H., Janssen, F., Meyer, V., Jörgensen, B. B., Huettel, M. and De Beer, D. (2003), 'Oxygen uptake by aquatic sediments measured with a novel non-invasive eddy-correlation technique', *Marine Ecology Progress Series* **261**(1), 75–83.

Bernoulli, D. (1738), *Hydrodynamica sive de viribus et motibus fluidorum commentarii*, Johann Reinhold Dulsecker.

Bottacin-Busolin, A. and Marion, A. (2010), 'Combined role of advective pumping and mechanical dispersion on time scales of bed form-induced hyporheic exchange', *Water Resources Research* **46**(8).

- Böttcher, M. E., Hespeneide, B., Llobet-Brossa, E., Beardsley, C., Larsen, O., Schramm, A., Wieland, A., Böttcher, G., Berninger, U.-G. and Amann, R. (2000), 'The biogeochemistry, stable isotope geochemistry, and microbial community structure of a temperate intertidal mudflat: an integrated study', *Continental Shelf Research* **20**(12), 1749–1769.
- Boudreau, B. P. (1996), 'The diffusive tortuosity of fine-grained unlithified sediments', *Geochimica et Cosmochimica Acta* **60**(16), 3139–3142.
- Boudreau, B. P. (1997), *Diagenetic models and their implementation*, Vol. 505, Springer Berlin.
- Boudreau, B. P., Huettel, M., Forster, S., Jahnke, R. A., McLachlan, A., Middelburg, J. J., Nielsen, P., Sansone, F., Taghon, G., Van Raaphorst, W., Webster, I., Weslawski, J. M., Wiberg, P. and Sundby, B. (2001), 'Permeable marine sediments: Overturning an old paradigm', *Eos, Transactions American Geophysical Union* **82**(11), 133–136.
- Canfield, D. E., Kristensen, E. and Thamdrup, B. (2005), *Aquatic geomicrobiology*, Gulf Professional Publishing.
- Cardenas, M. B. and Wilson, J. L. (2007), 'Dunes, turbulent eddies, and interfacial exchange with permeable sediments', *Water Resources Research* **43**(8).
- Codispoti, L. and Christensen, J. (1985), 'Nitrification, denitrification and nitrous oxide cycling in the eastern tropical south pacific ocean', *Marine Chemistry* **16**(4), 277–300.
- Coelingh, J., Van Wijk, A. and Holtslag, A. (1996), 'Analysis of wind speed observations over the north sea', *Journal of Wind Engineering and Industrial Aerodynamics* **61**(1), 51–69.
- D'Andrea, A. F., Lopez, G. R. and Aller, R. C. (2004), 'Rapid physical and biological particle mixing on an intertidal sandflat', *Journal of Marine Research* **62**(1), 67–92.
- De Groot, S. (1984), 'The impact of bottom trawling on benthic fauna of the north sea', *Ocean management* **9**(3), 177–190.
- de Haas, H., van Weering, T. C. and de Stigter, H. (2002), 'Organic carbon in shelf seas: sinks or sources, processes and products', *Continental Shelf Research* **22**(5), 691–717.
- De Jonge, V. and Van Beusekom, J. (1995), 'Wind-and tide-induced resuspension of sediment and microphytobenthos from tidal flats in the ems estuary', *Limnology and oceanography* **40**(4), 766–778.

- DeFlaun, M. F. and Mayer, L. M. (1983), 'Relationships between bacteria and grain surfaces in intertidal sediments', *Limnology and Oceanography* **28**(5), 873–881.
- deVries Klein, G. (1970), 'Depositional and dispersal dynamics of intertidal sand bars', *Journal of Sedimentary Research* **40**(4).
- Ducklow, H. W., Steinberg, D. K. and Buesseler, K. O. (2001), 'Upper ocean carbon export and the biological pump', *OCEANOGRAPHY-WASHINGTON DC-OCEANOGRAPHY SOCIETY-* **14**(4), 50–58.
- Ducrottoy, J.-P., Elliott, M. and de Jonge, V. N. (2000), 'The north sea', *Marine Pollution Bulletin* **41**(1), 5–23.
- Ehrenhauss, S. and Huettel, M. (2004), 'Advective transport and decomposition of chain-forming planktonic diatoms in permeable sediments', *Journal of Sea Research* **52**(3), 179–197.
- Einstein, A. (1905), 'über die von der molekularkinetischen theorie der wärme geforderte bewegung von in ruhenden flüssigkeiten suspendierten teilchen.', *Annalen der Physik* **324**(2), 289–306.
- Einstein, H. A. (1950), *The bed-load function for sediment transportation in open channel flows*, number 1026, US Department of Agriculture.
- Elliott, A. H. and Brooks, N. H. (1997a), 'Transfer of nonsorbing solutes to a streambed with bed forms: Laboratory experiments', *Water Resources Research* **33**(1), 137–151.
- Elliott, A. H. and Brooks, N. H. (1997b), 'Transfer of nonsorbing solutes to a streambed with bed forms: Theory', *Water Resources Research* **33**(1), 123–136.
- Emery, K. (1968), 'Relict sediments on continental shelves of world', *AAPG Bulletin* **52**(3), 445–464.
- Erismann, J. W., Bleeker, A., Galloway, J. and Sutton, M. (2007), 'Reduced nitrogen in ecology and the environment', *Environmental Pollution* **150**(1), 140–149.
- Fasham, M. J. (2003), *Ocean biogeochemistry: the role of the ocean carbon cycle in global change*, Springer Science & Business Media.
- Fehlman, H. M. (1985), 'Resistance components and velocity distributions of open channel flows over bedforms', *Phd Thesis* .

- Fick, A. (1855), 'Ueber diffusion', *Annalen der Physik* **170**(1), 59–86.
- Fleming, K., Johnston, P., Zwartz, D., Yokoyama, Y., Lambeck, K. and Chappell, J. (1998), 'Refining the eustatic sea-level curve since the last glacial maximum using far-and intermediate-field sites', *Earth and Planetary Science Letters* **163**(1), 327–342.
- Folk, R. L. (2000), 'Petrology of sedimentary rocks'.
- Gagan, M., Chivas, A. and Johnson, D. (1988), 'Cyclone-induced shelf sediment transport and the ecology of the great barrier reef.'
- Gao, H., Matyka, M., Liu, B., Khalili, A., Kostka, J. E., Collins, G., Jansen, S., Holtappels, M., Jensen, M. M. and Badewien, T. H. (2012), 'Intensive and extensive nitrogen loss from intertidal permeable sediments of the wadden sea', *Limnology and Oceanography* **57**(1), 185.
- Gao, H., Schreiber, F., Collins, G., Jensen, M. M., Kostka, J. E., Lavik, G., de Beer, D., Zhou, H.-y. and Kuypers, M. M. (2010), 'Aerobic denitrification in permeable wadden sea sediments', *The ISME journal* **4**(3), 417–426.
- Gattuso, J.-P., Frankignoulle, M. and Wollast, R. (1998), 'Carbon and carbonate metabolism in coastal aquatic ecosystems', *Annual Review of Ecology and Systematics* pp. 405–434.
- George, D. A. and Hill, P. S. (2008), 'Wave climate, sediment supply and the depth of the sand–mud transition: a global survey', *Marine Geology* **254**(3), 121–128.
- Gerlach, S. A. (1981), 'Marine pollution'.
- Glud, R. N. (2008), 'Oxygen dynamics of marine sediments', *Marine Biology Research* **4**(4), 243–289.
- Glud, R. N., Berg, P., Fossing, H. and Jørgensen, B. B. (2007), 'Effect of the diffusive boundary layer on benthic mineralization and o₂ distribution: A theoretical model analysis', *Limnology and Oceanography* **52**(2), 547–557.
- Gobet, A., Böer, S. I., Huse, S. M., van Beusekom, J. E., Quince, C., Sogin, M. L., Boetius, A. and Ramette, A. (2012), 'Diversity and dynamics of rare and of resident bacterial populations in coastal sands', *The ISME journal* **6**(3), 542–553.

- Grashorn, S., Lettmann, K. A., Wolff, J.-O., Badewien, T. H. and Stanev, E. V. (2015), 'East frisian wadden sea hydrodynamics and wave effects in an unstructured-grid model', *Ocean Dynamics* **65**(3), 419–434.
- Gross, M. G. (1977), 'Oceanography: A view of the earth'.
- Guillén, J. and Hoekstra, P. (1996), 'The "equilibrium" distribution of grain size fractions and its implications for cross-shore sediment transport: a conceptual model', *Marine Geology* **135**(1), 15–33.
- Guillen, J. and Hoekstra, P. (1997), 'Sediment distribution in the nearshore zone: Grain size evolution in response to shoreface nourishment (island of terschelling, the netherlands)', *Estuarine, Coastal and Shelf Science* **45**(5), 639–652.
- Hayes, M. O. (1967), 'Relationship between coastal climate and bottom sediment type on the inner continental shelf', *Marine Geology* **5**(2), 111–132.
- Huettel, A., Ziebis, W. and Forster, S. (1996), 'Flow-induced uptake of particulate matter in permeable sediments', *Limnology & Oceanography* **41**, 309–322.
- Huettel, M., Berg, P. and Kostka, J. E. (2014), 'Benthic exchange and biogeochemical cycling in permeable sediments', *Marine Science* **6**.
- Huettel, M., Røy, H., Precht, E. and Ehrenhauss, S. (2003), Hydrodynamical impact on biogeochemical processes in aquatic sediments, in 'The Interactions between Sediments and Water', Springer, pp. 231–236.
- Huettel, M. and Rusch, A. (2000), 'Transport and degradation of phytoplankton in permeable sediment', *Limnology and Oceanography* **45**(3), 534–549.
- Hunter, E. M., Mills, H. J. and Kostka, J. E. (2006), 'Microbial community diversity associated with carbon and nitrogen cycling in permeable shelf sediments', *Applied and Environmental Microbiology* **72**(9), 5689–5701.
- Huthnance, J. (1981), 'Waves and currents near the continental shelf edge', *Progress in Oceanography* **10**(4), 193–226.
- Jahnke, R. A. (2010), Global synthesis, in 'Carbon and Nutrient Fluxes in Continental Margins', Springer, pp. 597–615.

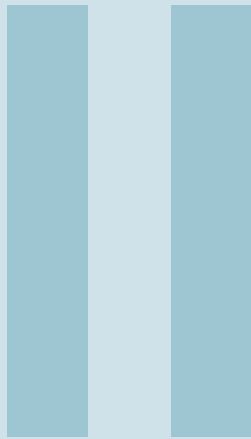
- Janssen, F., Cardenas, M. B., Sawyer, A. H., Dammrich, T., Krietsch, J. and de Beer, D. (2012), 'A comparative experimental and multiphysics computational fluid dynamics study of coupled surface–subsurface flow in bed forms', *Water Resources Research* **48**(8), n/a–n/a. W08514.
- Janssen, F., Faerber, P., Huettel, M., Meyer, V. and Witte, U. (2005), 'Pore-water advection and solute fluxes in permeable marine sediments (ii): Benthic respiration at three sandy sites with different permeabilities (german bight, north sea)', *Limnology and Oceanography* **50**(3), 779–792.
- Janssen, F., Huettel, M. and Witte, U. (2005), 'Pore-water advection and solute fluxes in permeable marine sediments (i): Calibration and performance of the novel benthic chamber system sandy', *Limnology and Oceanography* **50**(3), 779–792.
- Johannsen, A., Dähnke, K. and Emeis, K. (2008), 'Isotopic composition of nitrate in five german rivers discharging into the north sea', *Organic Geochemistry* **39**(12), 1678–1689.
- Jørgensen, B. B. (2000), Bacteria and marine biogeochemistry, in 'Marine geochemistry', Springer, pp. 173–207.
- Kelly-Gerreyn, B., Hydes, D. and Waniek, J. (2005), 'Control of the diffusive boundary layer on benthic fluxes: A model study', *Marine Ecology Progress Series* **292**, 61–74.
- Kempe, S. and Pegler, K. (1991), 'Sinks and sources of co₂ in coastal seas: the north sea', *Tellus B* **43**(2), 224–235.
- Kessler, A. J., Glud, R. N., Cardenas, M. B. and Cook, P. L. M. (2013), 'Transport zonation limits coupled nitrification-denitrification in permeable sediments', *Environmental Science & Technology* **47**(23), 13404–13411.
- Kjørboe, T. (2001), 'Formation and fate of marine snow: small-scale processes with large-scale implications', *Scientia marina* **65**(S2), 57–71.
- Knaapen, M., van Bergen Henegouw, C. and Hu, Y. (2005), 'Quantifying bedform migration using multi-beam sonar', *Geo-marine letters* **25**(5), 306–314.
- Kristensen, E. and Blackburn, T. (1987), 'The fate of organic carbon and nitrogen in experimental marine sediment systems: influence of bioturbation and anoxia', *Journal of Marine Research* **45**(1), 231–257.
- Krumbein, W., Monk, G. et al. (1943), 'Permeability as a function of the size parameters of unconsolidated sand', *Transactions of the AIME* **151**(01), 153–163.

- Lenhart, H.-J. and Pohlmann, T. (1997), 'The ices-boxes approach in relation to results of a north sea circulation model', *Tellus A* **49**(1), 139–160.
- Lettmann, K. A., Riedinger, N., Ramlau, R., Knab, N., Böttcher, M. E., Khalili, A., Wolff, J.-O. and Jørgensen, B. B. (2012), 'Estimation of biogeochemical rates from concentration profiles: A novel inverse method', *Estuarine, Coastal and Shelf Science* **100**, 26–37.
- Llobet-Brossa, E., Rabus, R., Böttcher, M. E., Könneke, M., Finke, N., Schramm, A., Meyer, R. L., Grötzschel, S., Rosselló-Mora, R. and Amann, R. (2002), 'Community structure and activity of sulfate-reducing bacteria in an intertidal surface sediment: a multi-method approach', *Aquatic Microbial Ecology* **29**(3), 211–226.
- Llobet-Brossa, E., Rosselló-Mora, R. and Amann, R. (1998), 'Microbial community composition of wadden sea sediments as revealed by fluorescence in situ hybridization', *Applied and environmental microbiology* **64**(7), 2691–2696.
- Lorke, A., Muller, B., Maerki, M. and Wuest, A. (2003), 'Breathing sediments: The control of diffusive transport across the sediment-water interface by periodic boundary-layer turbulence', *Limnology and Oceanography* **48**(6), 2077–2085.
- Malone, T. C., Hopkins, T. S., Falkowski, P. G. and Whitedge, T. E. (1983), 'Production and transport of phytoplankton biomass over the continental shelf of the new york bight', *Continental Shelf Research* **1**(4), 305–337.
- Mann, K. H. and Lazier, J. R. (2013), *Dynamics of marine ecosystems: biological-physical interactions in the oceans*, John Wiley & Sons.
- Marchant, H. K., Lavik, G., Holtappels, M. and Kuypers, M. M. (2014), 'The fate of nitrate in intertidal permeable sediments', *PloS one* **9**(8), e104517.
- Matyka, M., Khalili, A. and Koza, Z. (2008), 'Tortuosity-porosity relation in porous media flow', *Physical Review E* **78**(2), 026306.
- McCave, I. (2002), Sedimentary settings on continental margins—an overview, in 'Ocean margin systems', Springer, pp. 1–14.
- McGinnis, D. F., Sommer, S., Lorke, A., Glud, R. N. and Linke, P. (2014), 'Quantifying tidally driven benthic oxygen exchange across permeable sediments: An aquatic eddy correlation study', *Journal of Geophysical Research: Oceans* **119**(10), 6918–6932.

- Meysman, F. J., Middelburg, J. J. and Heip, C. H. (2006), 'Bioturbation: a fresh look at darwin's last idea', *Trends in Ecology & Evolution* **21**(12), 688–695.
- Middelburg, J. J., Soetaert, K., Herman, P. M. and Heip, C. H. (1996), 'Denitrification in marine sediments: A model study', *Global Biogeochemical Cycles* **10**(4), 661–673.
- Miller, D. (1989), 'Abrasion effects on microbes in sandy sediments.', *Marine ecology progress series. Oldendorf* **55**(1), 73–82.
- Moll, A. (1998), 'Regional distribution of primary production in the north sea simulated by a three-dimensional model', *Journal of Marine Systems* **16**(1), 151–170.
- Nelson, J. R., Eckman, J. E., Robertson, C. Y., Marinelli, R. L. and Jahnke, R. A. (1999), 'Benthic microalgal biomass and irradiance at the sea floor on the continental shelf of the south atlantic bight: Spatial and temporal variability and storm effects', *Continental Shelf Research* **19**(4), 477–505.
- Nittroer, C. A. and Wright, L. D. (1994), 'Transport of particles across continental shelves', *Reviews of Geophysics* **32**(1), 85–113.
- Oliver, J. S., Kvitek, R. G. and Slattery, P. N. (1985), 'Walrus feeding disturbance: scavenging habits and recolonization of the bering sea benthos', *Journal of Experimental Marine Biology and Ecology* **91**(3), 233–246.
- Otto, L., Zimmerman, J., Furnes, G., Mork, M., Saetre, R. and Becker, G. (1990), 'Review of the physical oceanography of the north sea', *Netherlands Journal of Sea Research* **26**(2), 161–238.
- Pilditch, C. A. and Miller, D. C. (2006), 'Phytoplankton deposition to permeable sediments under oscillatory flow: Effects of ripple geometry and resuspension', *Continental Shelf Research* **26**(15), 1806 – 1825.
- Pinet, P. R. (2011), *Invitation to oceanography*, Jones & Bartlett Publishers.
- Pope, S. (2000), *Turbulent Flows*, Cambridge University Press.
- Precht, E., Franke, U., Polerecky, L. and Huettel, M. (2004), 'Oxygen dynamics in permeable sediments with wave-driven pore water exchange', *Limnology and Oceanography* **49**(3), 693–705.
- Pugh, D. T. (1996), *Tides, surges and mean sea-level (reprinted with corrections)*, John Wiley & Sons Ltd.

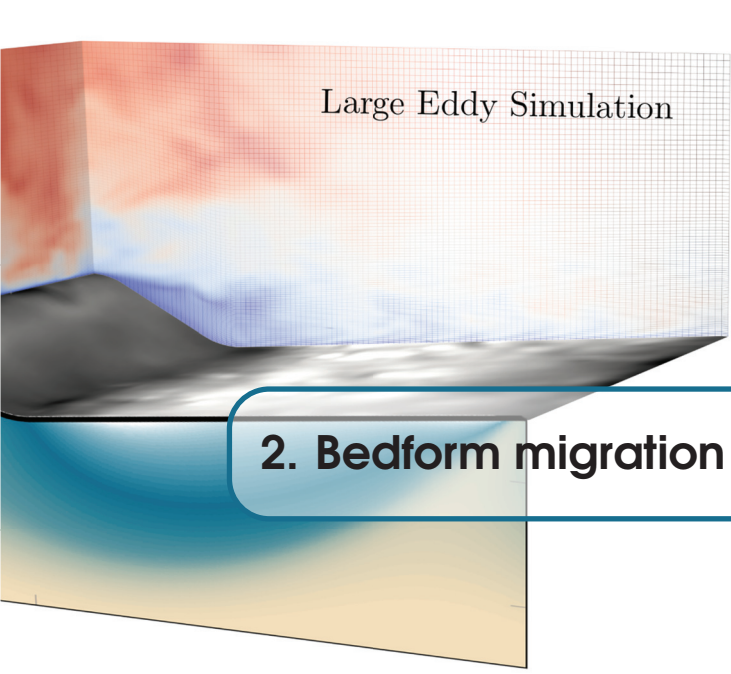
- Radach, G. and Pätsch, J. (2007), 'Variability of continental riverine freshwater and nutrient inputs into the north sea for the years 1977–2000 and its consequences for the assessment of eutrophication', *Estuaries and Coasts* **30**(1), 66–81.
- Rasmussen, H. and Jørgensen, B. B. (1992), 'Microelectrode studies of seasonal oxygen uptake in a coastal sediment: Role of molecular diffusion.', *Marine ecology progress series. Oldendorf* **81**(3), 289–303.
- Ravenschlag, K., Sahm, K. and Amann, R. (2001), 'Quantitative molecular analysis of the microbial community in marine arctic sediments (svalbard)', *Applied and Environmental Microbiology* **67**(1), 387–395.
- Reid, P., Taylor, A. and Stephens, J. (1993), The hydrography and hydrographic balances of the north sea, in 'Pollution of the North Sea', Springer, pp. 3–19.
- Reimers, C. E., Stecher III, H. A., Taghon, G. L., Fuller, C. M., Huettel, M., Rusch, A., Ryckelynck, N. and Wild, C. (2004), 'In situ measurements of advective solute transport in permeable shelf sands', *Continental Shelf Research* **24**(2), 183–201.
- Rusch, A., Huettel, M., Reimers, C. E., Taghon, G. L. and Fuller, C. M. (2003), 'Activity and distribution of bacterial populations in middle atlantic bight shelf sands', *FEMS Microbiology Ecology* **44**(1), 89–100.
- Rutherford, J., Latimer, G. and Smith, R. (1993), 'Bedform mobility and benthic oxygen uptake', *Water Res* **27**(10), 1545–1558.
- Santos, I. R., Eyre, B. D. and Huettel, M. (2012), 'The driving forces of porewater and groundwater flow in permeable coastal sediments: A review', *Estuarine, Coastal and Shelf Science* **98**, 1–15.
- Schwiderski, E. W. (1980), 'On charting global ocean tides', *Reviews of Geophysics* **18**(1), 243–268.
- Sverdrup, H. U., Johnson, M. W., Fleming, R. H. et al. (1942), *The Oceans: Their physics, chemistry, and general biology*, Vol. 7, Prentice-Hall New York.
- Thamdrup, B., Hansen, J. W. and Jørgensen, B. B. (1998), 'Temperature dependence of aerobic respiration in a coastal sediment', *FEMS Microbiology Ecology* **25**(2), 189–200.
- Thibodeaux, L. J. and Boyle, J. D. (1987), 'Bedform-generated convective transport in bottom sediment'.

- Thomas, H., Bozec, Y., Elkalay, K. and De Baar, H. J. (2004), 'Enhanced open ocean storage of CO₂ from shelf sea pumping', *Science* **304**(5673), 1005–1008.
- Traykovski, P. (2007), 'Observations of wave orbital scale ripples and a nonequilibrium time-dependent model', *Journal of Geophysical Research: Oceans (1978–2012)* **112**(C6).
- Traykovski, P., Hay, A. E., Irish, J. D. and Lynch, J. F. (1999), 'Geometry, migration, and evolution of wave orbital ripples at leo-15', *Journal of Geophysical Research: Oceans* **104**(C1), 1505–1524.
- van Beusekom, J. and Diel-Christiansen, S. (1994), *A synthesis of phyto and zooplankton dynamics in the North Sea environment*.
- Viollier, E., Rabouille, C., Apitz, S., Breuer, E., Chaillou, G., Dedieu, K., Furukawa, Y., Grenz, C., Hall, P., Janssen, F. et al. (2003), 'Benthic biogeochemistry: state of the art technologies and guidelines for the future of in situ survey', *Journal of Experimental Marine Biology and Ecology* **285**, 5–31.
- Walsh, J. J. (1991), 'Importance of continental margins in the marine biogeochemical cycling of carbon and nitrogen', *Nature* **350**(6313), 53–55.
- Weise, W. and Rheinheimer, G. (1977), 'Scanning electron microscopy and epifluorescence investigation of bacterial colonization of marine sand sediments', *Microbial Ecology* **4**(3), 175–188.
- Wollast, R. (1991), 'The coastal organic carbon cycle: fluxes, sources and sinks', *Ocean margin processes in global change* pp. 365–381.
- Wollast, R. (1998), 'Evaluation and comparison of the global carbon cycle in the coastal zone and in the open ocean', *The sea* **10**, 213–252.
- Yalin, M. (1972), *Mechanics of Sediment Transport*, Vol. 1, Pergamon Press.
- Yalin, M. S. (1985), 'On the determination of ripple geometry', *Journal of Hydraulic Engineering* **111**(8), 1148–1155.
- Ziebis, W., Huettel, M. and Forster, S. (1996), 'Impact of biogenic sediment topography on oxygen fluxes in permeable seabeds', *Marine Ecology Progress Series* **140**, 227–237.



Manuscripts

| | | |
|----------|---|------------|
| 2 | Bedform migration and benthic oxygen fluxes | 47 |
| 3 | Oxygen dynamics in subtidal sands | 81 |
| 4 | Regulation of microbial respiration in sands .. | 123 |
| 5 | Coupled nitrification-denitrification in sands . | 147 |
| 6 | Aerobic denitrification in sands | 185 |



Large Eddy Simulation

2. Bedform migration and benthic oxygen fluxes

The impact of bedform migration on benthic oxygen fluxes

Soeren Ahmerkamp

Max Planck Institute for Marine Microbiology, Bremen, Germany

Christian Winter

MARUM Center for Marine Environmental Sciences, Bremen, Germany

Felix Janssen^{1,2}

Max Planck Institute for Marine Microbiology, Bremen, Germany

Marcel MM Kuypers and Moritz Holtappels³

Max Planck Institute for Marine Microbiology, Bremen, Germany

doi: 10.1175/JPO-D-12-0164.1

Published in: Journal of Geophysical Research Biogeosciences

Additional Affiliations:

¹*Alfred Wegener Institute - Helmholtz Centre for Polar and Marine Research, Bremerhaven, Germany*

²*HGF-MPG Group for Deep Sea Ecology and Technology, Bremen, Germany*

³*MARUM Center for Marine Environmental Sciences, Bremen, Germany*

Contributions to the manuscript:

S.A., and M.H designed research. S.A. performed numerical modelling, mathematics, data analysis and data visualization. F.J. provided experimental data, C.W. provided assistance with mathematics and sediment transport theory. S.A., M.M.M.K. and M.H., conceived, wrote and edited the manuscript.

Abstract

Permeable sediments are found wide spread in river beds and on continental shelves. The transport of these sediments is forced by bottom water currents and leads to the formation of bedforms such as ripples and dunes. The bottom water flow across the bedforms results in pressure gradients that drive porewater flow within the permeable sediment and enhance the supply of reactive substrates for biogeochemical processes. This transport-reaction system has been extensively studied for the case of stationary bedforms, whereas bedform migration - the most ubiquitous form of sediment transport - has been often ignored. To study the impact of sediment transport on porewater flow we incorporated an empirical model of bedform migration into a numerical transport-reaction model for porous media, using oxygen as reactive solute. The modeled oxygen flux changes significantly as soon as the sediment divides into an upper mobile layer (migrating bedform) and a stationary layer underneath. The bedform is increasingly flushed with oxic bottom water, whereas pressure gradients and porewater flow reverse at increasing rate underneath the bedform. This suppresses net porewater displacement and reduces the oxygen penetration depth up to 90%. In effect, the overall oxygen uptake decreases significantly with bedform migration although bottom water velocities increase. This counterintuitive effect is systematically described for a range of different sediment types, current velocities and respiration rates and should be considered in future studies.

2.1 Introduction

Although the coastal ocean comprises less than 20% of the entire ocean area, it sustains more than 50% of the global marine production (Wollast, 1991) and is thus a hotspot for nutrient and organic matter cycling. In coastal areas, shallow water depths and enhanced mixing of the water column result in a tight coupling between pelagic primary production and benthic degradation of organic matter, and thus a fast recycling of nutrients. Exposed to surface gravity waves such as tides and wind-generated waves, coastal sediments undergo frequent re-distribution and sorting, leaving behind coarser grained (sandy) sediments, which cover approximately 50-70% of coastal areas (Huettel et al., 2014; Emery, 1968). The presence of various bedforms, such as dunes and ripples, are indicative of sediment transport and a continuously changing seabed topography (Kösters and Winter, 2014). The interaction of bottom water flow and bedform topography in combination with the high permeability of sandy sediments leads to a pressure-driven advective porewater flow (Thibodeaux and Boyle, 1987) which is most widespread in coastal waters (Santos et al., 2012; Huettel et al., 1996) and rivers (Thibodeaux and Boyle, 1987; Rutherford et al., 1993, 1995). Solute fluxes between the sediment pore space and overlying water may be several orders of magnitude higher compared to diffusion-dominated systems (Huettel et al., 2014). Porewater advection enhances solute exchange but also the influx of particulate organic matter which is retained in the sediment and fuels microbial activity (Huettel and Rusch, 2000). Comprehensive in situ studies have shown that advective porewater flow can cause a 10-fold increase of net oxygen uptake in intertidal sediments (de Beer et al., 2005; Precht et al., 2004). Also, high denitrification rates in these sediments have been reported (Marchant et al., 2014; Gao et al., 2012; Rao et al., 2008; Gao et al., 2010) which may counteract the increased riverine and atmospheric nitrogen input to coastal areas, emphasizing the ecological importance of these sediments.

Using either numerical and analytical models (Cardenas et al., 2008; Grant et al., 2014), flume studies (Precht and Huettel, 2003) or in situ studies (Reimers et al., 2004), the effects of advective porewater flow in permeable sediments have been studied almost exclusively for the case of stationary, i.e. non migrating bedforms. Although bedforms are known to undergo constant changes, only very few flume experiments considered the effect of sediment transport and bedform evolution on benthic microbial processes (Precht et al., 2004), and no systematic studies have been performed so far. Bedform migration needs to be considered to fully address porewater transport but adds another level of complexity and another boundary condition in mass transport modelling. In many model studies boundary conditions are handled independently from each other (Bardini et al., 2012; Kessler et al.,

2013, 2015) even though well established empirical models exist that link for example bedform migration to bottom water velocity or sediment grain diameter to permeability (Coleman and Melville, 1994; Gangi, 1985). Applying these relations reduces the number of possible parameter combinations and allows investigating the integrated response of the porewater flow to changing boundary conditions. To our knowledge there are no systematic quantifications of net fluxes that cover a wide range of natural conditions.

In this model study the dynamic transport of solutes and sediments as found under realistic conditions is simulated by introducing bedform migration to the transport-reaction equation. By non-dimensionalizing transport-reaction equations the range of parameter values is extended to cover a large variety of possible in situ conditions. Empirical models are applied to relate bedform migration and permeability to the median grain size of the sediment, so that the magnitude of the resulting net fluxes are finally controlled by grain size, bottom water velocity and microbial activity (in terms of volumetric respiration rates), i.e., by parameters that may easily be measured and quantified under field conditions.

2.2 Methods

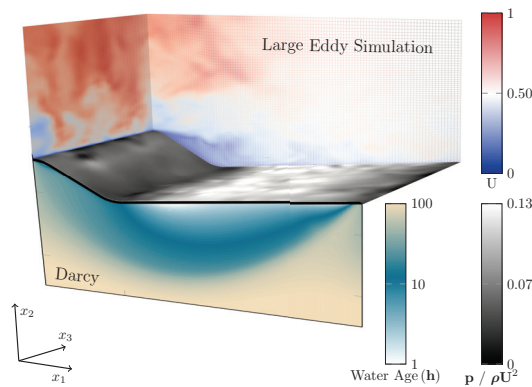


Figure 2.1: Instantaneous bottom water velocity (red to blue) and pressure distribution (black to white) along the bedform for $Re = 2400$. The LES domain is coupled to the Darcy domain via the averaged pressure distribution. The pseudocolors in the Darcy domain indicate the water age.

A multiphysical approach is used that couples a turbulence-resolving, Large Eddy Simulation (LES)-type hydrodynamical model of the bottom water flow with the porewater flow in the porous Darcy domain. The LES domain and the Darcy domain are separated by a single bedform (see figure 2.1). Based on the bedform height η , the dimensions in the water column are in longitudinal direction 10η and in transversal direction 5η . The Darcy domain is two dimensional and extends 15η in vertical direction and 10η in longitudinal

direction. Similar to previous studies (Cardenas and Wilson, 2007), a sequential approach couples the water column - the upper domain - with the benthic domain below. The

pressure distribution along the bedform surface is extracted from the LES model and used as boundary condition for benthic porewater advection which is solved following Darcy's law. The bedform migration is considered in the transport-reaction equation by using a frame of reference that moves at the speed and in direction of the migrating bedform, for which a simple coordinate transformation is sufficient (figure 2.3 b). This approach simplifies the calculations and is physically identical to the use of a moving grid. The migration celerity is determined by an empirical model based on sediment grain size and the bed shear stress, which is directly extracted from the LES model. Another empirical model is used to relate grain size to permeability.

The model equations are used in non-dimensional formulation and their derivation is presented in supporting information S2. In the following, most variables are shown as non-dimensional variables. Dimensional variables are marked by bold characters.

2.2.1 Model formulation

Large Eddy Simulations are used to resolve the turbulent flow above the bedform, the larger energy-containing coherent structures are resolved, and the smaller scales at which energy dissipates are parameterized. Mathematically, this is performed by the spatial filtering of the Navier-Stokes and continuity equation (see also (Scalo et al., 2012a)):

Navier Stokes Equations

$$\frac{\partial \bar{u}_i}{\partial t} + \frac{\partial \bar{u}_i \bar{u}_j}{\partial x_j} = -\frac{\partial \bar{p}}{\partial x_i} + \frac{1}{Re} \frac{\partial^2 \bar{u}_i}{\partial x_j \partial x_j} - \frac{\partial \tau_{ij}}{\partial x_j} - \frac{\mathbf{f}}{\rho \mathbf{U}^2} \delta_{1j} \quad (2.1)$$

$$\frac{\partial \bar{u}_i}{\partial x_i} = 0 \quad (2.2)$$

Here δ_{ij} is the Kronecker delta, $Re = \mathbf{U}\eta/\nu$ is the Reynolds number, where \mathbf{U} is the bottom water velocity (average velocity at the upper boundary), η is the bedform height and ν is the kinematic viscosity of sea water. The spatial coordinates are represented by x_i where x_1 is the longitudinal direction, x_2 is the wall-normal direction and x_3 is the transversal direction. \bar{u}_i is the filtered velocity vector, and t the time. The overbar denotes spatially averaged quantities. Further, ρ is the density, p is the pressure and \mathbf{f} is the forcing term which is a constant longitudinal pressure gradient. $\tau_{ij} = \overline{u_j u_i} - \bar{u}_i \bar{u}_j$ are the subgrid stresses, not resolved by the grid. This subgridscale is modelled by means of a dynamic model using the Lagrangian averaging technique (Charles Meneveau and Cabot, 1996). The Navier-Stokes equations are solved in the OpenFoam® environment based on the pisoFoam solver. The following equations are implemented into the source code (see also

S1).

The bottom water flow field causes a pressure gradient at the sediment-water interface which drives porewater advection in the porous domain. The model solves Darcy's law in the porous domain, and the continuity equation (Cardenas and Wilson, 2007; Scalo et al., 2012a):

Darcy's Law

$$u_{p,i} = -Re \frac{k}{\phi} \frac{\partial \langle p \rangle}{\partial x_i} \quad (2.3)$$

$$\frac{\partial u_{p,i}}{\partial x_i} = 0 \quad (2.4)$$

where k is the permeability and ϕ is the porosity and $u_{p,i}$ is the pressure driven porewater velocity. The chevron brackets $\langle \rangle$ denote temporal averages of the dynamic pressure at the sediment-water interface. Averaged over a period of one minute, the pressure distribution was found to be stable. The sediment acts as a low pass filter for the mass transport and, therefore, temporal fluctuations are neglected.

Above a critical bottom water velocity, the bed shear stress at the sediment-water interface will cause mobilization of sediment and thus sediment transport. For a given rippled seabed, sediment is continuously eroded at the stoss side of the ripples and deposited at the lee side which causes a train-like bedform migration (figure 2.3 b). Associated with sediment erosion and deposition is the release of porewater at the stoss side and trapping of bottom water at the lee side, respectively. The exchange of pore and bottom water during bedform migration is implemented into the transport-reaction equation below by means of a coordinate transformation (see supporting information S3). The result is an additional advection term in longitudinal direction. The non-dimensional transport-reaction equation reads:

Transport-Reaction Equations

$$\phi \frac{\partial C}{\partial t} + \phi \frac{\partial}{\partial x_i} [(u_{p,i} - c_{ph} \delta_{1j}) C] = \phi \frac{\partial}{\partial x_i} \left[\left(\frac{1}{Pe} + D_t \right) \frac{\partial C}{\partial x_i} \right] - R_c \quad (2.5)$$

where C is the solute concentration, c_{ph} the bedform celerity after the coordinate transformation and $Pe = \mathbf{U}\eta/\mathbf{D}$ is the Péclet number, where \mathbf{D} denotes the molecular diffusion. The dispersion coefficient D_t is implemented after Bear and Buchlin (1978) in tensorial formulation. D_t is a function of $u_{p,i}$ multiplied with factors for the longitudinal (α_L) and transversal dispersion (α_T). α_T and α_L control the smearing of solute concentration

gradients in porous media, i.e. the diffusion like displacement of water parcels along the flow path. The longitudinal component α_L is in the range of the sediment pore size, while the transversal component is at least one order of magnitude smaller (Bear and Buchlin, 1978). The reaction term R_c depends on the concentration and follows the Monod kinetic:

$$R_c = Dak \frac{C}{K_m + C} \quad (2.6)$$

where $Dak = R \cdot Re$ is the Damköhler Number (described below), R is the maximum reaction rate, and K_m is the half-saturation coefficient. The transport-reaction equation and Darcy equation are non-dimensionalized following Scalo et al. (2012b) and Higashino et al. (2004) (see supporting information S2). The parameter values used in this study are shown in table 2.1. As stated above, bold symbols denote dimensional quantities, whereas normal style symbols denote dimensionless quantities.

2.2.2 Bedform migration

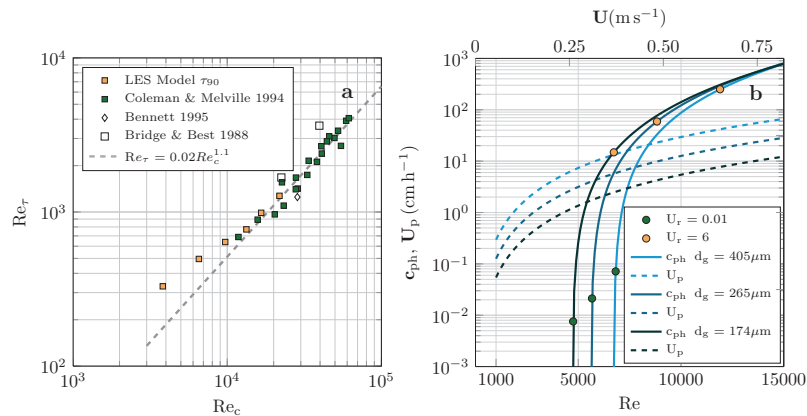


Figure 2.2: (a) Linear scaling of the friction Reynolds number Re_τ with channel Reynolds Re_c number including data from various authors. The linear fit is based on data by Coleman and Melville (1994). Figure (b) bedform celerity (c_{ph}) and pressure driven advective porewater flow (U_p) for different characteristic grain sizes as a function of the Reynolds number. The quantities are scaled for a representative bedform height of $\eta = 0.02$ m.

The mechanistics of bedform initialization, development and migration are still not fully understood. Thus migration velocities must be based on empirical relations, that either predict the sediment transport or the bedform migration itself (Bhaganagar and Hsu, 2009). For this investigation the migration is implemented using an empirical description

after Coleman and Melville (1994), which has been derived from flume experiments:

$$c_{ph} = \frac{\left(\frac{\eta}{d_g} - 3.5\right)^{1.3}}{40} \cdot (\mathbf{u}_\tau - \mathbf{u}_{\tau_{cr}})(\theta - \theta_{cr}) \quad (2.7)$$

where d_g is a characteristic grain diameter, $\mathbf{u}_\tau = (\tau/\rho)^{0.5}$ and $\mathbf{u}_{\tau_{cr}} = (\tau_{cr}/\rho)^{0.5}$ are the shear velocity and critical shear velocity, respectively, where τ is the bed shear stress and ρ the water density. Further, the bedshear stress is non-dimensionalised and represented as the Shields parameter $\theta = \tau/[(\rho_s - \rho)\mathbf{g}d_g]$ and critical Shields parameter $\theta_{cr} = \tau_{cr}/[(\rho_s - \rho)\mathbf{g}d_g]$. The critical shields parameter defines the threshold for the initialization of motion. Here, we use an empirical relation based on the non-dimensional grain size, i.e. Bonneville parameter, after Soulsby (1997). Coleman and Melville (1994) determined the shear velocity by fitting the logarithmic law of the wall (Karman, 1930) to the velocity profile for flat bed conditions.

Coleman and Melville (1994) based the Reynolds number on the half channel height (h) $Re_c = \mathbf{UH}/\nu$. Using \mathbf{u}_τ the friction Reynolds number can be defined as $Re_\tau = \mathbf{u}_\tau \eta/\nu$. The experimental data of Coleman and Melville (1994) suggests that Re_τ increases linearly with Re_c on a logarithmic scale and can be approximated by:

$$Re_\tau \approx 0.02Re_c^{1.10} \quad (2.8)$$

The fit is shown in figure 2.2 a. This relationship has the advantage that it can be directly integrated into the equations.

2.2.3 Governing non-dimensional numbers

The characteristics of the modeled system are described by non-dimensional numbers, representing the relative dominance of different forces, time scales, or transport processes. Besides the Reynolds number, we introduce the non-dimensional velocity U_r which relates the pressure-induced porewater velocity and the bedform celerity c_{ph} :

$$U_r = \frac{c_{ph}}{U_p} \quad (2.9)$$

U_p is the characteristic porewater velocity induced by the pressure gradient (derived from Darcy's law) and defined as:

$$U_p = 2 \mathbf{k} \frac{\mathbf{U} \Delta p}{\phi \nu \lambda} = 2 \frac{kRe \Delta p}{\phi \lambda} \quad (2.10)$$

where λ is the ripple length and Δp the non-dimensional characteristic pressure difference, which is the pressure induced by the hydraulic head. From a pressure distribution Δp can be calculated as the difference between pressure maximum and pressure minimum, or two times the amplitude of the main harmonic signal. Therefore, U_p can be seen as the maximum porewater velocity induced by the characteristic pressure along half the bedform length $\lambda/2$. The flow field induced by the pressure gradient is two dimensional, with varying porewater velocities along different pathlines. A concise description is difficult and therefore the definition of a characteristic porewater flow is useful.

Using U_p , the Péclet number for the porous media can be determined as:

$$Pe_p = \frac{\eta \mathbf{U}}{\mathbf{D}} U_p = Pe U_p \quad (2.11)$$

which defines the ratio of advective to diffusive timescales. Due to the two dimensional velocity field, fast and slow pathlines co-occur in the sediment with highest velocities generally found in the vicinity of the sediment surface.

The competition between the transport rate and the reaction rate, here oxygen respiration, is expressed by the first order Damköhler number (henceforth Damköhler number):

Damköhler number

$$Dak_p = \frac{\mathbf{R}}{\mathbf{C}_0} \frac{\eta}{\mathbf{U} U_p} = \frac{ReR}{U_p} \quad \frac{\text{Reaction Rate}}{\text{Transport Rate}} \quad (2.12)$$

where \mathbf{C}_0 is the concentration of oxygen in the bottom water. The Damköhler number compares the relative rates of reaction to advective transport. If $Dak_p > 1$ the oxygen respiration dominates and controls the distribution and fate of oxygen. Most of the oxygen is consumed close to the sediment-water interface. If $Dak_p < 1$ the system is transport dominated and oxygen penetrates deep into the bedform and are partially recirculated back to the overlying water.

2.2.4 Model setup and parametrization

All parameter values used in this study are shown in table 2.1. The bedform geometry of Janssen et al. (2012) (bedform height and length: $\eta = 0.02$ m and $\lambda = 0.2$ m) was adopted as a reference for this investigation. Janssen et al. (2012) performed experiments in a flume with permeable bedforms that were exposed to unidirectional flow in 0.1m water depth to study advective porewater flow and its forcing by the current velocity. The bedform geometry controls the porewater flow and thus the residence time of a solute

Table 2.1: Model parameters and sources.

| | | Scaled by | Natural Range | Values Adopted | Reference |
|---|--------------------------|---|--|---|------------------------------------|
| η (m) | Bedform Height | | 0.005m - 0.1m | 0.02m | Janssen et al. (2012) |
| H (m) | Half Channel Height | | 0.4 | | Janssen et al. (2012) |
| ν (m ² /s) | Kinematic Viscosity | | $1.1 \cdot 10^{-6} \text{m}^2 \text{s}^{-1}$ | $1.1 \cdot 10^{-6} \text{m}^2 / \text{s}$ | Weast et al. (19 88) |
| λ (m) | Bedform Length | η | - | 0.2m | Janssen et al. (2012) |
| ϕ | Porosity | | 0.3-0.6 | 0.4 | Huettel et al. (2014) |
| U (m/s) | Bottom Water Velocity | | 0.1 – 1m/s | 0.1 – 0.9m/s | Kösters and Winter (2014) |
| U_p | Porewater Flow | U | $10^{-4} - 10^{-5} \text{m/s}$ | $10^{-3} - 10^{-7} \text{m/s}^{1b}$ | Reimers et al. (2004) |
| k (m ²) | Intrinsic Permeability | η^2 | $10^{-10} - 10^{-12} \text{m}^2$ | $10^{-10} - 10^{-12} \text{m}^2$ | Wilson et al. (2008) |
| Δp (Pa) | Pressure Head | ρU^2 | 0.06-0.1 | 0.1 | Huettel et al. (1996) ^a |
| α | Relative Dispersion | α_L / α_T | 8-24 | 10 | Bear and Buchlin (1978) |
| α_L | Longitudinal Dispersion | η | $(1.4 - 7.3) \cdot 10^{-3} \text{m}$ | $2 \cdot 10^{-3} \text{m}$ | Rao et al. (2007) ^a |
| c_{ph} | Bedform migration | U | 0.1 – 90cmh ⁻¹ | 0 – 200cm h ⁻¹ | Miles and Thorpe (2015) |
| C_0 ($\mu \text{mol l}^{-1}$) | Oxygen Concentration | C | $< 350 \mu \text{mol l}^{-1}$ | $280 \mu \text{mol l}^{-1}$ | Weast et al. (19 88) |
| R ($\mu \text{mol l}^{-1} \text{h}^{-1}$) | Consumption Rate | CU^2/ν | $10 - 100 \mu \text{mol l}^{-1} \text{h}^{-1}$ | $10 - 90 \mu \text{mol l}^{-1} \text{h}^{-1}$ | de Beer et al. (2005) |
| K_m ($\mu \text{mol l}^{-1}$) | Half Saturation Constant | C | $35 \mu \text{mol l}^{-1}$ | - | |
| Dimensionless Numbers Equation | | | | | |
| Re | Reynolds Number | $U\eta/\nu$ | - | 1000 – 15000 | |
| U_p | Porewater Flow | $2k \frac{Re}{\phi} \frac{\Delta p}{\lambda}$ | - | $10^{-2} - 10^{-6}$ | |
| Pe | Péclet Number | $Re Sc U_p$ | - | 0.1 – 300 | |
| Sc | Schmidt Number | ν/D | - | 500 | |

^a A asterik denotes values that are recalculated from the given data. The pressure data by Huettel et al. (1996) was non-dimensionalized using ρU^2 . The dispersion coefficients calculated by Rao et al. (2007) where used to estimate α_L ($\alpha_L = D_f U_f^{-1}$, where U_f is the porewater velocity used for the core incubations).

^b The values of U_p are calculated based on the model setup, but the range is shown for comparison.

in the sediment (Rutherford et al., 1993) and therefore determines - in combination with reaction rates - the solute flux between porewater and bottom water. It is known that the bedform wavelength scales with the grain size: $1000d_g$ with an aspect ratio η/λ of approx. 7-10 (Soulsby, 1997; Van Rijn et al., 1993; Yalin, 1972), which encompasses the here presented geometry. Testing different bedform geometries exceeds the scope of this investigation. Preceding publications focusing on biogeochemical processes inside the sediment have often neglected dispersion effects. However, the transversal dispersion does strongly enhance the retention time of solutes in porewater (Elliott and Brooks, 1997b; Bottacin-Busolin and Marion, 2010). The longitudinal dispersion adopted in the present work is based on measurements for continental shelf sediments ($\alpha_L = 2 \cdot 10^{-3} \text{m}$ (Rao et al., 2007)), whereas the transversal dispersion is calculated based on experimental data where a ratio of α_T/α_L between 8 and 24 was found (Bear and Buchlin, 1978).

This study focusses on oxygen fluxes; with oxygen being the energetically most favorable electron acceptor which often governs the distribution of other electron acceptors such as nitrate, iron and manganese oxides. Three typical porewater reaction rates are tested: low respiration ($10 \mu \text{mol l}^{-1} \text{h}^{-1}$), medium respiration ($90 \mu \text{mol l}^{-1} \text{h}^{-1}$), and high respiration ($180 \mu \text{mol l}^{-1} \text{h}^{-1}$). The grain size distribution determines the permeability and the bedform celerity (see above). On continental shelves characteristic grain diameters of permeable sediments typically vary between $d_g = 150 \mu \text{m} - 500 \mu \text{m}$ (Kösters and Winter, 2014). Here grain sizes of $174 \mu \text{m}$, $265 \mu \text{m}$, $405 \mu \text{m}$ were considered. Different empirical

relations exist linking permeabilities to grain sizes. Here we used $\mathbf{k} = Da \cdot 735 \cdot 10^6 \cdot d_g^2$ (where Da is the conversion factor for unit Darcy into m^2 ($=9.869 \cdot 10^{-13}$)), which resulted in permeabilities of $2.2 \cdot 10^{-11} m^2$, $5.1 \cdot 10^{-11} m^2$ and $1.5 \cdot 10^{-10} m^2$ (Gangi, 1985).

The following different model experiments were carried out: The LES derived pressure distribution along the bedform surface and the wall shear were extracted for 6 different Reynolds numbers ($Re = 1500-10000$, with corresponding bottom water velocities of $U = 5 - 80 \text{ cm s}^{-1}$). As a validation of the LES model, the pressure distribution along the bedform was compared to measurements of Janssen et al. (2012) ($U = 12 \text{ cm s}^{-1}$, $Re = 2200$). Then the transport-reaction equation for the porous domain was solved, including oxygen respiration and bedform migration. The Reynolds number, i.e. the bottom water velocity, was increased subsequently from $Re = 1000 - 15000$ in intervals of 250 until stationarity was reached. This procedure was repeated for three different grain sizes, three respiration rates and two dispersion factors (with/ without dispersion) which sums up to a total of approximately 1000 model experiments.

2.3 Results

2.3.1 Model validation

The pressure distribution along the bedform surface drives the advective porewater flow inside permeable sediments. In figure 2.3 a) the pressure distribution derived from the LES model is presented. Along the upstream slope of the ripple the time-averaged (1min interval) pressure increased to a maximum in the middle of the stoss side. The global minimum is found close to the crest, whereas at the lee side a low pressure plateau is found.

The pressure distribution is in strong agreement with the measurements of Janssen et al. (2012) suggesting that the LES model is capable to reproduce natural conditions. Compared to the modeled pressure distribution obtained using a Reynolds Averaged Navier Stokes (RANS) approach (Janssen et al., 2012), deviations to the measured pressure distribution were considerably smaller for the LES. This becomes especially visible for the local pressure in the region at the stoss side where the flow reattaches. Here, the LES model shows strong fluctuations of the instantaneous pressure distribution due to the turbulent structures that encounter the bedform stoss side. The averaged pressure distribution itself is also similar to dunes where η is of $\mathcal{O}(10 \text{ cm})$ (Fehlman, 1985).

By extracting the pressure from the LES model a characteristic pressure difference (spacial pressure head variation) can be estimated as $\Delta p \approx 0.1$ (two times the amplitude

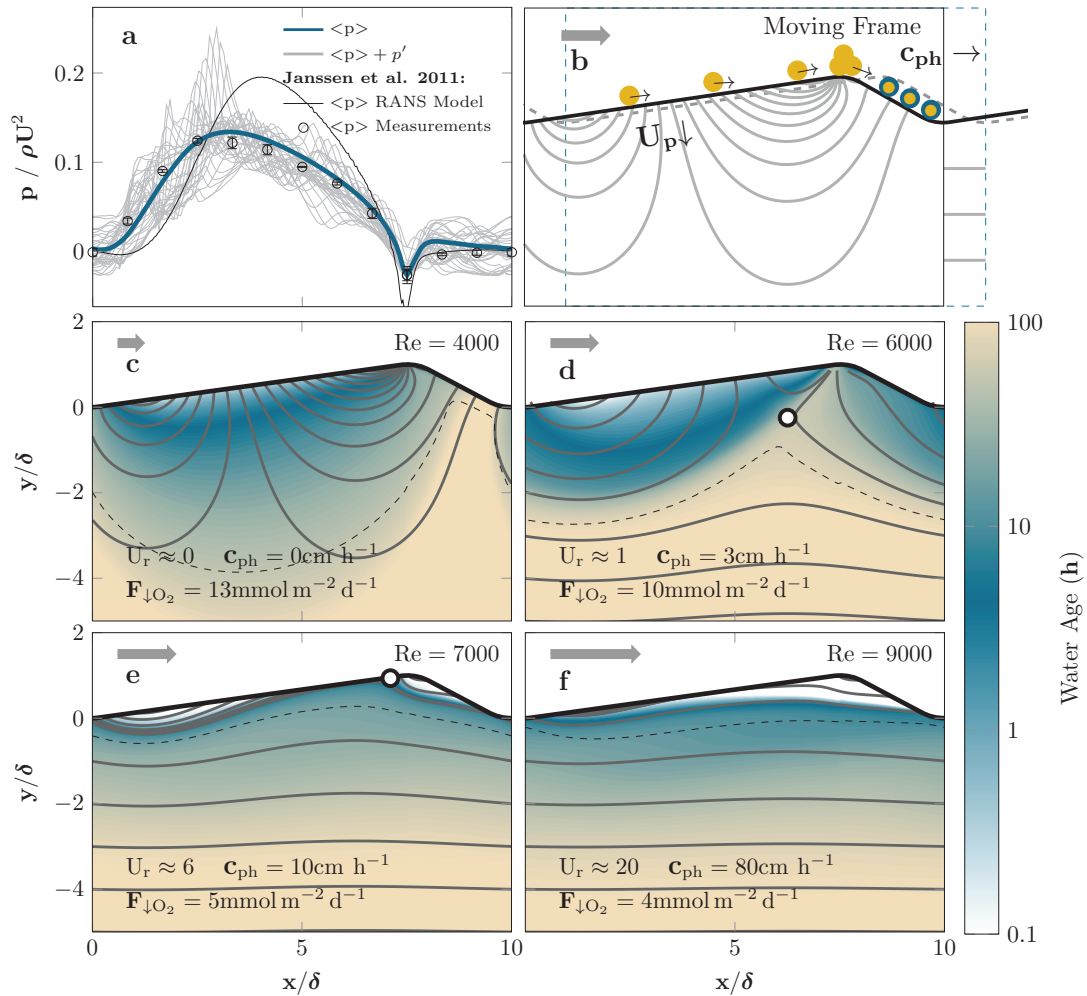


Figure 2.3: (a) LES derived pressure distribution along the bedform surface in comparison to measurements and a preceding RANS approach. (b) Schematics of the moving frame are shown. The yellow bullets represent sediment grains, that get mobilised when the critical Shields parameter is exceeded. At the lee side of the bedform the blue contours around the grains illustrate the trapping of porewater accompanied with grain deposition. (c) - (f) Effect of bedform migration for increasing Reynolds numbers. The corresponding grain size is $d_g = 174 \mu\text{m}$, the bedform height is scaled by $\eta = 0.02 \text{ m}$. Therefore, the Reynolds numbers correspond to bottom water velocities of $U = 22, 33, 39, 50 \text{ cm s}^{-1}$ as indicated by the grey arrows. The color denotes the age of water after entering the sediment. The dashed line indicates the oxygen penetration depth for a reaction rate of $R = 10 \mu\text{mol l}^{-1} \text{ h}^{-1}$.

of the pressure distribution in 2.3 a which can be approximated as $\Delta p = 2\sqrt{2}\sigma$ where σ is the standard deviation of the pressure). For Reynolds numbers varying between $Re = 2000-10000$ only minimal deviations are found between the non-dimensional pressure distributions, as well as the characteristic difference Δp . Therefore, the distribution presented can be scaled by ρU^2 . This is in agreement with prior investigations (Cardenas and Wilson, 2007), which found that the location of eddy reattachment and the pressure distribution barely change for varying flow conditions. In previous laboratory experiments with bedform heights ranging from 1 cm ripples to 20 cm dunes the characteristic pressure head was found to vary between $\Delta p = 0.06 - 0.1$ (Huettel et al., 1996; Fehlman, 1985; Elliott and Brooks, 1997b) (recalculated values).

To estimate the bedform celerity, the bed shear stress can directly be calculated from the LES model. Insertion of the spacial averaged bed shear stress in equation 2.7 would underestimate the shear stress that is actually responsible for the sediment erosion at the stoss side, because the average value is lowered by the values in the trough (Bhaganagar and Hsu, 2009). Therefore, τ_{90} the 90th percentile of the bed shear stress is extracted and used as the governing shear stress, which is in good agreement with measurements (Coleman and Melville, 1994; Bennett and Best, 1995; Bridge and Best, 1988) as shown in figure 2.2 a. The linear increase of the friction Reynolds number with the channel Reynolds number is well presented by equation 2.8. Henceforth, equation 2.8 is used for varying Reynolds numbers to determine the bed shear and subsequently the migration celerity. In figure 2.2 b typical migration celerities are shown for the considered grain sizes. In continental shelf regions migration celerities were measured and found to vary in similar ranges $c_{ph} = 0.1 - 4 \text{ cm h}^{-1}$ (Traykovski et al., 1999) and in intertidal systems up to $c_{ph} = 90 \text{ cm h}^{-1}$ (Miles and Thorpe, 2015).

2.3.2 Solute transport for migrating bedforms

With the resolved pressure distribution at the sediment surface the advective porewater flow inside the sediment can be calculated and inserted into the transport-reaction equation 2.5. To simulate the range of natural environmental conditions the transport-reaction equations were solved stationary ($\frac{\partial C}{\partial t} = 0$), i.e. no changes over time, for different bottom water velocities, grain sizes and oxygen respiration rates, which includes a corresponding range of permeabilities and bedform migration velocities derived from the empirical relations. As an example, the patterns of solute transport are shown for a grain size of $d_g = 174 \mu\text{m}$, a reaction rate of $R = 10 \mu\text{mol l}^{-1} \text{h}^{-1}$ and for 4 different current velocities, i.e. 4 different Reynolds numbers (figure 2.3 c-f and suppl. animation S5).

The bedform migration is directly coupled to the shear velocity, therefore the bottom

water flow determines if and how fast the bedform migrates. In figure 2.3 c) the water age (age of a water parcel following the streamlines) under a bedform is shown for $Re = 4000$, $U = 0.22 \text{ m s}^{-1}$, where no migration is predicted. The distribution of the porewater age and the oxygen penetration depth (based on η_{99} , i.e. the isoline where 99% of the solute is consumed) is in agreement with patterns observed (Ziebis et al., 1996; Elliott and Brooks, 1997a) and modelled before (Cardenas et al., 2008). The solute penetrates from the stoss side into the bedform and is consumed along the pathline. The water age distribution indicates that old porewater is released at the lee side of the bedform along a chimney-like structure. The penetration depth reaches down to 6 cm (based on $\eta = 0.02 \text{ m}$), which is distinctly deeper than for pure diffusion (Glud, 2008). The streamlines start and end at the sediment surface.

At the onset of bedform migration (figure 2.3 d), the porous matrix of the sediment divides into an upper mobile layer and a stationary layer underneath. The deposition of sand grains at the lee side of the bedform traps bottom water while sediment erosion at the stoss side causes the release of porewater. Thus an exchange of bottom and porewater takes place due to the moving porous matrix. However it does not cause a flow within the porous matrix. True porewater flow is driven only by pressure gradients from current-bedform interactions. Nevertheless, bedform migration is highly effective because it leads to oscillating pressure gradients and flow reversals in the sediment layers below the bedform. At certain depths, pressure gradients reverse too fast and porewater flow is too slow to allow for a substantial net vertical displacement. At these depths solute transport is driven only by dispersion and diffusion. Although dispersion increases with porewater velocity, it cannot compensate the hindered advective transport. As a result, the two interfering transport processes of bedform migration and pressure driven porewater flow cause the separation of a flushed upper layer from a sealed lower layer.

In figure 2.3 d, the layer separation is visualized by the different orientation of the streamlines, which reflect the sum of the pressure driven porewater flow and the longitudinal movement of the reference frame. Streamlines that start and end at the sediment surface denote the layer where pressure driven porewater flow from surface to surface takes less time than it takes the bedform to migrate over a full bedform length. Thus an exchange with bottom water still takes place. In contrast, the horizontal streamlines at depth denote the layer where porewater flow reverses before reaching the sediment surface. The streamlines start and end in the sediment and their vertical deflection show the amplitude of the vertical porewater oscillation.

Another emerging feature is the point of stagnation (circle in figure 2.3 d-e) which occurs where the velocities of pressure driven pore water flow and bedform migration are

equal in magnitude and direction (Bottacin-Busolin and Marion, 2010). It is the upper most point of the sealed layer and moves upwards as bedform migration is further increased (see suppl. animation). At the arrival of the point of stagnation at the sediment-water interface (see also figure 2.3 e), bedform migration starts dominating over the characteristic porewater flow ($U_r = 6$) (figure 2.3 e). Here the shape of the oxygen distribution changes distinctly. Most of the oxygen enters the bedform at the lower stoss side where pressure is highest and close to the crest at the lee side due bedform migration and porewater trapping. The oxygen penetration depth is strongly reduced but the flushed regions have high porewater velocities which lead to very low porewater ages.

When bedform migration is further increased ($U_r > 6$) (figure 2.3 f), the bedform celerity fully dominates over the pressure driven porewater flow and hence no point of stagnation is found anymore. The solute penetration from the stoss side is mostly hindered and the bedform is fully flushed due to the combined sediment deposition and porewater trapping at the lee side. In summary, with increasing bedform migration, gradients of porewater age and oxygen change from a two dimensional to a one dimensional vertical orientation, i.e. anoxic porewater is always found underneath oxic porewater but not in the same layer. Because the pressure distribution is tied to the fast migrating bedform frequent vertical reversal of the porewater flow suppresses any net vertical advective transport underneath the bedforms. However, porewater is still moving up- and downwards and this movement in combination with dispersion and diffusion controls the solute transport at greater depth.

2.3.3 Impact of bedform migration on net oxygen fluxes

The net flux of oxygen across the sediment-water interface is estimated for 3 exemplary grain sizes, 3 oxygen respiration rates, and for bottom water velocities ranging from $U = 5 - 80 \text{ cm s}^{-1}$ ($Re=1000-15000$, $\eta = 0.02 \text{ m}$) both with and without dispersion. The parameters cover typical ranges for North Sea sediments as summarized in table 2.1. Evolutions of the associated net oxygen fluxes with increasing Reynolds number are summarized in figure 2.4.

The net oxygen fluxes for different grain sizes and oxygen respiration rates vary in magnitude but follow similar trends along increasing bottom water velocities. For stationary bedforms (no migration) the net oxygen fluxes strongly increase with bottom water velocity. As soon as the shear stress and Shields parameter exceed their critical value the bedform starts to migrate ($U_r > 0$). For increasing bottom water velocities the net oxygen fluxes are affected by the increasing migration celerity and start to drop off at $U_r > 0.01$ ($c_{ph} = 0.01, 0.1, 0.5 \text{ cm h}^{-1}$). The ascending U_r indicates that the migration

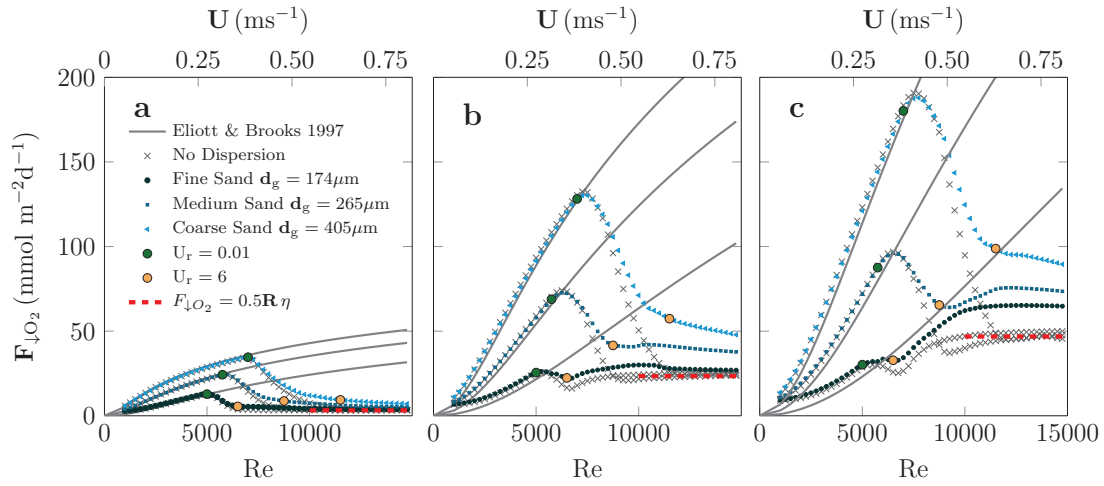


Figure 2.4: Net fluxes for different reaction rates $\mathbf{R} = 10 \mu\text{mol l}^{-1} \text{h}^{-1}$ (a), $\mathbf{R} = 90 \mu\text{mol l}^{-1} \text{h}^{-1}$ (b), $\mathbf{R} = 180 \mu\text{mol l}^{-1} \text{h}^{-1}$ (c) and grain sizes $\mathbf{d}_g = 174, 265, 405 \mu\text{m}$ along increasing Reynolds numbers. The second abscissa shows the bottom water velocity for a corresponding bedform height of $\eta = 0.02 \text{ m}$. The red line indicates the oxygen net flux for a fully flushed bedform.

celerity increases faster than the advective porewater flow (compare figure 2.2 b).

The net oxygen fluxes decrease further until the ratio of migration celerity to characteristic porewater flow is well above unity ($U_r \approx 6$). In figure 2.4 this equilibrium is visible as a local minimum (see also figure 2.3 e). The point of stagnation arrives at the sediment-water interface. A further increase of the bottom water velocity leads to domination of bedform migration ($U_r > 6$, $\mathbf{c}_{ph} = 10, 55, 200 \text{ cm h}^{-1}$). The net fluxes approach a plateau, which is defined by the theoretical net flux calculated for a fully flushed bedform. At the plateau the role of dispersion for the solute supply to deeper sediment layers becomes clearly visible. Without dispersion the fluxes converge fast towards the theoretical net flux. For cases with dispersion the net fluxes do not converge. They slowly drop off and remain clearly above the theoretical net flux. This behaviour becomes more pronounced for higher respiration rates ($\mathbf{R} = 90 \mu\text{mol l}^{-1} \text{h}^{-1}$ and $\mathbf{R} = 180 \mu\text{mol l}^{-1} \text{h}^{-1}$).

With increasing respiration rates the oxygen fluxes increase strongly. For the smallest respiration rate $\mathbf{R} = 10 \mu\text{mol l}^{-1} \text{h}^{-1}$ (figure 2.4 a) the fluxes vary in between $1 - 50 \text{ mmol m}^{-2} \text{d}^{-1}$. The transport rates are dominating the respiration rates as reflected in an average Damköhler number (average for all bottom water velocities) smaller than unity. The penetrating front reaches deep into the bedform and a substantial amount of oxic porewater is released without being consumed. For higher respiration rates $\mathbf{R} = 90 \mu\text{mol l}^{-1} \text{h}^{-1}$ and $\mathbf{R} = 180 \mu\text{mol l}^{-1} \text{h}^{-1}$ (figure 2.4 b - c) the respiration rates dominate over transport rates yielding average Damköhler numbers larger than unity. Most

of the oxygen that enters the bedform is consumed close to the surface leading to increased net fluxes between $20 - 190 \text{ mmol m}^{-2} \text{ d}^{-1}$.

Considering that the bed shear stress, responsible for the bedform migration, is a function of the bottom water velocity the net flux is controlled by three parameters, namely: grain size, bottom water velocity and respiration rate. This relationship is summarized in the phase space of grain size and bottom water velocity (figure 2.5) for a respiration rate $\mathbf{R} = 180 \mu\text{mol l}^{-1} \text{ h}^{-1}$. Larger grain sizes shift the onset of bedform migration towards higher bottom water velocities. In combination with the enhanced permeability the fluxes are strongly increased. E.g., for the largest grain size $\mathbf{d}_g = 405 \mu\text{m}$ the two fold increased permeability, compared to $\mathbf{d}_g = 265 \mu\text{m}$, leads to a net flux difference of approximately $50 \text{ mmol m}^{-2} \text{ d}^{-1}$ for $U = 0.25 \text{ m s}^{-1}$. On the other hand, the increase of the $U_r = 0.01$ line - bedform migration occurs at higher bottom velocities for larger grain sizes - leads to a total difference of $90 \text{ mmol m}^{-2} \text{ d}^{-1}$ between the two maxima for $\mathbf{d}_g = 405 \mu\text{m}$ and $\mathbf{d}_g = 275 \mu\text{m}$, emphasizing the importance of the grain size.

2.4 Discussion & environmental implications

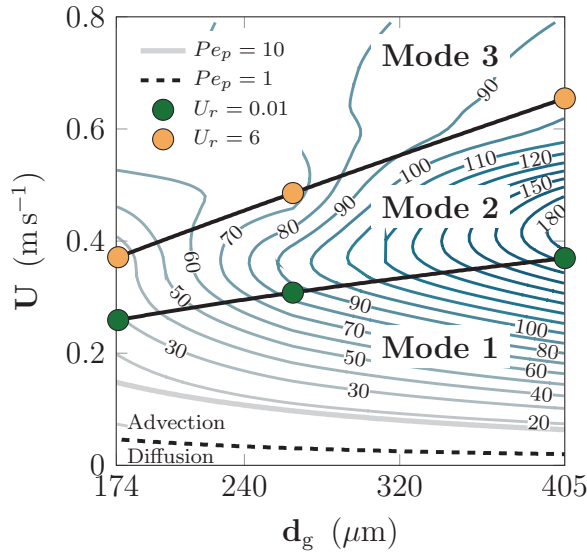


Figure 2.5: Governing modes of porewater flow shown in the phase space of grain size and bottom water velocity. Isolines indicate oxygen net fluxes (in $\text{mmol m}^{-2} \text{d}^{-1}$) for a reaction rate of $\mathbf{R} = 180 \mu\text{mol l}^{-1} \text{h}^{-1}$. The migration celerities for $U_r = 0.01$ are $c_{\text{ph}} = 0.01, 0.1, 0.5 \text{ cm h}^{-1}$, and $c_{\text{ph}} = 10, 55, 200 \text{ cm h}^{-1}$ for $U_r = 6$.

of penetration depths of a few cm found in this study (see Fig. 3). Further, bedform migration is implemented by using a moving frame of reference, which assumes a stable bedform geometry that does not change over the range of applied bottom water velocities ($U = 5 - 80 \text{ cm s}^{-1}$). This is a valid assumption for uni-directional flow in the absence of waves (e.g. Baas, 1994; Richards, 1980) and was also used in previous model studies (Kessler et al., 2015; Bottacin-Busolin and Marion, 2010; Elliott and Brooks, 1997b). The maximum applied bottom water velocity (80 cm s^{-1}) was within the range of velocities (up to 90 cm s^{-1}) used by (Coleman and Melville, 1994) to establish the empirical relation for bedform migration. However, bottom water velocities beyond the upper range ($75 - 80 \text{ cm s}^{-1}$), as found in e.g. fast flowing rivers, can cause a change in bedform geometry and a subsequent wash out of the bedform (Raudkivi, 1997), which is not reflected

This study investigates the effect of bedform migration on benthic exchange fluxes using an inter-linked and thus realistic forcing of pressure driven porewater flow and bedform migration.

Similar to many previous studies (e.g. Kessler et al., 2015, 2013; Cardenas and Wilson, 2007) and for the sake of computational efficiency the model was based on a few simplifying assumptions. We neglected microscale transport processes at the very sediment surface such as shear driven flow in the Brinkman Layer (Brinkman, 1949) and turbulent pressure fluctuations (Scalo et al., 2012b; Higashino et al., 2004). These processes affect the upper $100 \mu\text{m}$ to mm of the sediment (Goharzadeh et al., 2005; Kaviani, 2012) which is negligible compared to the shift

by the model. At such velocities much of the upper sediment layer is mobilized and gets hypersaturated. This layer would behave like a fluid with strongly altered permeabilities. For the here applied conditions the bedforms are quasi static with respect to the bottom water velocity and the extent of the mobile sheet layer is negligible. Fast flowing rivers with high bed permeability may exhibit a significant underflow velocity of the porewater induced by stream gradients (e.g. Bottacin-Busolin and Marion, 2010). However, this is not considered here because stream gradients are not present in continental shelf sediments. Even for river sediments in the permeability range used in this study and typical stream gradients of order cm per km the underflow velocity is an order of magnitude smaller than the smallest characteristic porewater flow in this study and can thus be neglected.

The model results indicate that bedform migration cannot be neglected and may strongly attenuate flux estimates based on models assuming stationary bedforms or plain beds. The empirical coupling of the governing transport parameters, i.e. the dependence of permeability and migration celerity on grain size and bottom water velocity, allows for the distinction of three different modi of porewater transport in permeable sediments (figure 2.5):

Modes of Porewater Flow

Mode 1. The bedform is stationary and pressure driven advective porewater flow is dominant ($U_r \ll 1$), resulting in a deep solute penetration and high oxygen uptake rates,

Mode 2. The competition of bedform migration and advective driven porewater flow leads to the formation of a redox seal. The deeper sediment layer shows suppressed vertical net transport which decreases with increasing bottom water velocities ($U_r = 0.01 - 6$),

Mode 3. Bedform migration is dominant and only the bedform itself is well flushed ($U_r > 6$). The transport in the sediment below is controlled by diffusion and dispersion and fluxes stagnate at low values, independent of further acceleration of the bottom water velocity.

The general patterns of solute distributions (figure 2.3) were previously observed in flume experiments (Precht et al., 2004) for a narrow range of boundary conditions. The here presented model is capable of simulating oxygen fluxes based on a few parameters, i.e. grain size, bottom water velocity and respiration rate, as summarized in figure 2.5.

In a semi-analytical approach Elliott and Brooks (1997b) investigated the residence time of a conservative solute in the sediment for the simplified case of a constant sinusoidal pressure head over a flat bed. By introducing solute reactivity and after reformulation of the model (see equation S.21-28 in supporting information S4) we found that the fluxes for

stationary bedforms is determined by the bedform length and Damköhler number, which can be estimated from experiments and in situ measurements. Despite the simplifying assumptions of the traditional Elliot model, it compares well with our model (10% maximum deviation) for the case of stationary bedforms (figure 2.4). However, at migrating bedforms, the pressure driven advective porewater flow is deteriorated by bedform migration and our model strongly deviates from the Elliot model, because the latter does not consider bedform migration. Fast bedform migration and the resulting fast vertical flow reversal leads to a suppression of net porewater displacement and the formation of a redox seal (Huettel et al., 2014) which separates deeper anoxic regions from the oxic bedform above. The strength of the concentration gradient and the oxygen flux between these two layers depends on the dispersive transport. While no dispersion and no diffusion would lead to a step change of oxygen concentrations, the up and down movement of water parcels in combination with dispersion enhances the gradient driven downward transport (Bottacin-Busolin and Marion, 2010). The effect can be significant as shown for the case of high oxygen respiration rates in fine sand, i.e. high Damköhler numbers, where increasing bedform migration even enhances the oxygen fluxes at moderate and high reaction rates (figure 2.4). This setting may be found on intertidal flats where respiration rates in fine sand are in the range of $100 \mu\text{mol l}^{-1} \text{h}^{-1}$ and larger (de Beer et al., 2005; Gao et al., 2012).

In contrast to our finding, negligible effect of bedform migration on oxygen uptake and denitrification was reported in a recent model study that simulated migrating bedforms using a travelling sinusoidal pressure distribution over a flat bed (Kessler et al., 2015). The travelling speed (i.e. bedform migration) was neither coupled to bottom water velocity nor to sediment grain size and results were presented only for a single reaction rate ($100 \mu\text{mol l}^{-1} \text{h}^{-1}$) and a single permeability ($4 \cdot 10^{-11} \text{ m}^2$). However, such a reduced parameter combination cannot thoroughly capture the effect of bedform migration but reflects a rather specific solution. Even in our study there are specific parameter combinations that, taken separately, could lead to biased conclusions. In figure 2.4 b) for example, the effect of bedform migration seems negligible for a reaction rate of $90 \mu\text{mol l}^{-1} \text{h}^{-1}$ and a grain size of $174 \mu\text{m}$ (permeability of $2.2 \cdot 10^{-11} \text{ m}^2$) - parameter values that are comparable to those used by Kessler et al. (2015) - whereas for the majority of parameter combinations the effect is clearly visible. The high dispersion coefficient is another possible reason why the effect of bedform migration was not observed in Kessler et al. (2015). The dispersivity controls the vertical solute transport across the established redox seal. Especially for a flat bed model in which bedform elevation is neglected, dispersion is the only way to exchange solutes between sediment and water column when bedform migration is fast. The effect of bedform migration can be strongly reduced by an increased

dispersivity, and indeed, a dispersion coefficient of 1 cm used in Kessler et al. (2015) is rather high of $\theta(\eta)$ and not of pore scale magnitude.

The modeled oxygen fluxes as a function of bottom water velocity, grain size and reaction rates vary widely between 3 and 190 mmol m⁻² d⁻¹ which is comparable to the range of measured oxygen uptake rates. Eddy correlation measurements, which may provide the most realistic oxygen uptake rates for permeable sediments (Berg et al., 2003), revealed that oxygen uptake of marine subtidal sands can vary between 3 and 30 mmol m⁻² d⁻¹ (Reimers et al., 2012; Berg et al., 2013; McGinnis et al., 2014), whereas for intertidal systems, where nutrient availability and organic matter input is high, net oxygen fluxes were found to range between $F_{\downarrow O_2} = 105 - 170$ mmol m⁻² d⁻¹ (de Beer et al., 2005).

In this study, the complex porewater transport was investigated as the main controlling variable for benthic oxygen uptake. However, the oxygen sink within the sediment, i.e. the distribution of the maximum oxygen reaction rate (R), was assumed to be similar throughout the porous domain. The maximum reaction rate usually depends on the availability of labile particulate organic matter. Different from solutes, particles can be retained in the pore space and its accumulation depends largely on the filtration capacity of the sands (Rusch et al., 2001). In contrast, bedform migration and the accompanied sediment erosion may remove particulate organic matter and thus may counteract the accumulation by filtration. It is likely that reaction rates are regulated by the transport dynamics of particulate organic matter and may show considerable differences with sediment depth. Further, the here presented oxygen uptake is simplified since it does not consider the oxidation of reduced substrates that diffuse upward from deeper sediment layers. However, the implementation of empirical or mechanistic models to parameterize the reaction rate and abiotic oxidation is a task for future studies.

In conclusion, the integrated model approach allows for investigating complex transport processes that control sediment biogeochemistry and benthic exchange rates. The results strongly suggest that sediment transport such as bedform migration has a significant impact on porewater transport, solute distributions and benthic net fluxes. This has to be considered in order to understand the dynamic processes in sandy sediments and especially their function as natural filter systems in coastal waters.

Acknowledgements

We would like to acknowledge the constructive discussions with Bo Liu and Arzhang Khalili. In addition, we would like to acknowledge Carsten John for computational support.

We thank the reviewers for their constructive comments and suggestions. The study was funded by the Max Planck Society and DFG-Research Center/Cluster of Excellence "The Ocean in the Earth System" at the University of Bremen. The data and model (C/C++ and Python) presented are available upon request from the corresponding author.

2.5 Supplementary Information

2.5.1 Model domain

For the LES model (figure 1), the domain length was set to 10η (i.e. one ripple length) in longitudinal direction, 5η in transversal and vertical direction, respectively. The mesh was generated using Gmsh (version 2.7.0). To accurately describe the wall-bounded flow the vertical grid resolution was adapted to $\Delta x_2^+ = x_2 u_\tau / \nu \approx 1.5$ which ensured the first grid point to be in the viscous sublayer. The bed layer was therefore fully resolved and a wall function was not needed. The grid finally consisted of $N_{x_1} = 120$, $N_{x_2} = 100$, $N_{x_3} = 35$ grid points, i.e., 420000 nodes in total. In vertical direction a geometric progression of 1.02 decreased the spacing towards the bedform. Similar grid resolutions and types were used for Large Eddy Simulations on flow across dunes [Omidyeganeh and Piomelli, 2011]. The grid was decomposed into 8 subgrids using scotch decomposition and parallelised using the open Message Passing Interface (MPI) code. The inlet and outlet open boundary conditions were assumed to be cyclic, therefore the generated turbulence corresponded to an infinite 2D rippled seabed. The top boundary was set to slip condition which represents the open channel flow. In this study, the turbulent statistics were in equilibrium after a bulk flow of 100 times the length of the bedform λ .

In order to drive the 2D model of the porous domain the pressure was averaged in transversal direction. To accurately describe the advective transfer of oxygen an inlet-outlet boundary condition was imposed. Depending on the flow field a Dirichlet boundary condition (fixed concentration) is given for the inflow and Neumann boundary condition (zero concentration gradient) for the outflow, respectively. The grid for the porous domain covers an area of 10η in longitudinal direction and 15η in vertical direction. The bedform migration term may lead to strong gradients of the concentration and to avoid numerical diffusion the advection term was discretised using a central scheme which compensates for such effects (e.g. MUSCL) [Kurganov and Tadmor, 2000]. The oxygen net flux is directly extracted from the boundary by integrating the advective (J_a) and diffusive (J_d)

fluxes along the surface:

$$F_{\downarrow O_2} = \iint_S (J_a + J_d) \cdot n_i \, dS \quad (\text{A.2.13})$$

where S is the surface and n_i the normal vector pointing at the surface.

2.5.2 Non-dimensionalization

The permeability of the porous domain varies between $O(10^{-9}m^2 - 10^{-11}m^2)$ therefore $Re_p = \sqrt{k}U/\nu \ll 1$ and the transport can be modeled by using Darcy's law:

$$\mathbf{u}_{p,i} = -\frac{\mathbf{k}}{\mu\phi} \frac{\partial \mathbf{p}}{\partial \mathbf{x}_i} \quad (\text{A.2.14})$$

where \mathbf{k} is the permeability, ϕ the porosity, μ the dynamic viscosity and \mathbf{p} the surface pressure. Equation A.2.14 is coupled to the overlying fluid domain by the pressure which is extracted from the Large Eddy Simulation. Furthermore, the oxygen concentration \mathbf{C} is calculated by solving the transport-reaction equation:

$$\phi \frac{\partial \mathbf{C}}{\partial \mathbf{t}} + \phi \frac{\partial}{\partial \mathbf{x}_i} \mathbf{u}_{p,i} \mathbf{C} = \phi \frac{\partial}{\partial \mathbf{x}_i} \left[(\mathbf{D} + \mathbf{D}_t) \frac{\partial \mathbf{C}}{\partial \mathbf{x}_i} \right] - \mathbf{R}_c \quad (\text{A.2.15})$$

where \mathbf{D} is the diffusion coefficient corrected for permeable sediments and \mathbf{D}_t the dispersion tensor, \mathbf{c}_{ph} is the ripple migration celerity, \mathbf{C} the concentration. The celerity can be derived by transforming to a moving coordinate system as shown in A.2. \mathbf{R}_c is the solute reaction term, which is assumed to follow the Monod kinetics

$$\mathbf{R}_c = \frac{\mathbf{R}\mathbf{C}}{\mathbf{K}_m + \mathbf{C}} \quad (\text{A.2.16})$$

with \mathbf{R} being the maximum reaction and \mathbf{K}_m the half saturation constant.

Variables in equation A.2.14-A.2.15 are non dimensionalised by the length scale η which is the ripple height, bottom water velocity \mathbf{U} , time scale η/\mathbf{U} , and pressure by $\rho\mathbf{U}^2$ which

reads:

$$u_{p,i} = \frac{\mathbf{u}_{p,i}}{\mathbf{U}} \quad \frac{\partial}{\partial x_i} = \frac{\partial}{\partial \mathbf{x}_i} \eta \quad t = \mathbf{t} \frac{\mathbf{U}}{\eta} \quad k = \frac{\mathbf{k}}{\eta^2} \quad p = \frac{\mathbf{p}}{\rho \mathbf{U}^2} \quad C = \frac{\mathbf{C}}{\mathbf{C}_0} \quad (\text{A.2.17})$$

this is equivalent to

$$u_{p,i} \mathbf{U} = \mathbf{u}_{p,i} \quad \frac{1}{\eta} \frac{\partial}{\partial x_i} = \frac{\partial}{\partial \mathbf{x}_i} \quad t \frac{\eta}{\mathbf{U}} = \mathbf{t} \quad k \eta^2 = \mathbf{k} \quad p \mathbf{U}^2 \rho = \mathbf{p} \quad C \mathbf{C}_0 = \mathbf{C} \quad (\text{A.2.18})$$

substitution into equation A.2.14 yields

$$u_{p,i} \mathbf{U} = - \frac{k \eta^2}{\mu \phi} \frac{\partial p}{\partial x_i} \frac{\rho \mathbf{U}^2}{\eta} \quad (\text{A.2.19})$$

and rearranging yields

$$u_{p,i} = - \frac{k \eta \mathbf{U}}{\phi \nu} \frac{\partial p}{\partial x_i} \quad (\text{A.2.20})$$

Introducing the Reynolds number $Re = \eta \mathbf{U} / \nu$ the equation simplifies to

$$\boxed{u_{p,i} = -Re \frac{k}{\phi} \frac{\partial p}{\partial x_i}} \quad (\text{A.2.21})$$

This procedure is repeated for equation A.2.15:

$$\frac{\mathbf{C}_0 \mathbf{U}}{\eta} \frac{\partial C}{\partial t} + \frac{\mathbf{U} \mathbf{C}_0}{\eta} \frac{\partial}{\partial x_i} u_{p,i} C = \frac{\mathbf{C}_0}{\eta^2} \frac{\partial}{\partial x_i} \left[(\mathbf{D} + \mathbf{D}_t) \frac{\partial C}{\partial x_i} \right] - \mathbf{R}_c \quad (\text{A.2.22})$$

rearranging the equation yields

$$\frac{\partial C}{\partial t} + \frac{\partial}{\partial x_i} u_{p,i} C = \frac{1}{\eta \mathbf{U}} \frac{\partial}{\partial x_i} \left[(\mathbf{D} + \mathbf{D}_t) \frac{\partial C}{\partial x_i} \right] - \frac{\eta}{\mathbf{U} \mathbf{C}_0} \mathbf{R}_c \quad (\text{A.2.23})$$

Introducing the Péclet number $Pe = Sc Re$ with the Schmidt number $Sc = \nu / D$ and the

non-dimensional dispersion $D_t = \mathbf{D}_t / (\mathbf{U}\eta)$ the equation simplifies to

$$\frac{\partial C}{\partial t} + \frac{\partial}{\partial x_i} u_{p,i} C = \frac{\partial}{\partial x_i} \left[\left(\frac{1}{Pe} + D_t \right) \frac{\partial C}{\partial x_i} \right] - \frac{\eta}{\mathbf{U}C_0} \mathbf{R}_c \quad (\text{A.2.24})$$

Finally, the reaction term is non-dimensionalised:

$$R = \frac{\mathbf{R}v}{C_0 \mathbf{U}^2} \quad K_m = \frac{\mathbf{K}_m}{C_0} \quad (\text{A.2.25})$$

substitution yields

$$R_c = \frac{\mathbf{U}^2}{v} \frac{R C C_0^2}{C_0 K_m + C_0 C} \quad (\text{A.2.26})$$

rearranging yields

$$R_c = \frac{\mathbf{U}^2 C_0}{v} \frac{RC}{K_m + C} \quad (\text{A.2.27})$$

Resubstituting into equation A.2.28 yields the non dimensional diffusion-advection-reaction equation:

$$\boxed{\frac{\partial C}{\partial t} + \frac{\partial}{\partial x_i} u_{p,i} C = \frac{\partial}{\partial x_i} \left[\left(\frac{1}{Pe} + D_t \right) \frac{\partial C}{\partial x_i} \right] - Re \frac{RC}{K_m + C}} \quad (\text{A.2.28})$$

2.5.3 Transport equation for moving bedforms

The non dimensional advection diffusion reaction equation reads:

$$\frac{\partial C}{\partial t} + \frac{\partial}{\partial x_i} u_{p,i} C = \frac{1}{\partial x_i} \left[\left(\frac{1}{Pe} + D_t \right) \frac{\partial C}{\partial x_i} \right] - R_c \quad (\text{A.2.29})$$

In this approach it is assumed the surface displacement η_s is proportional to the divergence of the sediment flux q_s , which follows the Exner equation:

$$\frac{\partial \eta_s}{\partial t} \propto -\nabla \cdot q_s \quad (\text{A.2.30})$$

Assuming that the erosion at the stoss side is constant and deposition takes place at the lee side the temporal change is equal to a spatial change. The bedform has a train-like continuous motion. This movement can be modeled either by a moving grid or included as a coordinate transformation. Introducing the moving frame for the coordinates system $x'_1 = x_1 - c_{ph}t$ and $\tau = t$ yields:

$$\begin{aligned} & \frac{\partial C}{\partial \tau} \frac{\partial \tau}{\partial t} + \frac{\partial}{\partial x'_1} \frac{\partial x'_1}{\partial t} C + \frac{\partial}{\partial x'_1} \frac{\partial x'_1}{\partial x_1} u_{p,1} C + \frac{\partial}{\partial \tau} \frac{\partial \tau}{\partial x_1} u_{p,1} C = \\ & \left(\frac{1}{\partial x'_1} \frac{\partial x'_1}{\partial x_1} + \frac{1}{\partial \tau} \frac{\partial \tau}{\partial x_1} \right) \left[\left(\frac{1}{Pe} + D_t \right) \left(\frac{\partial C}{\partial x'_1} \frac{\partial x'_1}{\partial x_1} + \frac{\partial C}{\partial \tau} \frac{\partial \tau}{\partial x_1} \right) \right] - R_c \end{aligned} \quad (\text{A.2.31})$$

Calculating the derivatives:

$$\frac{\partial C}{\partial \tau} - \frac{\partial}{\partial x'_1} c_{ph} C + \frac{\partial}{\partial x'_1} u_{p,1} C = \frac{1}{\partial x'_1} \left[\left(\frac{1}{Pe} + D_t \right) \frac{\partial C}{\partial x'_1} \right] - R_c \quad (\text{A.2.32})$$

For notation τ is changed to t and x'_1 to x_1 . The x_2 and x_3 coordinates do not change:

$$\frac{\partial C}{\partial t} + \frac{\partial}{\partial x_i} (u_{p,i} - c_{ph} \delta_{1j}) C = \frac{1}{\partial x_i} \left[\left(\frac{1}{Pe} + D_t \right) \frac{\partial C}{\partial x_i} \right] - R_c \quad (\text{A.2.33})$$

2.5.4 Reformulation of Elliot's model

The average mixing depth for a non reactive tracer in an advection dominated system ($Pe_p \ll 1$) is given by the empirical relation [*Elliott and Brooks(1997)*]:

$$\frac{m(t)}{\phi} = \frac{\lambda}{2\pi} \ln \left(0.42 \left(\frac{2\pi}{\lambda} \right)^2 \kappa h_m \frac{t}{\phi} + 1 \right) \quad (\text{A.2.34})$$

where $\kappa = \frac{kg}{\nu}$ is the hydraulic conductivity, k the permeability, ν the kinematic viscosity and g gravitational acceleration. λ is the bedform wavelength and $h_m = \frac{\Delta p}{2\rho g}$ the hydraulic head with Δp the pressure induced by the hydraulic head. Substituting yields:

$$\frac{m(t)}{\phi} = \frac{\lambda}{2\pi} \ln \left(0.42 \frac{(2\pi)^2}{\lambda^2} \frac{kg}{\nu} \frac{\Delta p}{2\rho g} \frac{t}{\phi} + 1 \right) \quad (\text{A.2.35})$$

Now following the non dimensionalisation of the present work

$$\Delta p \rho U^2 = \Delta p \quad k \eta^2 = \mathbf{k} \quad p \rho U^2 = \mathbf{p} \quad \lambda \eta = \lambda \quad t \frac{\eta}{U} = \mathbf{t} \quad (\text{A.2.36})$$

Substitution yields:

$$\frac{m(t)}{\phi} = \frac{\lambda}{2\pi} \ln \left(0.42 \frac{(2\pi)^2 k \eta^2 \mathbf{g} \rho U^2 \Delta p}{\eta^2 \lambda^2 \mathbf{v}} t \frac{\eta}{U} + 1 \right) \quad (\text{A.2.37})$$

rearranging and substituting $Re = \frac{Uh}{\mathbf{v}}$

$$\frac{m(t)}{\phi} = \frac{\lambda}{2\pi} \ln \left(2 \cdot 0.42 \pi^2 \frac{k}{\lambda} \frac{Re}{\phi} \frac{\Delta p}{\lambda} t + 1 \right) \quad (\text{A.2.38})$$

the characteristic porewater velocity is defined as $U_p = 2 k \frac{Re}{\phi} \frac{\Delta p}{\lambda}$, substitution yields:

$$\boxed{\frac{m(t)}{\phi} = \frac{\lambda}{2\pi} \ln \left(0.42 \pi^2 \frac{U_p}{\lambda} t + 1 \right)} \quad (\text{A.2.39})$$

To estimate the time for a water parcel reaching a zero concentration a simplified reaction expression with zero order kinetics ($K_m = 0$) had to be applied using $t = \frac{C_0}{\mathbf{R}}$. This expression can be inserted into equation A.2.39 to calculate the mean penetration depth of the reactive solute as a function of the Damköhler number:

Elliott's Model

$$\frac{\mathbf{m}(Dak_p)}{\phi} = \frac{\lambda}{2\pi} \ln \left(0.42 \pi^2 \frac{1}{Dak_p \lambda} + 1 \right) \quad (\text{A.2.40})$$

Further, the net flux $\mathbf{F}_{\downarrow O_2}$ can now be determined by integrating the reaction rate over the mean penetration depth:

$$\mathbf{F}_{\downarrow O_2} \approx \mathbf{R} \cdot \mathbf{m}(\tau) \quad (\text{A.2.41})$$

2.5.5 Supporting Movie

The supporting movie shows the oxygen distribution for a grain size of $d_g = 174 \mu\text{m}$, a reaction rate of $R = 10 \mu\text{mol l}^{-1} \text{h}^{-1}$ and for Reynolds numbers increasing from 1000 to 15000. Each frame indicates a stationary result for the provided parameters (scaled for a reference bedform height of $\eta = 0.02 \text{ m}$). The white circle indicates the point of stagnation (see article text), while the black solid lines represent the streamlines.

Bibliography

- Baas, J. H. (1994), 'A flume study on the development and equilibrium morphology of current ripples in very fine sand', *Sedimentology* **41**(2), 185–209.
- Bardini, L., Boano, F., Cardenas, M., Revelli, R. and Ridolfi, L. (2012), 'Nutrient cycling in bedform induced hyporheic zones', *Geochimica et Cosmochimica Acta* **84**, 47–61.
- Bear, J. and Buchlin, J.-M. (1978), 'Modelling and applications of transport phenomena in porous media', **5**.
- Bennett, S. and Best, J. (1995), 'Mean flow and turbulence structure over fixed, two-dimensional dunes: implications for sediment transport and bedform stability', *Sedimentology* **42**(3), 491–513.
- Berg, P., Long, M. H., Huettel, M., Rheuban, J. E., McGlathery, K. J., Howarth, R. W., Foreman, K. H., Giblin, A. E. and Marino, R. (2013), 'Eddy correlation measurements of oxygen fluxes in permeable sediments exposed to varying current flow and light', *Limnology and Oceanography* **58**(4), 1329–1343.
- Berg, P., R y, H., Janssen, F., Meyer, V., J rgensen, B. B., Huettel, M. and De Beer, D. (2003), 'Oxygen uptake by aquatic sediments measured with a novel non-invasive eddy-correlation technique', *Marine Ecology Progress Series* **261**(1), 75–83.
- Bhaganagar, K. and Hsu, T.-J. (2009), 'Direct numerical simulations of flow over two-dimensional and three-dimensional ripples and implication to sediment transport: Steady flow', *Coastal Engineering* **56**(3), 320–331.
- Bottacin-Busolin, A. and Marion, A. (2010), 'Combined role of advective pumping and mechanical dispersion on time scales of bed form–induced hyporheic exchange', *Water Resources Research* **46**(8).

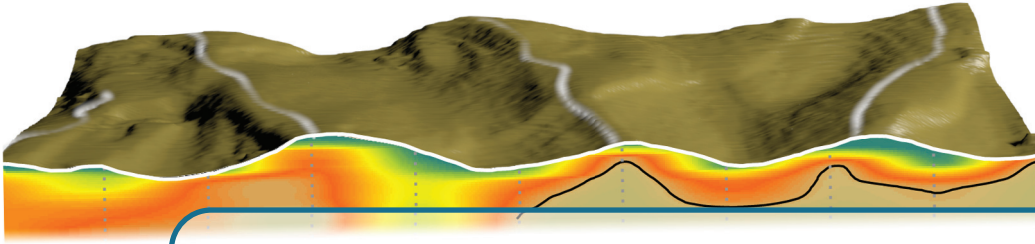
- Bridge, J. S. and Best, J. L. (1988), 'Flow, sediment transport and bedform dynamics over the transition from dunes to upper-stage plane beds: implications for the formation of planar laminae', *Sedimentology* **35**(5), 753–763.
- Brinkman, H. (1949), 'A calculation of the viscous force exerted by a flowing fluid on a dense swarm of particles', *Applied Scientific Research* **1**(1), 27–34.
- Cardenas, M. B., Cook, P. L., Jiang, H. and Traykovski, P. (2008), 'Constraining denitrification in permeable wave-influenced marine sediment using linked hydrodynamic and biogeochemical modeling', *Earth and Planetary Science Letters* **275**(1), 127–137.
- Cardenas, M. B. and Wilson, J. L. (2007), 'Dunes, turbulent eddies, and interfacial exchange with permeable sediments', *Water Resources Research* **43**(8).
- Charles Meneveau, T. S. L. and Cabot, W. H. (1996), 'A lagrangian dynamic subgrid-scale model of turbulence.', *Journal of Fluid Mechanics* **319**, pp 353–385.
- Coleman, S. E. and Melville, B. W. (1994), 'Bed-form development', *Journal of Hydraulic Engineering* **120**, 544–560.
- de Beer, D., Wenzhöfer, F., Ferdelman, T. G., Boehme, S. E., Huettel, M., van Beusekom, J. E., Böttcher, M. E., Musat, N. and Dubilier, N. (2005), 'Transport and mineralization rates in north sea sandy intertidal sediments, silt-rømø basin, wadden sea', *Limnol. Oceanogr* **50**(1), 113–127.
- Elliott, A. H. and Brooks, N. H. (1997a), 'Transfer of nonsorbing solutes to a streambed with bed forms: Laboratory experiments', *Water Resources Research* **33**(1), 137–151.
- Elliott, A. H. and Brooks, N. H. (1997b), 'Transfer of nonsorbing solutes to a streambed with bed forms: Theory', *Water Resources Research* **33**(1), 123–136.
URL: [10.1029/96WR02784](https://doi.org/10.1029/96WR02784)
- Emery, K. (1968), 'Relict sediments on continental shelves of world', *AAPG Bulletin* **52**(3), 445–464.
- Fehlman, H. M. (1985), 'Resistance components and velocity distributions of open channel flows over bedforms', *Phd Thesis* .
- Gangi, A. F. (1985), 'Permeability of unconsolidated sands and porous rocks', *Journal of Geophysical Research: Solid Earth (1978–2012)* **90**(B4), 3099–3104.

- Gao, H., Matyka, M., Liu, B., Khalili, A., Kostka, J. E., Collins, G., Jansen, S., Holtappels, M., Jensen, M. M. and Badewien, T. H. (2012), 'Intensive and extensive nitrogen loss from intertidal permeable sediments of the wadden sea', *Limnology and Oceanography* **57**(1), 185.
- Gao, H., Schreiber, F., Collins, G., Jensen, M. M., Kostka, J. E., Lavik, G., de Beer, D., Zhou, H.-y. and Kuypers, M. M. (2010), 'Aerobic denitrification in permeable wadden sea sediments', *The ISME journal* **4**(3), 417–426.
- Glud, R. N. (2008), 'Oxygen dynamics of marine sediments', *Marine Biology Research* **4**(4), 243–289.
- Goharzadeh, A., Khalili, A. and Jørgensen, B. B. (2005), 'Transition layer thickness at a fluid-porous interface', *Physics of Fluids (1994-present)* **17**(5), 057102–1–5.
- Grant, S. B., Stolzenbach, K., Azizian, M., Stewardson, M. J., Boano, F. and Bardini, L. (2014), 'First-order contaminant removal in the hyporheic zone of streams: Physical insights from a simple analytical model', *Environmental science & technology* **48**(19), 11369–11378.
- Higashino, M., Gantzer, C. J. and Stefan, H. G. (2004), 'Unsteady diffusional mass transfer at the sediment/water interface: Theory and significance for {SOD} measurement', *Water Research* **38**(1), 1 – 12.
- Huettel, A., Ziebis, W. and Forster, S. (1996), 'Flow-induced uptake of particulate matter in permeable sediments', *Limnology & Oceanography* **41**, 309–322.
- Huettel, M., Berg, P. and Kostka, J. E. (2014), 'Benthic exchange and biogeochemical cycling in permeable sediments', *Marine Science* **6**.
- Huettel, M. and Rusch, A. (2000), 'Transport and degradation of phytoplankton in permeable sediment', *Limnology and Oceanography* **45**(3), 534–549.
- Janssen, F., Cardenas, M. B., Sawyer, A. H., Dammrich, T., Krietsch, J. and de Beer, D. (2012), 'A comparative experimental and multiphysics computational fluid dynamics study of coupled surface-subsurface flow in bedforms', *Water Resources Research* **48**.
- Karman, T. (1930), 'Mechanische ähnlichkeit und turbulenz', *Proc. 3. Int. Cong. Appl. Mech* pp. 322–346.
- Kaviany, M. (2012), *Principles of heat transfer in porous media*, Springer Science & Business Media.

- Kessler, A. J., Cardenas, M. B. and Cook, P. L. (2015), 'Bedform migration has negligible effect on denitrification in hyporheic zones of permeable sediments', *Journal of Geophysical Research: Biogeosciences*.
- Kessler, A. J., Glud, R. N., Cardenas, M. B. and Cook, P. L. M. (2013), 'Transport zonation limits coupled nitrification-denitrification in permeable sediments', *Environmental Science & Technology* **47**(23), 13404–13411.
- Kösters, F. and Winter, C. (2014), 'Exploring german bight coastal morphodynamics based on modelled bed shear stress', *Geo-Marine Letters* **34**(1), 21–36.
- Marchant, H. K., Lavik, G., Holtappels, M. and Kuypers, M. M. (2014), 'The fate of nitrate in intertidal permeable sediments', *PloS one* **9**(8), e104517.
- McGinnis, D. F., Sommer, S., Lorke, A., Glud, R. N. and Linke, P. (2014), 'Quantifying tidally driven benthic oxygen exchange across permeable sediments: An aquatic eddy correlation study', *Journal of Geophysical Research: Oceans* **119**(10), 6918–6932.
- Miles, J. and Thorpe, A. (2015), 'Bedform contributions to cross-shore sediment transport on a dissipative beach', *Coastal Engineering* **98**, 65–77.
- Precht, E., Franke, U., Polerecky, L. and Huettel, M. (2004), 'Oxygen dynamics in permeable sediments with wave-driven pore water exchange', *Limnology and Oceanography* **49**(3), 693–705.
- Precht, E. and Huettel, M. (2003), 'Advective pore-water exchange driven by surface gravity waves and its ecological implications', *Limnology and Oceanography* **48**(4), 1674–1684.
- Rao, A. M., McCarthy, M. J., Gardner, W. S. and Jahnke, R. A. (2007), 'Respiration and denitrification in permeable continental shelf deposits on the south atlantic bight: Rates of carbon and nitrogen cycling from sediment column experiments', *Continental Shelf Research* **27**(13), 1801–1819.
- Rao, A. M., McCarthy, M. J., Gardner, W. S. and Jahnke, R. A. (2008), 'Respiration and denitrification in permeable continental shelf deposits on the south atlantic bight: n_2 : Ar and isotope pairing measurements in sediment column experiments', *Continental Shelf Research* **28**(4), 602–613.
- Raudkivi, A. (1997), 'Ripples on stream bed', *Journal of Hydraulic Engineering* **123**(1), 58–64.

- Reimers, C. E., Oezkan-Haller, H., Berg, P., Devol, A., McCann-Grosvenor, K. and Sanders, R. D. (2012), 'Benthic oxygen consumption rates during hypoxic conditions on the oregon continental shelf: Evaluation of the eddy correlation method', *Journal of Geophysical Research: Oceans (1978–2012)* **117**(C2).
- Reimers, C. E., Stecher III, H. A., Taghon, G. L., Fuller, C. M., Huettel, M., Rusch, A., Ryckelynck, N. and Wild, C. (2004), 'In situ measurements of advective solute transport in permeable shelf sands', *Continental Shelf Research* **24**(2), 183–201.
- Richards, K. J. (1980), 'The formation of ripples and dunes on an erodible bed', *Journal of Fluid Mechanics* **99**(03), 597–618.
- Rusch, A., Forster, S. and Huettel, M. (2001), 'Bacteria, diatoms and detritus in an intertidal sandflat subject to advective transport across the water-sediment interface', *Biogeochemistry* **55**(1), 1–27.
- Rutherford, J., Boyle, J., Elliott, A., Hatherell, T. and Chiu, T. (1995), 'Modeling benthic oxygen uptake by pumping', *Journal of Environmental Engineering* **121**(1), 84–95.
- Rutherford, J., Latimer, G. and Smith, R. (1993), 'Bedform mobility and benthic oxygen uptake', *Water Research* **27**(10), 1545–1558.
- Santos, I. R., Eyre, B. D. and Huettel, M. (2012), 'The driving forces of porewater and groundwater flow in permeable coastal sediments: A review', *Estuarine, Coastal and Shelf Science* **98**, 1–15.
- Scalo, C., Piomelli, U. and Boegman, L. (2012a), 'High-schmidt-number mass transport mechanisms from a turbulent flow to absorbing sediments', *Physics of Fluids (1994-present)* **24**(8), 085103.
- Scalo, C., Piomelli, U. and Boegman, L. (2012b), 'Large-eddy simulation of oxygen transfer to organic sediment beds', *Journal of Geophysical Research: Oceans* **117**(C6).
- Soulsby, R. (1997), *Dynamics of marine sands: a manual for practical applications*, Centre for Advanced Engineering, University of Canterbury.
- Thibodeaux, L. J. and Boyle, J. D. (1987), 'Bedform-generated convective transport in bottom sediment'.
- Traykovski, P., Hay, A. E., Irish, J. D. and Lynch, J. F. (1999), 'Geometry, migration, and evolution of wave orbital ripples at leo-15', *Journal of Geophysical Research: Oceans (1978–2012)* **104**(C1), 1505–1524.

- Van Rijn, L. C., van Rijn, L. C. and van Rijn, L. C. (1993), *Principles of sediment transport in rivers, estuaries and coastal seas*, Vol. 2, Aqua publications Amsterdam.
- Weast, R. C., Astle, M. J. and Beyer, W. H. (1988), *CRC handbook of chemistry and physics*, Vol. 69, CRC press Boca Raton, FL.
- Wilson, A. M., Huettel, M. and Klein, S. (2008), 'Grain size and depositional environment as predictors of permeability in coastal marine sands', *Estuarine, Coastal and Shelf Science* **80**(1), 193–199.
- Wollast, R. (1991), 'The coastal organic carbon cycle: fluxes, sources and sinks', *Ocean margin processes in global change* pp. 365–381.
- Yalin, M. (1972), *Mechanics of Sediment Transport*, Vol. 1, Pergamon Press.
- Ziebis, W., Huettel, M. and Forster, S. (1996), 'Impact of biogenic sediment topography on oxygen fluxes in permeable seabeds', *Marine Ecology Progress Series* **140**, 227–237.



3. Oxygen dynamics in subtidal sands

Regulation of benthic oxygen fluxes in permeable sediments of the coastal ocean

Soeren Ahmerkamp

Max Planck Institute for Marine Microbiology, Bremen, Germany

Christian Winter, Knut Krämer

Marum Center for Marine Environmental Sciences of Bremen, Germany

Dirk de Beer, Felix Janssen^{1,2}

Max Planck Institute for Marine Microbiology, Bremen, Germany

Jana Friedrich

Helmholtz Centre for Materials and Coastal Research, Geesthacht, Germany

Marcel MM Kuypers and Moritz Holtappels^{1,3}

Max Planck Institute for Marine Microbiology, Bremen, Germany

Submitted: Limnology & Oceanography

Additional Affiliations:

¹*Alfred Wegener Institute - Helmholtz Centre for Polar and Marine Research, Bremerhaven, Germany*

²*HGF-MPG Group for Deep Sea Ecology and Technology, Bremen, Germany*

³*MARUM Center for Marine Environmental Sciences, Bremen, Germany*

Contributions to the manuscript:

S.A., and M.H. designed research. S.A. and F.J. and M.H. developed methodology, designed and constructed LanceALot. S.A. performed measurements, data analysis and data representation. C.W. and K.K. assisted with deployments of LanceALot and conducted grain size analysis. J.F. provided measurements of organic carbon and ammonium. S.A. and M.H. and D.B. and M.M.M.K., conceived, wrote and edited the manuscript.

Abstract

Large areas of the global shelf area are composed of sandy sediments in which reactive solutes are transported via porewater advection fueling active microbial communities. In order to investigate the advective oxygen transport under *in situ* conditions in the North Sea we developed a benthic observatory for the combined measurements of (i) current velocity, (ii) topography scans, and (iii) multiple benthic oxygen profiles to capture the dynamic change of currents, seabed topography and corresponding benthic oxygen distributions in sandy sediments. At a total of 16 stations, the oxycline was found at depths of 1 – 6 cm and often correlated with the topography of stationary and migrating bedforms. The transient forcing along tidal cycles was found to intricate the oxygen distributions in various ways. The release of anoxic porewater in narrow outlets, previously described in model studies, was not observed. However, the combination of changing bottom water currents and bedform migration led to fluctuating oxygen penetration depths which formed up to 5 cm strong layers of highly variable redox conditions. Volumetric oxygen respiration rates were measured on board in flow through reactors. Bedform migration was found to reduce these rates by up to 50%, presumably caused by the washout of organic carbon that is otherwise trapped in the pore space of the sediment. Integrating the oxygen consumption rates over the oxygen penetration depth, oxygen fluxes of 8 – 34 mmol m⁻² d⁻¹ were estimated. Grain size, current velocity and oxygen respiration rates controlled to a large extent the measured oxygen fluxes which, moreover, agreed well with the outcome of a simple mechanistic flux model for permeable sediments.

3.1 Introduction

Covering just 6-8% of the ocean surface (Sverdrup et al., 1942) continental shelves contribute to approximately 25% of the global primary production and, hence, play a crucial role for the oceanic biosphere (Jahnke, 2010). Since the Industrial Revolution the coastal seas are increasingly affected by nutrient input from river runoffs and atmospheric deposition leading to eutrophication and significant changes in many coastal ecosystems (Boyer et al., 2006; Rabalais et al., 2002).

The North Sea is a prominent example for an anthropogenically eutrophied continental shelf. As a marginal sea of the Atlantic Ocean the North Sea is encompassed by land masses. Therefore, the coastal waters are exposed to large river runoffs leading to high nutrient inputs which fuel photosynthetic carbon fixation (Gerlach, 1981). As a result of the shallow water depths (mostly below 80 m) a large fraction of the fixed organic carbon reaches the sea floor (Otto et al., 1990). While the deep North Sea has been identified as a sink for the atmospheric carbon the shallow North Sea is a source for carbon which elucidates the important role of benthic carbon remineralization (Thomas et al., 2004). In accordance to most continental shelves, also the North Sea sediment is mostly composed of relict silica sand (Emery, 1968).

In general, sandy sediments are low in organic carbon (Janssen et al., 2005; de Beer et al., 2005) and, as a result of the low specific surface area of sand grains, harbor fewer microbial cells compared to muddy sediments (Rusch et al., 2003; DeFlaun and Mayer, 1983). These two facts led to the misconception that sandy sediments are deserts of microbial activity and that the contribution to biogeochemical fluxes is minor (Boudreau et al., 2001). However, in the last two decades it has been shown that this assumption has neglected an important intrinsic characteristic of sand: the permeability, the ability to allow advective fluid flow through the pore space (Thibodeaux and Boyle, 1987). In the subtidal zone of continental shelves the advective porewater flow is mainly driven by the interaction between omnipresent bedforms and the overlying bottom water currents (Santos et al., 2012). The bedforms act as an obstacle, and following Bernoulli's principle, cause a local acceleration of the bottom water currents which generates a pressure gradient pumping organic-rich bottom water through the pore room of the sandy sediment (Huettel et al., 1996).

It was inferred from flume experiments (Huettel et al., 1996), modelling studies (Janssen et al., 2012; Cardenas and Wilson, 2007) and volumetric rate measurements (Reimers et al., 2004; Rao et al., 2007; Marchant et al., 2014) that the advective porewater flow through sandy sediments has strong implications for the biogeochemical cycling on continental

shelves (Santos et al., 2012; Huettel et al., 2014). By pumping bottom water across the sediment-water interface the benthic infauna is supplied with electron acceptors and donors. The organic matter is degraded by a diverse microbial community that lives mostly attached to the sand grains (Rusch et al., 2003). Remineralization products, such as nutrients and reduced substances, are released back to the water column enhancing the benthic pelagic coupling (Huettel et al., 1996). In contrast to cohesive sediments in which diffusion transport limits oxygen penetration to a few millimeter, the advective transport in sandy sediments leads to extended oxic and suboxic zones in which microbial processes enhance benthic remineralization and denitrification and thus counteract anthropogenic eutrophication (Rao et al., 2007; Gao et al., 2012; Marchant et al., 2014, 2016).

In nature, the above described transport and reaction processes occur under highly variable hydrodynamic and morphodynamic conditions. Strong tides are characteristic for shallow coastal waters and the mere presence of bedforms is indicative of a mobile sea bed. In situ measurements that capture these dynamics are rare. However, flume experiments showed that the oxic zone moves with the migrating bedform which potentially leads to variable conditions of oxic and anoxic (Precht and Huettel, 2003; Precht et al., 2004). Further, bedform migration involves a new mode of porewater exchange. Porewater is released at the stoss side of the bedform due to erosion of sediment grains, while bottom water is trapped at the lee side due to deposition of sediment grains (Elliott and Brooks, 1997; Rutherford et al., 1993). A model study, which linked bedform migration to the hydrodynamic forcing found that the combined effect of erosion and deposition of sand grains leads to the separation of the sediment into an upper mobile layer and a stationary layer underneath. While the mobile layer becomes increasingly flushed along increasing bedform migration, the stationary layer underneath becomes isolated which may ultimately reduce benthic oxygen fluxes by up to 90% (Ahmerkamp et al., 2015a).

The in situ investigation of sandy sediments on continental shelves is a challenging task. In shallow waters (below 100 m), the transient nature of the driving hydrodynamics (waves and tides) and the mobile seabed complicate the assessment. The effect of porewater advection on biogeochemical processes has thus been studied predominantly in flume experiments (e.g. Janssen et al., 2012) and model simulations (e.g. Cardenas and Wilson, 2007), mostly under steady state conditions. However, it is necessary to investigate the interaction of transient hydro- and morphodynamics and its effect on benthic fluxes under natural conditions to examine the laboratory finding and to identify from a multitude of variables those that control benthic fluxes in natural environments.

We developed an automated benthic observatory for the simultaneous acquisition of current velocity, topography scanning, and high resolution oxygen profiling. In combi-

nation with on board measurements of microbial oxygen respiration rates and sediment properties, we aimed to describe and quantify how the interplay of abiotic factors (sediment permeability, hydro- and morphodynamic forcing) and biotic factors (microbial rates, organic carbon content) effect oxygen penetration and oxygen fluxes. Based on the measurements the controlling variables were identified and a simple model was constructed that allows for estimating benthic oxygen fluxes in permeable sediments.

3.2 Methods

3.2.1 Study site

Investigations were carried out in the German Bight which is the southeastern part of the North Sea encompassed by Netherlands, Denmark and Germany. Deployments took place during four field trips with the research vessel *Heincke* (He447, He432, He417, He412) in November 2013, March 2014, September 2014 and July 2015, respectively.

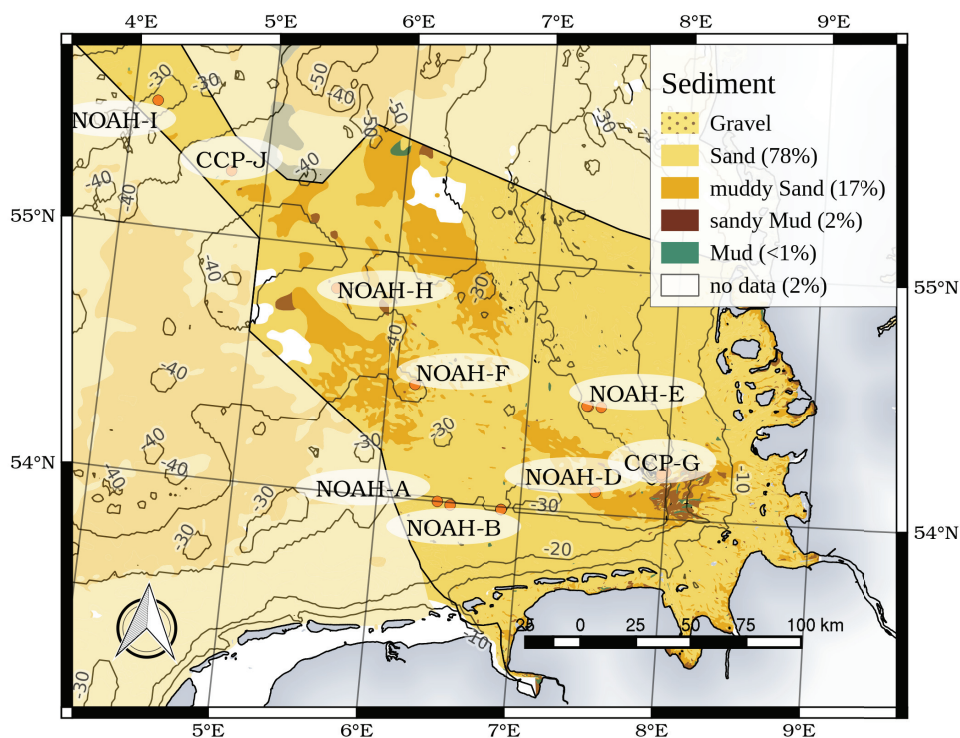


Figure 3.1: Lander stations in the German Bight during the R/V *Heincke* cruises. The colors indicate the main grain size fractions after Folk (2000). The exclusive economic zone of Germany is depicted as the bold black line, while the thin lines indicate the bathymetry with values in meters (*Data provided by Geopotential Deutsche Nordsee and EMODnet*).

The German Bight is characterized by strong discharges from the rivers Elbe, Rhine Ems and Weser leading to anthropogenic nutrient enrichment fueling high primary production (Brockmann et al., 1988; Hickel et al., 1993; van Beusekom, 2005). Shallow water depths of less than 40 m cause strong benthic-pelagic coupling because the retention times of aggregates in the water column are short (Simon et al., 2002). Benthic heterotrophic degradation is, therefore, driven by a pelagic plankton bloom triggered by the increasing temperature and stratification in spring and summer (Chiswell, 2011; Van Duyl and Kop, 1994). Further, the shallow coastal waters are characterized by strong hydrodynamic forcing caused by semi-diurnal tides and wind-induced surface gravity waves (Grashorn et al., 2015).

The sea-floor is mostly covered by clastic sediments (Figure 3.1) of which 95% are composed of sand (fraction above 63 μm) that are potentially subject to advective porewater flow (Janssen et al., 2005). Less than 3% are covered by cohesive sediments such as mud and sandy mud (fraction below 63 μm). For the purpose of this study, sandy sediments are subclassified into sand (at least 90% sand content) and muddy sand (mostly sand with 10%-50% mud) (see Figure 3.1, after Folk (2000)). The general composition of the sediments has some relation to the water depth. In water depths of 15 – 30 m the median grain size ranges mostly between 200 μm and 500 μm . Muddy sand regions are located in water depths of 30 – 45 m with median grain sizes ranging between 100 μm and 200 μm .

3.2.2 In situ measurements

In total, 16 lander deployments were carried out on 9 stations which were chosen as representative stations for habitat mapping within the NOAH project (North Sea Observation and Assessment of Habitat). The positions were selected based on the governing grain size distribution to cover the full range as present in the North Sea. In general, the stations have only few large scale morphological features, such as reefs, sand waves and dunes. Only station CCP – G.I and CCP – G.II were characterized by large dunes which, in combination with sediment sorting, led to heterogeneous sediment distributions.

The measurements in subtidal regions of the German Bight require autonomous observatories which sustain strong current and wave forcing. Therefore, a quadropod with a base area of 1.5 m \times 1.5 m was designed, which ensures a stable positioning and minimal movements during deployment. To minimize hydrodynamic disturbance underneath the frame, the legs were inclined in a 30° angle (Figure A.3.12). The distance between the sea floor and observatory base was adjusted to 1.50 m. An accurate positioning of the benthic observatory towards the tidal currents was achieved by using a launcher with a remotely operated releaser allowing online reading of the instrument's heading (Herbst

Environmental Science) (Figure A.3.12 a). The observatory was released when facing the main flow direction. Retrieval was achieved by means of a popup buoy (875-PUB, Teledyne Benthos).

Bottom water oxygen was measured using an optode (Aandera 3835, RD Instruments) mounted on top of the lander. Bottom water currents were measured using an acoustic Doppler velocimeter (ADV, Vector, Nortek and and acoustic Doppler current profiler (ADCP, 1200 kHz, Teledyne, RD Instruments). Additional instruments for oxygen profiling and topography mapping were attached to a motor driven carriage mounted underneath the lander and connected to a PC/104 board (EM104P-I6023, intel) via a RS-485 bus and Firewire 1394. The serial communication and deployment protocol was implemented into Python 2.7 based on a Debian GNU/Linux distribution.

Oxygen profiling

Oxygen profiles in the sediment were measured using optodes with a tip diameter of $430\ \mu\text{m}$ (Bare Fiber Oxygen Minisensor, Ultra High Speed, Pyroscience). Four optodes were mounted in a row of 5 cm intervals to a linear drive that allows for an accurate vertical positioning (Figure A.3.12 b). The linear drive itself was attached to the carriage allowing for horizontal positioning. The bare fibers were glued into needles of 20 cm length and 1 mm diameter using epoxy resin so that the dead volume in the needle was filled and the tip of the needle protrudes approximately 0.5 mm beyond the sensor tip. This minimized abrasion of the fluorescent coating and increased stability during penetration. Under in situ conditions this allowed for some 25 – 30 consecutive profiles in the rigid sediments before the signal intensity fell below its critical value. However, the response time of the sensor was slightly increased. By using deoxygenated water, a step change of oxygen could be simulated and the response time t_{90} determined. In average the response time was within $0.7(0.2)$ s (Data not shown, number in brackets denotes standard deviation of three different optodes). Obviously, tip width and response time limit the spatial and temporal resolution, respectively. Best compromise between minimum smearing and maximum resolution in terms of space and time was found by adjusting the vertical displacement of the profile measurements to 0.2 mm and 0.5 mm in discrete steps. In each depth the optodes were left for 2 s before measurement. The profiling depth was usually 10 cm and the time for the simultaneous profiling of 4 optodes took approximately 5 min. This was repeated 3 times so that in total, 12 profiles separated by 5 cm intervals were taken covering a total length 60 cm. The complete profiling took 20 min and was repeated in 1 hour intervals. The optodes were calibrated at every deployment using in situ measurements of bottom water oxygen and zero oxygen reading in the anoxic part of the sediment.

Topography mapping

The measurement of local topography is based on the laser scanning technique after Cook et al. (2007) and Glud et al. (2003). It consists of a laser (658 nm, 40 mW streamline laser, sela inc.) projecting from above (90° angle) a 30 cm long line onto the sea bed which is oriented perpendicular to the direction of the sledge movement. This laser line is recorded by a camera (Guppy Pro, AVT) adjusted in a 45° angle to the laser sheet and the direction of the carriage movement. Laser and camera were mounted to the carriage which was moved in longitudinal direction by a linear drive. For each surface scan the speed was kept constant at a velocity of 2.5 mm s^{-1} and 160 pictures were recorded at intervals of 2 s. From the deflection of the laser line along spatial gradients the topography was reconstructed.

After deployments the laser was replaced by a chess board pattern and the instruments were immersed into North Sea water to take calibration pictures. Based on these, raw pictures from the bedform recordings were rectified. Afterwards, each picture was decomposed into pixel slices perpendicular to the laser line. In each pixel slice the intensity maximum was determined. A five-point Gaussian fit around the maximum intensity increased the resolution to sub-pixel scale. The final image reconstruction was post processed using an outlier detection and median filter. The resolution is mainly limited due to the error in rectification and peak locking in cases of overexposure. In strong light conditions the accuracy of peak determination was lowest but still within 5px leading to a maximum error of $\Delta z = 1 \cdot 10^{-3} \text{ m}$ and $\Delta z = 1 \cdot 10^{-4} \text{ m}$ under good light conditions. Laser surface scans were performed in intervals of 50 min and 10 min, respectively. The final topography reconstruction encompasses an area of $0.8 \text{ m} \times 0.3 \text{ m}$ with a grid resolution of $\delta x = 5 \cdot 10^{-3} \text{ m}$ and $\delta y = 2 \cdot 10^{-3} \text{ m}$ - where δx is the longitudinal direction and δy the transversal direction, respectively.

From the bedform reconstructions the characteristic bedform height δ was determined using the standard deviation σ of the local height displacement η_{xy} , i.e. $\delta = 2\sqrt{2}\sigma_\eta$ (Stonedahl et al., 2010). Bedform wavelength λ and migration celerity c_{ph} were determined by the auto-correlation and cross-correlation function, respectively (Ayoub et al., 2014). For comparison and for visualization, an edge detection algorithm was implemented as described by Traykovski (2007). A top-hat filter was used to extract the bedform features from the reconstructions. The results were fairly similar, even though the edge detection was more susceptible to noise.

Bottom water currents

To determine the effects of hydrodynamics on the bedforms we calculated the shear stress and wave properties. Bedform migration is initialized when the overlying fluid exceeds a critical velocity and sediment starts to move. The force acting on the sediment surface is summarized by the bed shear stress which is determined by fitting the velocity profile of the ADCP to the log law:

$$U(z) = \frac{U_*}{\kappa} \cdot \ln\left(\frac{z}{z_0}\right) \quad (3.1)$$

where z is the depth, and $\kappa = 0.41$ the Karman constant. The free variables were the roughness length (z_0) and the shear velocity ($U_* = \sqrt{\frac{\tau}{\rho}}$) with τ the shear stress and ρ the water density. As reference for the theoretical initialization of sediment movement a critical shear stress is determined based on the non-dimensional grain size $D_* = d_g \left[\frac{g(s-1)}{\rho v^2} \right]^{1/3}$ after Soulsby (1997):

$$\frac{\tau_{cr}}{(s-1)gd_g} = \frac{0.3}{1 + 1.2D_*} + 0.55(1 - e^{-0.20D_*}) \quad (3.2)$$

where g is acceleration due to gravity, ν is the kinematic viscosity, $s = \frac{\rho_s}{\rho_w}$ the density ratio between silica sediment (ρ_s) and water (ρ_w), and d_g the median grain size.

In order to determine the influence of waves, the wave orbital velocity is computed. The wave direction is determined by rotating the coordinate system until variance is maximized. Subsequently, after inspection of the spectrum, the signal is high pass filtered using a 2nd order Butterworth filter with a cutoff frequency of 0.02 Hz to separate the tidal component U from the fluctuating components (u' and v'), of which the variance can be used to calculate the wave orbital velocity (Wiberg and Sherwood, 2008):

$$U_{orb} = \sqrt{2(\text{Var}(u') + \text{Var}(v'))} \quad (3.3)$$

3.2.3 Ex situ measurements

Flow through reactors

Microbial oxygen respiration was measured in flow through reactors which mimic the in situ conditions. Therefore, at each station sediments were sampled using a box corer (Oktopus, Standard Box Corer 2500) with an base area of 0.50 m × 0.50 m. The upper two

centimeters of sediment were subsampled, and immediately after collection the sediments were homogenized and large shell debris was sieved using a 1 mm sieve. Experiments were performed on board in a cold room at in situ temperature at least 4 hours after retrieving the sediments. Bottom water was collected at 1 m to 2 m above the sea floor by a rosette water sampler and kept in darkened 5 l Duran bottles which were continuously mixed using a magnet stirrer while air was injected.

Acrylic flow through reactors were immersed in water and carefully filled with the pooled sediment avoiding any gas inclusions. Using peristaltic pumps (ISMATEC, Reglo digital MS-4/6) the bottom water was pumped through the flow through reactors which have the advantage that the reaction rate can be measured to high accuracy under conditions of realistic porewater flow (Rao et al., 2007). The inner diameter was $d = 10$ cm while the length of the core was $L_c = 20$ cm. Radial grooves in the lids of the reactor ensured a homogeneous percolation. Sediment discharge into the tubing was avoided by covering the grooves with a plankton net ($80 \mu\text{m}$ mesh). The chambers were wrapped in foil to exclude light penetration and primary production. Oxygen consumption in the core was measured with optode flow-through cells (OXFTC, Pyroscience) attached to the inlet (C_{in}) and outlet (C_{out}). In between the flow-through cells and reactors polyetheretherketone (PEEK) tubing ensured minimal diffusion of atmospheric oxygen into the system. By using the retention time $r_t = L_c/u$ with u as the porewater velocity, the reaction rate in porewater can be estimated:

$$R = \frac{(C_{out} - C_{in})}{r_t} \quad (3.4)$$

As a proxy for the homogeneity of the porewater flow, breakthrough curves of a conservative solute were determined. After finishing the respiration experiments, sodium bromide was added to the reservoir to a final concentration of 5 mmol l^{-1} . At the outlet, conductivity, as a proxy of the sodium bromide concentration, was measured at 5 s intervals. In all experiments the maximum smearing induced by the dispersion was well below 50% of the core length (see appendix A.1). This indicates that the slowest pathways have a retention time that is 1.5 times as long as the average. Therefore, it was ensured that the oxygen concentration is well above zero for $1.5r_t$ to ensure no bias in the respiration measurements. Depending on the reaction rate this was achieved by adjusting the porewater velocity to $3.6 - 18 \text{ cm h}^{-1}$ which is in the range of natural porewater advection (Reimers et al., 2004).

Sediment characteristics

Sediment samples were retrieved using a multicorer (Oktopus, MC-8/100). Sediment layers of 0.5 cm – 1 cm were homogenized and frozen at -20°C on board. For carbon analysis the sediment samples were dried and grinded. In an element analyzer (CE instruments) the total carbon content was determined. Subsequently, in another subsample the inorganic carbon was determined coulometrically (UIC Coulometrics, CM 5012 CO_2 Coulometer) after being acidified. From the difference between total carbon content and inorganic carbon the organic carbon was calculated as weight percentage.

Grain size distributions were measured using a laser diffraction particle size analyzer (Beckman Coulter, LS 200) for 92 size classes ranging from 0.4 to $2000\mu\text{m}$. Prior to measurements the samples were treated with hydrogen peroxide to remove organic matter. Based on the median of the grain size distribution (d_g) the permeability was determined following the empirical relation by Gangi (1985):

$$k = Dar \cdot 735 \cdot 10^6 \cdot d_g^2 \quad (3.5)$$

where k is the permeability and Dar is the conversion factor for unit Darcy into m^2 ($=9.869 \cdot 10^{-13}$).

3.2.4 Oxygen flux estimations

Under stationary conditions the benthic oxygen flux can be determined by integrating the volumetric oxygen respiration rates R over the oxygen penetration depth θ :

$$F_{\downarrow O_2} = \delta R \theta \quad (3.6)$$

where θ is the porosity. Because of the transient hydrodynamic condition the spatial and temporal average of the penetration depth was calculated and applied in Equation 3.6.

This study focuses on permeable sediments. Nevertheless, some stations turned out to be impermeable to flow as they could not be percolated in the flow through reactors. Therefore, the transport processes are governed by diffusion. For those stations respiration rates were estimated by inversely solving the stationary diffusion-reaction using the Tikhonov regularization technique (Berg et al., 1998; Wang et al., 2008; Lettmann et al., 2012). Parameters such as bioturbation and bioirrigation could not be estimated in the in situ measurements, therefore, we assume a simplified diffusive transport in cohesive

sediments:

$$-D_p \cdot \frac{\partial^2 C}{\partial z^2} = -R \quad (3.7)$$

where z is the depth, R the respiration rate, D_p the diffusion coefficient corrected for tortuosity and temperature.

3.2.5 Oxygen flux modelling

The advective transport through permeable sediments complicates the modelling of solute fluxes as compared to cohesive sediments. Facing the many variables such as current velocity, bedform geometry and permeability it is useful to establish characteristic variables that allow for a better description of the system. Following Darcy's law the porewater flow is a function of the pressure gradient in the sediment, the permeability k , the porosity θ and the kinematic viscosity of the fluid ν . A non-dimensional characteristic pressure difference of $\Delta p = 0.1$ along the bedform was found for bedform dimensions that apply also for this study (Ahmerkamp et al., 2015a). In dimensions, Δp scales with the square of the bottom water velocity U and can be used to define a characteristic porewater velocity. The full derivation can be found in Ahmerkamp et al. (2015a):

$$U_p = 2 \frac{k U^2 \Delta p}{\theta \nu \lambda} \quad (3.8)$$

U_p can be seen as the maximum pore water velocity induced by the characteristic pressure along half the bedform length 0.5λ . Based on this parameter the non-dimensional Damköhler number can be defined:

$$Da_\lambda = \frac{\tau_t}{\tau_r} \quad (3.9)$$

which describes the relative timescales of oxygen reaction $\tau_r = CR^{-1}$ to oxygen transport $\tau_t = \lambda U_p^{-1}$. When transport rates dominate the reactive solute gets transported deeply into the bedform. On the other hand, high respiration rates lead to an almost complete consumption in the vicinity of the sediment surface. Despite the inherent complexity of the two-dimensional advective porewater transport it was shown for stationary bedforms, that the spatially averaged oxygen penetration depth is proportional to the logarithm naturalis

of the reciprocal Damköhler number (Elliott and Brooks, 1997; Ahmerkamp et al., 2015b):

$$\delta_M = \frac{\lambda}{2\pi} \cdot \ln(0.42\pi^2 \cdot Da_\lambda^{-1} + 1) \quad (3.10)$$

From δ_M the flux can be calculated by integrating the respiration rate (analogous to Equation 3.6):

$$F_{M,\downarrow O_2} = \delta_M \theta R \quad (3.11)$$

The characteristic porewater velocity is also a useful variable to better describe the relative strength of bedform migration. The velocity ratio of bedform migration to pressure driven advective porewater flow is given by:

$$U_r = \frac{c_{ph}}{U_p} \quad (3.12)$$

3.3 Results

3.3.1 Hydro- and morphodynamics

Bedform length, height and migration were determined (Table 3.1) and the corresponding hydrodynamics investigated. At three stations (⁴³²NOAH – I, ⁴³²CCP – J and ⁴³²NOAH – H) no small scale bedforms were observed. Smaller scale roughness elements below the cm scale are not significant for advective porewater flow (Huettel et al., 2014). At the remaining 13 stations bedforms were observed and categorized based on the sediment classification of the respective stations: sand and muddy sand.

Sandy sediment was found at 11 stations of which 10 stations exhibit bedforms of variable length ranging between 0.11 m to 0.29 m. This variation of bedform length was strongly correlated to the grain size which can be used to reduce the complexity of parameters. In Figure 3.2 a the bedform wavelength is compared to the median grain size d_g and scales well at a slope of 1:490. This behavior persists for stationary bedforms (e.g. ⁴³²NOAH – E) that showed no movement during deployment as well as bedforms under strong transient forcing (e.g. ⁴³²NOAH – B). Qualitatively this is in agreement with prior investigations (Raudkivi, 1997), but, in direct comparison $\lambda = 490d_g$ falls underneath typical scalings of $600d_g < \lambda < 2000d_g$ derived from flume experiments (Yalin, 1985). The mismatch might be induced by the relative narrow grain size distribution considered

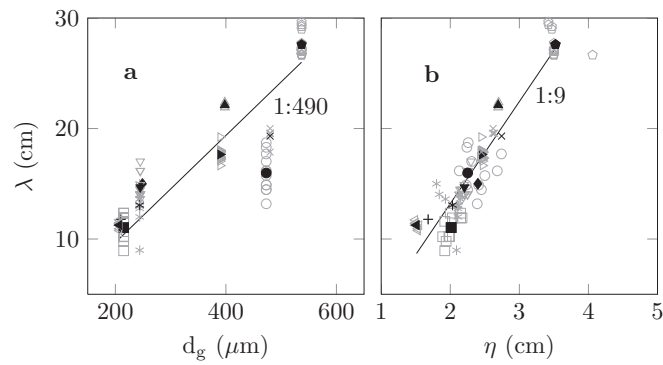


Figure 3.2: Correlations emphasizing the controlling parameter for the bedform geometry. In **a** the wavelength λ scales well with the median grain size d_g . In **b** the bedform height to wavelength ratio follows a fixed steepness of 1:9. The black solid symbols denote averaged values of the respective stations, while the light gray symbols represent individual measurements. The symbols represent the respective stations from Table 3.1.

in the flume experiments by Yalin (1985). Analysis of stations that fall off the $490d_g$ line ($^{417}\text{CCP} - \text{G.I}$, $^{417}\text{CCP} - \text{G.II}$) revealed that the bedform shape was 3-dimensional (compare also Figure A.3.13 **d**).

The ratio of bedform height and wavelength stayed constant at a ratio of 1:9 (Figure 3.2 **b**). The shapes were asymmetric with a gentle stoss side and a steep lee side. The orientation of the bedforms followed the main tidal flow directions. In conjunction, this indicates that the bedforms were largely generated by uni-directional flow (Dey, 2014). The strength of the average bottom current velocities followed the trend of the semi-diurnal tidal cycle with velocities ranging from 7 cm s^{-1} to 21 cm s^{-1} (Figure 3.3 and Table 3.1). The tidal amplitude was similar for all stations with slight variations induced by spring and neap tide. Waves were present during all deployments, but the near bed wave motion did not exceed 8 cm s^{-1} . Most of the time the oscillating near bed wave motion ranged in between 2 cm s^{-1} and 5 cm s^{-1} . The bedform geometry was not found to correlate with the magnitude of the current velocity nor with near bed wave motions.

Bedform migration was observed at seven stations ranging from 0.2 to 28 cm h^{-1} (Figure 3.3, mean values in Table 3.1). Along the tidal cycle three different states of migration were identified including (i) no bedform migration, (ii) bedform migration during tidal peak flow and (iii) continuous bedform migration. The temporal behavior of bedform migration is depicted in figure 3.3 for chosen stations. As soon as the shear stress exceeded its critical value bedforms started to migrate and accelerated towards the tidal peak (Figure 3.3 **b-d**). After reaching the peak values, the bedforms decelerated and either stopped (Figure 3.3 **b**) or continued migrating at low celerities (speed of bedform

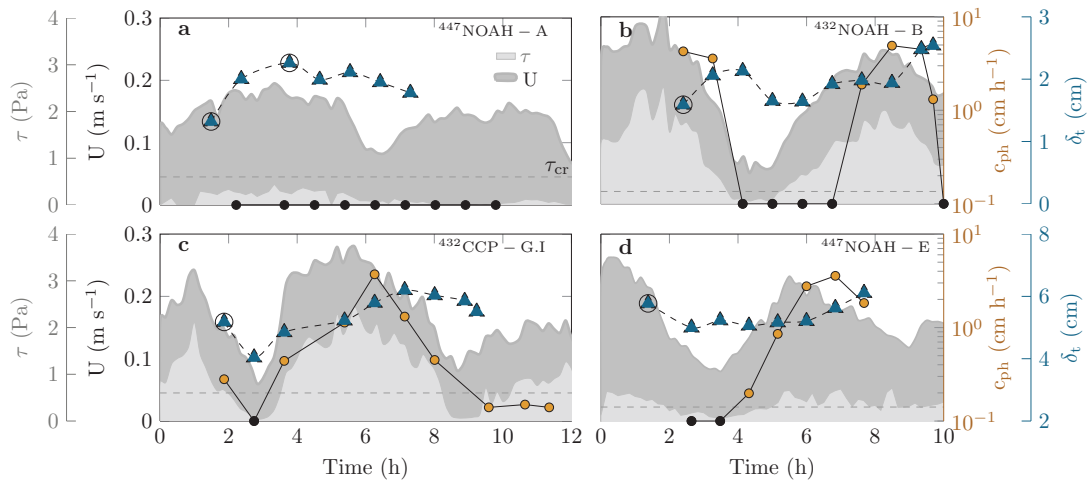


Figure 3.3: The transient behavior of the spatially averaged oxygen penetration depth (δ_t) and bedform migration (c_{ph}) during a tidal cycle is shown for representative stations with the bottom water velocity (U) and shear stress (τ) in the background as shaded areas. The circles around triangles indicate the measurements used for Figure 3.5 and Figure A.3.13. Bedform migration symbols on top of the abscissa indicate no detectable bedform migration. The dashed line indicates the critical shear stress at which sediment movement is theoretically initialized. In **d** the penetration depth is scaled by a factor of two for visualization purposes.

migration) (Figure 3.3 **c**). Seasonal variations of morphodynamics were visible for the different stations. The magnitude of bedform migration was similar for the summer and autumn cruises He432 and He447 but highest celerities were measured during the spring cruise He417 (averaged up to 6.6 cm h^{-1}), despite the fact that wave and currents were in a similar range. Inspection of the photographic images (Data not shown) reveals strong macrofaunal activity in summer and autumn. The organisms might stabilize bedforms.

Bedforms were usually not present where sediment was composed of muddy and mostly impermeable sand. These stations were typically located in deeper waters ($> 30 \text{ m}$) (compare Figure 3.5 **a**). One exception was, $^{447}\text{NOAH} - \text{D}$ (Figure A.3.13 **c**) which had the largest bedforms, in terms of length and height. On $^{447}\text{NOAH} - \text{F}$ (Figure A.3.13 **b**) topographies were clearly visible but the cross-correlation analysis revealed that the bedforms were randomly distributed, as multiple peaks occurred. In combination, with small scale roughness elements this indicates biogenic mounds (Ziebis et al., 1996; Cook et al., 2007).

3.3.2 Oxygen penetration

Spatially averaged penetration depths were calculated from the oxycline defined here as the isoline where oxygen decreased to 5% of the bottom water concentration. The values (Table 3.1) ranged from 0.9 cm for stations with muddy sand (e.g. ⁴³²CCP – J, ⁴⁴⁷NOAH – D) to 6.4 cm for stations with coarse sand (e.g. ⁴¹⁷CCP – G.I, ⁴³²CCP – G.I). A significant correlation between grain size and penetration depth was found (Figure 3.4). The shallowest penetration depths were found at stations that were located in water deeper than 30 m, where sediments were composed of muddy sand. Deepest penetration depths were found at stations with large median grain diameters (e.g. ⁴⁴⁷CCP – G.I). Permeability seemed to be the main controlling parameter for penetration depth whereas no significant correlation was found for oxygen respiration rates.

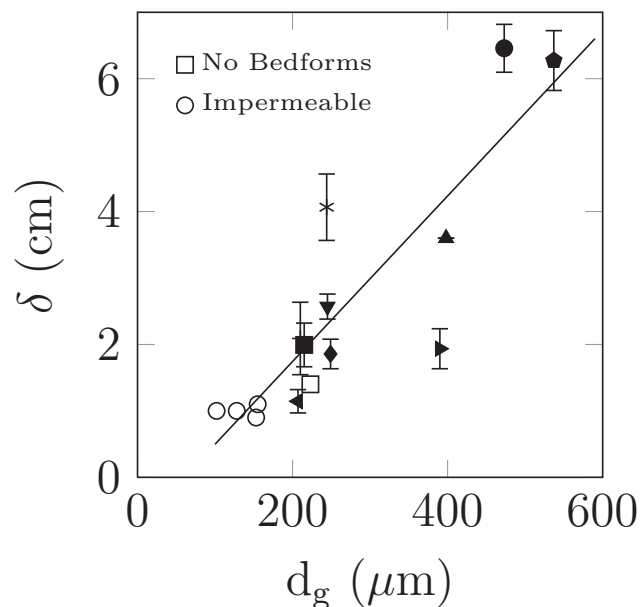


Figure 3.4: The average penetration depth (δ) of oxygen is proportional to the median grain size ($\delta = 1.3 \cdot 10^{-4}d_g - 7.5 \cdot 10^{-3}$, $R^2 = 0.66$ only permeable stations) indicating the presence of advective porewater flow. Open circles depict penetration depths of stations covered by impermeable sediments. The whiskers denote the standard deviations of the measurements.

In Figure 3.5 three examples are depicted which show typical bedform topographies and associated oxygen distributions. In order to get a better visual impression of the oxygen penetration depth, 12 oxygen profiles per transect were bilinearly interpolated to a 2-dimensional distribution. On top the surface reconstruction was projected with an inclination angle of 30° . During lander deployment it was ensured, that the sledge faces the main flow direction. Figure 3.5 **a** is shown as a reference example for impermeable muddy

| Station | GPS | Depth d_g | U | θ | k | C_{org} | C | R | δ | $\delta \frac{\partial T}{\partial t}$ | λ | η | U_p | $c_{p,h}$ | Da_λ | Pe_λ | q_s | $F_{\downarrow O_2}$ | N | | |
|----------------------------|-------------------------|-------------|-------------------------|----------|--------------|----------------------|------------------------|--------------------------------------|----------|--|-----------|--------|--------------------|--------------------|--------------|--------------|--|------------------------------------|----------------------|-------|-------|
| | | m | $\mu\text{m cm s}^{-1}$ | | m^2 | wt.% | $\mu\text{mol l}^{-1}$ | $\mu\text{mol l}^{-1} \text{h}^{-1}$ | cm | $\text{cm} \text{h}^{-1}$ | cm | cm | cm h^{-1} | cm h^{-1} | | | $\text{m}^3 \text{m}^{-2} \text{d}^{-1}$ | $\text{mmol m}^{-2} \text{d}^{-1}$ | | | |
| 44 ^o NOAH - D | 55°30.05'N 4°10.11'E | 32 | 102 | 15 | 0.45 | $< 10^{-12}$ | 0.15 | 282 | 25* | 1.0 | 0.1 | 35 (†) | 4.1 | 0 | 0 | 0 | 10 | nd | 3* | 5,2 | |
| 44 ^o NOAH - F | 54°26.24'N 7°25.35'E | 36 | 128 | 10 | 0.5 | $< 10^{-12}$ | 0.2 | 282 | 20* | 1.1 | nd | nd | nd | nd | nd | nd | nd | nd | 3* | 1,1 | |
| 43 ^o CCP - J | 55°15.51'N 4°44.97'E | 38 | 153 | 5 | 0.46 | $< 10^{-12}$ | 0.4 | 255 | 10* | 0.9 | nd | nd | nd | nd | nd | nd | nd | nd | 1* | 1,1 | |
| 43 ^o NOAH - H | 54°49.50'N 5°34.70'E | 39 | 155 | 5 | 0.40 | $< 10^{-12}$ | 0.4 | 253 | 10* | 1.1 | nd | nd | nd | nd | nd | nd | nd | nd | 1* | 1,1 | |
| 43 ^o NOAH - I | 55°30.05'N 4°10.11'E | 27 | 223 | 7 | 0.38 | $3.6 \cdot 10^{-11}$ | 0.03 | 256 | 129 | 1.4 | nd | nd | nd | nd | nd | nd | nd | nd | 16(4) | 1,5 | |
| 43 ^o NOAH - E | 54°26.24'N 7°25.35'E | 24 | 249 | 10 | 0.41 | $4.5 \cdot 10^{-11}$ | 0.05 | 246 | 71 | 1.9 | 0.5 | 15 | 2.4 | 0 | 0.6 | 0 | 6 | 250 | $0.27 \cdot 10^{-2}$ | 13(3) | 10,10 |
| 44 ^o NOAH - B | 55°15.51'N 4°44.97'E | 25 | 207 | 13 | 0.4 | $3.1 \cdot 10^{-11}$ | 0.08 | 275 | 144 | 1.1 | 1 | 11 | 1.5 | 0 | 0.7 | 0 | 6.0 | 200 | $1.8 \cdot 10^{-2}$ | 16(5) | 4,7 |
| 44 ^o NOAH - A | 54°49.50'N 5°34.70'E | 28 | 390 | 15 | 0.4 | $1.1 \cdot 10^{-10}$ | 0.10 | 267 | 78 | 1.9 | 0.6 | 18 | 2.5 | 0 | 1.8 | 0 | 2.6 | 900 | $0.73 \cdot 10^{-2}$ | 14(3) | 7,19 |
| 41 ^o NOAH - B | 53°59.19'N 7°52.07'E | 29 | 210 | 17 | 0.42 | $3.2 \cdot 10^{-11}$ | 0.19 | 318 | 138 | 2.1 | 0.5 | 12 | 1.7 | 0 | 1.3 | 0 | 4.4 | 450 | $1.0 \cdot 10^{-2}$ | 29(9) | 1,3 |
| 44 ^o CCP - G.I | 54°10.39'N 7°57.52'E | 22 | 398 | 17 | 0.36 | $1.2 \cdot 10^{-10}$ | 0.26 | 266 | 64 | 3.6 | nd | 22 | 2.7 | 0.6 | 2.0 | 1.2 | 2.5 | 1250 | $1.7 \cdot 10^{-2}$ | 20(3) | 1,5 |
| 44 ^o NOAH - E | 53°59.23'N 6°52.23'E | 25 | 245 | 10 | 0.39 | $4.4 \cdot 10^{-11}$ | 0.06 | 276 | 42 | 2.6 | 0.9 | 15 | 2.2 | 3.9 | 0.3 | 1.0 | 6.4 | 150 | $3 \cdot 10^{-2}$ | 13(3) | 8, 15 |
| 43 ^o CCP - G.I | 54°10.39'N 7°57.52'E | 20 | 537 | 15 | 0.43 | $2.1 \cdot 10^{-10}$ | 0.3 | 235 | 52 | 6.3 | 0.4 | 28 | 3.5 | 0.3 | 3.3 | 1.0 | 1.7 | 2300 | $1.2 \cdot 10^{-2}$ | 34(9) | 9,15 |
| 43 ^o NOAH - B | 53°59.23'N 6°52.23'E | 24 | 215 | 19 | 0.39 | $3.4 \cdot 10^{-11}$ | 0.29 | 244 | 62 | 2.8 | 0.4 | 11 | 2.0 | 1.1 | 1.7 | 1.9 | 1.3 | 600 | $6.0 \cdot 10^{-2}$ | 16(3) | 10,11 |
| 41 ^o CCP - G.I | 54°10.11'N 7°57.31'E | 19 | 473 | 21 | 0.42 | $1.6 \cdot 10^{-10}$ | 0.08 | 314 | 15 | 6.4 | 0.2 | 16 | 2.3 | 0.9 | 7.7 | 6.5 | 0.1 | 3500 | $10 \cdot 10^{-2}$ | 10(2) | 10,19 |
| 41 ^o CCP - G.II | 54°10.13'N 7°59.49'E | 20 | 480 | 22 | 0.42 | $1.7 \cdot 10^{-10}$ | 0.24 | 313 | 15 | nd | nd | 19 | 2.7 | nd | nd | 0.7 | nd | nd | $9.1 \cdot 10^{-2}$ | nd | 0,12 |
| 41 ^o NOAH - E | 54°26.25'N 7°24.57'E | 25 | 244 | 16 | 0.49 | $4.3 \cdot 10^{-11}$ | 0.12 | 303 | 16 | 4.0 | 0.5 | 13 | 2.1 | 4.7 | 1.1 | 4.9 | 0.7 | 400 | $6.7 \cdot 10^{-2}$ | 8(2) | 9,16 |

Table 3.1: Sediment characteristics for the varying stations. The values for the bottom water velocity U , characteristic porewater velocity U_p , penetration depth δ , bedform length λ , bedform height η , Damköhler number Da , Peclet number Pe are averaged over the the sample size which is given by N in the last column (the first value denotes the number of oxygen transects and the latter the number of surface scans). The values for organic carbon c_{org} are averaged over the first 3 cm. Notice, that each transect includes 12-16 profiles and each surface scan is composed of at least 210 single pictures. Orange color indicates stationary bedforms and blue color migrating bedforms. The gray colors denote stations with impermeable sediments. nd indicates values that could not determined as one of respective devices failed. Permeability $< 1 \cdot 10^{-12}$ indicates sediments that are impermeable to flow. The numbers in brackets denote the uncertainties.

sand without considerable bedform topographies. Oxygen in such impermeable sediments followed the the surface topography and showed only little lateral variations whereas vertical oxygen gradients were strong. Oxygen penetrated down to 0.9 cm – 1.1 cm (Figure A.3.14 a). Similar trends were visible for all stations that were composed of muddy sand ($d_g = 102 \mu\text{m}$ to $d_g = 155 \mu\text{m}$). Even at muddy sand stations $^{447}\text{NOAH} - \text{D}$ and $^{447}\text{NOAH} - \text{F}$ where bedforms were detected (Figure A.3.13 a - b), the oxygen profiles had only little variation. During the rate measurements in the flow through reactors it turned out that these sediments could not be percolated, indicating the absence of advective transport and the dominance of diffusive transport.

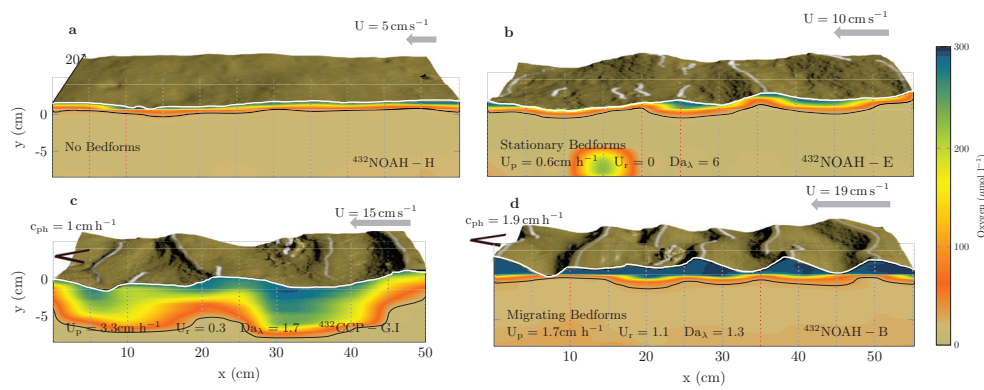


Figure 3.5: Examples for surface morphology and oxygen distribution are depicted: **a** reference case without bedforms. **b** stationary bedform where oxygen penetrates from the stoss side into the bedform. **c** migrating bedforms. The black line indicates the penetration depth where oxygen decreases down to 5% of the bottom water concentration. The white line on top of the bedforms are the results of the edge detecting algorithm and serves as a guide to the eye. The numbers given in the figures represent the instantaneous values during the measurement while Table 3.1 represents tidal averages. The flow direction is always from right towards left as indicated by the gray arrows.

Figure 3.5 **b** shows the oxygen distribution underneath a stationary bedform for sandy sediment. In between 0.2 m and 0.5 m along the x-axis two bedforms were detected. The oxygen penetration depth varied in between 1 cm and 2.5 cm depending on the position along the bedform. Oxygen penetrated deeper into the bedform at the stoss side compared to the lee side. At the stoss side the oxycline followed the shape of the bedform while it was inclined towards the surface at the lee side. This becomes explicitly visible in the individual oxygen profiles (Figure A.3.14 **b**). The stoss side profile showed a concave shape with a 2 cm penetration depth indicating the advective transport. The lee side profile flattens off within 1 cm showing a convex shape. Even though similar patterns were visible for all stationary and slowly migrating bedforms (Figure A.3.13 **c-f**) the penetration depth

varied from 1 cm to 6.4 cm in accordance to the length of the bedform and the permeability of the sediment.

Stations with migrating bedforms showed a large variability in the oxygen distributions. The example depicted in Figure 3.5 c shows bedforms that were completely flushed with oxygenated water with a strong vertical gradient underneath (see also A.3.14 c). In this example, the dominance of another mode of porewater transport becomes apparent. During bedform migration, porewater is released at the stoss side of the bedform due to erosion of sand grains, while bottom water is trapped at the lee side due to re-deposition of sand grains. With increasing bedform migration, the bedform becomes flushed (Ahmerkamp et al., 2015a). This becomes also apparent in Figure 3.3 c as a drop in the spatially averaged penetration depth as soon as bedform migration stops for a short time period in which the excess oxygen is consumed. The combination of fast bedform migration ($U_r = 1.1$) and high respiration rates ($Da = 1.3$) cause the clear separation of the flushed bedforms from the anoxic sediment underneath. At other stations A.3.13 e-f the median grain size was larger with values of 473 μm and 537 μm , respectively. In one case, the respiration rate was less dominant ($Da = 0.1$, Figure A.3.13 f) in the other case the relative bedform migration were decreased ($U_r = 0.3$, Figure A.3.13 e). Both caused a significant deepening of the oxygen penetration.

3.3.3 Transient oxygen penetration

Over the tidal cycle the oxygen penetration depths responded to the changing current velocities and migrating bedforms (Figure 3.3). The variation of penetration depths indicates that a certain volume of sediment changed regularly between oxic and anoxic conditions. This zone, here referred as variable redox zone, is calculated based on the minimum and maximum deflection of the oxycline along a tidal cycle (Figure 3.6). In Table 3.1 the relative thickness of the variable redox zone is represented as δ_T , calculated as the ratio of the spatially averaged thickness of the variable redox zone over the thickness of the permanently oxic zone.

The variable redox zone was prominent but never exceeded the thickness of the permanently oxic zone ($0.2 < \delta_T < 1$, Table 3.1). In general, the thickness of the variable redox zone tended to increase with increasing respiration rates and a significant correlation was found for increasing Damköhler numbers (Figure 3.7). For stationary bedforms the variable redox zone had a strongly fluctuating thickness depending on the position underneath the bedform (Figure 3.6 a). For migrating bedforms the thickness of the variable redox zone was constant with only little variability (Figure 3.6 b-c).

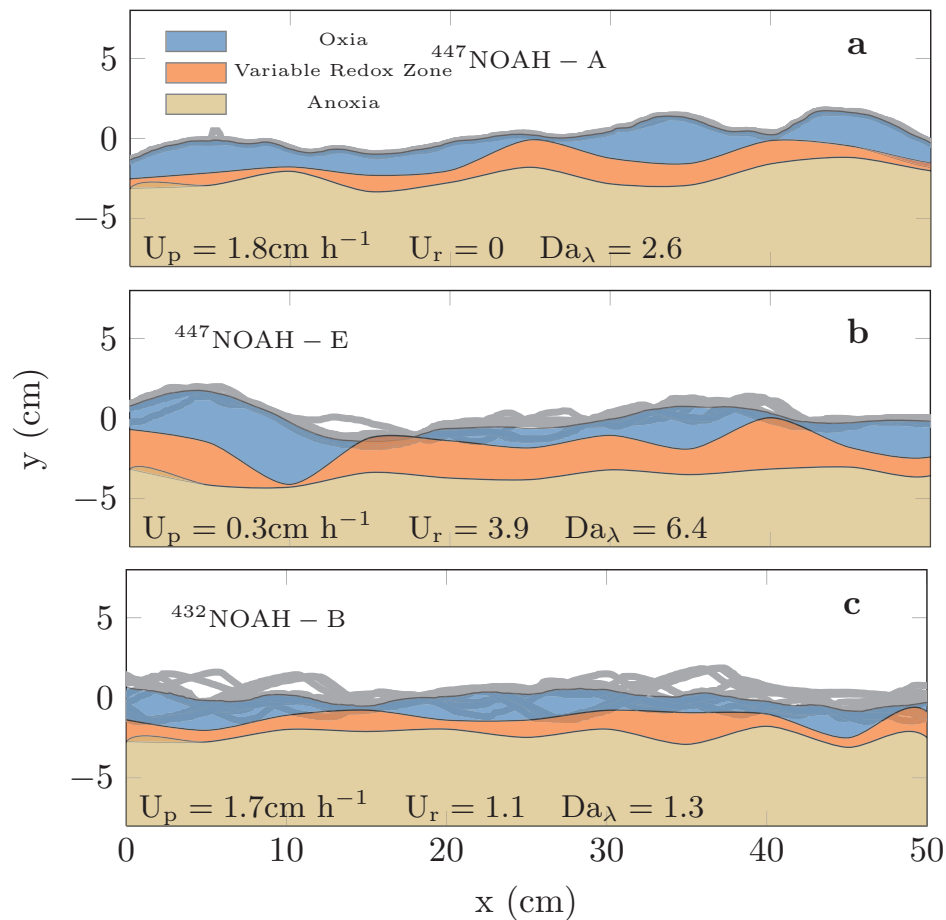


Figure 3.6: Three examples of oxygen penetration depths over a tidal cycle. The orange shaded region indicates the variability, i.e. upper and lower end, of the penetration depths along the tidal cycle. In this variable redox the conditions of oxia and anoxia are highly variable. The gray line depicts the sediment-water interface for all conducted surface scans. In **a** the bedforms were stationary and the variability of the penetration depth is just induced by the transient currents. In **b** and **c** the bedforms were migrating and the variability of oxygen penetration depths is induced by the migrating bedform as well as transient currents. As the upper end for the oxic region the average surface height was used.

3.3.4 Oxygen respiration and organic carbon content

Oxygen respiration rates were determined in *ex situ* experiments using flow-through reactors. The porewater velocity was adjusted to $3.6 - 18 \text{ cm h}^{-1}$ which is in the range of previously measured *in situ* porewater velocities (Reimers et al., 2004).

In sandy sediments, oxygen respiration rates varied over one order of magnitude in between $15 \mu\text{mol l}^{-1} \text{ h}^{-1}$ and $144 \mu\text{mol l}^{-1} \text{ h}^{-1}$ for sandy sediments (Table 3.1). Respiration rates at stations with bedform migration were significantly lower than respiration

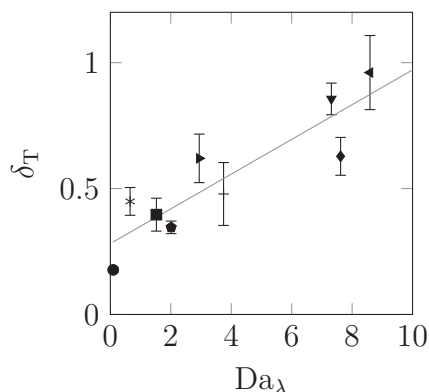


Figure 3.7: The relative thickness of the variable redox zone (δ_T), in which conditions of oxia and anoxia vary along a tidal cycle, scales well with the Damköhler number ($\delta_T = 0.07 \cdot Da_\lambda + 0.28$, $R^2 = 0.8$).

rates with stationary bedforms (Figure 3.8). Stations with bedform migration had respiration rates in between $15 \mu\text{mol l}^{-1} \text{h}^{-1}$ and $64 \mu\text{mol l}^{-1} \text{h}^{-1}$. Stations without bedform migration had respiration rates in between $71 \mu\text{mol l}^{-1} \text{h}^{-1}$ and $144 \mu\text{mol l}^{-1} \text{h}^{-1}$.

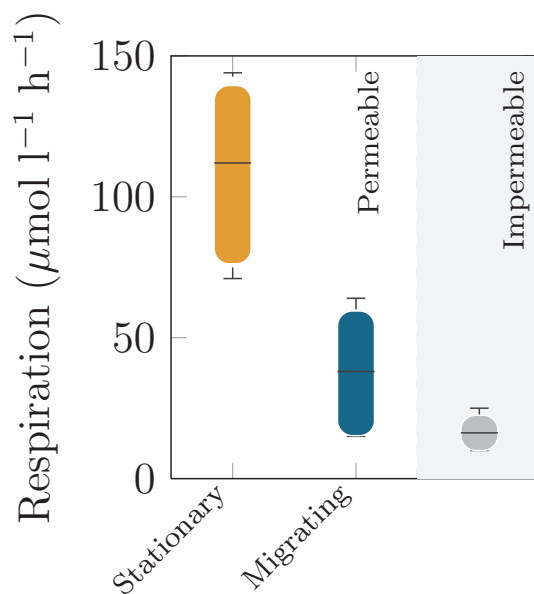


Figure 3.8: Boxplots of the respiration rates in permeable sediments for stationary and migrating bedforms as well as impermeable sediments. The upper black line indicates the maximum, the lower black line the minimum, the black line in the box the mean and margins of the coloured box represent the 75th percentile and 25th percentile. The means of the two groups differ significantly from each other (ANOVA, $F_{2,13} = 19.71$, $p < 0.002$).

Sediments that could not be percolated in flow-through reactors were regarded as impermeable to flow with permeabilities lower than 10^{-12}m^2 (Huettel et al., 2014) (compare Table 3.1). This was the case for all stations with muddy sand, i.e. $^{432}\text{CCP} - \text{J}$, $^{432}\text{NOAH} - \text{H}$, $^{447}\text{NOAH} - \text{D}$ and $^{447}\text{NOAH} - \text{F}$. Based on the profile measurements respiration rates were determined by inversely solving the diffusion-reaction equation (Equation 3.7) (Lettmann et al., 2012; Berg et al., 1998). The respiration rates were averaged down to the oxycline and ranged in between $10 \mu\text{mol l}^{-1} \text{h}^{-1}$ and $25 \mu\text{mol l}^{-1} \text{h}^{-1}$.

In general, the investigated sediments were poor in organic carbon with weight percentages ranging from ranging from 0.03 % to 0.37 % which is comparable to previous measurements in this region (e.g. Janssen et al. (2005); de Beer et al. (2005); Cook et al. (2007)). Organic carbon content did not correlate with respiration rates indicating that the measured organic carbon content was not a limiting factor.

In Figure A.3.15 the particulate organic carbon content for all stations is averaged in depth intervals of 1 cm. For migrating bedforms the particulate organic carbon content stayed lowest within the first 2 – 3 cm - which was the typical bedform height - and then increases distinctly with depth (compare A.3.14 **b,d**). For stationary bedforms the trend seems to be similar but with a much larger variability.

3.3.5 Oxygen flux estimations

The simultaneous analysis of volumetric respiration rates - as determined in ex situ experiments - and oxygen penetration depths - based on in situ lander measurements - allows for the estimation of benthic oxygen fluxes. Equation 3.6 assumes steady state conditions, i.e. the amount of oxygen transported into the sediment and microbial respiration are in equilibrium. Induced by the transient nature of tides the porewater flow varies in strength which induces a response lag of the penetration depth (Figure 3.3). For flood tides and the increasing bottom water velocities the penetration depth varied in between 1 – 2 cm (Figure 3.6). With typical porewater velocities of $1 - 10 \text{cm h}^{-1}$ the transport lag was in the range of $1 - 10 \text{h}$, but the tidal currents increased only for 3 hours before a maximum velocity was reached. On the other hand with reduced currents during slack water the penetration depth moved upward as the excess oxygen was consumed. This respiration lag can be estimated from the respiration timescale $\tau_R = CR^{-1}$, where C is the bottom water oxygen concentration. Typical values based on the respiration measurements ranged in between $\tau_r \approx 2 \text{h}$ to $\tau_r \approx 18 \text{h}$. Both response lags were in the same range but longer than the timescale of tidally induced changes leading to a damped signal of the penetration depth which was indeed measured (Figure 3.3). Hence, fluxes should be estimated using the temporal average of oxygen penetration depth along a tidal cycle, whereas fluxes could

be biased when calculated for specific time points.

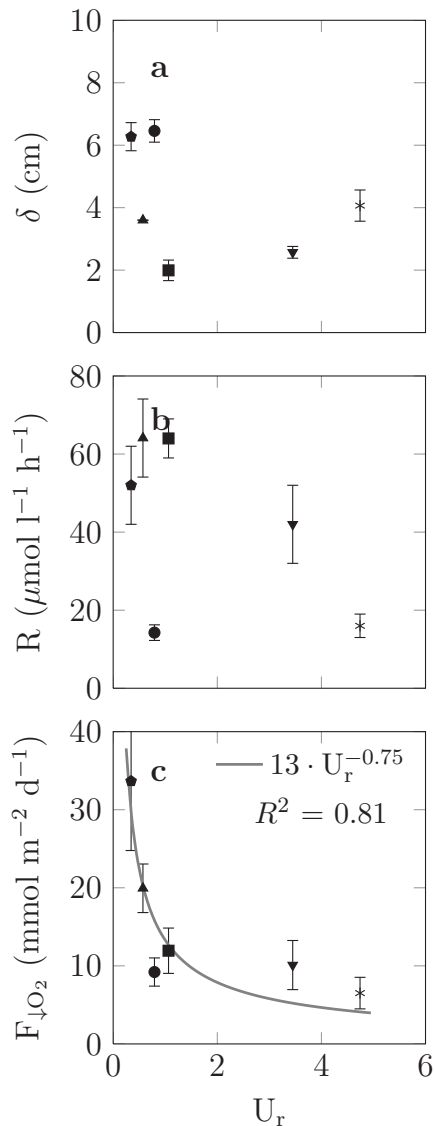


Figure 3.9: The impact of bedform migration on the penetration depth **a**, respiration rate **b** and oxygen fluxes **c** along an increasing dominance of bedform migration over porewater velocity as depicted by U_r .

Applying the spatial and temporal average of oxygen penetration depths, oxygen net fluxes were calculated and varied between $8 \text{ mmol m}^{-2} \text{ d}^{-1}$ and $34 \text{ mmol m}^{-2} \text{ d}^{-1}$ for permeable sediments, whereas, net fluxes at stations with muddy sand varied between $1 \text{ mmol m}^{-2} \text{ d}^{-1}$ and $3 \text{ mmol m}^{-2} \text{ d}^{-1}$. For permeable sediments, large oxygen fluxes coincided with large median grain sizes, which corresponds to the increasing penetration depth (Figure 3.4). However, the correlation does not explain the full variability since also very high rates led to high oxygen fluxes despite a small grain size ($^{417}\text{NOAH-B}$, $29 \text{ mmol m}^{-2} \text{ d}^{-1}$, $d_g = 210 \mu\text{m}$).

When pooling all stations with bedform migration, it was found that 46% of the flux variability could be explained by the migration celerity of the bedforms (Figure A.3.16). High oxygen fluxes coincided with rather low migration celerities and lowest oxygen fluxes were found at highest migration celerities. This correlation was significantly increased when the net oxygen flux was plotted as a function of the relative migration celerity U_r (Figure 3.9). About 81% of the variability could be explained by using U_r in a power-law. Interestingly, this effect was not exclusively caused by a shallowing oxygen penetration depth as suggested in a recent modeling study (Ahmerkamp et al., 2015a). Also the volumetric oxygen respiration rates seemed to decrease with increasing migration

celerity (Figure A.3.16 **a-b**). This corresponds to the overall decrease of respiration rates for migrating bedforms (Figure 3.9) and can be explained by an increased washout of organic particulate matter at higher migration celerity. As a result, it was the interplay

of shallowing penetration depths and decreased respiration rates that caused a significant response of the net flux to increasing dominance of bedform migration.

When calculating the oxygen flux, the integration of rates include only oxic respiration. Thus, the flux calculation do not include the re-oxidation of reduced substance such as NH_4^+ , H_2S , CH_4 , Fe^{2+} , Mn^{2+} which diffuse upwards from deeper sediment layers (Glud, 2008). Nevertheless, the relative contribution was estimated from porewater profiles of ammonium (Figure A.3.14 **d**). By calculating the vertical gradient below the oxycline the upward flux of ammonium was estimated to range between $0.05 \text{ mmol m}^{-2} \text{ d}^{-1}$ and $0.08 \text{ mmol m}^{-2} \text{ d}^{-1}$ for a diffusivity of $10^{-9} \text{ m}^2 \text{ s}^{-1}$. The composition of organic matter in the sediments revealed a relatively constant atomic ratio $C : N$ in between 5 to 9 which is close to the Redfield composition of biomass ($C : N$ is $106 : 16 = 6.6$ or in terms of oxygen $O_2 : N$ $138 : 16 = 8.6$). Considering this range the oxygen demand for the reoxidation of reduced electron acceptors was estimated to range between $0.3 - 0.9 \text{ mmol m}^{-2} \text{ d}^{-1}$ which is less than 10% of the oxygen flux due to oxygen respiration.

Bioirrigation was present for most stations with sandy sediments (Figure 3.5 **b** and A.3.13 **c,d**) but it was excluded from the flux estimates as the oxygen profiling did not allow for quantification of irrigation and the rate measurements did not include the consumption of macrofauna (Glud, 2008; Meysman, Galaktionov, Gribsholt and Middelburg, 2006). The calculated fluxes therefore reflect the microbial oxygen uptake and the uptake of all meiofauna that passed the 1 mm sieve.

3.4 Discussion

3.4.1 Geometrical limitations

The advective porewater transport in permeable sediments is strongly coupled to the hydro- and morphodynamic forcing. Fast oxygen and topography measurements were therefore necessary to capture the dynamics in the oxygen distribution along a tidal cycle. Fast responding needle optodes ($t_{90} < 0.7 \text{ s}$) allowed for a fast profiling, however, the sensor tip width of 1 mm did not allow for resolving very steep oxygen gradients of less than a few millimeter which are often found in highly active muddy sediments. Nevertheless, with penetration depths of 1 cm to 6 cm as found in this study we are confident that the oxygen profiles are trustworthy. Induced by technical limitations of the used instruments fast bedform migration might lead to a misalignment between the topography scans and oxygen measurements. A full transect of oxygen profiling took approximately 20 min. The upper limit of average bedform migration was around $6 - 7 \text{ cm h}^{-1}$ which could lead to a maximum horizontal misalignment between surface and oxygen distribution of less

than 2 – 2.5 cm. This was the case for only two stations where the fast bedform migration coincided with very low rates and, therefore, high penetration depths. In these instances the misalignment has a minor effect on the measured penetration depth as the oxygen distribution showed only little spatial variability in the upper centimeters. The spatial and temporal accuracy is high enough to cover most of the variability along a tidal cycle.

3.4.2 Oxygen flux measurements

We measured oxygen penetration depths between 1 cm and 6 cm in sediments with grain sizes ranging from 210 μm to 540 μm . At several stations the penetration depths correlated with the topography of the bedform and showed a dampened and phase shifted response to tidal currents (Figure 3.3). By integrating the measured volumetric respiration rates down to the averaged oxygen penetration depths, fluxes in permeable sediments could be estimated ranging from 8 $\text{mmol m}^{-2} \text{d}^{-1}$ and 34 $\text{mmol m}^{-2} \text{d}^{-1}$. The estimated oxygen fluxes represent a conservative range, reflecting mostly physically driven oxygen transport and microbial respiration but neglecting bioirrigation and oxygen uptake by benthic macrofauna. The oxygen fluxes due to re-oxidation of reduced substances that diffuse upwards from deeper layers was less than 10% of the uptake via oxygen respiration.

The advantage of this approach is that it is less invasive with respect to the hydro- and morphodynamic forcing of the oxygen transport. It is therefore a promising approach to overcome the challenges of measuring oxygen fluxes in permeable sediments under dynamic forcing which limits the traditional core and chamber incubations. In most chamber incubations hydrodynamic forcing is excluded or an arbitrary pressure gradient is imposed by stirring. These limitations were addressed by Janssen et al. (2005) who presented chamber incubations in North Sea sediments in which the stirring and, therefore, the pressure gradient was adapted to the ambient bottom water velocity. For grain sizes between 163 μm to 672 μm they measured oxygen fluxes between 8 $\text{mmol m}^{-2} \text{d}^{-1}$ and 37 $\text{mmol m}^{-2} \text{d}^{-1}$ which agrees well with the oxygen fluxes measured in this study. However, benthic chamber incubations with adapted stirring speed impose an artificial pressure field on the sediment and cause non steady state conditions and a transient adjustment of the oxygen distribution in the sediment and thus potentially transient flux. Furthermore, sediment transport and the associated porewater exchange are suppressed in the enclosed volume of the chamber.

Another commonly applied approach to measure oxygen fluxes non-invasively is the eddy covariance technique (Berg et al., 2003), which, however, comes with its own set of limitations regarding non-steady state conditions (Holtappels et al., 2013), benthos heterogeneity (Rheuban and Berg, 2013), and sensor biases (Holtappels et al., 2013).

Eddy covariance measurements on continental shelves covered by permeable sediments range from $10 \text{ mmol m}^{-2} \text{ d}^{-1}$ to $104 \text{ mmol m}^{-2} \text{ d}^{-1}$ for the Mid-Atlantic coast (Hume et al., 2011), $17 - 19 \text{ mmol m}^{-2} \text{ d}^{-1}$ for West Falmouth Harbor (Berg et al., 2013), $6 - 283 \text{ mmol m}^{-2} \text{ d}^{-1}$ in the northeastern Gulf of Mexico (Berg and Huettel, 2008; Gihring et al., 2010) and $10 \text{ mmol m}^{-2} \text{ d}^{-1}$ in North Sea sediments (McGinnis et al., 2014). In summary, the here presented measurements of oxygen fluxes are average in global comparison but cover the upper range of what was reported for permeable sediments in the North Sea.

3.4.3 Variables controlling oxygen flux

Besides averaged flux estimations the measurements collected with the benthic observatory allowed for further insights into the coupled transport-reaction processes in permeable sediments. At all stations with permeable sediments the oxygen distribution followed the small scale topography of bedforms, suggesting that pressure gradients across bedforms were the predominant driver for porewater transport in the surface layers. This agrees with a number of preceding flume studies (e.g. Huettel et al., 2014; Huettel and Rusch, 2000) and modelling studies (e.g. Cardenas and Wilson, 2007; Cardenas et al., 2008; Kessler et al., 2012). However, despite large similarities some deviations in comparison to laboratory studies were found. We did not observe the previously described pathway of anoxic porewater from the deep sediment to the sediment-water interface (also known as 'anoxic chimneys'), neither for migrating bedforms nor for stationary bedforms. This means that reduced substances such as ammonium are most likely oxidized in the vicinity of the surface, but are not recirculated back into the water column as often described before (e.g. Kessler et al., 2013; Huettel et al., 2014).

The oscillating tides further intricate oxygen transport. With unsteady direction and magnitude of bottom water velocities the actual oxic zone adapts with some time lag. This time lag depends on the relative strength of respiration rate and transport rate (i.e. Damköhler number) and leads to a damped response of the penetration depth, especially for low Damköhler numbers. Hence, with decreasing bottom water velocities excess oxygen might be located underneath the areas that are still fueled by the advective porewater flow. This oxygen is respired within $2 - 18 \text{ h}$. On the other hand, along increasing bottom water velocities oxygen gets transported into deeper sediment layers, but depending on the porewater velocity it might take $1 - 10 \text{ h}$ to penetrate and reach steady state conditions. These transient effects can be observed by near-instantaneous oxygen flux measurements as detected with eddy covariance technique (McGinnis et al., 2014).

Flux studies with stationary bedforms revealed that particulate organic matter accumu-

lates in the sediment leading to the idea of bedforms as biocatalytic filters (Huettel et al., 1996; Huettel and Rusch, 2000; Ren and Packman, 2004). This picture holds for stationary bedforms, but must be adapted for migrating bedforms which induce the flushing of this filter. The decreased organic carbon content in the upper layer (Figure A.3.15) and especially the reduced respiration rate in this layer at stations with migrating bedforms (Figure 3.8) suggest that particulate organic matter which has been accumulated in the upper sediment layer is flushed into the water column as soon as the sediment gets perturbed and bedform migration is initialized.

Indeed, we found that oxygen fluxes decreased significantly with $U_r^{-0.75}$, i.e. with increasing relative bedform migration (Figure 3.9 c). Besides the flushing of organic matter, this effect was also caused by a shallowing of the oxygen penetration depth (Figure 3.9 a) as described previously in a model study (Ahmerkamp et al., 2015b). It was shown that the penetration depth of oxygen decreases as soon as increasing bottom water velocities initialize bedform migration - a counter-intuitive effect given the fact that increasing bottom water velocities should increase the pressure driven advective flux. The flushing of organic matter is not yet included in many models. However, further evidence for the flushing effect comes from flume experiments where cultures of diatoms, resembling particulate organic matter, were added to the permeable sediment (Pilditch and Miller, 2006). In combination with mechanical abrasion of bacteria from sand grains (Nickels et al., 1981) it was concluded that the flushing reduces microbial respiration and thus benthic oxygen fluxes. However, on longer time scales particulate organic matter is redistributed and clogging is suppressed which maintains the system and enhances the benthic-pelagic coupling. Non-local mixing of detritus via bioturbation (Meysman, Middelburg and Heip, 2006) may still lead to an accumulation of organic matter in deeper sediment layers. Further, some of the particulate organic matter will be transported deeper than the characteristic bedform height, which is then not affected by flushing via sediment transport.

Important microbial reactions such as denitrification are confined to a specific redox-zone underneath the bedform where the limiting substrate is available and the inhibitory effect of oxygen is reduced, at least temporarily. A prominent layer with variable redox conditions was observed and the extent of this variable redox zone is mainly a function of the Damköhler number. In combination with the transient tidal forcing bedform migration constantly changes the extent and position of the variable redox zone along a tidal cycle. This leads to a large scale dispersion promoting a constantly oxidized upper layer and variable oxic-anoxic layer below (Figure 3.6) with variable chemical gradients to which microorganisms are exposed to. It was suggested that the variable redox conditions found

in these layers would favor the occurrence of denitrification irrespective of the availability of oxygen as the energetically more favorable electron acceptor (Chen and Strous, 2013). Indeed, denitrification under aerobic conditions was predominantly found in permeable sediments (Rao et al., 2007; Gao et al., 2012; Marchant et al., 2016).

3.4.4 Modelling oxygen fluxes

Giving the relative strength of reaction rates to transport rates we found the Damköhler number (Equation 3.9, Table 3.1) of the sediments in the German Bight to vary between 0.1 to 6.4. The oxygen distribution responded to the different Damköhler numbers in accordance to previous modelling studies (Azizian et al., 2015; Ahmerkamp et al., 2015a). When transport rates dominated (low Damköhler number) the reactive solute was transported deeply into the sediment and some of the solute was recirculated back into the water column without being consumed (e.g. A.3.13 e). When respiration rates dominated (high Damköhler number) the reactive solute was almost completely consumed in the vicinity of the sediment surface (e.g. Figure 3.5 b).

This behavior is reflected in Equation 3.10 which describes the spatially averaged oxygen penetration depth as a function of inverse Damköhler number and the wavelength of the bedform. Subsequently, oxygen penetration depth was calculated from the input variables as they appear in Equation 3.10, i.e. current velocity U , bedform length λ , oxygen concentration C , oxygen respiration rate R , permeability k (modeled from grain size after Equation 3.5), and porosity θ . The modeled and measured oxygen penetration depths compared well (Figure 3.10 a). Despite the fact that the model assumes purely advective porewater flow and stationary bedforms, it performs well on the large range of parameters found in the German Bight during this study. Subsequently, the oxygen net fluxes was modeled by applying Equation 3.11. Also the modeled and measured oxygen net fluxes compared well (Figure 3.10 b). The agreement between measured and modeled results suggest that benthic oxygen fluxes in permeable sediments of the German Bight were to a high degree controlled by advective porewater flow and microbial respiration rates. Deviations were mainly found at the lower and upper end of penetration depths.

The potential variability induced by the error of the measurements were calculated from error propagation and are depicted by the shaded areas in figure 3.10. While the error of the bedform length, respiration rate and bottom water velocity seem to have a minor effect within the observed scales, most of the variability can be explained by the permeability. Based on the median grain size we used the empirical relation by Gangi (1985). Even though different empirical relations exist, they all have in common that the permeability is a quadratic function of the grain diameter (Wilson et al., 2008; Glover

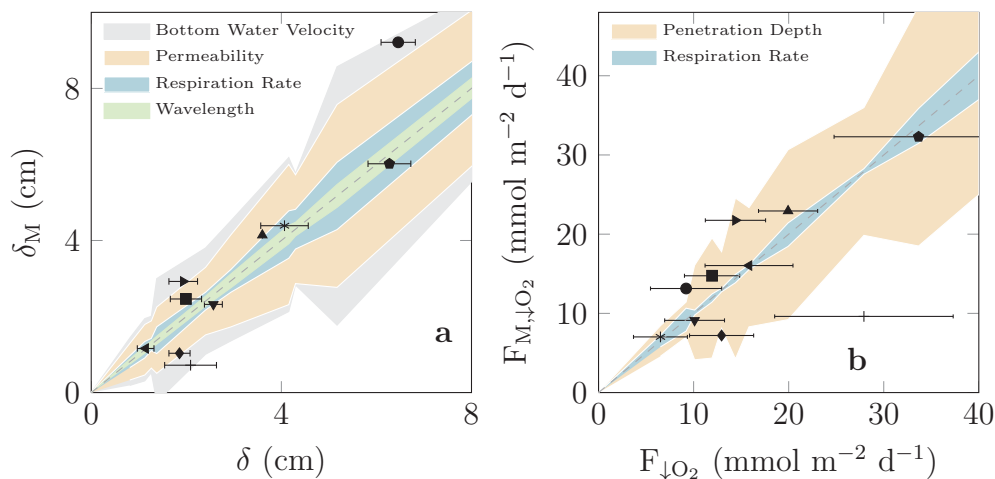


Figure 3.10: Comparison of the measured and modeled data (Eq. 3.10-3.11). In **a** the penetration depth and in **b** the oxygen flux is shown (M subscript denotes model). The dashed line indicates the 1:1 line. The intervals surrounding the dashed line emphasize the possible uncertainties of the model based on the error of the different variables. For the measured penetration depth and bottom water velocity the error is based on the standard deviation, for permeability and wavelength 50% deviation is assumed and for the respiration rate the range between the biological replicates is used. The whiskers denote the standard deviations of the measured penetration depth **a** and fluxes **b**.

and Walker, 2008; Krumbein and Monk, 1943). Therefore, qualitatively the linear trend between model and measurements remains similar, even though the slope might deviate from the 1:1 line. Considering that also the bedform length and porosity are a function of the grain size (Figure 3.2) the main controlling variables for advective oxygen fluxes in permeable sediments reduce to: grain size, bottom water velocity and respiration rate. In contrast to diffusion controlled fluxes, two purely physical variables (U and d_g) are among the the controlling variables. This might explain the counter intuitive results of Sokoll et al. (2016) who measured benthic denitrification fluxes in permeable sediments which correlated well with grain size, but not with microbial reaction rates. The variability of U and d_g in natural environments is high and thus their effect on benthic fluxes is expected to be more significant compared to the relatively low variability of e.g. molecular diffusion in cohesive sediments.

3.4.5 Conclusion

The present study reveals that oxygen penetration and oxygen fluxes in permeable sediments of the North Sea are strongly coupled to the hydrodynamic forcing and seabed morphology. So far, transport processes in permeable sediments were mostly studied in

laboratory environments under stationary and very confined boundary conditions, whereas process studies under in situ conditions are rare. In a series of lander deployments conducted in the shallow North Sea we found average oxygen penetration depths of 1 cm to 6 cm which increase with the grain size and, considering the respiration rates, can only be explained by advective porewater transport. At many stations the oxycline correlated with the topography of the bedforms. Measured oxygen penetration depths in combination with ex situ respiration rate measurements allowed for the calculation of oxygen fluxes ranging between $8 \text{ mmol m}^{-2} \text{ d}^{-1}$ to $34 \text{ mmol m}^{-2} \text{ d}^{-1}$.

The transient forcing along a tidal cycle in combination with bedform migration was presumably the reason why the release of reduced compounds through 'anoxic-chimneys' was not observed. The oxygen penetration depth responded to the changing bottom water velocities with a time lag. This transient adaptation decouples the integrated benthic oxygen consumption from the oxygen flux across the sediment-water interface. In combination with the mobility of the bedforms the transient adaptation further leads to a variable redox zone where conditions switch between oxic and anoxic. The extent of this zone was best described by the non-dimensional Damköhler number. Further, migrating bedforms led to reduced oxygen fluxes as they cause a shallowing of the penetration depth and a reduction of the respiration in surface sediments. The latter is caused by the wash out of organic matter during sediment transport as indicated by the decreased organic carbon content in mobile sediments.

Despite the transient forcing it was found that oxygen penetration depths and fluxes were predictable and strongly dependent on the inverse of the Damköhler number for which the four main controlling variables were grain size, current velocity, oxygen concentration and respiration rates.

Acknowledgements

We are grateful for help with the technical development of the benthic observatory LanceALot by Paul Faerber, Volker Meyer and Georg Herz. We are thankful to the captain and crew members of the R/V Heincke (412, 417, 432, 447) for their outstanding collaboration and support during the survey, Tomas Wilkop for his logistic support. We sincerely thank Gabi Klockgether and Kirsten Imhoff for technical assistance, Julia Amelsberg for help with measurements. We also thank Hannah Marchant and Andreas Neumann with whom discussion helped improve the manuscript. The study was funded by the Max Planck Society and the DFG-Research Center/Cluster of Excellence "The Ocean in the Earth System" at the University of Bremen.

3.5 Supplementary information

3.5.1 Breakthrough curves for flow through reactors

Breakthrough curves were determined by measuring conductivity changes induced by sodium bromide as an inert tracer (5 mmol l^{-1}). The conductivity signal as indication for bromide can be clearly seen (Figure A.3.11) and also the variation between the different grain sizes. Rao et al. (2007) fitted the error function, which is the analytical solution for the 1-dimensional diffusion advection equation under defined boundary conditions, to the tracer curve to determine the dispersion coefficient. In non-dimensional formulation the error-function reads:

$$C^* = 0.5 \cdot \operatorname{erf} \left(1 - \frac{t^*}{2\sqrt{D_L^* t^*}} \right) \quad (\text{A.3.13})$$

where $t^* = \frac{t}{r_t}$, $C^* = \frac{C}{C_0}$, $D_L^* = \frac{\alpha_L}{L_c} \cdot \frac{U}{U} = \frac{\alpha_L}{L_c}$, with t the time, $r_t = \frac{L_c \phi}{u}$ the retention time, C_0 the maximum sodium bromide concentration, ϕ the porosity, L_c the length of the core, α_L the longitudinal dispersion coefficient, and u the porewater velocity. In this study the unknowns α_L and ϕ are directly determined from the porewater age distribution, where the second moment is $2D_L^*$ and the maximum is shifted along the x-axis depending on the porosity. For comparison the determined values are substituted into Equation A.3.13 and shown as grey lines in Figure A.3.11.

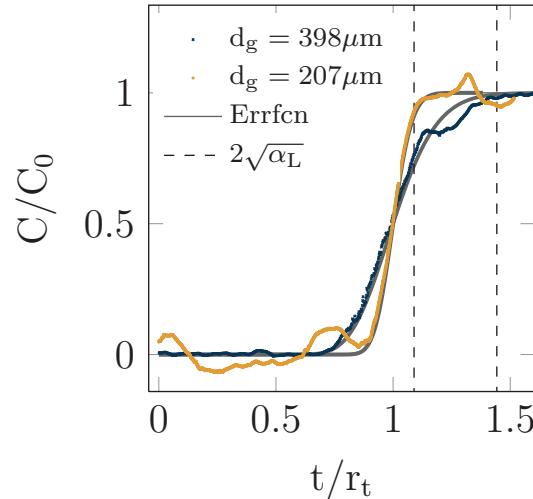


Figure A.3.11: Breakthrough curves measured at the outlet of the flow-through incubations for two grain sizes. The longitudinal dispersion coefficients are $\alpha_L = 0.3 \text{ cm}$ for $d_g = 207 \mu\text{m}$ and $\alpha_L = 0.9 \text{ cm}$ for $d_g = 398 \mu\text{m}$. Despite the fluctuations the error-function represents the curves well indicating a uniform percolation of the flow-through reactors.

3.5.2 Additional figures

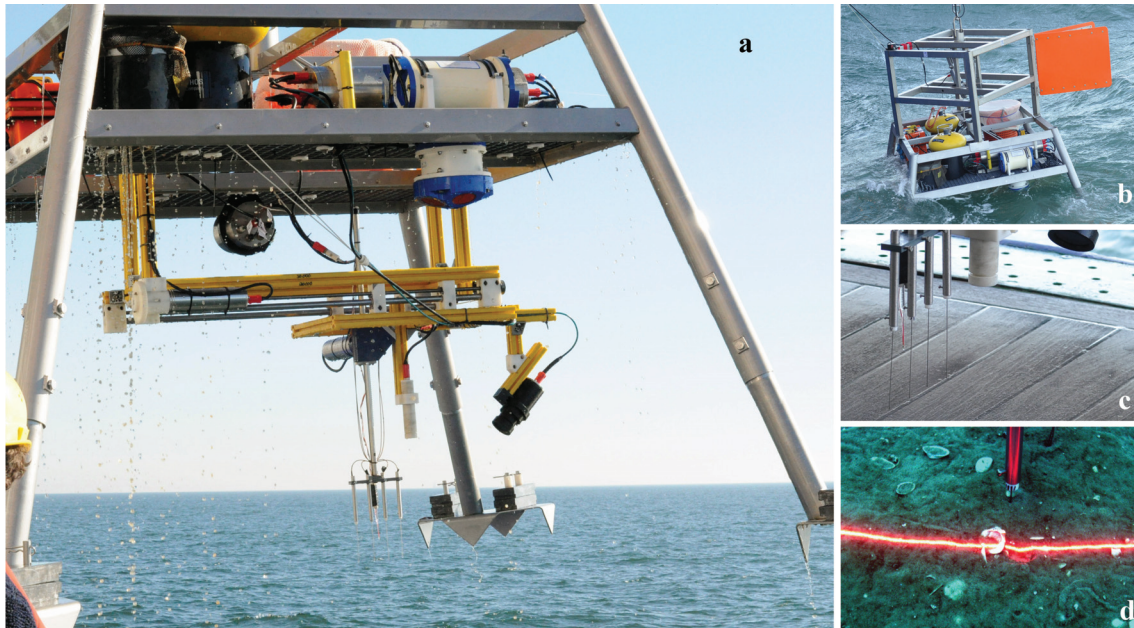


Figure A.3.12: In **a** the lander 'Lance-A-Lot' is depicted. In yellow the carriage is visible with the camera, optodes and laser mounted. **b** shows the launcher system. **c** shows the four optodes mounted to the linear drive and in **d** the line laser is depicted with an optode lowered into sediment during a deployment.

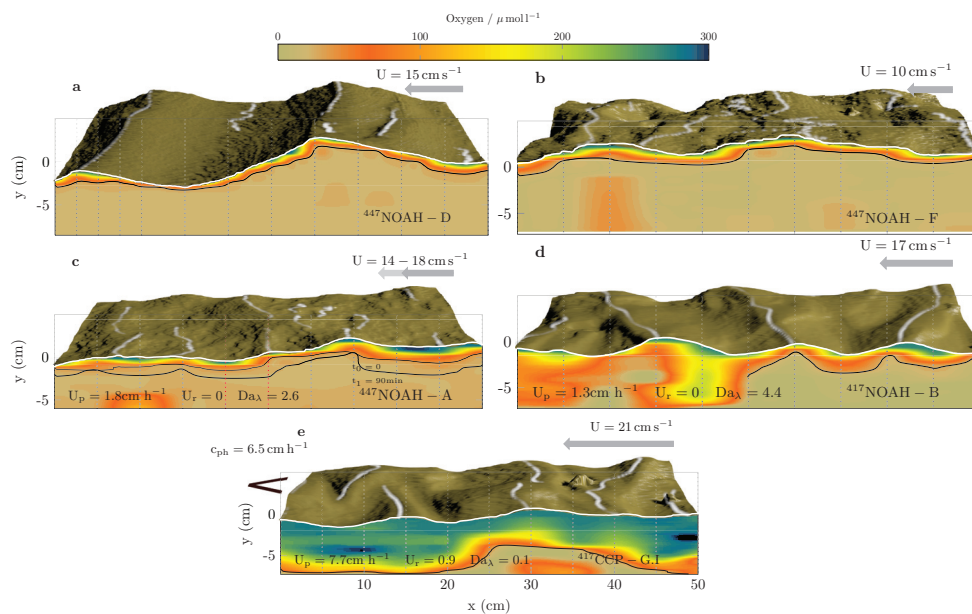


Figure A.3.13: Further examples of oxygen distribution correlated to the surface topography are depicted: **a-b** stationary bedforms where advective porewater flow can be neglected. **c-d** stationary bedforms with varying bedform wavelengths. **e-f** migrating bedforms.

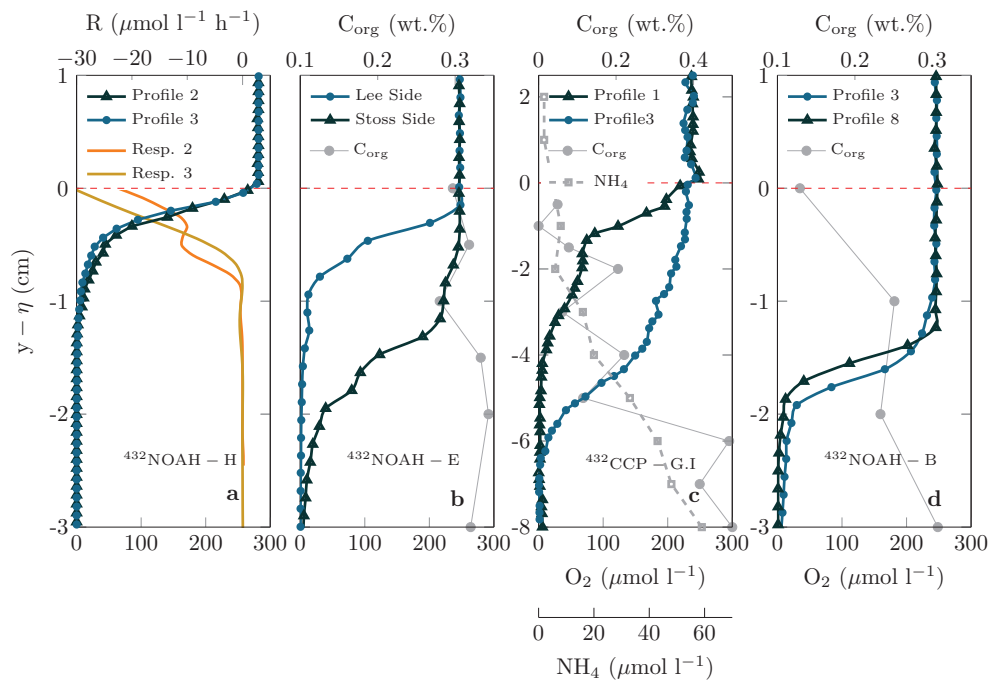


Figure A.3.14: Oxygen profiles for four representative stations are depicted. **c** example for sediments that are impermeable to flow with the inversely modeled oxygen respiration in orange. **a** depicts a stoss side and lee side profile with the organic carbon profile in gray. **b** and **d** profiles for slowly migrating bedforms. Notice the different scaling along the y-axis for **d**. **d** also shows an ammonium profile which is used to estimate re-oxidation of reduced substances.

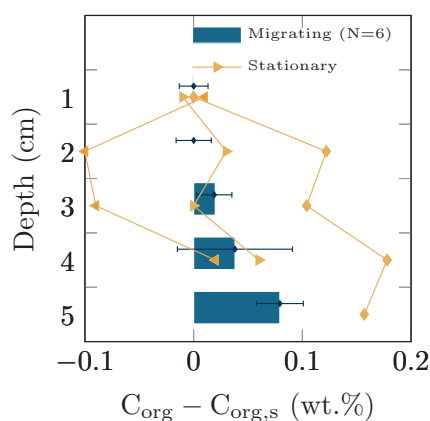


Figure A.3.15: The average total organic carbon content is shown at depth intervals of 1 cm for migrating and stationary bedforms. The error bars denote the standard deviations. For stationary bedforms no significant trend of total organic carbon with increasing depth was found. For migrating bedforms the depth-binned total organic carbon increased significantly with depth despite some fluctuations ($R^2 = 0.6$, t-test: $p = 0.01$). By analyzing the individual organic carbon profiles for stations with migrating bedforms the increasing trend for most stations persisted (significant for all stations despite $^{447}\text{CCP} - \text{G.I}$ and $^{417}\text{NOAH} - \text{E}$ t-test: $p < 0.05$).

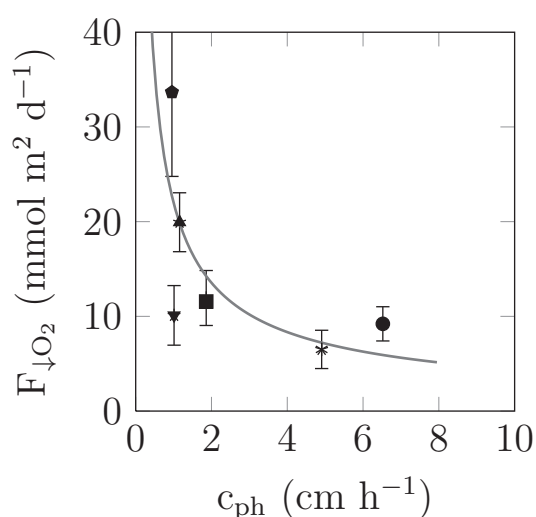


Figure A.3.16: The oxygen fluxes decrease with increasing bedform migration. Even though the trend is clearly visible the correlation is not very strong.

Bibliography

- Ahmerkamp, S., Winter, C., Janssen, F., Kuypers, M. M. and Holtappels, M. (2015a), 'The impact of bedform migration on benthic oxygen fluxes', *Journal of Geophysical Research: Biogeosciences* **120**(11), 2229–2242.
- Ahmerkamp, S., Winter, C., Janssen, F., Kuypers, M. M. and Holtappels, M. (2015b), 'The impact of bedform migration on benthic oxygen fluxes', *Journal of Geophysical Research: Biogeosciences* .
- Ayoub, F., Avouac, J.-P., Newman, C., Richardson, M., Lucas, A., Leprince, S. and Bridges, N. (2014), 'Threshold for sand mobility on mars calibrated from seasonal variations of sand flux', *Nature communications* **5**.
- Azizian, M., Grant, S. B., Kessler, A. J., Cook, P. L. M., Rippy, M. A. and Stewardson, M. (2015), 'Bedforms as biocatalytic filters: A pumping and streamline segregation (pass) model for nitrate removal in permeable sediments', *Environmental science & technology* .
- Berg, P. and Huettel, M. (2008), 'Integrated benthic exchange dynamics', *Oceanography* **21**(4), 164.
- Berg, P., Long, M. H., Huettel, M., Rheuban, J. E., McGlathery, K. J., Howarth, R. W., Foreman, K. H., Giblin, A. E. and Marino, R. (2013), 'Eddy correlation measurements of oxygen fluxes in permeable sediments exposed to varying current flow and light', *Limnology and Oceanography* **58**(4), 1329–1343.
- Berg, P., Risgaard-Petersen, N. and Rysgaard, S. (1998), 'Interpretation of measured concentration profiles in sediment pore water', *Limnology and Oceanography* **43**(7), 1500–1510.
- Berg, P., Røy, H., Janssen, F., Meyer, V., Jörgensen, B. B., Huettel, M. and De Beer, D. (2003), 'Oxygen uptake by aquatic sediments measured with a novel non-invasive eddy-correlation technique', *Marine Ecology Progress Series* **261**(1), 75–83.
- Boudreau, B. P., Huettel, M., Forster, S., Jahnke, R. A., McLachlan, A., Middelburg, J. J., Nielsen, P., Sansone, F., Taghon, G., Van Raaphorst, W., Webster, I., Weslawski, J. M., Wiberg, P. and Sundby, B. (2001), 'Permeable marine sediments: Overturning an old paradigm', *Eos, Transactions American Geophysical Union* **82**(11), 133–136.

- Boyer, E. W., Howarth, R. W., Galloway, J. N., Dentener, F. J., Green, P. A. and Vörösmarty, C. J. (2006), 'Riverine nitrogen export from the continents to the coasts', *Global Biogeochemical Cycles* **20**(1).
- Brockmann, U., Billen, G. and Gieskes, W. (1988), North sea nutrients and eutrophication, in W. Salomons, B. Bayne, E. Duursma and U. Förstner, eds, 'Pollution of the North Sea', Springer Berlin Heidelberg, pp. 348–389.
- Cardenas, M. B., Cook, P. L., Jiang, H. and Traykovski, P. (2008), 'Constraining denitrification in permeable wave-influenced marine sediment using linked hydrodynamic and biogeochemical modeling', *Earth and Planetary Science Letters* **275**(1), 127–137.
- Cardenas, M. B. and Wilson, J. L. (2007), 'Dunes, turbulent eddies, and interfacial exchange with permeable sediments', *Water Resources Research* **43**(8).
- Chen, J. and Strous, M. (2013), 'Denitrification and aerobic respiration, hybrid electron transport chains and co-evolution', *Biochimica et Biophysica Acta (BBA)-Bioenergetics* **1827**(2), 136–144.
- Chiswell, S. M. (2011), 'Annual cycles and spring blooms in phytoplankton: don't abandon sverdrup completely', *Marine Ecology Progress Series* **443**, 39–50.
- Cook, P. L., Wenzhöfer, F., Glud, R. N., Janssen, F. and Huettel, M. (2007), 'Benthic solute exchange and carbon mineralization in two shallow subtidal sandy sediments: Effect of advective pore-water exchange', *Limnology and Oceanography* **52**(5), 1943–1963.
- de Beer, D., Wenzhöfer, F., Ferdelman, T. G., Boehme, S. E., Huettel, M., van Beusekom, J. E., Böttcher, M. E., Musat, N. and Dubilier, N. (2005), 'Transport and mineralization rates in north sea sandy intertidal sediments, sylvt-rømø basin, wadden sea', *Limnol. Oceanogr* **50**(1), 113–127.
- DeFlaun, M. F. and Mayer, L. M. (1983), 'Relationships between bacteria and grain surfaces in intertidal sediments', *Limnology and Oceanography* **28**(5), 873–881.
- Dey, S. (2014), *Fluvial Processes: Hydrodynamic and Sediment Transport Phenomena*, Springer.
- Elliott, A. H. and Brooks, N. H. (1997), 'Transfer of nonsorbing solutes to a streambed with bed forms: Theory', *Water Resources Research* **33**(1), 123–136.
- Emery, K. (1968), 'Relict sediments on continental shelves of world', *AAPG Bulletin* **52**(3), 445–464.

- Folk, R. L. (2000), 'Petrology of sedimentary rocks'.
- Gangi, A. F. (1985), 'Permeability of unconsolidated sands and porous rocks', *Journal of Geophysical Research: Solid Earth (1978–2012)* **90**(B4), 3099–3104.
- Gao, H., Matyka, M., Liu, B., Khalili, A., Kostka, J. E., Collins, G., Jansen, S., Holtappels, M., Jensen, M. M. and Badewien, T. H. (2012), 'Intensive and extensive nitrogen loss from intertidal permeable sediments of the wadden sea', *Limnology and Oceanography* **57**(1), 185.
- Gerlach, S. A. (1981), 'Marine pollution'.
- Gihring, T. M., Lavik, G., Kuypers, M. M. and Kostka, J. E. (2010), 'Direct determination of nitrogen cycling rates and pathways in arctic fjord sediments (svalbard, norway)', *Limnology and Oceanography* **55**(2), 740–752.
- Glover, P. and Walker, E. (2008), 'Grain-size to effective pore-size transformation derived from electrokinetic theory', *Geophysics* **74**(1), E17–E29.
- Glud, R. N. (2008), 'Oxygen dynamics of marine sediments', *Marine Biology Research* **4**(4), 243–289.
- Glud, R. N., Gundersen, J. K., Røy, H. and Jørgensen, B. B. (2003), 'Seasonal dynamics of benthic o₂ uptake in a semienclosed bay: Importance of diffusion and faunal activity', *Limnology and Oceanography* **48**(3), 1265–1276.
- Grashorn, S., Lettmann, K. A., Wolff, J.-O., Badewien, T. H. and Stanev, E. V. (2015), 'East frisian wadden sea hydrodynamics and wave effects in an unstructured-grid model', *Ocean Dynamics* **65**(3), 419–434.
- Hickel, W., Mangelsdorf, P. and Berg, J. (1993), 'The human impact in the german bight: Eutrophication during three decades (1962–1991)', *Helgoländer Meeresuntersuchungen* **47**(3), 243–263.
- Holtappels, M., Glud, R. N., Donis, D., Liu, B., Hume, A., Wenzhöfer, F. and Kuypers, M. M. (2013), 'Effects of transient bottom water currents and oxygen concentrations on benthic exchange rates as assessed by eddy correlation measurements', *Journal of Geophysical Research: Oceans* **118**(3), 1157–1169.
- Huettel, A., Ziebis, W. and Forster, S. (1996), 'Flow-induced uptake of particulate matter in permeable sediments', *Limnology & Oceanography* **41**, 309–322.

- Huettel, M., Berg, P. and Kostka, J. E. (2014), 'Benthic exchange and biogeochemical cycling in permeable sediments', *Marine Science* **6**.
- Huettel, M. and Rusch, A. (2000), 'Transport and degradation of phytoplankton in permeable sediment', *Limnology and Oceanography* **45**(3), 534–549.
- Hume, A. C., Berg, P. and McGlathery, K. J. (2011), 'Dissolved oxygen fluxes and ecosystem metabolism in an eelgrass (*zostera marina*) meadow measured with the eddy correlation technique', *Limnology and Oceanography* **56**(1), 86.
- Jahnke, R. A. (2010), Global synthesis, in 'Carbon and Nutrient Fluxes in Continental Margins', Springer, pp. 597–615.
- Janssen, F., Cardenas, M. B., Sawyer, A. H., Dammrich, T., Krietsch, J. and de Beer, D. (2012), 'A comparative experimental and multiphysics computational fluid dynamics study of coupled surface–subsurface flow in bed forms', *Water Resources Research* **48**(8). W08514.
- Janssen, F., Huettel, M. and Witte, U. (2005), 'Pore-water advection and solute fluxes in permeable marine sediments (ii): Benthic respiration at three sandy sites with different permeabilities (german bight, north sea)', *Limnology and Oceanography* **50**(3), 779–792.
- Kessler, A. J., Glud, R. N., Cardenas, M. B. and Cook, P. L. M. (2013), 'Transport zonation limits coupled nitrification-denitrification in permeable sediments', *Environmental Science & Technology* **47**(23), 13404–13411.
- Kessler, A. J., Glud, R. N., Cardenas, M. B., Larsen, M., Bourke, M. F. and Cook, P. L. (2012), 'Quantifying denitrification in rippled permeable sands through combined flume experiments and modeling', *Limnology and Oceanography* **57**(4), 1217–1232.
- Krumbein, W. and Monk, G. (1943), 'Permeability as a function of the size parameters of unconsolidated sand', *Transactions of the AIME* **151**(01), 153–163.
- Lettmann, K. A., Riedinger, N., Ramlau, R., Knab, N., Böttcher, M. E., Khalili, A., Wolff, J.-O. and Jørgensen, B. B. (2012), 'Estimation of biogeochemical rates from concentration profiles: A novel inverse method', *Estuarine, Coastal and Shelf Science* **100**, 26–37.
- Marchant, H. K., Holtappels, M., Lavik, G., Ahmerkamp, S., Winter, C. and Kuypers, M. M. (2016), 'Coupled nitrification–denitrification leads to extensive n loss in subtidal permeable sediments', *Limnology and Oceanography* .

- Marchant, H. K., Lavik, G., Holtappels, M. and Kuypers, M. M. (2014), 'The fate of nitrate in intertidal permeable sediments', *PLoS one* **9**(8), e104517.
- McGinnis, D. F., Sommer, S., Lorke, A., Glud, R. N. and Linke, P. (2014), 'Quantifying tidally driven benthic oxygen exchange across permeable sediments: An aquatic eddy correlation study', *Journal of Geophysical Research: Oceans* **119**(10), 6918–6932.
- Meysman, F. J., Galaktionov, O. S., Gribsholt, B. and Middelburg, J. J. (2006), 'Bioirrigation in permeable sediments: Advective pore-water transport induced by burrow ventilation', *Limnology and Oceanography* **51**(1), 142–156.
- Meysman, F. J., Middelburg, J. J. and Heip, C. H. (2006), 'Bioturbation: a fresh look at darwin's last idea', *Trends in Ecology & Evolution* **21**(12), 688–695.
- Nickels, J. S., Bobbie, R. J., Martz, R. F., Smith, G. A., White, D. C. and Richards, N. L. (1981), 'Effect of silicate grain shape, structure, and location on the biomass and community structure of colonizing marine microbiota', *Applied and environmental microbiology* **41**(5), 1262–1268.
- Otto, L., Zimmerman, J., Furnes, G., Mork, M., Saetre, R. and Becker, G. (1990), 'Review of the physical oceanography of the north sea', *Netherlands Journal of Sea Research* **26**(2), 161–238.
- Pilditch, C. A. and Miller, D. C. (2006), 'Phytoplankton deposition to permeable sediments under oscillatory flow: Effects of ripple geometry and resuspension', *Continental Shelf Research* **26**(15), 1806 – 1825.
- Precht, E., Franke, U., Polerecky, L. and Huettel, M. (2004), 'Oxygen dynamics in permeable sediments with wave-driven pore water exchange', *Limnology and Oceanography* **49**(3), 693–705.
- Precht, E. and Huettel, M. (2003), 'Advective pore-water exchange driven by surface gravity waves and its ecological implications', *Limnology and Oceanography* **48**(4), 1674–1684.
- Rabalais, N. N., Turner, R. E., Dortch, Q., Justic, D., Bierman Jr, V. J. and Wiseman Jr, W. J. (2002), 'Nutrient-enhanced productivity in the northern gulf of mexico: past, present and future', pp. 39–63.
- Rao, A. M., McCarthy, M. J., Gardner, W. S. and Jahnke, R. A. (2007), 'Respiration and denitrification in permeable continental shelf deposits on the south atlantic bight: Rates

- of carbon and nitrogen cycling from sediment column experiments', *Continental Shelf Research* **27**(13), 1801–1819.
- Raudkivi, A. J. (1997), 'Ripples on stream bed', *Journal of Hydraulic Engineering* **123**(1), 58–64.
- Reimers, C. E., Stecher III, H. A., Taghon, G. L., Fuller, C. M., Huettel, M., Rusch, A., Ryckelynck, N. and Wild, C. (2004), 'In situ measurements of advective solute transport in permeable shelf sands', *Continental Shelf Research* **24**(2), 183–201.
- Ren, J. and Packman, A. I. (2004), 'Modeling of simultaneous exchange of colloids and sorbing contaminants between streams and streambeds', *Environmental science & technology* **38**(10), 2901–2911.
- Rheuban, J. E. and Berg, P. (2013), 'The effects of spatial and temporal variability at the sediment surface on aquatic eddy correlation flux measurements', *Limnology and Oceanography: Methods* **11**(7), 351–359.
- Rusch, A., Huettel, M., Reimers, C. E., Taghon, G. L. and Fuller, C. M. (2003), 'Activity and distribution of bacterial populations in middle atlantic bight shelf sands', *FEMS Microbiology Ecology* **44**(1), 89–100.
- Rutherford, J., Latimer, G. and Smith, R. (1993), 'Bedform mobility and benthic oxygen uptake', *Water Research* **27**(10), 1545–1558.
- Santos, I. R., Eyre, B. D. and Glud, R. N. (2012), 'Influence of porewater advection on denitrification in carbonate sands: Evidence from repacked sediment column experiments', *Geochimica et Cosmochimica Acta* **96**, 247 – 258.
- Simon, M., Grossart, H.-P., Schweitzer, B. and Ploug, H. (2002), 'Microbial ecology of organic aggregates in aquatic ecosystems', *Aquatic Microbial Ecology* **28**(2), 175–211.
- Sokoll, S., Lavik, G., Sommer, S., Goldhammer, T., Kuypers, M. M. and Holtappels, M. (2016), 'Extensive nitrogen loss from permeable sediments off north-west africa', *Journal of Geophysical Research: Biogeosciences* .
- Soulsby, R. (1997), *Dynamics of marine sands: a manual for practical applications*, Thomas Telford.
- Stonedahl, S. H., Harvey, J. W., Wörman, A., Salehin, M. and Packman, A. I. (2010), 'A multiscale model for integrating hyporheic exchange from ripples to meanders', *Water resources research* **46**(12).

- Sverdrup, H. U., Johnson, M. W. and Fleming, R. H. (1942), *The Oceans: Their physics, chemistry, and general biology*, Vol. 7, Prentice-Hall New York.
- Thibodeaux, L. J. and Boyle, J. D. (1987), 'Bedform-generated convective transport in bottom sediment'.
- Thomas, H., Bozec, Y., Elkalay, K. and De Baar, H. J. (2004), 'Enhanced open ocean storage of CO₂ from shelf sea pumping', *Science* **304**(5673), 1005–1008.
- Traykovski, P. (2007), 'Observations of wave orbital scale ripples and a nonequilibrium time-dependent model', *Journal of Geophysical Research: Oceans (1978–2012)* **112**(C6).
- van Beusekom, J. E. (2005), 'A historic perspective on wadden sea eutrophication', *Helgoland Marine Research* **59**(1), 45–54.
- Van Duyl, F. and Kop, A. (1994), 'Bacterial production in north sea sediments: clues to seasonal and spatial variations', *Marine Biology* **120**(2), 323–337.
- Wang, G., Spivack, A. J., Rutherford, S., Manor, U. and D'Hondt, S. (2008), 'Quantification of co-occurring reaction rates in deep seafloor sediments', *Geochimica et Cosmochimica Acta* **72**(14), 3479–3488.
- Wiberg, P. L. and Sherwood, C. R. (2008), 'Calculating wave-generated bottom orbital velocities from surface-wave parameters', *Computers & Geosciences* **34**(10), 1243–1262.
- Wilson, A. M., Huettel, M. and Klein, S. (2008), 'Grain size and depositional environment as predictors of permeability in coastal marine sands', *Estuarine, Coastal and Shelf Science* **80**(1), 193–199.
- Yalin, M. S. (1985), 'On the determination of ripple geometry', *Journal of Hydraulic Engineering* **111**(8), 1148–1155.
- Ziebis, W., Huettel, M. and Forster, S. (1996), 'Impact of biogenic sediment topography on oxygen fluxes in permeable seabeds', *Marine Ecology Progress Series* **140**, 227–237.



4. Regulation of microbial respiration in sands

Sediment surface area and porewater flow regulate microbial respiration in permeable sediments

Soeren Ahmerkamp

Max Planck Institute for Marine Microbiology, Bremen, Germany

Chao Peng, David Probandt, Hannah K. Marchant

Max Planck Institute for Marine Microbiology, Bremen, Germany

Marcel MM Kuypers and Moritz Holtappels^{1,2}

Max Planck Institute for Marine Microbiology, Bremen, Germany

In preperation: Applied and Environmental Microbiology

Additional Affiliations:

¹*Alfred Wegener Institute - Helmholtz Centre for Polar and Marine Research, Bremerhaven, Germany*

²*MARUM Center for Marine Environmental Sciences, Bremen, Germany*

Contributions to the manuscript:

S.A. and M.H. designed research. C.P. performed experiments, H.K.M carried out MIMS measurements, D.P. carried out confocal microscopy measurements, S.A. performed data analysis. S.A., M.M.M.K. and M.H., conceived, wrote and edited the manuscript.

Abstract

The efficient porewater transport in permeable sediments fuels microbial activity at rates similar to or even above those in muddy sediments. Abundance and activity of the microbial community which lives attached to sand grains is likely to be regulated by sediment properties such as porosity, grain size and grain surface area. To investigate the role of the sediment matrix on remineralization rates, we incubated North Sea sediment in flow through reactors after it was sieved and separated into 5 different fractions of median grain sizes ranging from 277 μm to 882 μm . Sediment characteristics, including grain surface area, permeability, dispersion, grain size distribution and cell abundances were measured along with oxygen consumption and denitrification rates. Volumetric oxygen consumption ranged from 14 to 77 $\mu\text{mol l}^{-1} \text{h}^{-1}$ while the nitrogen-loss via denitrification was between 3.7 and 8.4 $\mu\text{mol l}^{-1} \text{h}^{-1}$ giving an $O_2 : N$ consumption ratio of 7:1. Oxygen consumption and denitrification rates were linearly correlated to the cell abundances which ranged from $2.9 \cdot 10^{-8}$ cells cm^{-3} to $5.4 \cdot 10^{-8}$ cells cm^{-3} . Cell abundances increased significantly with grain surface area but decreased with porewater dispersion - as indication for shear stress. Furthermore, cell-specific oxygen consumption rates were found to increase linearly from 0.005 $\text{fmol cell}^{-1}\text{h}^{-1}$ to 0.06 $\text{fmol cell}^{-1}\text{h}^{-1}$ along increasing porewater advection indicating transport limitation of either electron acceptors or labile organic carbon. The significant correlations between grain surface area, cell abundance and rates allow for first attempts to parameterize microbial activity in sandy sediments.

4.1 Introduction

Permeable sediments cover 50% of the continental shelves and were found to play a key role in nitrogen and carbon cycling (Huettel et al., 2014). Benthic remineralization associated to nitrogen-loss in these sediments is driven by a tight coupling of physical transport rates and microbial reactions (Manuscript II, Boudreau, 1997). On a centimeter scale bedforms interact with the overlying currents creating pressure gradients. These pressure gradients pump bottom water through the pore space providing electron acceptors and donors to highly active microbial communities (Boudreau et al., 2001). At the same time, degradation products and reduced materials are released back to the water column accelerating the benthic-pelagic coupling (Huettel et al., 1998).

On a micrometer scale the vast majority of the microbial communities lives attached to sand grains (Musat et al., 2006; Rusch et al., 2003). In numbers, bacterial cells range in between $10^8 - 10^9$ cells cm^{-3} (Böer et al., 2009; Rusch et al., 2003) from which only 0.2% live in the pore water (Rusch et al., 2003). Therefore, sand grains coated by organic matter (Mayer, 1994) provide a preferred environment. But, the frequent mobilization of sand grains induces mechanical abrasion which forces the microbes into cracks and depression (Miller, 1989; Nickels et al., 1981). In these microenvironments the microbes are provided with the varying electron acceptors and donors supplied by the bottom water which is advected through the pore space.

However, the advective porewater transport brings solutes only into the vicinity of microbes from where the transport into the microenvironments and ultimately to the microbial cells is governed by diffusion. This might lead to chemical conditions around the microbes that differ from the surrounding porewater creating a dependence of microbial reactions on the strength of concentration gradients, i.e. diffusion limitation (Jahnke, 1985; Jørgensen, 1977). Quantification of remineralization rates, therefore, requires experimental designs that reproduce the porewater advection on centimeter scales and also the micrometer transport to the microbes that live attached to the sand grains.

In the last decade flow-through reactors have emerged as the most reliable instrument to study microbial bulk reactions with respect to advective porewater transport (Rao et al., 2008; Marchant et al., 2014; Santos et al., 2012; Evrard et al., 2013). Providing well-defined conditions, volumetric oxygen respiration rates in these reactors have been found to range in between $10 - 250 \mu\text{mol l}^{-1} \text{h}^{-1}$ and nitrogen-loss via denitrification in between $1 - 15 \mu\text{mol l}^{-1} \text{h}^{-1}$ (Marchant et al., 2016; Evrard et al., 2013; Santos et al., 2012; Rao et al., 2008). In manipulative experiments it was shown that the addition of dissolved organic carbon stimulates benthic remineralization leading to an up to 5-fold increase

of oxygen respiration rates (Rusch et al., 2006). Additionally oxygen respiration rates were found to respond to increasing porewater advection (Reimers et al., 2004; Rusch et al., 2006). However, despite the increasing number of measurements the regulation mechanisms of respiration rates with respect to bacterial cell abundances and sediment properties are not well understood.

We conducted manipulative *ex situ* experiments to examine the regulating mechanisms of oxygen respiration and denitrification rates in permeable sediments. Sediments were sampled in the subtidal of the North Sea and sieved into different grain size fractions. In flow-through-incubations the sediments were exposed to varying porewater velocities. Oxygen respiration rates, denitrification rates and combined nitrate and nitrite production rates were measured and cell abundances determined. Additionally, the various physical properties of the sediment such as dispersion, permeability, porosity and surface to volume ratio were measured to gain insights into the controlling variables.

4.2 Methods

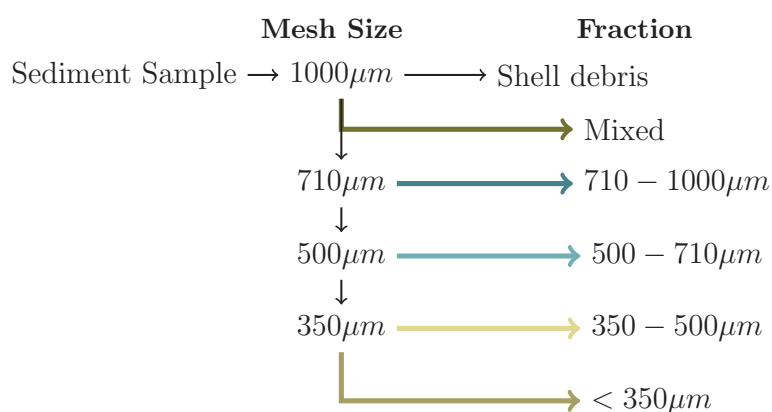
4.2.1 Study site

Sampling was conducted in the subtidal North Sea during RV Heincke cruise 432 in Autumn 2014. The sampling site (GPS 54° 10.48' N, 7° 57.44' E) was located in the German Bight between Helgoland and Bremerhaven, where nutrient supply of Weser and Elbe is fueling primary production (Brockmann et al., 1988). The water depth was around 20 meters indicating a strong hydrodynamic forcing and short settling timescales of particulate organic carbon. Typical bottom water velocities range between 7 - 21 cm s⁻¹ with an additional contribution of the wave orbits by up to 8 cm s⁻¹ (Ahmerkamp et al., 2015). The temperature during the sampling campaign was around 17°C. Sediments were collected using a Van Veen grab. The first two centimeters of the sediment were subsampled and placed into transport boxes. The samples were completely immersed in sea water. Additional bottom water was collected and stored in the dark.

4.2.2 Flow through reactors

The experiments were performed approximately 24 hours after retrieval in acrylic flow through reactors similar to those of Rao et al. (2007). The flow through reactors have the advantage that the physical transport can be controlled and microbial processes can be estimated to high accuracy (Roychoudhury et al., 1998; Reimers et al., 2004; Rao et al., 2008; Santos et al., 2012; Marchant et al., 2014). With a relatively large inner diameter of $d = 10$ cm and a length of $L_c \approx 20$ cm, it was ensured that microbial reaction rates were

not biased by the heterogeneity of the permeable sediment. The length represents typical streamlines in the upper few centimeter of the permeable sediment (Janssen et al., 2012). Radial grooves at the inlet lid and outlet lid of the reactor allowed for a homogenous percolation. Sediment discharge into the tubing was avoided by covering inlet and outlet with a plankton net ($80\ \mu\text{m}$ mesh). Prior to the addition of sediment, the flow through reactors were immersed in sea water and all gas bubbles were removed. The retrieved sediment was homogenized and separated into five different grain size fractions using sieves with mesh sizes of $1000\ \mu\text{m}$, $710\ \mu\text{m}$, $500\ \mu\text{m}$ and $355\ \mu\text{m}$. The resulting fractions were filled into five flow through reactors following the scheme: Here, the mixed fraction



represents the retrieved sediment which only had one sieving iteration with a relatively large $1\ \text{mm}$ mesh to remove the minor amounts of larger shell debris and macrofauna. Then sediments were released in small amounts into the flow through reactor and left to settle by gravitation which avoided trapping of air bubbles. After reaching a column height of $20\ \text{cm}$, the flow through reactors were tightly sealed with piston like lids which had two O-rings attached. To allow for long running periods two $20\ \text{l}$ duran bottles were used as reservoirs filled with the sampled sea water. For experiments under oxic both were continuously aerated and under anoxia degassed with argon. As connection from reservoir to the measuring devices for oxygen and dinitrogen, i.e. optode chambers and membran inlet mass spectrometer for continuous measurements, $1.71\ \text{mm}$ TygonTM tubing was used (approx. $20\ \text{cm}$). To avoid any diffusive gas exchange between tubing and atmosphere we used polyetheretherketone tubing at inlet and outlet of the flow through reactor (approx. $3\ \text{cm}$). In addition, by using a valve combination at inlet and outlet $12\ \text{ml}$ glass syringes (Fortuna Optima) could be filled for subsampling of nitrate - nitrite. The core percolation was driven by two peristaltic pumps with 4 channels each (ISMATEC, Reglo digital MS-4/6). The pump volume was adjusted to reproduce porewater velocities between $1\ \text{cm h}^{-1}$ to $30\ \text{cm h}^{-1}$ as typically found in permeable sediments (Reimers et al.,

2004). The experiments were performed in the absence of light at an ambient temperature of 19°C.

Oxygen respiration, denitrification and nitrate- nitrite production

Oxygen respiration, denitrification and combined nitrate- nitrite production were estimated by measuring the difference of the respective solutes between inlet (C_{in}) and outlet (C_{out}) of the flow through reactor. Based on this difference the reaction rates were estimate by calculating the temporal gradient:

$$R = \frac{(C_{in} - C_{out})}{r_t} \quad (4.1)$$

where $r_t = \theta L_c u^{-1}$ is the retention time, with L_c the length of the core, u the porewater velocity and θ the porosity.

Oxygen was continuously measured using optode flow-through cells (OXFTC, Pyroscience) for 11 different porewater velocities. After adjusting the pump volume it was ensured that a steady state was reached, i.e. stabilized constant rates. This was typically after 1.5 times the retention time - the time a water parcel travels from inlet to outlet. In addition to the oxygen reads, inlet and outlet porewater was subsampled and frozen at -20° C. After finishing the experiments combined nitrate and nitrate production were measured on a CLD 60 Chemiluminescence NO analyzer (Ecophysics) (Braman and Hendrix, 1989). Briefly, the sample porewater was injected into Vanadium(III)-chlorid which reduces nitrate and nitrite to nitrogen monoxid. The chemiluminescence reaction of nitrogen monoxid with ozone was then recorded and integrated. The combined nitrate and nitrite concentration was calculated based on a standard solution calibration using sodium nitrate.

To determine the denitrification rates under anoxic conditions the reservoir water was degased using argon and amended with $70 \mu\text{mol l}^{-1}$ inorganic 15-nitrate. Argon, 28-dinitrogen, 29-dinitrogen and 30-dinitrogen were continuously measured at the outlet by using a membrane-inlet mass spectrometer (GAM200, IPI). Denitrification was calculated by using the isotope pairing method based on the dinitrogen production (Holtappels et al., 2011; Thamdrup and Dalsgaard, 2002). The porewater velocity for the denitrification experiments was in between 9 cm h^{-1} to 12 cm h^{-1} depending on the porosity of the respective sediment fractions. The experiments under anoxic conditions were performed after three weeks of oxic incubations.

Cell counts

Quantification of the total cell abundance was performed by taking subsamples of the incubated sediment from the flow through reactors in between the oxygen respiration measurements. Approximately 0.5 – 1 ml of sediment were fixed in a formaldehyde solution (1% in phosphate buffered saline, PBS) at room temperature. Repeated centrifugation and replacement of the supernatant with the PBS solution ensured a complete fixation of the sample. Cells were then extracted from the grains by sonication (Sonopuls HD70) with a UW 70 sonication probe (Bandelin). To ensure comparability each sample was sonicated 5 times for 30 seconds at a low intensity (25% power, cycle 20). Between the sonication steps the supernatant was collected and replaced by the PBS solution. In total, 5 ml of supernatant per sample was pooled and 200 μl to 500 μl are subsampled and diluted in 10 ml PBS:EtOH solution. Subsequently cells were filtered on 0.2 μm Isopore[®] membrane filters (Millipore). Finally, filters were dried at 40° C and embedded in 0.1% Phor agarose gel (Biozym, low melting temperature gel with strength larger than 800 g cm^{-2}) and stored at -20°C .

To allow for an accurate cell enumeration SYBR Green I (Invitrogen) was used to stain the cells. The 10000x SYBR Green I stock solution was diluted 1:50 in sterile 1 mol l^{-1} Tris HCl with a pH of 7.5. Subsequently 60 μL were transferred onto a petri dish. Filter pieces were stained for 20 minutes and stabilized in mounting medium (Mowiol[®] 4-99 Sigma). Cells were counted using an epifluorescence microscope (Leica DMI6000B) at an excitation wavelength of 498nm. For each filter 28 to 61 randomly chosen grids encompassing an area of 1000 μm^2 were counted with at least 1300 SYBR Green signals.

In situ colonization on sand grains

To visualize the microbial community on surfaces of sediment grains, we applied double stranded DNA specific fluorescent staining and confocal laser scanning microscopy. Sediment was fixed as described and stored at -20°C in phosphate buffered saline/ethanol solution until further processed. For in situ visualization of microbial cell colonization on sand grain surfaces, fixed sediment was SYBR green I stained as described and air dried on whatman[®] cellulose paper (GE Healthcare, Great Britain). To allow inverted microscopy, a hole was drilled into a microscopy glass slide and covered on one side with a polylysine coated cover slip. Stained sediment and MOWIOL mounting medium was added onto the cover slip and air dried. Confocal laser scanning microscopy was performed with a LSM 780 system (Carl Zeiss, Germany). The sample was excited using a 488 nm Laser. The SYBR green I signal was detected in the range 499 – 552 nm, and in parallel the transmitted light signal was recorded to visualize the sediment grain surface. Images were

recorded using a 40x/1.3 Apochromat objective. Minimal subsequent image processing was performed with software IMARIS (Bitplane, Switzerland) and AutoQuant (Media Cybernetics, USA).

Breakthrough curves

As a proxy for the homogeneity of the flow within the core incubation and to estimate dispersion and porosity an argon-breakthrough curve was measured using the membrane-inlet mass spectrometer. The argon-breakthrough represents the cumulative of the porewater age distribution, of which the first moment is the retention time and the second moment the longitudinal dispersion $D_L = \alpha_L u$. To allow for a better comparison, the time variable t and longitudinal dispersion D_L were non-dimensionalized using the characteristic retention time t_r , core length L_c and characteristic porewater velocity u : $t^* = t t_r^{-1}$, $\alpha_L^* = D_L u^{-1} L_c^{-1} = \alpha_L L_c^{-1}$, where an asteriks denotes non dimensional variables. For the 1-D scalar-transport equation and boundary conditions as present in the flow-through reactors an analytical solution exists (Roychoudhury et al., 1998):

$$\frac{C}{C_0} = 0.5 \cdot \operatorname{erf} \left(\frac{1 - t^*}{2 \sqrt{\alpha_L^* t^*}} \right) \quad (4.2)$$

This function is similar to the cumulative function of the Gaussian distribution, where $\sigma = \sqrt{2\alpha_L^*}$ is the standard deviation. So far, most studies used Equation 4.2 as a fit function for the breakthrough curves (Rao et al., 2007). Here, we directly estimated the unknown porosity via the retention time and dispersion from the second moment of the porewater age distribution (Roychoudhury et al., 1998).

To ensure that the electron acceptors, i.e. oxygen and nitrate, are not completely consumed within the flow through reactor the Damköhler number is calculated, which represents the relative rates of reaction to transport:

$$Da = \frac{R}{C_{in}} \cdot \frac{L\theta}{u} \quad (4.3)$$

where L is the length scale. In case $Da > 1$ the solute would be completely consumed within the core. To account for the additional dispersion the longitudinal dispersion coefficient is added to the core length $L = L_c + \sqrt{2\alpha_L u t_r}$. For the measured dispersion coefficients L was typically 10% to 40% larger then the core itself, this is the lengthscale to which dispersion would affect the respiration rate measurements.

Sediment characterization

Grain size distributions were measured using a laser diffraction particle size analyzer (Beckman Coulter, LS 200) and binned into 92 size classes ranging from $d_0 = 0.4 \mu m$ to $d_1 = 2000 \mu m$. Prior to measurements the samples were acidified to remove calcium carbonates. From the measured grain size distribution the theoretical surface area to volume ratio S_V, T can be calculated:

$$S_{V,T} = 6(1 - \theta) \int_{d_0}^{d_1} \frac{p(d_g)}{d_g} dd_g \quad (4.4)$$

where $p(d_g)$ is the probability density function of the respective sediment fractions and d_g the diameter of the grains. Equation 4.4 assumes spherical grains, which is not necessarily the case. Therefore, the surface area per mass ($A m^{-1}$) was also measured via nitrogen adsorption using a Brunnauer-Emmett-Teller analyzer (Quantachrome Quantasorb Jr.) (see also Mayer (1994)). Based on density of the ρ_p particles the surface to volume ratio can be calculated:

$$S_V = \rho_p \frac{A}{m} (1 - \theta) \quad (4.5)$$

The permeability of the sediment fractions was estimated by measuring the pressure drop along the flow through reactor. Along the flow direction two tubes were attached in $\delta = 10$ cm distance to the core. The pressure drop is visible as a difference between the water heads ($h_1 - h_0$) within the tubes. Based on Darcy's law the porewater velocity can be calculated:

$$u = \frac{k}{\mu \theta} \nabla p \quad (4.6)$$

where k is the permeability, μ the dynamic viscosity, θ the porosity and ∇p the pressure gradient. The pressure gradient can be determined based on the hydrostatic pressure drop between the tubes $\nabla p = \rho g (h_1 - h_0) \delta^{-1}$, where ρ is the water density, g the acceleration by gravity. Substitution and rearranging yields:

$$k = \frac{u \mu \delta}{\rho g (h_1 - h_0)} \theta \quad (4.7)$$

4.3 Results

4.3.1 Sediment properties

The medians of the sediment fractions ranged from 277 μm to 882 μm and were in strong agreement with the mesh sizes of the sieves (Figure 4.1, Table 4.3.1). The distributions indicate slight variations in the sediment sorting. The mixed sediment fraction had the widest distribution, i.e. largest standard deviation, followed by largest grain size fraction. Along decreasing grain sizes the distribution became narrower, i.e. smaller sorting coefficient. This is also reflected by the porosity which did not monotonically increase along increasing grain sizes. This is expected as a wider distribution results in a more compact packing (Bear and Buchlin, 1978). The sediment distribution with the smallest median grain sizes had two overlapping peaks, where one was around 200 μm and the second peak was around 450 μm . In general, the distributions tailed towards larger grain sizes.

| Fraction | Grain Size Median (μm) | Sorting | Permeability (m^2) | Porosity | Dispersion (m) | S_V (m^2cm^{-3}) | |
|----------|--|---------|----------------------------------|----------|-------------------|--------------------------------------|------------|
| | | | | | | Sphere equivalent | Measured |
| 1 | 496 | 2.2 | $6.6(1.1) \cdot 10^{-12}$ | 0.30 | $3 \cdot 10^{-3}$ | $1.3 \cdot 10^{-2}$ | 0.51(0.05) |
| 2 | 277 | 1.4 | $6.5(0.6) \cdot 10^{-12}$ | 0.35 | $4 \cdot 10^{-3}$ | $7.8 \cdot 10^{-3}$ | 0.44(0.04) |
| 3 | 481 | 1.4 | $4.2(0.3) \cdot 10^{-11}$ | 0.41 | $7 \cdot 10^{-3}$ | $5.3 \cdot 10^{-3}$ | 0.13(0.01) |
| 4 | 621 | 1.5 | $1.9(1.4) \cdot 10^{-10}$ | 0.45 | $5 \cdot 10^{-3}$ | $3.9 \cdot 10^{-3}$ | 0.13(0.01) |
| 5 | 882 | 1.6 | $1.5(0.8) \cdot 10^{-10}$ | 0.42 | $8 \cdot 10^{-3}$ | $6.4 \cdot 10^{-3}$ | 0.32(0.03) |

Table 4.1: The sediment characteristics for the different sediment fractions are depicted. The numbers in brackets denote the standard deviation for the permeability and the uncertainty for the surface to volume ratio. The permeability was determined from the pressure drop along the flow through reactor for different porewater velocities (Equation 4.7). Porosity and longitudinal dispersion were calculated from the breakthrough curve (see text). The surface to volume ratio was measured using the Brunnauer-Emmett-Teller method (accurate to 10%) and additionally calculated a theoretical value from Equation 4.4. Sorting represents the uniformity coefficient of the sediment distribution.

Under *in situ* conditions the permeability controls the strength of the porewater advection induced by the pressure head along bedforms (Huettel et al., 2014). By keeping the porewater advection constant, the hydraulic head inducing such an advection can be determined for the respective sediment fractions. This hydraulic head was measured as described in the methods section and then used to estimate the permeability using Equation 4.7. The permeability was found to cover two orders of magnitude ranging between $6.5 \cdot 10^{-12} \text{m}^2$ to $1.9 \cdot 10^{-10} \text{m}^2$ (Table 4.3.1) which is in the typical range of permeable sediments (Huettel et al., 2014). For the sieved sediment fractions the permeability increased with increasing median grain sizes. Discrepancies were mainly found for the largest and mixed sediment fractions. The permeability of $1.5 \cdot 10^{-10} \text{m}^2$ as found for the largest sediment fraction is close to the detection limit as the hydraulic head becomes very small.

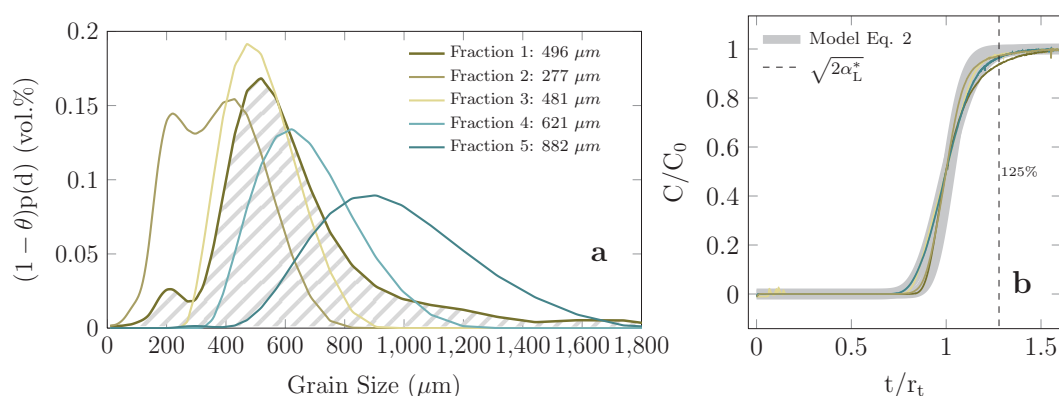


Figure 4.1: Physical properties of the different sediment types. Figure **a** shows the sediment distribution of the five different fractions where the shaded distribution indicates the mixed sediment fraction. Figure **b** shows the breakthrough curve determined by using argon as an inert tracer. The light grey color in the background indicates the breakthrough curves determined from Equation 4.2 based on the estimated parameters. The dashed line indicates the cutoff used for the Damköhler number.

On the other hand, the mixed sediment had a low permeability which might be induced by the compact packing of the wide sediment distribution (Krumbein and Monk, 1943). Repetitive experiments with varying porewater velocities led to similar permeabilities. This indicates that increasing porewater velocities did not affect permeability.

For a more precise description of the homogeneity of the flow path, breakthrough curves were determined following Rao et al. (2007) (Figure 4.1 **b**). For all sediment fractions the breakthrough curves did not indicate a buildup of preferential pathways, or volumes that were not percolated. This would be visible as a prolonged tail towards larger water ages. The longitudinal dispersion coefficients ranged in between $3 \cdot 10^{-3}$ m to $8 \cdot 10^{-3}$ m which is of typical pore space magnitude. This reveals that the smearing of solutes within the core was mainly induced by shear-dispersion along the boundary layer of the grains (Bear and Buchlin, 1978). This is also reflected by the high correspondance to the analytical breakthrough model. The breakthrough curves also show the distribution of flow path lengths inside the flow through reactor. During the experiments the path length variation was up to 25% of the core length (based on the second moment of the porewater age distribution, compare Figure 4.1 **b**). This is essential for the rate estimations as we ensured that oxygen and nitrate were not consumed to less than 25% of the inflow concentrations, otherwise the reaction rates would be biased by the limitation of the electron acceptors along some of the flow paths.

Using the Brunauer - Emmett - Teller method based on dinitrogen sorption, the surface

area to volume ratio was found to range in between $0.13 \text{ m}^2 \text{ cm}^{-3}$ - $0.51 \text{ m}^2 \text{ cm}^{-3}$. The largest surface to volume ratio was found for the mixed sediment fraction ($0.51 \text{ m}^2 \text{ cm}^{-3}$) followed by smallest sediment fraction ($0.44 \text{ m}^2 \text{ cm}^{-3}$) and the largest sediment fraction ($0.32 \text{ m}^2 \text{ cm}^{-3}$). The midrange fractions had the smallest surface to volume ratios around $0.13 \text{ m}^2 \text{ cm}^{-3}$. The theoretical surface to volume ratios calculated based on the grain size distribution ranged in between 0.0039 - $0.013 \text{ m}^2 \text{ cm}^{-3}$. Despite similar trends the calculated values deviated by factors between 25 and 56 (Table 4.3.1). Subsequently, the measured surface to volume ratio is used for subsequent analysis.

4.3.2 Sediment grain colonization and cell counts

The colonization of sediment grains was investigated based on confocal laser scanning microscopy. Most sediment grains exhibited clear signals showing successful colonization of grain surfaces in sandy sediments. Cells of coccoid, rod-like and filamentous morphology were found with maximum size dimensions of $1.2 \mu\text{m}$, $2 \mu\text{m}$ and $25 \mu\text{m}$, suggesting the dominance of microbial cells. Biofilms covered sand grains unevenly, being particular dense in cracks and depressions of sediment grains (Figure 4.2). Smooth and round sediment grains with little variation of fine structures were less colonized. Since handling of sediment grains was done with greatest caution, this results indicates, that biofilms colonize sheltered regions on the sediment grain.

The cell numbers varied in between $2.9 \cdot 10^8 \text{ cells cm}^{-3}$ and $5.4 \cdot 10^8 \text{ cells cm}^{-3}$. Statistical analysis revealed that the mean cell abundances differed significantly from each other (ANOVA, $p < 0.01$) besides for the midrange fractions with median grain sizes of $481 \mu\text{m}$ and $621 \mu\text{m}$ (ANOVA, $p = 0.3$). The cell abundance was neither correlated to sieving iterations as indicator for mechanical abrasion nor to mean grain diameter. But, the cell numbers were strongly correlated to the surface to volume ratio (Figure 4.3). Based on this relationship the areal cell density was estimated to range in between $6.4 \cdot 10^{-3}$ to $1.4 \cdot 10^{-2} \text{ cells } \mu\text{m}^{-2}$. This is equivalent to an available area of $156 \mu\text{m}^2$ to $714 \mu\text{m}^2$ per cell.

Along increasing surface to volume ratios the cell densities decreased which indicates an additional control mechanism. The variability might be induced by different hydrodynamic regimes, i.e. increasing shear stress along increasing porewater advection. An indicator for the shear stress acting on the grains is the longitudinal dispersion. Indeed, large dispersion coincided with small cell abundances. Normalization of the cell surface to volume ratio by the longitudinal dispersion led to a linear increase with the cell abundances (Figure 4.3 b).

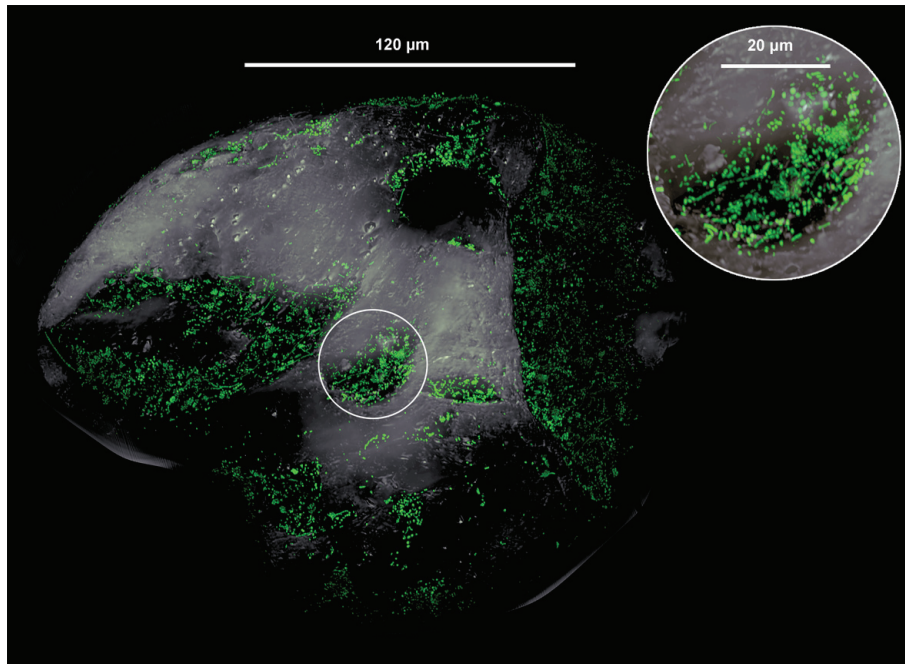


Figure 4.2: The bacterial colonization of a representative sand grain is shown. Cells exhibit coccoid, rod-like and filamentous morphologies and are mostly found in cracks and depressions of the sand grain.

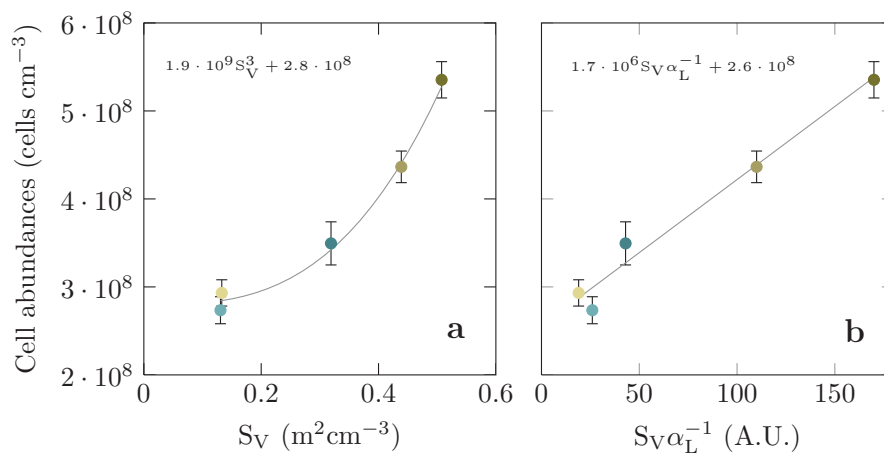


Figure 4.3: In figure **a** the cell abundances are directly correlated to the measured surface to volume ratio. The increase along increasing surface to volume ratios follows a powerlaw. Normalizing the surface to volume ratio by the dispersion, which is an indicator for the shear stress, linearizes the trend (**b**).

4.3.3 Oxygen respiration

Seawater was pumped at porewater velocities of 1 cm h^{-1} to 30 cm h^{-1} through the flow through reactors representing the range as measured in continental shelves sediments (Reimers et al., 2004). The bulk oxygen respirations in the porewater varied in between

| Fraction | Median Grain Size (μm) | Cell counts (cells cm^{-3}) | Oxygen Respiration ($\mu\text{mol l}^{-1} \text{h}^{-1}$) | Denitrification ($\mu\text{mol l}^{-1} \text{h}^{-1}$) | Nitrate- Nitrite Production ($\mu\text{mol l}^{-1} \text{h}^{-1}$) |
|----------|--|--|--|---|---|
| | | | Mean | * | |
| 1 | 496 | $5.4(0.2) \cdot 10^8$ | 62(2) | 65(3) | 8.4(0.8) |
| 2 | 277 | $4.4(0.2) \cdot 10^8$ | 42(2) | 43(2) | 6.1(0.2) |
| 3 | 481 | $2.9(0.1) \cdot 10^8$ | 27(2) | 26(1) | 3.7(0.3) |
| 4 | 621 | $2.7(0.2) \cdot 10^8$ | 27(3) | 27(2) | 3.8(0.1) |
| 5 | 882 | $3.5(0.3) \cdot 10^8$ | 32(4) | 32(3) | 4.1(0.4) |

Table 4.2: Microbial reaction rates for the different grain size fractions presented in per liter porewater. The cell numbers are presented in cell counts per cubic centimeter of wet sediment. The oxygen respiration rates are shown as averages and (*) based on the porewater velocity of the denitrification experiments. The numbers in brackets denote the range for denitrification experiments, standard deviation of residuals for oxygen respiration and standard deviation for nitrate- nitrate production.

$14 \mu\text{mol l}^{-1} \text{h}^{-1}$ and $77 \mu\text{mol l}^{-1} \text{h}^{-1}$ and were correlated to the cell abundances (Figure 4.4). The respiration rates increased along increasing porewater velocities as described in the subsequent section. By averaging, the largest respiration rate of $65 \mu\text{mol l}^{-1} \text{h}^{-1}$ was found for the mixed sediment fraction, followed by the smallest sediment fraction with $43 \mu\text{mol l}^{-1} \text{h}^{-1}$ (Figure 4.5 a). The midrange sediment fractions had smallest respiration rates scattering around $27 \mu\text{mol l}^{-1} \text{h}^{-1}$. The respiration rates for the largest sediment fraction increased in correspondance to the cell abundances to $32 \mu\text{mol l}^{-1} \text{h}^{-1}$.

By normalizing the bulk respiration rates to the cell numbers the theoretical consumption of single cells was estimated to range in between 0.03 to $0.06 \text{ fmol cell}^{-1} \text{h}^{-1}$ (Figure 4.5 b). This procedure assumes that all bacterial cells respire oxygen, which was probably not the case. But, it allows for normalization by considering that the relative amount of oxygen respiring cells stays similar. In general, the rates of the different sediment cores coincide. But, slight variations for the mixed sediment fraction and smallest sediment fraction at the upper porewater velocities were observed.

Along increasing porewater velocities a significant increase of the oxygen respiration rates was observed. Two separate trends become visible by separating the data into a range that falls below and a range above the critical Damköhler number (Equation 4.3, compare Figure 4.5 a,b open symbols). At the lower end of porewater velocities the electron acceptors were limiting ($Dak < 1$). Here, the rates increased at very steep slopes declining towards the critical Damköhler number. When reaching the the critical Damköhler number the increasing trend persisted but followed a linear slope. The slopes for the different sediment fractions varied in between $0.9 - 1.4 \mu\text{mol l}^{-1} \text{h}^{-1}/(\text{cm h}^{-1})$. The sediment properties were not directly correlated to the slopes. A temporal adaptation could not be accounted for the variations as the porewater velocity was not adjust in a monotonical order. Furthermore, after finishing the experiments some of the reaction

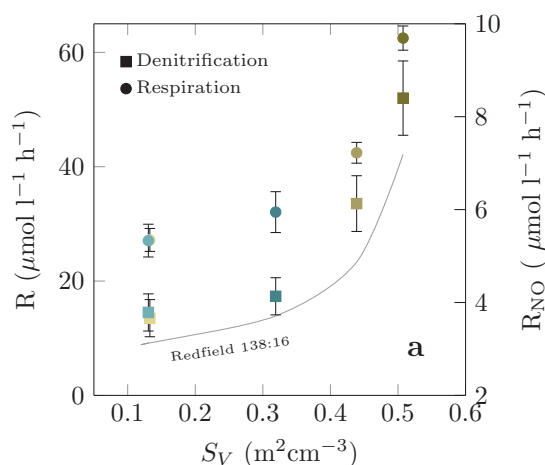


Figure 4.4: The oxygen respiration rates and denitrification rates are shown against cell abundance. The cell abundances are scaled by the porosity to represent cells per liter porewater. The oxygen respiration rates presented are based on a porewater velocity of $8 - 10 \text{ cm h}^{-1}$ to match the denitrification porewater velocity. In **b** the ordinates are scaled by the redfield ratio $R : R_{\text{NO}} = 138 : 16$.

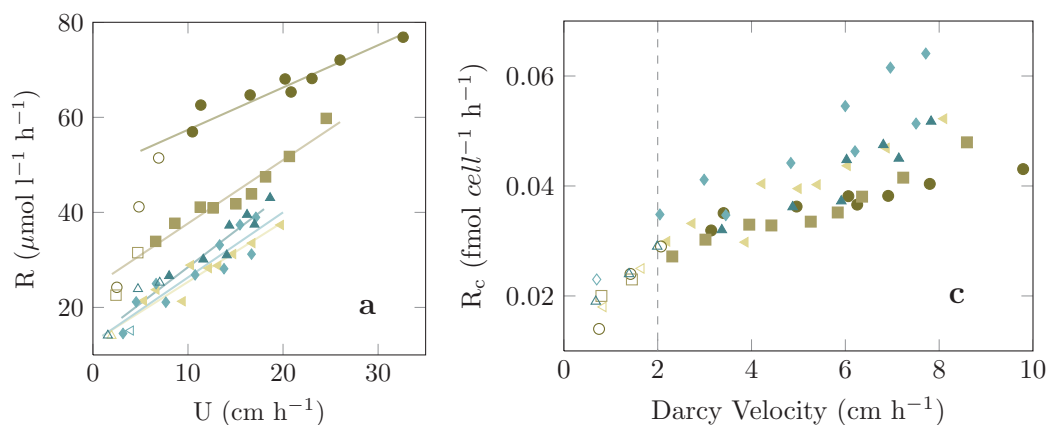


Figure 4.5: In **a** the increasing respiration rates (R) are shown against the porewater velocity (U). Measurements where oxygen was completely consumed within the core or which are affected by dispersion (i.e. $Da > 1$) are shown as open symbols. For the remaining measurements the respiration rates increase linearly with the imposed porewater velocity. **b** By normalizing the respiration to single cells (assuming oxygen respiration by every cell) respiration rates coincide. The porewater velocity is scaled by the porosity to the Darcy velocity which leads to a coinciding critical Darcy velocity around 2 cm h^{-1} (i.e. $Da > 1$).

rates were double-checked based on randomly chosen porewater velocities. Despite some variations the presented trends persisted as discussed later.

4.3.4 Nitrate- nitrite production

Under oxic conditions organic matter gets remineralized and ammonium is released, which is then oxidized to nitrite and nitrate. Assuming a biomass composition that follows the Redfield ratio, the total NO_x production based on the oxic remineralization would follow a ratio of 16 : 138 for N : O_2 (Redfield, 1958; Santos et al., 2012; Eyre and Ferguson, 2009). The nitrate and nitrite production rates in the flow through reactors ranged in between $0.5 \mu\text{mol l}^{-1} \text{h}^{-1}$ and $11 \mu\text{mol l}^{-1} \text{h}^{-1}$. Due to the large scatter, no significant differences between the different sediment fractions were observed. Along increasing porewater velocities a slight increase could be observed but the trend was not significant (data not shown). By relating the oxygen respiration to the nitrite and nitrate production a significant correlation was found at a slope of 0.102 ($R^2 = 0.4$, t-test: $p = 6 \cdot 10^{-8}$), which is only slightly underneath the expected value of Redfield N : $\text{O}_2 = 16 : 138 = 0.1159$.

4.3.5 Denitrification

In order to determine denitrification rates, sea water was degassed and amended with 15-nitrate. Experiments were performed at constant porewater velocities of 9 cm h^{-1} - 12 cm h^{-1} . The denitrification rates were roughly an order of magnitude below the oxygen respiration and ranged in between $3.6 \mu\text{mol l}^{-1} \text{h}^{-1}$ to $8.4 \mu\text{mol l}^{-1} \text{h}^{-1}$. In strong correspondence to the oxygen respiration rates the largest denitrification rates were found for the mixed sediment fraction ($8.4 \mu\text{mol l}^{-1} \text{h}^{-1}$) followed by the smallest sediment fraction ($6.1 \mu\text{mol l}^{-1} \text{h}^{-1}$) and largest sediment fraction ($4.1 \mu\text{mol l}^{-1} \text{h}^{-1}$). The midrange fractions denote the lower limit ($3.6 - 3.7 \mu\text{mol l}^{-1} \text{h}^{-1}$). The denitrification rates under anoxic conditions cover a similar range as the combined nitrate-nitrate production rates under oxic conditions.

4.4 Discussion

We performed core incubations with five different sediment fractions under advective flow conditions to investigate the regulation mechanisms of reaction rates in permeable sediments. Flow-through-reactors were used in which the complex transport processes of permeable sediments are simplified so that the interaction of microbial reaction and solute transport can be described with high accuracy (Rao et al., 2007; Santos et al., 2012; Marchant et al., 2014). By homogenizing and sieving, the transport and reaction rates were less biased by the large scale heterogeneity caused by shell debris and the few macrofauna. As a result, the transport processes were well-defined and the supply of electron acceptors and electron donors from the reservoir water were controlled to a high degree.

The measured oxygen respiration rates (up to $77 \mu\text{mol l}^{-1} \text{h}^{-1}$) and denitrification rates (up to $8.4 \mu\text{mol l}^{-1} \text{h}^{-1}$) were within the range of rates measured recently for continental shelf sediments (Rao et al., 2007; Marchant et al., 2016). Similar to previous observations denitrification rates were significantly correlated to oxygen respiration following a slope that is close to the Redfieldian ratio of $\text{O}_2 : \text{N} = 138 : 16$. This indicates that the remineralization pathways were closely coupled to the elemental composition of the biomass itself (Santos et al., 2012). The good agreement to preceding investigations proves that the mechanical abrasion induced by the sieving has a minor impact on the bacterial abundances. This is further supported by the total cell numbers (around $4 \cdot 10^8 \text{ cells cm}^3$) which represent an intermediate value reported for continental shelf sediments ranging from $1 \cdot 10^8 \text{ cells cm}^{-3}$ to $2.3 \cdot 10^9 \text{ cells cm}^{-3}$ (Rusch et al., 2006; Musat et al., 2006; Böer et al., 2009).

Preceding investigations on sandy sediments have either focused on bacterial cell abundances (e.g. Rusch et al., 2003; DeFlaun and Mayer, 1983) or volumetric reaction rates (e.g. Rusch et al., 2006; Marchant et al., 2014). Volumetric reaction rates were strongly tied to the bacterial cell abundances leading to cell specific oxygen consumption rates of $0.031 \cdot 10^{-2} \text{ fmol cell}^{-1} \text{h}^{-1}$ and denitrification rates of $0.0042 \cdot 10^{-2} \text{ fmol cell}^{-1} \text{l}^{-1}$. The cell abundances were correlated to the measured sediment surface to volume ratio resulting in areal cell densities of $10^{-2} \text{ cells } \mu\text{m}^{-2}$. This implies that on the grain surface a characteristic occupied cell area exists which leads to an optimal supply of solutes and removal of degradation products. In this study the characteristic area was on average $300 \mu\text{m}^2$. This is in strong agreement with prior investigations that found characteristic cell areas to remain stable around $200 \mu\text{m}^2$ for silts, fine sands (Dale, 1974) and pebbles (Tsernoglou and Anthony, 1971; Batoosingh and Anthony, 1971). In conclusion, the surface area regulates to a large extent the potential remineralization rates in sediments where bacterial cells live attached to grains.

However, the sediment surface area is not sufficient to explain the full complexity of remineralization rates. We found indirect evidence that the shear stress has a negative impact on the cell abundances, because they decreased with the dispersion coefficient. Cracks and depressions on the sand grains are sheltered regions in which shear forces are weaker and, indeed, it has been shown that the microtopographic features are preferably colonized (Weise and Rheinheimer, 1977). Under *in situ* conditions the mechanical abrasion is also induced by moving sand grains might reinforce the colonization of these microenvironments (Nickels et al., 1981). Therefore, areal cell densities are heterogenous and locally increased. Within the colonized patches the high cell specific reaction rates may cause a limitation of electron acceptors and electron donors. This would lead to a

dependence of the reaction rates on the transport rates (Ahmerkamp et al., 2015). This is supported by our experiments in which the increase of transport rates, i.e. porewater advection, led to increasing oxygen respiration rates (Figure 4.5).

In general, for the transport limitation two scales become relevant: (i) the net transport into the flow-through-reactor and (ii) the transport from the bulk porewater towards the cells. (i) To account for the net transport and ensure that the electron acceptors (oxygen and nitrate) are not completely consumed within the flow-through-reactor, the Damköhler number was calculated (Equation 4.3). Porewater velocities that lead to a Damköhler number below unity will lead to a linear increase of the calculated reaction rates along increasing porewater velocities (compare open symbols Figure 4.5). This is an experimental artifact that can be also observed in the studies of Rusch et al. (2006); Santos et al. (2012). Nevertheless, beyond this critical Damköhler number the oxygen respiration still increased significantly, although with reduced slopes (Figure 4.5). Previous studies were reexamined for regions above the critical Damköhler number and similar slopes of $1.6 - 2.2 \mu\text{mol l}^{-1} \text{h}^{-1}/(\text{cm h}^{-1})$ were found (Rusch et al., 2006; Reimers et al., 2004). Eventhough the bulk concentration of the electron acceptors were not limiting the rates, the net transport, of electron donors into the reactor might become relevant. It was shown that the addition of acetate stimulates oxygen respiration which indicates a potential limitation of labile dissolved organic matter (Rusch et al., 2006). However, little is known about the uptake of labile organic matter. The molecules that occur under in situ conditions are complex and very diverse, therefore, further investigations are needed to see the effect on the reaction rates. In addition to the transport limitation on a macroscale the electron acceptors and donors can be transport limited on a microscale.

(ii) Despite the advective porewater transport, the bacterial cells are located in a diffusion dominated microenvironment - surrounded by organic matter (Nickels et al., 1981) and a boundary layer. If solutes are completely consumed in the vicinity of the cells diffusion limitation can occur (Jahnke, 1985; Jørgensen, 1977), resulting in a dependence of the bulk reaction on bulk concentrations and hence a correlation to the porewater advection. Considering a single cell reaction rate of $R_c = 0.04 \text{ fmol cell}^{-1} \text{ h}^{-1}$ and a cell diameter of $0.2 \mu\text{m}$, the reaction rate per cell volume can be estimated to be around $700 \text{ mol m}^{-3} \text{ h}^{-1}$. Assuming a continuous layer of bacterial cells a thickness of $7 \mu\text{m}$ is necessary for diffusion limitation. However, bacterial layers of several cells thickness have not been observed on sediment grains (Weise and Rheinheimer, 1977). But, considering the diffusive boundary layer and organic carbon coating diffusion limitation cannot be completely ruled out.

To conclude, the remineralization rates in permeable sediments are largely regulated by the sediment surface area that is available for microbial colonization. However, the

colonization seems affected by shear stress and mechanical abrasion induced by moving sand grains which forces the microbes into cracks and depression. Within this microenvironments transport limitation might occur on a macroscale due to diffusion limitation. It is a task for future studies to investigate this regulation mechanisms for sediment distributions as found under *in situ* conditions. The validation will allow for a simplified parametrization in mathematical models.

Acknowledgements

We are grateful for help with the measurement on the Brunnauer-Emmett-Teller analyzer by Martin Kölling and Christian Winter for measurements on the Coulter laser diffraction particle size analyzer. We are thankful to the captain and crew members of the R/V Heincke 432 for their outstanding collaboration and support during the survey. We sincerely thank Georg Herz and Gabriele Klockgether for technical assistance. The study was funded by the Max Planck Society and DFG-Research Center/Cluster of Excellence “The Ocean in the Earth System” at the University of Bremen.

Bibliography

- Ahmerkamp, S., Winter, C., Janssen, F., Kuypers, M. M. and Holtappels, M. (2015), ‘The impact of bedform migration on benthic oxygen fluxes’, *Journal of Geophysical Research: Biogeosciences* **120**(11), 2229–2242.
- Batoosingh, E. and Anthony, E. (1971), ‘Direct and indirect observations of bacteria on marine pebbles’, *Canadian journal of microbiology* **17**(5), 655–664.
- Bear, J. and Buchlin, J.-M. (1978), ‘Modelling and applications of transport phenomena in porous media’, **5**.
- Böer, S., Arnosti, C., Van Beusekom, J. and Boetius, A. (2009), ‘Temporal variations in microbial activities and carbon turnover in subtidal sandy sediments’, *Biogeosciences* **6**(7), 1149–1165.
- Boudreau, B. P. (1997), *Diagenetic models and their implementation*, Vol. 505, Springer Berlin.
- Boudreau, B. P., Huettel, M., Forster, S., Jahnke, R. A., McLachlan, A., Middelburg, J. J., Nielsen, P., Sansone, F., Taghon, G., Van Raaphorst, W., Webster, I., Weslawski, J. M.,

- Wiberg, P. and Sundby, B. (2001), 'Permeable marine sediments: Overturning an old paradigm', *Eos, Transactions American Geophysical Union* **82**(11), 133–136.
- Braman, R. S. and Hendrix, S. A. (1989), 'Nanogram nitrite and nitrate determination in environmental and biological materials by vanadium (iii) reduction with chemiluminescence detection', *Analytical Chemistry* **61**(24), 2715–2718.
- Brockmann, U., Billen, G. and Gieskes, W. (1988), North sea nutrients and eutrophication, in W. Salomons, B. Bayne, E. Duursma and U. Förstner, eds, 'Pollution of the North Sea', Springer Berlin Heidelberg, pp. 348–389.
- Dale, N. G. (1974), 'Bacteria in intertidal sediments: factors related to their distribution', *Limnology and Oceanography* **19**(3), 509–518.
- DeFlaun, M. F. and Mayer, L. M. (1983), 'Relationships between bacteria and grain surfaces in intertidal sediments', *Limnology and Oceanography* **28**(5), 873–881.
- Evrard, V., Glud, R. N. and Cook, P. L. (2013), 'The kinetics of denitrification in permeable sediments', *Biogeochemistry* **113**(1-3), 563–572.
- Eyre, B. D. and Ferguson, A. J. (2009), 'Denitrification efficiency for defining critical loads of carbon in shallow coastal ecosystems', pp. 137–146.
- Holtappels, M., Lavik, G., Jensen, M. M. and Kuypers, M. M. (2011), '15n-labeling experiments to dissect the contributions of heterotrophic denitrification and anammox to nitrogen removal in the omz waters of the ocean', *Method Enzymol* **486**, 223–251.
- Huettel, M., Berg, P. and Kostka, J. E. (2014), 'Benthic exchange and biogeochemical cycling in permeable sediments', *Marine Science* **6**.
- Huettel, M., Ziebis, W., Forster, S. and III, G. L. (1998), 'Advective transport affecting metal and nutrient distributions and interfacial fluxes in permeable sediments', *Geochimica et Cosmochimica Acta* **62**(4), 613 – 631.
- Jahnke, R. (1985), 'A model of microenvironments in deep-sea sediments: Formation and effects on porewater profiles', *Limnology and Oceanography* **30**(5), 966–971.
- Janssen, F., Cardenas, M. B., Sawyer, A. H., Dammrich, T., Krietsch, J. and de Beer, D. (2012), 'A comparative experimental and multiphysics computational fluid dynamics study of coupled surface–subsurface flow in bed forms', *Water Resources Research* **48**(8), n/a–n/a. W08514.

- Jørgensen, B. (1977), 'Bacterial sulfate reduction within reduced microniches of oxidized marine sediments', *Marine Biology* **41**(1), 7–17.
- Krumbein, W. and Monk, G. (1943), 'Permeability as a function of the size parameters of unconsolidated sand', *Transactions of the AIME* **151**(01), 153–163.
- Marchant, H. K., Holtappels, M., Lavik, G., Ahmerkamp, S., Winter, C. and Kuypers, M. M. (2016), 'Coupled nitrification–denitrification leads to extensive n loss in subtidal permeable sediments', *Limnology and Oceanography* .
- Marchant, H. K., Lavik, G., Holtappels, M. and Kuypers, M. M. (2014), 'The fate of nitrate in intertidal permeable sediments', *PloS one* **9**(8), e104517.
- Mayer, L. M. (1994), 'Surface area control of organic carbon accumulation in continental shelf sediments', *Geochimica et Cosmochimica Acta* **58**(4), 1271–1284.
- Miller, D. (1989), 'Abrasion effects on microbes in sandy sediments.', *Marine ecology progress series. Oldendorf* **55**(1), 73–82.
- Musat, N., Werner, U., Knittel, K., Kolb, S., Dodenhof, T., Van Beusekom, J. E., De Beer, D., Dubilier, N. and Amann, R. (2006), 'Microbial community structure of sandy intertidal sediments in the north sea, sylt-romo basin, wadden sea', *Systematic and Applied Microbiology* **29**(4), 333–348.
- Nickels, J. S., Bobbie, R. J., Martz, R. F., Smith, G. A., White, D. C. and Richards, N. L. (1981), 'Effect of silicate grain shape, structure, and location on the biomass and community structure of colonizing marine microbiota', *Applied and environmental microbiology* **41**(5), 1262–1268.
- Rao, A. M., McCarthy, M. J., Gardner, W. S. and Jahnke, R. A. (2007), 'Respiration and denitrification in permeable continental shelf deposits on the south atlantic bight: Rates of carbon and nitrogen cycling from sediment column experiments', *Continental Shelf Research* **27**(13), 1801–1819.
- Rao, A. M., McCarthy, M. J., Gardner, W. S. and Jahnke, R. A. (2008), 'Respiration and denitrification in permeable continental shelf deposits on the south atlantic bight: n_2 : Ar and isotope pairing measurements in sediment column experiments', *Continental Shelf Research* **28**(4), 602–613.
- Redfield, A. C. (1958), 'The biological control of chemical factors in the environment', *American scientist* pp. 230A–221.

- Reimers, C. E., Stecher III, H. A., Taghon, G. L., Fuller, C. M., Huettel, M., Rusch, A., Ryckelynck, N. and Wild, C. (2004), 'In situ measurements of advective solute transport in permeable shelf sands', *Continental Shelf Research* **24**(2), 183–201.
- Roychoudhury, A., Viollier, E. and Van Cappellen, P. (1998), 'A plug flow-through reactor for studying biogeochemical reactions in undisturbed aquatic sediments', *Applied Geochemistry* **13**(2), 269–280.
- Rusch, A., Huettel, M., Reimers, C. E., Taghon, G. L. and Fuller, C. M. (2003), 'Activity and distribution of bacterial populations in middle atlantic bight shelf sands', *FEMS Microbiology Ecology* **44**(1), 89–100.
- Rusch, A., Huettel, M., Wild, C. and Reimers, C. E. (2006), 'Benthic oxygen consumption and organic matter turnover in organic-poor, permeable shelf sands', *Aquatic Geochemistry* **12**(1), 1–19.
- Santos, I. R., Eyre, B. D. and Glud, R. N. (2012), 'Influence of porewater advection on denitrification in carbonate sands: Evidence from repacked sediment column experiments', *Geochimica et Cosmochimica Acta* **96**, 247 – 258.
- Thamdrup, B. and Dalsgaard, T. (2002), 'Production of n₂ through anaerobic ammonium oxidation coupled to nitrate reduction in marine sediments', *Applied and environmental microbiology* **68**(3), 1312–1318.
- Tsernoglou, D. and Anthony, E. (1971), 'Particle size, water-stable aggregates, and bacterial populations in lake sediments', *Canadian journal of microbiology* **17**(2), 217–227.
- Weise, W. and Rheinheimer, G. (1977), 'Scanning electron microscopy and epifluorescence investigation of bacterial colonization of marine sand sediments', *Microbial Ecology* **4**(3), 175–188.

5. Coupled nitrification-denitrification in sands

Coupled nitrification-denitrification leads to extensive N loss in sub-tidal permeable sediments

Hannah K. Marchant

Max Planck Institute for Marine Microbiology, Bremen, Germany

Moritz Holtappels^{1,2}, Gaute Lavik, Soeren Ahmerkamp

Max Planck Institute for Marine Microbiology, Bremen, Germany

Christian Winter

MARUM Center for Marine Environmental Sciences, Bremen, Germany

Marcel MM Kuypers

Max Planck Institute for Marine Microbiology, Bremen, Germany

doi: 10.1002/lno.10271

Published in: *Limnology & Oceanography*

Additional Affiliations:

¹*Alfred Wegener Institute - Helmholtz Centre for Polar and Marine Research, Bremerhaven, Germany*

²*MARUM Center for Marine Environmental Sciences, Bremen, Germany*

Contributions to the manuscript:

H.K.M. and M.M.M.K. and M.H. designed research. H.K.M and C.W. carried out field-work, H.K.M carried out GC-IRMS measurements and data analysis. C.W. performed grain size analysis and provided in situ data. H.K.M., and M.H. and S.A., carried out modeling and areal rate estimates. H.K.M., M.H., G.L. and M.M.M.K., conceived, wrote and edited the manuscript

Abstract

We investigated microbial pathways of nitrogen transformation in highly permeable sediments from the German Bight (South-East North Sea) by incubating sediment cores percolated with ^{15}N -labeled substrates under near in situ conditions. In incubations with added $^{15}\text{NH}_4^+$, production of $^{15}\text{NO}_2^-$ occurred while the sediment was oxic, indicating ammonia oxidation. Similarly, $^{15}\text{NO}_3^-$ production during $^{15}\text{NO}_2^-$ incubations indicated nitrite oxidation. Taken together these findings provide direct evidence of high nitrification rates within German Bight sands. The production of $^{15}\text{N} - \text{N}_2$ upon addition of $^{15}\text{NO}_3^-$ revealed high denitrification rates within the sediment under oxic and anoxic conditions. Denitrification rates were strongly and positively correlated with oxygen consumption rates, suggesting that denitrification is controlled by organic matter availability. Nitrification and denitrification rates were of the same magnitude and the rapid production of $^{15}\text{N} - \text{N}_2$ in incubations with added $^{15}\text{NH}_4^+$ confirmed close coupling of the two processes. Areal rates of N-transformation were estimated taking advective transport of substrates into account and integrating volumetric rates over modeled oxygen and nitrate penetration depths, these ranged between 22 and 94 $\mu\text{mol N m}^{-2} \text{ h}^{-1}$. Furthermore, results from the ^{15}N -labeling experiments show that these subtidal permeable sediments are, in sharp contrast to common belief, a substantial source of N_2O . Our combined results show that nitrification fuels denitrification by providing an additional source of nitrate, and as such masks true N-losses from these highly eutrophic sediments. Given the widespread occurrence of anthropogenically influenced permeable sediments, coupled benthic nitrification-denitrification might have an important but so far neglected role in N-loss from shelf sediments.

5.1 Introduction

Shallow coastal seas are subject to high loads of anthropogenic inorganic nitrogen inputs from both riverine sources and atmospheric deposition. These inputs cause eutrophication, which has negative impacts on the ecosystem ranging from changes in species composition, increased phytoplankton blooms and bottom water hypoxia (Rabalais, 2002). Eutrophication in shallow coastal seas is alleviated by denitrification, which is stimulated by high nitrate and organic matter (OM) inputs. The heterotrophic denitrification that occurs in shallow sediments therefore makes these environments significant hotspots of N-loss in global budgets (Devol et al., 1997; Gao et al., 2012; Gruber and Galloway, 2008).

Until recently, benthic nitrogen cycling studies were carried out mainly in muddy sediments. However, up to 70% of all continental shelves are comprised of coarse grained sandy sediments (Emery, 1968), in which pore water advection can occur (Huettel et al., 2003). Advection transports bottom water into the sediment at timescales up to three orders of magnitude higher than diffusion (Huettel et al., 2014). This supplies the sediment with organic matter and electron acceptors, and furthermore, increases oxygen penetration depths, which oscillate within the sediment dependent on tidal forcing and ripple migration (Cook et al., 2007; Huettel et al., 2003). As a result of advective solute supply, high rates of organic matter mineralization occur in permeable sediments (De Beer et al. 2005), and benthic denitrification rates are amongst the highest in the marine environment (Gao et al., 2010, 2012). Furthermore, variations in oxygen concentrations appear to stimulate the co-occurrence of aerobic and anaerobic processes, for example denitrification (which is considered to be a predominantly anaerobic process), has been observed in oxic permeable sediments using diverse experimental set-ups (Gao et al., 2010; Marchant et al., 2014; Rao et al., 2008).

The German Bight is an example of a shallow eutrophied coastal sea, which is dominated by permeable sediments and receives extensive anthropogenic dissolved inorganic nitrogen (DIN) inputs from riverine and atmospheric sources (Pätsch et al., 2010; van Beusekom, 2005). Fluxes of DIN out of the German Bight are lower than the anthropogenic and advective influxes (Beddig et al., 1997; Pätsch et al., 2010), indicating that high levels of benthic N-loss must occur. Furthermore, based upon natural abundance stable isotope signatures of nitrate, it has been suggested that intense N-recycling occurs through nitrification, possibly within the sediment (Dähnke et al., 2010).

Benthic N-loss studies in permeable sediments have so far focused on the increased flux of nitrate and organic matter from the water column, therefore little is known about the extent of nitrification. Nitrification has been observed in permeable sediments under

diffusive conditions, yet very few, if any, measurements of ammonia oxidation and nitrite oxidation have been undertaken under advective conditions. If occurring, benthic nitrification could provide a secondary nitrate source for denitrification or recycle remineralized N to the environment. The catalytic properties of permeable sediments, which has led to their description as ‘natural bioreactors’ (Huettel et al., 2014) makes nitrification and its subsequent coupling to denitrification likely to occur.

So far however, coupled nitrification-denitrification has rarely been measured directly in eutrophied permeable sediments. In fact in the Wadden Sea nearby the German Bight, the comparatively low ratio of nitrification to denitrification could not support significant amounts of coupled nitrification-denitrification (Marchant et al., 2014). Furthermore, a modeling study has suggested that advection may have a negative impact on nitrification if ammonium generated by remineralization is returned directly to the water column without entering oxic sediment regions (Kessler et al., 2013). In contrast to these findings, coupled nitrification-denitrification has been predicted to occur in permeable sediments from more oligotrophic regions based on isotope pairing studies (Rao et al., 2007, 2008), and sustains N-loss in the Gulf of Mexico when water column nitrate concentrations are low (Gihring et al., 2010). Evidence from permeable bed reactors, which are used frequently in wastewater treatment, also suggests that permeable sediments should foster suitable conditions for coupled nitrification-denitrification. Wastewater treatment has taken advantage of the prevalence of coupled nitrification-denitrification for many decades (Prakasam and Loehr, 1972; Sharma and Ahlert, 1977); in a process with many parallels to permeable sediments, oxygenated, ammonium rich wastewater is percolated or pumped through permeable media which is colonized with microbes. The ammonium is nitrified and subsequently a switch to anoxic conditions is achieved by increasing the path length of the permeable bed, or intermittently removing the oxygen, whereupon denitrification occurs (e.g. Guo et al., 2005; Yoo et al., 1999). In simultaneous nitrification-denitrification reactors the spatial or temporal separation of nitrification and denitrification is not even required and the two processes occur while the reactor is oxic (e.g. Münch et al., 1996; Tait et al., 2013).

Studying processes such as coupled nitrification-denitrification in permeable sediments represents a challenge as the advective transport of water and its associated solutes into the sediment must be mimicked. A number of methods have been applied to mimic these conditions, most of which require ex situ incubations. Whole core incubations, in which seawater is percolated into undisturbed sediment were initially used to investigate rates in permeable sediments (Polerecky et al., 2005), however provide low time resolution when optode foils cannot be used (as is the case with N-loss measurements). In recent

years however, methods in which sediment is homogenized either in gas-tight bags (Gao et al., 2012), stirred bioreactors (Gao et al., 2010), modified whole cores (Marchant et al., 2014), or flow through columns (Rao et al., 2007, 2008) have been shown to exhibit similar processes (i.e. denitrification in the presence of oxygen has been observed in all), and remarkably similar volumetric rates for the upper few centimeters of permeable sands. The modified whole core method (Marchant et al., 2014) provides increased sampling resolution and allows multiple experiments to be carried out on the same sediment. This is particularly important when investigating detailed relationships between N-cycling processes and when considering the extrapolation of volumetric rates to areal rates. Both of which are required to better understand the role that sandy sediments play in N-loss, especially in highly active eutrophied coastal zones such as the German Bight .

The extent to which nitrification and denitrification might be coupled in sediments is dependent on the availability of ammonium, nitrate, organic matter and oxygen. In permeable sediments the supply of these is determined by advective porewater transport which depends on the physical properties of the sediments (Huettel et al., 2014). Consequently transport-reaction models fueled by measured volumetric rates, sediment characteristics and current speed are required to estimate realistic areal rates.

We investigated the role of nitrification and denitrification in permeable subtidal sediments from the German Bight during summer when water column nitrate concentrations are comparatively low ($6\text{--}8\ \mu\text{mol L}^{-1}$). By combining core percolation and ^{15}N labeling experiments we aimed to measure nitrification, dissimilatory N-reduction and their associated N_2O production. Furthermore, we modified a model in order to take into account both the advective transport of porewater and volumetric rates of interdependent biogeochemical processes; enabling us to extrapolate areal rates of nitrification and denitrification in this complex flow-dominated system. This allowed us to gain insights into the importance of both organic matter and nitrification in controlling N-loss in subtidal sandy sediments.

5.2 Materials and Methods

5.2.1 Sediment sampling

Sampling was conducted at three stations in the North Sea around Helgoland on board the RV Heincke from 22 June 2012 to 28 June 2012. At each station sediment was collected in a box corer and the top 5 cm were subsampled on deck, homogenized and filled into 3 PVC cores (height 9 cm, I.D 10.3 cm). Cores were sealed with rubber stoppers fitted with inflow and outflow ports controlled by 2 way valves. Bottom water was collected using a rosette water sampler and incubations were carried out immediately on board at in situ

temperature.

5.2.2 Sediment characteristics

Sub samples of sediment were collected from box cores, transferred to 50 ml falcon tubes (Sarstedt) and returned to Bremen. Porosity was calculated from 5 replicates by carefully filling a known volume of sediment into volumetric measuring cylinders, ensuring that pore spaces were saturated with water. The weight loss of a known volume of sediment after drying at 60 °C was then determined. Grain size distribution was determined on a Beckman Coulter LS Particle Analyzer at the Center for Marine Environmental Sciences (MARUM), University of Bremen and results were analyzed using the GRADISTAT software with the Folk and Ward method as described in Blott and Pye (2001). Permeability of homogenized sediments was measured in triplicate (i.e. sediment columns were repacked between each measurement) using the falling head approach and a setup similar to that described in (Rocha et al., 2005).

5.2.3 Sediment core incubations

Nitrogen cycling processes under changing oxygen concentrations (i.e. oxic to anoxic) were determined within percolated sediment cores. The incubations (detailed below) were designed to mimic in situ conditions, where water rich in nitrate, oxygen and organic matter is advected into the sediment and follows curved flow paths. Over time, the air saturated bottom water becomes anoxic and is eventually returned to the water column.

| Incubation | Replicates per site | ¹⁵ N amendment (μmol L ⁻¹) | ¹⁴ N amendment (μmol L ⁻¹) | Other amendment | Processes targeted |
|--|---------------------|---|---|------------------------------|---|
| ¹⁵ NH ₄ ⁺ exp + ¹⁴ NO _x | 3 | NH ₄ ⁺ (75) | NO ₂ ⁻ (100) + NO ₃ ⁻ (150) | - | Ammonia oxidation |
| ¹⁵ NO ₂ ⁻ exp | 3 | NO ₂ ⁻ (100) | NO ₃ ⁻ (150) | - | Nitrite oxidation/reduction |
| ¹⁵ NO ₃ ⁻ exp | 3 | NO ₃ ⁻ (75) | - | - | Denitrification/DNRA |
| ¹⁵ NH ₄ ⁺ + ATU exp. | 2 | NH ₄ ⁺ (75) | - | 86 μmol L ⁻¹ ATU* | Anammox/coupled nitrification-denitrification |
| ¹⁵ NH ₄ ⁺ + Acet. exp | 1 | NH ₄ ⁺ (75) | - | 10 Pa acetylene [†] | Anammox |

*Allylthiourea was added to block ammonia oxidation to investigate anammox. ATU did not fully block ammonia oxidation so instead this experiment was used to show the close coupling between nitrification and denitrification.

[†]Acetylene at this concentration fully inhibits ammonia oxidation, but only partly inhibits anammox (Jensen et al. 2007).

Table 5.1: Summary of sediment core incubations. Replicates refer to the number of unique sediment cores used for each incubation.

The sampling method, whereby the porewater within the core is rapidly replaced by air saturated, substrate amended water prior to the first time point, captures dynamic conditions in the sediment i.e., the first time point, taken at zero minutes equates to air saturated conditions. Over time, the oxygen concentration in the core drops to below detection limits, and therefore sampling porewater over time from the same core allows

measurement of processes first under oxic and then anoxic conditions. As water is sampled regularly, porewater within the core is only stagnant for short periods of time; therefore this method mimics the flow of water through the sediment in a similar way to flow through columns. In this modified version of the percolation method (see Marchant et al. (2014) for further details of the sampling protocol), water is initially replaced by pumping from the bottom of the core and then sampling also takes place from the bottom of the core by letting water flow into Exetainers. This allows greater control than percolating from the top of the core; however is essentially the same principle. Previously we have demonstrated that volumetric rates obtained from the sediment this way are the same as rates using the traditional core percolation method (Marchant et al., 2014).

Volumetric rates of oxygen consumption, ammonia oxidation, nitrite oxidation, denitrification, dissimilatory nitrate reduction to ammonium (DNRA) and anammox were determined at each station in triplicate sediment cores which were percolated with various combinations ^{14}N and ^{15}N inorganic compounds. Four incubations were carried out consecutively on triplicate cores at each station and these are summarized in Table 1. Each incubation was carried out in the same way.

Briefly, bottom water was amended with ^{14}N and ^{15}N inorganic compounds and various inhibitors as appropriate (i.e. NO_3^- , NO_2^- and/or NH_4^+ (see below)). The water was aerated before being pumped upwards through the sediment core with a peristaltic pump, exchanging the entire porewater volume in the core with the aerated, N-amended water. After this, porewater was sampled over time from an attachment at the bottom of the core. 6 ml of porewater was sampled per time point into Exetainers (Labco, High Wickham, UK) pre-filled with 100 μl saturated HgCl_2 , taking care to ensure no bubbles were trapped in the Exetainers. 12 time points were taken between 0 and 250 minutes, time points varied per incubation and station and can be seen in Figure S2.

5.2.4 ^{15}N Labeling experiments

Incubations were carried out using ^{15}N labeled substrates to determine rates of ammonia oxidation, nitrite oxidation and denitrification, DNRA, anammox and coupled nitrification-denitrification (Table 5.1). To identify ammonia oxidation rates, $^{15}\text{NH}_4^+$ was added to the incubations, as well as pools of $^{14}\text{NO}_2^-$ and $^{14}\text{NO}_3^-$ ($^{15}\text{NH}_4^+$ + $^{14}\text{NO}_x$ exp.). These unlabeled pools were added to lower the likelihood that the produced $^{15}\text{NO}_2^-$ would be further oxidized to $^{15}\text{NO}_3^-$ or reduced to N_2 in subsequent reactions. Similarly, for nitrite oxidation determinations, $^{15}\text{NO}_2^-$ was added to the incubations, as well as a pool of $^{14}\text{NO}_3^-$. The addition of ^{14}N pools to these incubations would prevent observations of coupled nitrification-denitrification. A further incubation was performed using $^{15}\text{NH}_4^+$ and

ATU ($^{15}\text{NH}_4^+$ + ATU exp). The ATU addition should have inhibited nitrification, however this was not the case (see results and discussion), therefore this experiment was instead used to follow the transformation of ammonium into nitrite, nitrate and N_2 (coupled nitrification-denitrification). To determine whether anammox was present to any significant extent, one core from the low and intermediate permeability stations was incubated with $^{15}\text{NH}_4^+$, the ambient background NO_3^- and 10 Pa (4.1 μM) of acetylene ($^{15}\text{NH}_4^+$ + acet. exp), at this concentration, acetylene entirely blocks ammonia oxidation, but only partially inhibits anammox (Jensen et al. 2007), therefore any produced $^{29}\text{N}_2$ would have originated from anammox. Furthermore, in the denitrification experiment where $^{15}\text{NO}_3^-$ was added we compared the labeling percentage ($F^{15}\text{NO}_3^-*$) (Equation 5.1) based on the produced $^{29}\text{N}_2$ and $^{30}\text{N}_2$ at each time point with the labeling percentage ($F^{15}\text{NO}_3^-$) (Equation 5.2) from substrate measurements. Deviation between these two values can indicate the occurrence of anammox.

5.2.5 Oxygen determination

Oxygen was determined in each Exetainer using an O_2 microsensor (response time < 2 s), briefly, Exetainers were opened and the microsensor inserted before being closed again. This procedure took less than 5 seconds and did not result in any water loss from the Exetainers. Oxygen microsensors were constructed as described in (Revsbech, 1989) and calibration was performed before and after measurements using a 2 point calibration in air saturated seawater and seawater deoxygenated with N_2 .

5.2.6 ^{15}N analyses

The isotopic N composition of nitrogen and nitrous oxide gas at each time point was determined after replacing 2 ml of water within each Exetainer with a helium headspace. Gas from the headspace was injected directly into a GC-IRMS (VG Optima, Manchester, UK), and the isotope ratios of $^{28}\text{N}_2$, $^{29}\text{N}_2$ and $^{30}\text{N}_2$ or $^{44}\text{N}_2\text{O}$, $^{45}\text{N}_2\text{O}$ and $^{46}\text{N}_2\text{O}$ were determined. The concentration of $^{29}\text{N}_2$ and $^{30}\text{N}_2$ or $^{45}\text{N}_2\text{O}$ and $^{46}\text{N}_2\text{O}$ were calculated from the excess of each relative to an air sample or an N_2O sample (Holtappels et al., 2011).

$^{15}\text{NO}_2^-$ was determined in subsamples after conversion to N_2 by sulfamic acid. $^{15}\text{NO}_3^-$ was determined in a further subsample after NO_2^- removal with sulfamic acid, at which point spongy cadmium was applied to reduce NO_3^- to NO_2^- . After one further sulfamic acid treatment, N_2 was measured from a helium headspace using GC-IRMS as before (Füssel et al., 2011). $^{15}\text{NH}_4^+$ was determined in a different set of subsamples after hypobromite oxidation to N_2 (Preisler et al., 2007; Warembourg, 1993).

5.2.7 Total nitrate and nitrite determination

The combined concentration of nitrate and nitrite (NO_x) within each Exetainer was determined by a commercial chemiluminescence NO_x analyzer after reduction to NO with acidic Vanadium (II) chloride (Braman and Hendrix, 1989). Nitrite was determined after reduction to NO with acidic potassium iodide and nitrate was then calculated by the difference between NO_x and NO_2^- .

5.2.8 Volumetric rate calculations

Volumetric denitrification and DNRA rates were determined during both the oxic part of the incubation (where oxygen was still above $20 \mu\text{mol L}^{-1}$) and the anoxic part (where oxygen was below detection limit).

In the $^{15}\text{NO}_3^-$ labeling experiment (which was designed to determine denitrification rates), the possibility that anammox had a significant influence on the production of $^{29}\text{N}_2$ (p^{29}N_2) and $^{30}\text{N}_2$ (p^{30}N_2) was assessed. The labeling percentage of nitrate was calculated from p^{29}N_2 and p^{30}N_2 , assuming isotope pairing from denitrification only:

$$F^{15}\text{NO}_3^- * = 2 \left(\frac{\text{p}^{29}\text{N}_2}{\text{p}^{30}\text{N}_2} + 2 \right)^{-1} \quad (5.1)$$

Values obtained from Equation 5.1 were compared at each time point to measured concentrations of labeled and unlabeled nitrate ($F^{15}\text{NO}_3^-$)

$$F^{15}\text{NO}_3^- = \frac{^{15}\text{NO}_3^-}{^{14}\text{NO}_3^- + ^{15}\text{NO}_3^-} \quad (5.2)$$

As no significant difference was observed, denitrification rates were then calculated as D_{tot} according to (Nielsen, 1992).

DNRA rates were determined from the labeling percentage of nitrate (Equation 5.1) and the production of $^{15}\text{NH}_4^+$ ($\text{p}^{15}\text{NH}_4^+$):

$$\text{DNRA} = \frac{\text{p}^{15}\text{NH}_4^+}{F^{15}\text{NO}_3^- * } \quad (5.3)$$

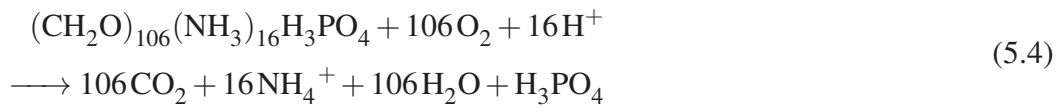
Ammonia oxidation rates were determined from the production of $^{15}\text{NO}_2^-$ during the oxic part of the incubations. A pool of $^{14}\text{NO}_2^-$ was added to the incubations to prevent further oxidation of $^{15}\text{NH}_4^+$ to $^{15}\text{NO}_3^-$. In some cases this can be insufficient; leading to the

formation of a small amount of $^{15}\text{NO}_3^-$, in such cases the $^{15}\text{NO}_3^-$ concentration was added to the $^{15}\text{NO}_2^-$ concentration before rate determination. Furthermore, during ammonia oxidation the pool of $^{15}\text{NH}_4^+$ can become significantly diluted with $^{14}\text{NH}_4^+$ formed during remineralization of organic matter. Therefore to avoid rate underestimations we corrected the produced $^{15}\text{NO}_2^-$ for the labeling percentage of ammonium at each time point (Equation 5.4).

Where tx refers to the time point and F_{NH_4} is the labeling percentage of ammonium determined by GC-IRMS. Ammonia oxidation rates were then calculated by the increase of NO_2^- over time.

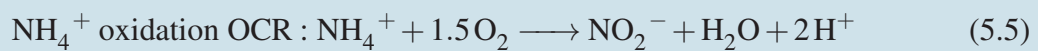
Nitrite oxidation rates were determined during the oxic part of the incubation from the production of $^{15}\text{NO}_3^-$ ($p^{15}\text{NO}_3^-$) after addition of $^{15}\text{NO}_2^-$. Due to sample limitations we did not correct these rates for changes in labeling percentage.

The amount of ammonium released during oxic respiration was compared to ammonia oxidation rates from ^{15}N -labeling experiments (assuming Redfield stoichiometry of organic matter). Briefly, aerobic respiration of organic matter with a Redfield stoichiometry would lead to production of NH_4^+ at a ratio of $106 \text{ O}_2 / 16 \text{ NH}_4^+$;

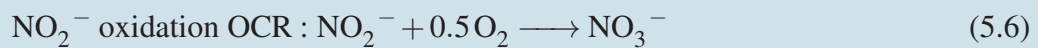


The oxygen consumed by ammonia oxidation and nitrite oxidation was calculated according to:

Ammonia Oxidation



Nitrite Oxidation



This oxygen consumption was subtracted from total oxygen consumption rate (OCR) to determine potential heterotrophic OCR (Equation 5.7). It should be noted however that the remaining OCR may still have been influenced by other autotrophic respirations.

Heterotrophic Oxygen Consumption Rate

$$\begin{aligned} \text{Heterotrophic OCR} = & \text{Total OCR} - (\text{NH}_4^+ \text{oxidation OCR}) \\ & - (\text{NO}_2^- \text{oxidation OCR}) \end{aligned} \quad (5.7)$$

All rates were determined from linear regressions of at least 4 time points, results of which are given in Table A.5.5.

5.2.9 O₂ and NO₃⁻ penetration depths and areal rates

Porewater concentrations of O₂ and NO₃⁻ were not measured during this cruise. In sediments where oxygen availability is controlled by advective fluxes, removing the sediment from the advective system could lead to underestimations in oxygen penetration depth. Additionally, porewater profiles of nitrate are of low resolution in permeable sediments (1 – 2 cm intervals) due to their low porosity. When nitrification is coupled to denitrification and the processes overlap spatially, precise penetration depths are essential in order to determine areal rates. Therefore, we took a modeling approach, which allowed us to estimate penetration depth by combining volumetric rates with advectively driven porewater transport. O₂ and NO₃⁻ penetration depths were derived from a transport model published by Elliott and Brooks (1997*b,a*), which investigated advective mass transport into permeable sediment as a function of time. The model allows for calculation of an “effective mean mixing depth”, from the integral of the residence time function of a solute, which is pumped into the sediment due to the interaction of bottom water currents and seabed topography (ripples). The model does not cover the full complexity found in situ, as diffusion and dispersion are neglected, both of which would lead to an additional transport into deeper sediment layers and increase benthic net fluxes. Therefore, the model approach used here represents a conservative estimate.

For stationary ripples with a simplified geometry Elliott and Brooks (1997*b*) derived an analytical solution to describe the increase of the effective mean mixing depth (*D*) of a solute as a function of time (*t*) after the initial appearance of the solute in the bottom water Equation 5.8.

Elliott's Model

$$D = \frac{1}{k} \ln \left(0.42 \frac{k^2 K h_m t}{\theta} + 1 \right) \quad (5.8)$$

Where *K* and θ are the measured hydraulic conductivity (in m/s) and porosity, respectively, and *k* is the wave number ($k = 2\pi/\lambda$) of the ripple length (λ in m). A dynamic

hydraulic head (h_m) of 4×10^{-4} m was calculated from measured mean bottom water currents (20 cm/s) and assumed ripple dimensions (height: 2 cm; length: 13 cm; similar to observations made during a subsequent cruise in the same region) using the empirical expression in Elliott and Brooks (1997b).

The effective mean mixing depth (D) is a parameter based on the residence time function, which includes both, the vertical and horizontal velocity components of porewater flow (see also Elliott and Brooks, 1997b). 2-dimensional flow patterns as described in many publications (see also Huettel et al., 1996; Thibodeaux and Boyle, 1987) are thus the basis of the model and are therefore fully considered in our calculation. This is reflected by the non-linear relation between effective mean mixing depth and time in Equation 5.8.

In detail, the effective mean mixing depth of O_2 was determined as follows: the time of O_2 depletion from bottom water entering the pore space was calculated from the initial O_2 concentration in the bottom water divided by the O_2 consumption rate per volume porewater assuming zero order kinetics. Thereafter the time of depletion was inserted into Equation 5.8 to estimate the effective mean mixing depth of O_2 . The effective mean mixing depth of NO_3^- was calculated in a similar way. Here, the volumetric rates of nitrification, denitrification and DNRA and their dependence on O_2 concentrations were considered to calculate the time of NO_3^- depletion and the NO_3^- mixing depth. To estimate areal rates, the rates per volume sediment were integrated over the mixing depth of the limiting substrate, i.e. O_2 consumption, nitrification, oxic denitrification and oxic DNRA were integrated down to the O_2 penetration depth, and anoxic denitrification and anoxic DNRA were integrated from below the oxycline down to the NO_3^- penetration depth.

In order to validate the Elliott model, oxygen fluxes and areal N-loss rates from the lower permeability station were compared to a two-dimensional numerical model which includes dispersion, diffusion, and a pressure distribution along a true bedform topography derived from Large-Eddy-Simulations (Ahmerkamp et al., 2015). Volumetric nitrification rates as well as aerobic and anaerobic denitrification rates were added to the transport reaction equations in the Ahmerkamp model and a monod kinetic was assumed for each, where the half saturation co-efficient was kept constant at 1/8 of the bottom water concentration of the respective solutes.

5.3 Results

5.3.1 Sediment characteristics and volumetric oxygen consumption rates

Experiments were carried out at three stations in the German Bight (Table 5.2); all three sites consisted of permeable sands which had significant differences in permeability, grain

size and porosity (Table 5.3). Station 1 had the lowest permeability and was comprised of well sorted medium sand (Figure A.5.7), hereafter it is referred to as the lower permeability station. Station 2 had higher permeability was comprised of moderately well sorted coarse sand, although it had an additional fine sand fraction leading to a fine skew. It is hereafter referred to as the intermediate permeability station. Station 3 had the highest permeability, and was comprised of moderately well sorted medium sand, however there was a coarse skew towards coarse grained sand which would have been greater if an additional fraction of shell fragments and gravel ($> 2\text{mm}$) had not been removed before analysis on the particle counter. This station is hereafter referred to as the higher permeability station. Total volumetric oxygen consumption rates differed significantly between each station ($p < 0.001$) (Figure 5.1). The highest rates (as calculated from the slope of the initial decrease in oxygen) were observed at the intermediate permeability station (268.5 ± 36.5 S.D. $\text{mmol m}^{-3}_{\text{sediment h}^{-1}}$), followed by the lower permeability station (149.2 ± 41.5 S.D. $\text{mmol m}^{-3}_{\text{sediment h}^{-1}}$), the lowest oxygen consumption rates were observed at the higher permeability station (60.2 ± 16.5 S.D. $\text{mmol m}^{-3}_{\text{sediment h}^{-1}}$).

| Site | Lat. N | Long. E | Depth (m) | Bottom water temp. ($^{\circ}\text{C}$) | Air temp. ($^{\circ}\text{C}$) | Salinity | Bottom water NO_3^- (μM) |
|------|------------|-----------|-----------|---|----------------------------------|----------|--|
| 1 | 54° 10,16' | 7° 59,70' | 21.0 | 12.9 | 14.1 | 32.1 | 6 |
| 2 | 54° 10,55' | 7° 57,24' | 23.3 | 13.2 | 12.8 | 31.5 | 8 |
| 3 | 54° 14,36' | 7° 51,31' | 18.4 | 12.8 | 12.6 | 32.0 | 7 |

Table 5.2: Station locations within the German Bight and water characteristics.

| Site | Porosity ($\pm\text{SD}$) | Mode/geometric mean (μm) | Sorting (σ) | Skewness (sk) | Permeability ($\pm\text{SD}$) (10^{-11}m^2) | Sediment type |
|------|-----------------------------------|---------------------------------------|----------------------|---------------|---|------------------------------------|
| 1 | 0.36 (± 0.002) | 430/440 | 1.37 | -0.02 | 2.16 (± 0.08) [†] | Well sorted medium sand |
| 2 | 0.40 (± 0.005) [*] | 568/579 | 1.51 | -0.12 | 4.09 (± 0.47) [†] | Moderately well sorted coarse sand |
| 3 | 0.36 (± 0.001) | 430/494 | 1.57 | 0.284 | 6.47 (± 0.23) [†] | Moderately well sorted coarse sand |

*Denotes that value is significantly different from other stations in pairwise comparisons (p -value < 0.05 (one-way anova)).

[†]Denotes that value is significantly different from other stations in pairwise comparisons (p -value < 0.05 (one-way anova)).

Table 5.3: Sediment characteristics.

5.3.2 Ammonia oxidation

Production of $^{15}\text{NO}_2^-$ in the presence of oxygen indicated that ammonia oxidation occurred at all three stations ($^{15}\text{NH}_4^+ + ^{14}\text{NO}_x\text{exp.}$); Figure A.5.8; Table A.5.5). Volumetric ammonia oxidation rates differed significantly between the stations ($p = 0.004$) were highest at the lower permeability station and lowest at the intermediate permeability station (Figure 5.2 a).

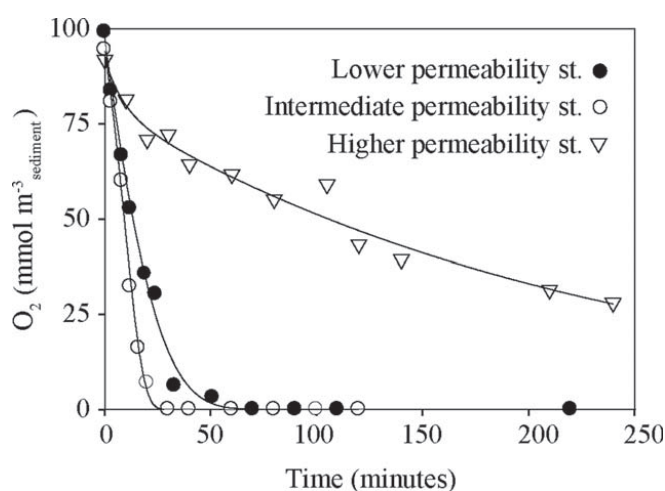


Figure 5.1: Examples of oxygen consumption profiles measured during the $^{15}\text{NH}_4^+$ addition experiment at all three stations.

5.3.3 Nitrite oxidation

In the presence of oxygen, production of $^{15}\text{NO}_3^-$ occurred after addition of $^{15}\text{NO}_2^-$ all 3 stations ($^{15}\text{NO}_2^-$ exp; Figure A.5.8; Table A.5.5). Volumetric nitrite oxidation rates calculated from the $^{15}\text{NO}_3^-$ production decreased from the lower permeability station to the higher permeability station; however there was no significant difference between the stations. Volumetric nitrate oxidation rates were always higher than ammonia oxidation rates, significantly so at the intermediate and higher permeability stations ($p < 0.002$) (Figure 5.2 a) and there was a weak but significant positive correlation between the two processes ($r^2 = 0.48$ $p = 0.04$).

5.3.4 Denitrification, anammox and DNRA

Dissimilatory nitrate reduction processes were determined after the addition of $^{15}\text{NO}_3^-$. $^{29+30}\text{N}_2$ production occurred at all 3 stations even when oxygen was present ($^{15}\text{NO}_3^-$ exp. Figure S2; Table A.5.5). This was determined to be a result of denitrification, as there was no conclusive evidence of anammox in any experiment (SI text). At the lower and higher permeability station, volumetric denitrification rates increased when the sediment became anoxic (Figure 5.2 b). At the intermediate permeability station, oxic denitrification rates were high in contrast to the other stations and upon anoxia the denitrification rate did not increase. As a consequence of the high oxic denitrification rates at the intermediate permeability station, NO_3^- concentrations were already low when the sediment became anoxic ($\sim 10 \mu\text{mol L}^{-1}$) and dropped to below detection limit by the time the incubations were terminated. Therefore we assume that anoxic denitrification rates were most likely

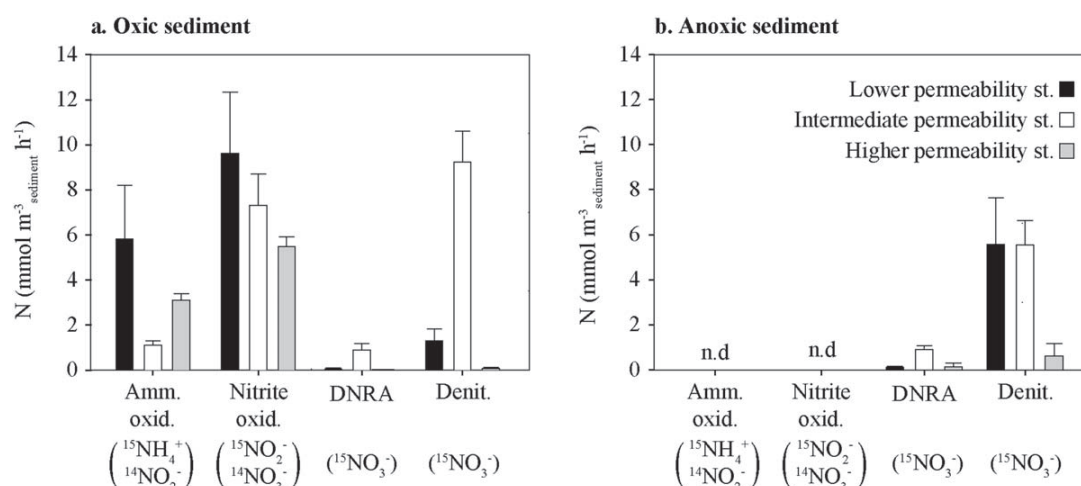


Figure 5.2: Volumetric rates of nitrogen cycling processes at all three stations, determined from the **a** oxic and **b** anoxic phase of the incubation. Substrate additions are shown in brackets in the axis legend, for further details see table 1. Error bars are SD, $n = 3$ ($n=2$ at Station 3, $^{15}\text{NO}_3^-$ addition experiment) n.d. = not detected.

substrate limited and thus underestimated. Hence when comparing oxygen consumption rates and denitrification rates we used the anoxic denitrification rates from the higher and lowest permeability stations and oxic rates from the intermediate permeability station. When these denitrification rates were compared to the OCR, there was a significant positive correlation ($p = 0.002$ $r^2 = 0.83$ (Figure 5.3).

In the $^{15}\text{NO}_3^-$ addition experiment the production of $^{15}\text{NH}_4^+$ was also observed at all three stations, indicative of DNRA ($^{15}\text{NO}_3^-$ exp; Figure S2). Volumetric DNRA rates were low compared to denitrification ($< 20\%$) but generally showed similar trends (Figure 2). Similar to denitrification rates, DNRA rates were positively correlated to oxygen consumption rates (Figure A.5.9).

5.3.5 Coupled nitrification-denitrification

$86 \mu\text{mol L}^{-1}$ allylthiourea (ATU) was added to one set of incubations with the intention of inhibiting nitrification ($^{15}\text{NH}_4^+$ + ATU exp.). However, in this experiment, nitrification still occurred and instead, coupled nitrification-denitrification was observed. $^{15}\text{NH}_4^+$ was sequentially oxidized to $^{15}\text{NO}_2^-$ then $^{15}\text{NO}_3^-$, and $^{29+30}\text{N}_2$ production began almost immediately (Figure 4). The sum of all ^{15}N labeled products ($^{15}\text{NO}_2^-$, $^{15}\text{NO}_3^-$, $^{29+30}\text{N}_2$) increased constantly over the first 60 minutes of the incubation, until O_2 was depleted. At this point $^{15}\text{NO}_2^-$ and $^{15}\text{NO}_3^-$ concentrations decreased, while $^{15}\text{N}-\text{N}_2$ concentrations continued to increase. The successive increase and decrease of $^{15}\text{NO}_x$ coupled to the continuous increase of $^{15}\text{N} - \text{N}_2$ (Figure 5.4 **a** and Figure A.5.10) indicate close coupling

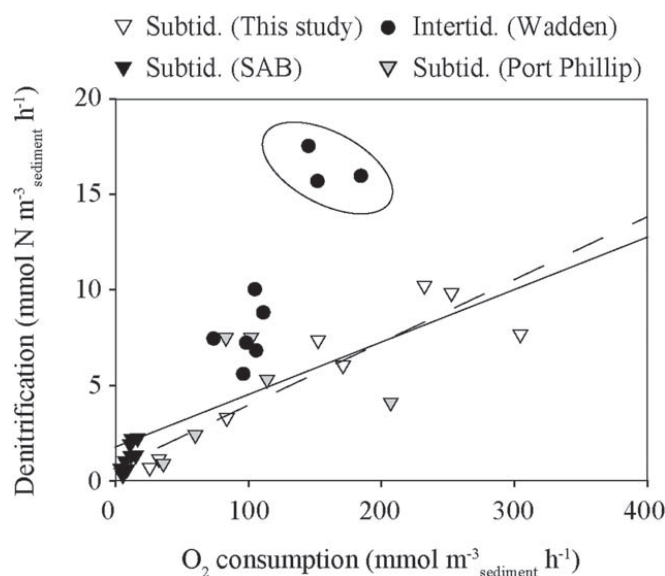


Figure 5.3: The correlation between oxygen consumption rates and denitrification rates in a variety of permeable sediments. The dashed line represents the correlation of rates from this study (Total OCR was used) ($p = 0.002$ $r^2 = 0.83$). The solid line represents of the correlation of all points ($p = <0.001$ $r^2 = 0.37$), excluding the three circled points which represent rates measured during winter in the Wadden Sea, when nitrate concentrations in the water column were on average $70 \mu\text{mol L}^{-1}$; which is significantly higher than that at the other time points and locations. The subtidal data from the SAB (South Atlantic Bight) are taken from (Rao et al., 2008), subtidal (Port Phillip) refers to the data in (Evrard et al., 2013) and the intertidal (Wadden) is from (Marchant et al., 2014).

of nitrification and denitrification. Coupled nitrification-denitrification also appeared to be occurring in the $^{15}\text{NO}_3^-$ addition experiment. Here the labeling percentage of NO_3^- ($\text{F}^{15}\text{NO}_3^-*$) dropped by $27 (\pm 1\text{SD}) \%$ at Station 1 during the oxic part of the incubation, suggesting that the $^{15}\text{NO}_3^-$ pool added at the start of the incubation was constantly diluted by the production of $^{14}\text{NO}_3^-$ via nitrification.

5.3.6 Nitrous oxide (N_2O) production

$^{15}\text{N} - \text{N}_2\text{O}$ formation occurred at all three stations in both the $^{15}\text{NH}_4^+$ addition and the $^{15}\text{NO}_3^-$ addition experiments ($^{15}\text{NH}_4^+ + ^{14}\text{NO}_x$ exp.; $^{15}\text{NO}_3^-$ exp. respectively; Figure S2). In the $^{15}\text{NO}_3^-$ addition experiment, the production of $^{45+46}\text{N}_2\text{O}$ occurred both in the presence and absence of oxygen at the lower and higher permeability stations. There was no difference between volumetric oxic and anoxic N_2O production rates at the higher permeability station ($p = 0.5$), whereas at the lower permeability station N_2O production rates were significantly higher under oxic conditions ($p = 0.05$) (Figure 5.5). At the intermediate permeability station, N_2O was only produced under oxic conditions. Despite

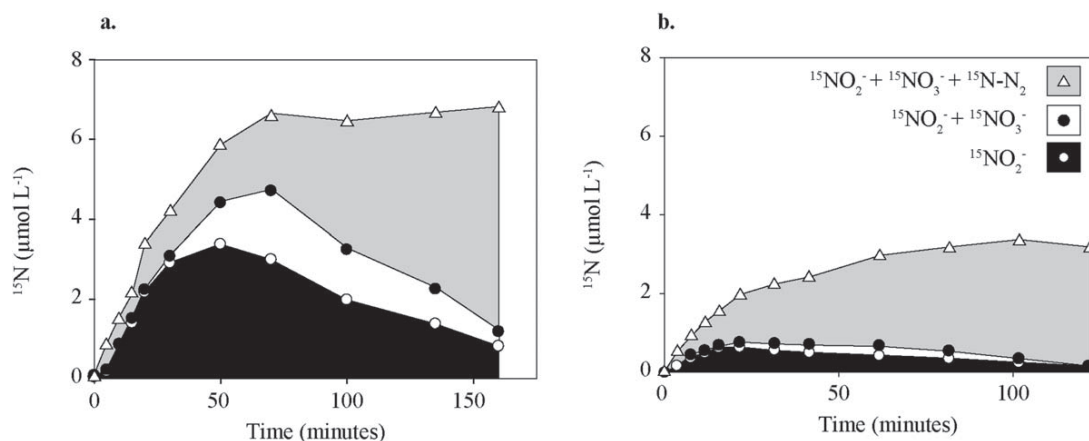


Figure 5.4: Evidence for coupled nitrification-denitrification. Stacked area plot of the production of ^{15}N -labeled after $^{15}\text{NH}_4^+$ and ATU addition. **a** Example from the lower permeability station **b** Example from the intermediate permeability station.

these differences, the ratio of produced $\text{N}_2\text{O}:\text{N}_2$ was always significantly higher during the oxic part of the incubations ($p = 0.002$) (Figure 5.5 **b**), this resulted from either higher oxic N_2O production rates and/or lower oxic denitrification rates in comparison to anoxic rates. There was little to no net N_2O consumption observed at any point in the $^{15}\text{NO}_3^-$ addition experiments at the lower and higher permeability stations, whereas at the intermediate permeability station (where we observed comparatively high oxic denitrification rates), N_2O was produced rapidly at the beginning of the incubation and consumed when the sediment became anoxic and nitrate was depleted ($^{15}\text{NO}_3^-$ exp- N_2O ; Figure A.5.8).

5.3.7 O_2 and NO_3^- penetration depths and areal rate estimates

To integrate volumetric rates into areal rates, the transport model of (Elliott and Brooks, 1997*b,a*) was applied. To determine nitrate and oxygen concentrations within the sediment along a flow path, we combined the volumetric nitrification rates from the $^{15}\text{NH}_4^+ + ^{14}\text{NO}_x$ amendment exp. with the oxygen consumption, denitrification and DNRA rates from the $^{15}\text{NO}_3^-$ amendment experiments. Two different scenarios were identified by combining the rate measurements with the bottom water nitrate concentration, one for the lower and higher permeability station and one for intermediate permeability station (upper panels; Figure A.5.8). At the lower and higher permeability stations, under oxic conditions, the production of nitrate via nitrification exceeded nitrate removal by denitrification and DNRA. Therefore, while oxygen was present, nitrate concentrations increased within the sediment. When oxygen concentrations reached zero, nitrate concentrations had increased from 6 and $7 \mu\text{mol L}^{-1}$ (bottom water concentration) to 8.9 and $11.8 \mu\text{mol L}^{-1}$ for the lower and higher permeability station respectively. When oxygen was entirely consumed, the rates of

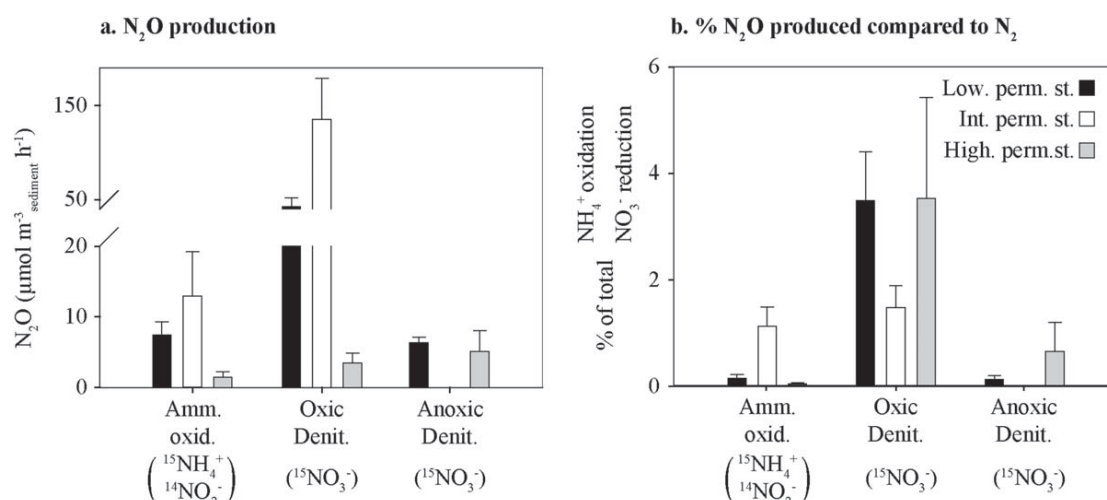


Figure 5.5: N₂O formation **a** Rates of N₂O formation from ammonia oxidation and denitrification **b** N₂O formation rates compared to total ammonia oxidation and denitrification rates. Substrate additions are shown in brackets in the axis legend, for further details see table 1. Error bars are SD, n = 3 apart from anoxic rates at the high permeability station in the ¹⁵NO₃⁻ addition experiment, where n = 2

denitrification and DNRA increased and prevailed until nitrate was entirely respired. At the intermediate permeability station while the sediment was oxic the respiration of nitrate by denitrification and DNRA exceeded the production of nitrate by nitrification. Therefore by the time that oxygen concentration reached zero, nitrate concentration had decreased from 8 μmol L⁻¹ (bottom water concentration) to 4.4 μmol L⁻¹.

The effective mixing depths as calculated from the model were 7.5 and 12.2 mm for the lower permeability station, 7.7 and 11.1 mm for the intermediate permeability station, and 30 and 52 mm for the higher permeability station, for O₂ and NO₃⁻ respectively (Figure A.5.8; middle panels). These effective mean mixing depths were used to integrate volumetric rates of oxygen respiration, nitrification, denitrification and DNRA over specific depth layers. From this integration we derived areal rates of denitrification, nitrification, DNRA and oxygen respiration for all 3 stations (Table 5.4).

| | Oxygen consumption | Nitrification | Denitrification | DNRA |
|------------------|---|---------------|-----------------|--------------|
| | (mmol m ⁻² d ⁻¹ ± SD) | | | |
| Lower perm. st. | 26.3 ± 1.3 | 1.15 ± 0.7 | 0.87 ± 0.1 | 0.02 ± 0.005 |
| Int. perm. st. | 49.6 ± 1.0 | 0.21 ± 0.05 | 2.28 ± 0.3 | 0.25 ± 0.05 |
| Higher perm. st. | 33.7 ± 2.1 | 2.98 ± 0.42 | 0.52 ± 0.03 | 0.11 ± 0.06 |
| p-value* | <0.001 | 0.006 | <0.001 | 0.013 |

*One way ANOVA.

Table 5.4: Mean areal oxygen and N-cycling rates in three permeable sediments in the German Bight determined using the Elliot and Brooks model.

The oxygen fluxes and areal N-loss rates predicted by the Elliott model were compared to a two-dimensional numerical model from (Ahmerkamp et al., 2015). For a parameterization based on the lower permeability station, the Elliott model was highly accurate and underestimates fluxes by only up to 10% for bottom water velocities ranging from 0.05 m s^{-1} to 0.5 m s^{-1} . For example, using a bottom water velocity of 0.2 m s^{-1} (as in the Elliott model) the Ahmerkamp model gave an areal O_2 flux of $28.1 \text{ mmol m}^{-2} \text{ d}^{-1}$ and an areal N-loss rate of $0.95 \text{ mmol m}^{-2} \text{ d}^{-1}$.

5.4 Discussion

5.4.1 N-loss in highly permeable sediments

Subtidal coastal sediments are often sites of anthropogenically induced eutrophication and as such, it is important to understand how they might remove or recycle anthropogenic N-inputs. In temperate coastal waters, nitrate concentrations are generally low in periods when primary production is high (van Beusekom, 2005) and consequently sedimentary nitrification could be an essential but so far understudied source of nitrate for denitrification. Here, we investigated three sediments which have permeabilities representative of the sands which cover approximately 60% of the German Bight (Janssen et al., 2005). By comparing these results to the growing number of observations in diverse other permeable sandy sediments, it is now becoming possible to recognise shared traits between them.

We found that anoxic denitrification was the major N-loss pathway within the highly permeable subtidal German Bight sediments (Figure 5.2). This is in line with other studies of sandy sediments, whether they be from subtidal regions with lower permeability (Rao et al., 2008) or from intertidal regions (Gao et al., 2012; Marchant et al., 2014). Despite all three sediments studied here being highly permeable, the variation in volumetric oxygen consumption rates (OCR) and denitrification rates between stations was greater than the variation between replicates from the same station (Table A.5.5). This suggests that differences in permeability, even at values above 10^{-11} m^2 have an effect on biogeochemical processes.

There was a strong correlation between OCR and denitrification (Figure 5.3). This correlation is not surprising as OCR is a robust proxy for the amount of labile organic matter in sediments (Glud, 2008). When volumetric denitrification rate data from studies on different permeable sediments - subtidal, intertidal, eutrophic and oligotrophic - are taken together, the strong positive correlation between volumetric OCR and denitrification rates persists (Figure 5.3); clearly indicating that denitrification potential is controlled by organic matter availability. This suggests that the differences in denitrification observed previously

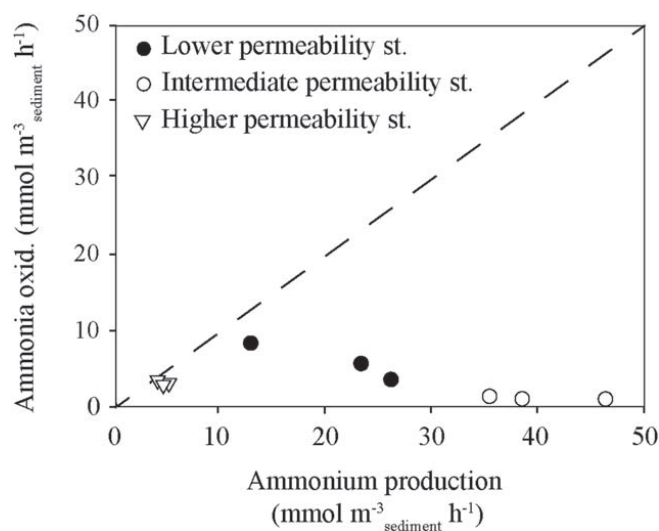


Figure 5.6: Ammonium available to support ammonia oxidation. Ammonium production within the sediment was calculated from the aerobic remineralization of organic matter by oxygen respiration. The dashed line represents the maximum rate of ammonia oxidation that could be supported by the NH_4^+ produced within the sediment. As all points fall below the line, enough ammonium would have been available to support the measured rates at all stations.

between intertidal and subtidal sandy sediments are not related to the tidal regime itself, but rather to the availability of labile organic matter within the sediment. Intriguingly, when water column nitrate concentrations and OCR are both high, denitrification rates increase more steeply (circled points, Figure 5.3), indicating that nitrate concentrations are a secondary controller of denitrification in permeable sediments. These relationships between volumetric OCR, nitrate and denitrification rates may allow better prediction of denitrification rates in sandy sediments. Generally increases in permeability are observed to lead to higher rates (Huettel et al., 2014); however this trend might not persist at very high permeabilities, as indicated by the comparatively low rates we observed at the most permeable station.

The average ratio between OCR and denitrification in our study is about 0.03 and well in line with previous results (Gao et al., 2010; Evrard et al., 2013; Marchant et al., 2014; Rao et al., 2008). This suggests that the relative contribution of denitrification to carbon remineralization is lower in permeable sediments than in cohesive sediments that are generally dominated by sulfate reduction (Jørgensen, 1982; Thamdrup and Canfield, 1996). While the overall denitrification rates were inefficient relative to oxygen consumption, they were generally higher than those in cohesive sediments, and as such seem to be more important for nitrate removal in coastal environments.

Anammox can significantly contribute to N-loss from sediments with low organic

carbon content (Sokoll et al., 2012; Song et al., 2013; Thamdrup and Dalsgaard, 2002), however our combined results from the $^{15}\text{NH}_4^+$ + acetylene exp. and the $^{15}\text{NO}_3^-$ labeling exp. indicate that anammox was not substantial (see SI text for further details). The predominance of denitrification over anammox in sandy sediments from many differing locations (Canion et al., 2014) likely results from the enhanced supply of organic matter by advection and the highly fluctuating oxygen conditions, both of which would favour denitrification.

DNRA also occurred in all 3 of the sediments; however it made up a relatively small proportion of the total volumetric NO_3^- reduction (DNRA + Denitrification); accounting for 2, 10 and 17%, for the lower, intermediate and higher permeability station, respectively. This is similar to the contribution of DNRA in intertidal permeable sediments (Marchant et al., 2014), but lower than in temperate diffusive sediments (An and Gardner, 2002; Jäntti and Hietanen, 2012; Koop-Jakobsen et al., 2010; Trimmer and Nicholls, 2009). There also seems to be a correlation between OCR and DNRA in permeable sediments, although it is not as strong as that between OCR and denitrification (Figure A.5.9). So far, this relationship has only been investigated in temperate, eutrophied sands. It remains to be seen whether similar background levels of DNRA are found in all permeable sediments, or whether differences in organic matter loading, nitrate concentrations and temperature affect the ratio of DNRA to denitrification in other permeable sediments.

5.4.2 Ammonia oxidation

We observed oxic ammonia oxidation occurring within the sediment at all three stations both with (Figure 5.4) and without (Figure 5.2 **b**) addition of allylthiourea (ATU). ATU should have inhibited ammonia oxidation (Ginestet et al., 1998), however only halved the rates. Similar observations of incomplete inhibition by ATU have been made previously and might be attributed to the presence of ammonia oxidizing Archaea (Santoro and Casciotti, 2011; Santoro et al., 2010), although we have no direct evidence this was the case in our study.

To date, ammonia oxidation has only been measured under advective conditions in permeable sediments from intertidal regions, where volumetric rates were an order of magnitude lower than those measured here (Marchant et al., 2014). However, ammonia oxidation measurements have been made in sandy sediments under diffusive conditions (see Blackburn and Henriksen, 1983; Ward, 2008, and references therein) and the rates from this study are in the upper range of those.

A modeling study has predicted that advection in permeable sediments might reduce the potential for benthic nitrification (Kessler et al., 2013). Kessler et al. (2013) hypothesized

that advective porewater flow would limit the ammonium available to ammonia oxidizers, as ammonium produced in anoxic sediments would be returned directly to the water column rather than be made available to supply ammonia oxidation. Comparison of the amount of ammonium produced in situ by aerobic remineralization (calculated from OCR) and the volumetric ammonia oxidation rates indicated that enough ammonium would have been released to support our observed rates (Figure 5.6). In addition to this, the occurrence of both DNRA and denitrification in the presence of oxygen would have provided further sources of ammonium. This indicates that previous reports of ammonia oxidation in sandy sediments made under diffusive conditions are more likely to be an underestimation than an overestimation, as advective flows increase oxygen availability and oxygen penetration depths, both of which enhance the potential for nitrification (Gihring et al., 2010; Jensen et al., 1994, 1996; Lohse et al., 1993).

It is interesting to note that of the two sets of ammonia oxidation rate measurements made so far under advective conditions in permeable sands, no generalizations can be made. Volumetric nitrification rates at a nearby intertidal location are consistently an order of magnitude lower than denitrification rates (Marchant et al., 2014), whereas in this study they were in the same range. Furthermore, in this study volumetric ammonia oxidation rates differed between each station, yet unlike denitrification did not correlate strongly with OCR (even though OCR could be described as a proxy for the amount of ammonia made available to support ammonia oxidation). Instead at the intermediate permeability station, where the highest OCR occurred, we observed the lowest ammonia oxidation rates. Therefore it appears that some other factor controls the potential for ammonia oxidation in permeable sediments – possibly competition for ammonia or other resources, such as surface area available for microbial colonization (Belser, 1979) or oxygen availability (Henriksen et al., 1993).

5.4.3 Nitrite oxidation

Ammonia oxidation is generally considered as the rate limiting step for nitrification (e.g. Ward, 2005) and the oxidation of nitrite as a separate process is often neglected. Our volumetric nitrite oxidation rates can currently only be considered as potential rates, as it is difficult to determine the robustness of the method we used due to the scarcity of previous measurements. It is possible that we underestimated the rates, as the co-occurrence of nitrate reduction (due to denitrification in the presence of oxygen) and ammonia oxidation during nitrite oxidation would have diluted the $^{15}\text{NO}_2^-$ pool with $^{14}\text{NO}_2^-$ and, thus, lowered $^{15}\text{NO}_3^-$ production. We added high starting concentrations of $^{15}\text{NO}_2^-$ ($100 \mu\text{mol L}^{-1}$) to minimize the influence of such dilutions. This addition may have stimulated

nitrite oxidation, in which case the nitrite oxidation rates would be overestimated. However, no evidence of stimulation of nitrite oxidation by the addition of NO_2^- has been observed previously in incubation experiments (Clark et al., 2008; Olson, 1981). Our volumetric nitrite oxidation rates were consistently higher than ammonia oxidation rates, assuming that nitrite oxidation was not stimulated by the nitrite additions, this could suggest that the two processes were partly uncoupled in these sediments. A similar uncoupling of the two processes has been observed in suboxic ocean waters where nitrite oxidation and nitrate reduction co-occur (Füssel et al., 2011; Isobe et al., 2012).

5.4.4 N_2O production

Until recently subtidal permeable sediments were not assumed to be hotspots of nitrogen cycling and therefore they were rarely considered as a source of N_2O . While N_2O oversaturations have been measured frequently in the water column throughout the North Sea (Law and Owens, 1990), they are generally attributed to water column nitrification. We observed significant $^{15}\text{N}_2\text{O}$ formation in the $^{15}\text{NH}_4^+ + ^{14}\text{NO}_x$ labeling experiment when oxygen was present and therefore concluded that oxic ammonia oxidation was the source. In the $^{15}\text{NO}_3^-$ experiment, $^{45+46}\text{N}_2\text{O}$ were produced both in the presence and absence of oxygen, indicating N_2O production from oxic and anoxic denitrification (Figure 5.5 a). The patterns of N_2O formation during denitrification observed at the lower and higher permeability stations are very similar to those in intertidal sandy sediments (unpublished data). i.e. the ratio between N_2O and N_2 production was always higher during the oxic part of the incubation (Figure 5.5 b) and net N_2O consumption did not occur until nitrate became limiting (Figure A.5.8).

5.4.5 Coupled nitrification-denitrification

Coupled nitrification-denitrification is present in many diffusively dominated sediments, where it is separated spatially due to the occurrence of nitrification in upper oxic sediment layers and denitrification in lower anoxic layers (Jenkins and Kemp, 1984). In these cases the extent of coupling is determined by the size of the nitrification zone and the diffusive transport of nitrate from the oxic layer to the deeper anoxic layer (for example as much as two thirds of nitrate diffuses upwards into the water column (Meyer et al., 2008). However, in permeable sediments, denitrification in the presence of oxygen as well as the advective transport of porewater within the sediment should allow much closer spatial and temporal coupling of the two processes.

Here we observed very closely coupled nitrification-denitrification. When $^{15}\text{NH}_4^+$ was added to permeable sediments from the German Bight ($^{15}\text{NH}_4^+ + \text{ATU}$ exp.), we observed

a temporal overlap in nitrification and denitrification (Figure 5.4 and Figure A.5.10). In fact upon addition of $^{15}\text{NH}_4^+$, the production of $^{15}\text{N} - \text{N}_2$ by denitrification began almost concurrently with ammonia oxidation and nitrite oxidation. Between one and two thirds of the $^{15}\text{NH}_4^+$ in the $^{15}\text{NH}_4^+$ + ATU amendment experiment was already nitrified and subsequently denitrified before oxygen had been consumed. This indicates very close spatial coupling of nitrification and denitrification in the permeable sediments when they were oxic. Furthermore, as porewater ages and becomes anoxic on short time scales in the German Bight, temporal coupling between nitrification under oxic conditions and denitrification under anoxic conditions will also occur without the need for diffusive flux of nitrate. The combination of such closely coupled nitrification-denitrification and high nitrification rates means that this process has the potential to be a major path of N-loss in the German Bight, most likely leading to higher N-losses than previously estimated from nitrate fluxes alone.

5.4.6 Coupled nitrification-denitrification and areal N-cycling rates

To estimate the impact of nitrification, denitrification, DNRA and the coupling between the processes on N-loss within the German Bight, it is necessary to upscale volumetric rates and examine areal rates. Generally in diffusive sediments, rates are integrated over the penetration depth of the appropriate solutes (e.g. oxygen in the case of nitrification, nitrate in the case of denitrification), which are determined from concentration profiles within the sediment. However in permeable sediments, advection plays a crucial role - flow paths of porewater start and end at the water-sediment-interface and are of different lengths. Therefore the penetration depth is a nonlinear function of time (Elliott and Brooks, 1997b), which can be determined by modeling.

Using the approach of Elliott and Brooks (1997b) we calculated mean effective mixing depths for both O_2 and NO_3^- for all three stations. Oxygen penetrated into the sediment 7.5, 7.7 and 30 mm at the lower, intermediate and higher permeability stations respectively (Figure A.5.11). Such O_2 penetration depths are realistic in comparison to in situ measurements made during a subsequent cruise to the same region, providing validation of the model. However, areal rates are potentially underestimated when calculating effective mean mixing depths using advection as transport by molecular diffusion and porewater dispersion is neglected. Despite this, areal oxygen consumption rates calculated from the model were in the same range as those measured in situ previously using an autonomous benthic chamber with controlled advective porewater exchange (Janssen et al., 2005). Furthermore, while the areal nitrification rates spanned a large range (Table 5.3), they are of the same magnitude as previous areal nitrification estimates from continental shelf

sediments e.g. $2.8 \text{ mmol m}^{-2} \text{ d}^{-1}$ (Laursen and Seitzinger, 2002).

At all stations nitrate penetrated deeper than oxygen, to 12.2, 11.1 and 53 mm respectively, therefore there was a layer of between 4 and 23 mm in which denitrification and DNRA could occur at their maximal rate. Here the important influence of coupled nitrification-denitrification within the sediment becomes apparent. Nitrification rates at the lower and higher permeability station exceeded oxic denitrification and DNRA rates, which meant that by the time the sediment became anoxic, nitrate concentrations were almost 1.5 times higher than the initial bottom water concentrations. This highlights the role that nitrification plays in sustaining N-loss in these sediments, as when bottom water concentrations of nitrate are low within the German Bight, e.g. in July when this study was carried out, extensive N-loss can still occur.

Nitrate concentrations are at their lowest in the German Bight during summer. In almost all other seasons, nitrate concentrations are higher than the $6 - 8 \mu\text{mol L}^{-1}$ measured in this study. This would have a number of consequences; firstly N-loss would increase. For example, increasing the bottom water nitrate concentration in the model to $35 \mu\text{mol L}^{-1}$ (a typical January concentration for this area (Dähnke et al., 2010) would lead to a doubling in N-loss to $110 \mu\text{mol N m}^{-2} \text{ h}^{-1}$. Secondly, the impact of coupled nitrification-denitrification would be less pronounced, in the same winter scenario, only 45 % of the nitrate required could be supplied by nitrification. Furthermore, as we did not sample in a prominent bloom or riverine run-off influenced season, organic matter (OM) concentrations were also likely to be comparatively low. Increases in organic matter concentrations would increase volumetric oxygen consumption and denitrification rates (see N-loss section), which has the effect of decreasing penetration depths calculated by the model, but still leading to higher areal N-loss rates.

It is therefore apparent that the highly permeable sediments we studied here have the potential to remove a significant amount of the atmospheric deposition and riverine fluxes of N to the German Bight. The important role of benthic nitrification in these sediments, which is closely coupled both spatially and temporally to denitrification means that significantly greater N-losses occur than would be expected from nitrate fluxes alone, especially in the periods of high primary production where nitrate concentrations are low. We can conclude therefore that the highly permeable subtidal sediments of the German Bight should also be considered as hotspots of N-cycling. Considering the strong relationship that is starting to emerge between OCR and volumetric denitrification rates in sandy sediments, it is becoming apparent that they likely provide a large sink for N that seems to be proportional to the increased inputs of nitrate and organic matter resulting from anthropogenic activity.

Acknowledgements

We sincerely thank cruise leader Thomas Lüdman as well as the captain and crew of the R.V. Heincke (HE-383). We are grateful to Gabi Klockgether and Sarah Kuschnerow for technical assistance. We also thank Felix Janssen with whom discussion helped improve the manuscript. Furthermore we thank two anonymous reviewers whose comments greatly improved the manuscript. This work was financially supported by the Max Planck Society and the DFG-Research Center/Cluster of Excellence “The Ocean in the Earth System” at the University of Bremen.

5.5 Supplementary information

5.5.1 Detecting anammox using multiple lines of investigation

We investigated possible $^{15}\text{N} - \text{N}_2$ production from anammox in three types of incubation. The addition of 10 Pa acetylene should block ammonia oxidation but only partially inhibit anammox (Jensen et al. 2007). Therefore in the $^{15}\text{NH}_4^+$ + acet. experiment, the production of $^{29}\text{N}_2$ would have indicated anammox. However we observed no production of any ^{15}N -labeled compound, including N_2O (results not shown). Nevertheless, it is possible that the acetylene may have entirely blocked anammox activity therefore this result is not entirely conclusive. To further test whether anammox was occurring, sediment from the low and intermediate permeability stations was incubated with $^{15}\text{NH}_4^+$ and allylthiourea (ATU), after which $^{29}\text{N}_2$ production was measured ($^{15}\text{NH}_4^+$ + ATU exp.) The ability to detect anammox using this incubation relies on the assumption that nitrification is inhibited by ATU. In the case that nitrification is not inhibited, $^{15}\text{NH}_4^+$ is oxidized to $^{15}\text{NO}_3^-$ at which point denitrification can also produce $^{29}\text{N}_2$ and $^{30}\text{N}_2$. We added $86 \mu\text{molL}^{-1}$ ATU, to block bacterial ammonia oxidation, however aerobic ammonia oxidation still occurred, therefore we were unable to use this incubation to determine anammox. As the anammox experiment with ATU was inconclusive, the $^{15}\text{NO}_3^-$ addition exp. was analyzed for indicators of anammox, and indicated that anammox was not a significant process within these sediments. In the $^{15}\text{NO}_3^-$ addition exp. $^{29}\text{N}_2$ and $^{30}\text{N}_2$ were produced, which we attributed to denitrification. However, part of the $^{29}\text{N}_2$ pool could also have been produced by anammox. To investigate whether this was the case we compared the labeling percentage ($F^{15}\text{NO}_3^-*$) (eq. 1) based on the produced $^{29}\text{N}_2$ and $^{30}\text{N}_2$ at each time point with the labeling percentage ($F^{15}\text{NO}_3^-$) (eq. 2) from substrate measurements. There was no difference between these two values; therefore providing no evidence that anammox occurred. Furthermore, in the $^{15}\text{NH}_4^+$ addition exp. (designed to determine ammonia oxidation rates), the presence of anammox would have been indicated by a decrease

of $^{15}\text{NH}_4^+$ concentrations under anoxic conditions, this was not the case. Therefore we concluded that anammox was not a significant process within these.

5.5.2 Additional Figures

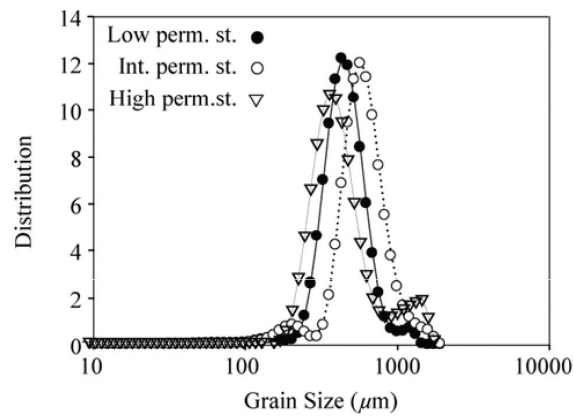


Figure A.5.7: Grain size distribution from each station.

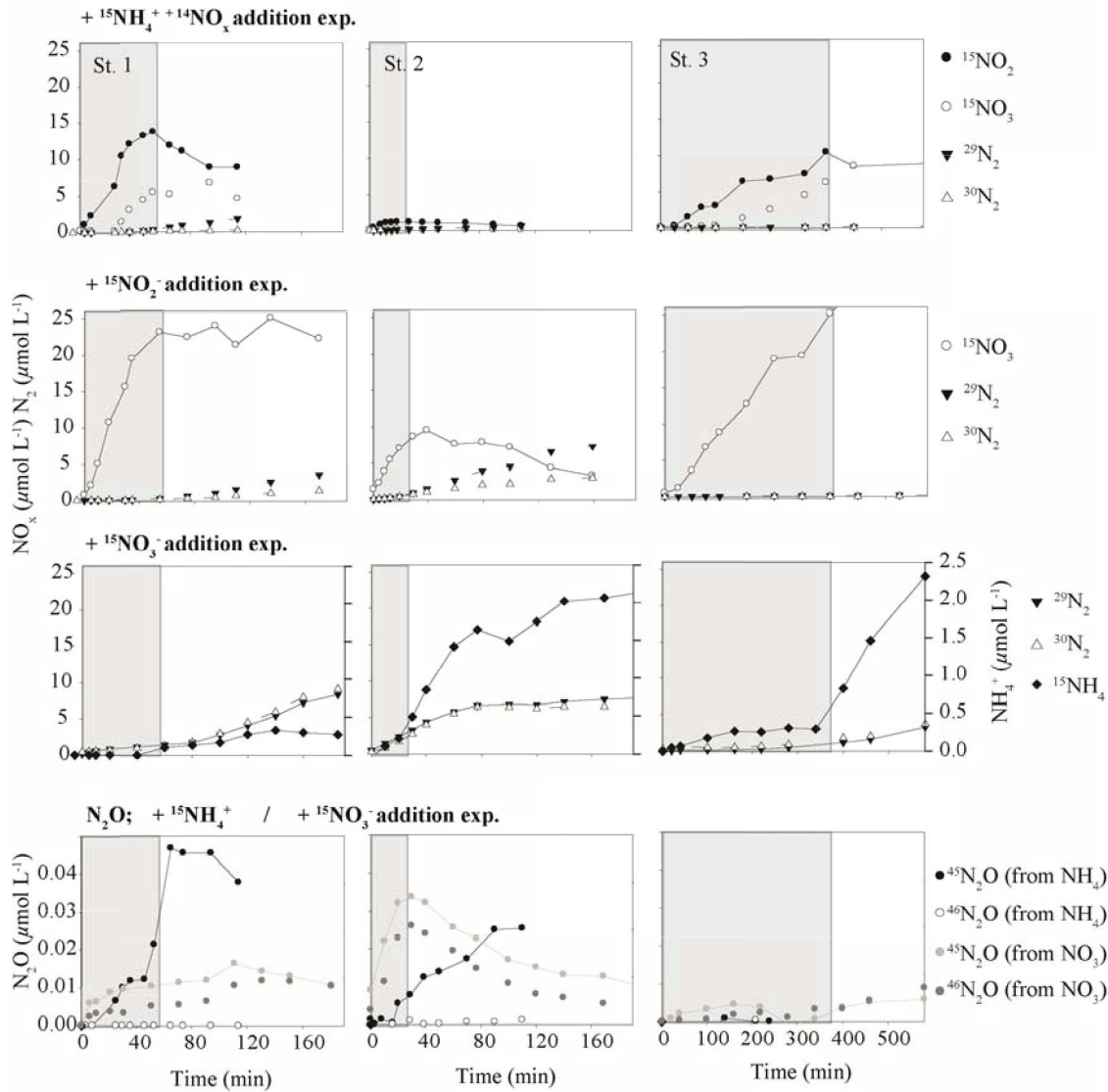


Figure A.5.8: Examples of nitrogen cycling processes at all 3 stations. Only the ^{15}N labeled compound added is described. The processes targeted by each incubation are as follows; $^{15}\text{NH}_4^+$ addition exp, ammonia oxidation. $^{15}\text{NO}_2^-$ addition experiment, nitrite oxidation. $^{15}\text{NO}_3^-$ addition exp, denitrification and DNRA. The bottom panels show the N_2O production in both the $^{15}\text{NH}_4^+$ addition exp and the $^{15}\text{NO}_3^-$ addition exp, for more details of incubations see Table 5.1. The shaded area represents the part of the incubations where oxygen was still present. Note that the time scale differs for the high permeability.

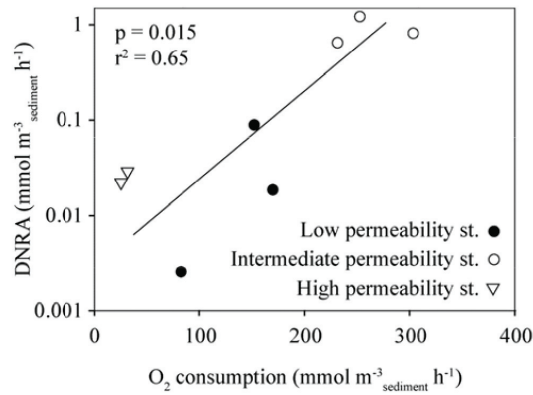


Figure A.5.9: Exponential correlation between heterotrophic oxygen consumption rates and DNRA rates ($r^2 = 0.65$ $p = 0.015$). Heterotrophic oxygen consumption was determined by subtracting oxygen consumption of ammonia oxidation and nitrite oxidation from total oxygen consumption.

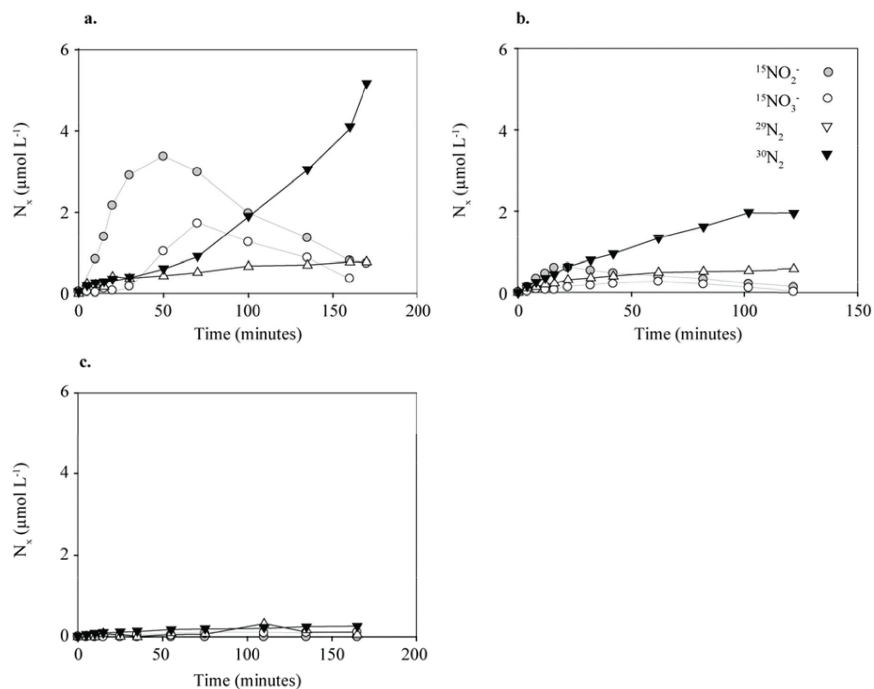


Figure A.5.10: Coupled nitrification-denitrification after addition of $^{15}\text{NH}_4^+$ and ATU. **a** Example from the low permeability station. **b** Example from the intermediate permeability station. **c** Successful inhibition of ammonia oxidation by 10 Pa acetylene

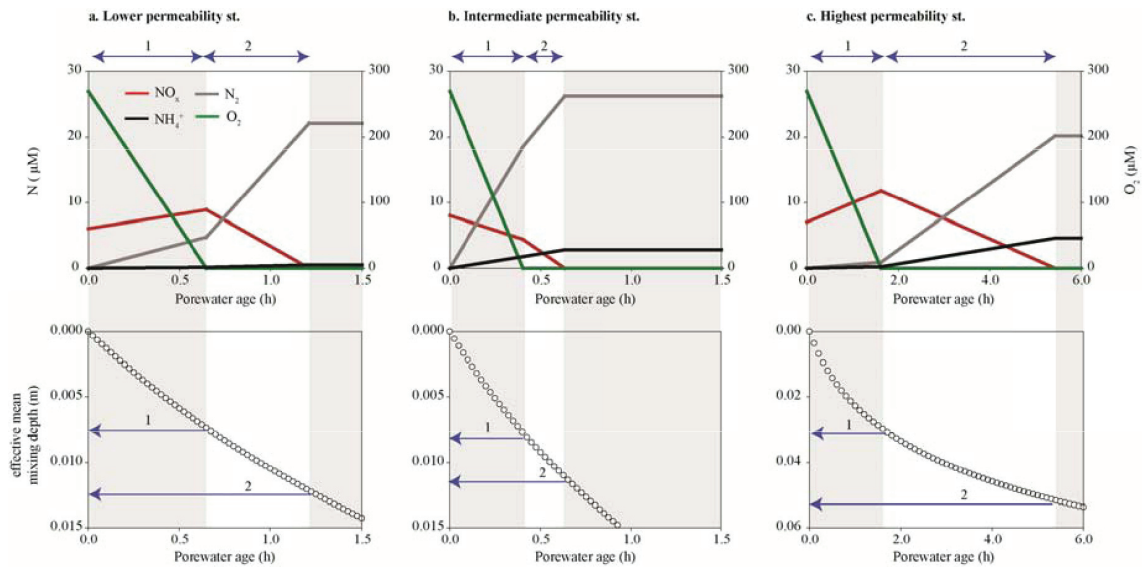


Figure A.5.11: Transforming volumetric rates into areal rates in sandy sediments subject to porewater advection and flow paths of variable lengths - an effective mean mixing depth approach. Upper panels: Combining the measured volumetric rates of ammonia oxidation (here shown as nitrification) with denitrification and DNRA rates allows for the prediction of concentrations within the sediment at different porewater ages. Net production of nitrate occurs at the lower and highest permeability stations while the sediment is oxic (1) and net consumption does not occur until the sediment becomes anoxic. (2) At the intermediate permeability station, net nitrate production does not occur as N-loss is higher than nitrification. Lower panels show the output of the Elliott model, which estimates the 'effective mean mixing depth' for a given porewater age. By combining the upper and middle panels, the blue lines and numbers then represent the time to which the appropriate rates were integrated. Note that the panels for the highest permeability station have different scales compared to the other stations.

| | | Core | Rate (mmol m ⁻³ h ⁻¹) | r ² | S.E. | Average | S.D. | One-way ANOVA (p-value) |
|---------------------------|------------------|------|---|----------------|------|---------|------|----------------------------|
| Ammonia Oxidation | Lower perm. st | 1 | 3.53 | 0.99 | 0.03 | | | |
| | | 2 | 5.62 | 0.98 | 0.11 | | | |
| | | 3 | 8.28 | 0.92 | 0.53 | 5.81 | 2.38 | |
| | Int. perm. st | 1 | 0.97 | 0.99 | 0.01 | | | |
| | | 2 | 1.02 | 0.99 | 0.01 | | | |
| | | 3 | 1.34 | 0.91 | 0.06 | 1.11 | 0.20 | |
| | Higher perm. st. | 1 | 3.03 | 0.96 | 0.25 | | | |
| | | 2 | 3.42 | 1.00 | 0.08 | | | |
| | | 3 | 2.83 | 0.99 | 0.10 | 3.09 | 0.30 | 0.004 |
| Nitrite Oxidation | Lower perm. st | 1 | 6.59 | 0.79 | 1.05 | | | |
| | | 2 | 10.58 | 0.97 | 0.50 | | | |
| | | 3 | 11.72 | 0.99 | 0.29 | 9.63 | 2.70 | |
| | Int. perm. st | 1 | 5.72 | 0.93 | 0.29 | | | |
| | | 2 | 7.98 | 0.93 | 0.23 | | | |
| | | 3 | 8.24 | 0.98 | 0.10 | 7.31 | 1.39 | |
| | Higher perm. st. | 1 | 5.04 | 0.99 | 0.28 | | | |
| | | 2 | 5.89 | 0.98 | 0.44 | | | |
| | | 3 | 5.54 | 0.98 | 0.45 | 5.49 | 0.43 | 0.14 |
| Oxic DNRA | Lower perm. st | 1 | 0.02 | 0.52 | 0.02 | | | |
| | | 2 | 0.09 | 0.50 | 0.07 | | | |
| | | 3 | 0.00 | 0.80 | 0.00 | 0.04 | 0.05 | |
| | Int. perm. st | 1 | 0.79 | 0.96 | 0.03 | | | |
| | | 2 | 1.20 | 0.90 | 0.06 | | | |
| | | 3 | 0.63 | 0.96 | 0.02 | 0.87 | 0.29 | |
| | Higher perm. st. | 1 | 0.03 | 0.87 | 0.02 | | | |
| | | 2 | 0.02 | 0.68 | 0.01 | | | |
| | | 3 | 0.00 | n.d | n.d | 0.02 | 0.01 | 0.01 |
| Oxic denitrification | Lower perm. st | 1 | 1.28 | 0.96 | 0.06 | | | |
| | | 2 | 1.84 | 1.00 | 0.03 | | | |
| | | 3 | 0.81 | 0.90 | 0.08 | 1.31 | 0.51 | |
| | Int. perm. st | 1 | 7.67 | 0.99 | 0.13 | | | |
| | | 2 | 9.83 | 0.99 | 0.17 | | | |
| | | 3 | 10.22 | 0.99 | 0.20 | 9.24 | 1.37 | |
| | Higher perm. st. | 1 | 0.11 | 0.63 | 0.02 | | | |
| | | 2 | 0.09 | 0.97 | 0.02 | | | |
| | | 3 | 0.00 | 0.42 | 0.01 | 0.10 | 0.01 | <0.001 |
| Anoxic DNRA | Lower perm. st | 1 | 0.14 | 0.86 | 0.03 | | | |
| | | 2 | 0.13 | 0.96 | 0.01 | | | |
| | | 3 | 0.08 | 0.94 | 0.01 | 0.12 | 0.03 | |
| | Int. perm. st | 1 | 0.78 | 0.99 | 0.02 | | | |
| | | 2 | 0.88 | 0.98 | 0.03 | | | |
| | | 3 | 1.07 | 0.97 | 0.04 | 0.91 | 0.15 | |
| | Higher perm. st. | 1 | 0.33 | 0.76 | 0.01 | | | |
| | | 2 | 0.08 | 0.85 | 0.05 | | | |
| | | 3 | 0.00 | n.d | n.d | 0.14 | 0.17 | 0.001 |
| Anoxic denitrification | Lower perm. st | 1 | 6.04 | 0.95 | 0.69 | | | |
| | | 2 | 7.37 | 1.00 | 0.21 | | | |
| | | 3 | 3.29 | 0.99 | 0.11 | 5.57 | 2.08 | |
| | Int. perm. st | 1 | 4.61 | 0.97 | 0.28 | | | |
| | | 2 | 5.27 | 0.98 | 0.23 | | | |
| | | 3 | 6.75 | 0.97 | 0.33 | 5.54 | 1.09 | |
| | Higher perm. st. | 1 | 1.13 | 0.95 | 0.14 | | | |
| | | 2 | 0.68 | 0.84 | 0.06 | | | |
| | | 3 | 0.01 | 0.59 | 0.01 | 0.91 | 0.32 | 0.03 |

Table A.5.5: Individual rates with r^2 and standard error of linear regression for each process from three replicate cores. Values in gray italics were not included in averages or further statistical tests. $n \leq 4$ for all linear regressions.

Bibliography

- Ahmerkamp, S., Winter, C., Janssen, F., Kuypers, M. M. and Holtappels, M. (2015), 'The impact of bedform migration on benthic oxygen fluxes', *Journal of Geophysical Research: Biogeosciences* **120**(11), 2229–2242.
- An, S. and Gardner, W. S. (2002), 'Dissimilatory nitrate reduction to ammonium (dnra) as a nitrogen link, versus denitrification as a sink in a shallow estuary (laguna madre/baffin bay, texas)', *Marine Ecology Progress Series* **237**(4), 41–50.
- Beddig, S., Brockmann, U., Dannecker, W., Körner, D., Pohlmann, T., Puls, W., Radach, G., Rebers, A., Rick, H.-J., Schatzmann, M. et al. (1997), 'Nitrogen fluxes in the german bight', *Marine Pollution Bulletin* **34**(6), 382–394.
- Belser, L. W. (1979), 'Population ecology of nitrifying bacteria', *Annual reviews in microbiology* **33**(1), 309–333.
- Blackburn, T. and Henriksen, K. (1983), 'Nitrogen cycling in different types of sediments from danish waters', *Limnology and Oceanography* **28**(3), 477–493.
- Braman, R. S. and Hendrix, S. A. (1989), 'Nanogram nitrite and nitrate determination in environmental and biological materials by vanadium (iii) reduction with chemiluminescence detection', *Analytical Chemistry* **61**(24), 2715–2718.
- Canion, A., Kostka, J., Gihring, T., Huettel, M., Van Beusekom, J., Gao, H., Lavik, G. and Kuypers, M. (2014), 'Temperature response of denitrification and anammox reveals the adaptation of microbial communities to in situ temperatures in permeable marine sediments that span 50° in latitude', *Biogeosciences* **11**(2), 309–320.
- Clark, D. R., Rees, A. P. and Joint, I. (2008), 'Ammonium regeneration and nitrification rates in the oligotrophic atlantic ocean: Implications for new production estimates', *Limnology and Oceanography* **53**(1), 52.
- Cook, P. L., Wenzhöfer, F., Glud, R. N., Janssen, F. and Huettel, M. (2007), 'Benthic solute exchange and carbon mineralization in two shallow subtidal sandy sediments: Effect of advective pore-water exchange', *Limnology and Oceanography* **52**(5), 1943–1963.
- Dähnke, K., Emeis, K., Johannsen, A., Nagel, B. et al. (2010), 'Stable isotope composition and turnover of nitrate in the german bight.', *Marine Ecology, Progress Series* **408**, 7–18.

- Devol, A. H., Codispoti, L. A. and Christensen, J. P. (1997), 'Summer and winter denitrification rates in western arctic shelf sediments', *Continental Shelf Research* **17**(9), 1029–1050.
- Elliott, A. H. and Brooks, N. H. (1997a), 'Transfer of nonsorbing solutes to a streambed with bed forms: Laboratory experiments', *Water Resources Research* **33**(1), 137–151.
- Elliott, A. H. and Brooks, N. H. (1997b), 'Transfer of nonsorbing solutes to a streambed with bed forms: Theory', *Water Resources Research* **33**(1), 123–136.
- Emery, K. (1968), 'Relict sediments on continental shelves of world', *AAPG Bulletin* **52**(3), 445–464.
- Evrard, V., Glud, R. N. and Cook, P. L. (2013), 'The kinetics of denitrification in permeable sediments', *Biogeochemistry* **113**(1-3), 563–572.
- Füssel, J., Lam, P., Lavik, G., Jensen, M. M., Holtappels, M., Günter, M. and Kuypers, M. M. (2011), 'Nitrite oxidation in the namibian oxygen minimum zone', *The ISME journal* **6**(6), 1200–1209.
- Gao, H., Matyka, M., Liu, B., Khalili, A., Kostka, J. E., Collins, G., Jansen, S., Holtappels, M., Jensen, M. M., Badewien, T. H. et al. (2012), 'Intensive and extensive nitrogen loss from intertidal permeable sediments of the wadden sea', *Limnology and Oceanography* **57**(1), 185.
- Gao, H., Schreiber, F., Collins, G., Jensen, M. M., Kostka, J. E., Lavik, G., de Beer, D., Zhou, H.-y. and Kuypers, M. M. (2010), 'Aerobic denitrification in permeable wadden sea sediments', *The ISME journal* **4**(3), 417–426.
- Gihring, T. M., Canion, A., Riggs, A., Huettel, M. and Kostka, J. E. (2010), 'Denitrification in shallow, sublittoral gulf of mexico permeable sediments', *Limnology and Oceanography* **55**(1), 43–54.
- Ginestet, P., Audic, J.-M., Urbain, V. and Block, J.-C. (1998), 'Estimation of nitrifying bacterial activities by measuring oxygen uptake in the presence of the metabolic inhibitors allylthiourea and azide', *Applied and Environmental Microbiology* **64**(6), 2266–2268.
- Glud, R. N. (2008), 'Oxygen dynamics of marine sediments', *Marine Biology Research* **4**(4), 243–289.
- Gruber, N. and Galloway, J. N. (2008), 'An earth-system perspective of the global nitrogen cycle', *Nature* **451**(7176), 293–296.

- Guo, H., Zhou, J., Su, J. and Zhang, Z. (2005), 'Integration of nitrification and denitrification in airlift bioreactor', *Biochemical Engineering Journal* **23**(1), 57–62.
- Henriksen, K., Blackburn, T., Lomstein, B. A. and McRoy, C. (1993), 'Rates of nitrification, distribution of nitrifying bacteria and inorganic n fluxes in northern bering-chukchi shelf sediments', *Continental Shelf Research* **13**(5), 629–651.
- Holtappels, M., Lavik, G., Jensen, M. M. and Kuypers, M. M. (2011), '15n-labeling experiments to dissect the contributions of heterotrophic denitrification and anammox to nitrogen removal in the omz waters of the ocean', *Method Enzymol* **486**, 223–251.
- Huettel, M., Berg, P. and Kostka, J. E. (2014), 'Benthic exchange and biogeochemical cycling in permeable sediments', *Marine Science* **6**.
- Huettel, M., Røy, H., Precht, E. and Ehrenhauss, S. (2003), Hydrodynamical impact on biogeochemical processes in aquatic sediments, in 'The Interactions between Sediments and Water', Springer, pp. 231–236.
- Huettel, M., Ziebis, W. and Forster, S. (1996), 'Flow-induced uptake of particulate matter in permeable sediments', *Limnology and Oceanography* **41**(2), 309–322.
- Isobe, K., Koba, K., Suwa, Y., Ikutani, J., Kuroiwa, M., Fang, Y., Yoh, M., Mo, J., Otsuka, S. and Senoo, K. (2012), 'Nitrite transformations in an n-saturated forest soil', *Soil Biology and Biochemistry* **52**, 61–63.
- Janssen, F., Huettel, M. and Witte, U. (2005), 'Pore-water advection and solute fluxes in permeable marine sediments (ii): Benthic respiration at three sandy sites with different permeabilities (german bight, north sea)', *Limnology and Oceanography* **50**(3), 779–792.
- Jäntti, H. and Hietanen, S. (2012), 'The effects of hypoxia on sediment nitrogen cycling in the baltic sea', *Ambio* **41**(2), 161–169.
- Jenkins, M. C. and Kemp, W. M. (1984), 'The coupling of nitrification and denitrification in two estuarine sediments I v2', *Limnol. Oceanogr* **29**(3), 609–6.
- Jensen, K., Sloth, N. P., Risgaard-Petersen, N., Rysgaard, S. and Revsbech, N. P. (1994), 'Estimation of nitrification and denitrification from microprofiles of oxygen and nitrate in model sediment systems', *Applied and Environmental Microbiology* **60**(6), 2094–2100.
- Jensen, K. et al. (1996), 'Nitrification and denitrification in wadden sea sediments (konigshafen, island of sylt, germany) as measured by nitrogen isotope pairing and isotope dilution', *Aquat. Microb. Ecol.* **11**, 181–191.

- Jørgensen, B. B. (1982), 'Mineralization of organic matter in the sea bed—the role of sulphate reduction', *Nature* **296**, 643–645.
- Kessler, A. J., Glud, R. N., Cardenas, M. B. and Cook, P. L. (2013), 'Transport zonation limits coupled nitrification-denitrification in permeable sediments', *Environmental science & technology* **47**(23), 13404–13411.
- Koop-Jakobsen, K., Giblin, A. E. et al. (2010), 'The effect of increased nitrate loading on nitrate reduction via denitrification and dnra in salt marsh sediments', *Limnology and Oceanography* **55**(2), 789.
- Laursen, A. E. and Seitzinger, S. P. (2002), 'The role of denitrification in nitrogen removal and carbon mineralization in mid-atlantic bight sediments', *Continental Shelf Research* **22**(9), 1397–1416.
- Law, C. and Owens, N. (1990), 'Denitrification and nitrous oxide in the north sea', *Netherlands Journal of Sea Research* **25**(1-2), 65–74.
- Lohse, L., Malschaert, J. F., Slomp, C. P., Helder, W. and van Raaphorst, W. (1993), 'Nitrogen cycling in north sea sediments: interaction of denitrification and nitrification in offshore and coastal areas', *Marine Ecology-Progress Series* **101**, 283–283.
- Marchant, H. K., Lavik, G., Holtappels, M. and Kuypers, M. M. (2014), 'The fate of nitrate in intertidal permeable sediments', *PloS one* **9**(8), e104517.
- Meyer, R. L., Allen, D. E. and Schmidt, S. (2008), 'Nitrification and denitrification as sources of sediment nitrous oxide production: A microsensor approach', *Marine Chemistry* **110**(1), 68–76.
- Münch, E. V., Lant, P. and Keller, J. (1996), 'Simultaneous nitrification and denitrification in bench-scale sequencing batch reactors', *Water Research* **30**(2), 277–284.
- Nielsen, L. P. (1992), 'Denitrification in sediment determined from nitrogen isotope pairing', *FEMS Microbiology Letters* **86**(4), 357–362.
- Olson, R. (1981), 'N-15 tracer studies of the primary nitrite maximum', *Journal of Marine Research* **39**(2), 203–226.
- Pätsch, J., Serna, A., Dähnke, K., Schlarbaum, T., Johannsen, A. and Emeis, K.-C. (2010), 'Nitrogen cycling in the german bight (se north sea)—clues from modelling stable nitrogen isotopes', *Continental Shelf Research* **30**(2), 203–213.

- Polerecky, L., Franke, U., Werner, U., Grunwald, B. and de Beer, D. (2005), 'High spatial resolution measurement of oxygen consumption rates in permeable sediments', *Limnol. Oceanogr. Methods* **3**, 75–85.
- Prakasam, T. and Loehr, R. (1972), 'Microbial nitrification and denitrification in concentrated wastes', *Water Research* **6**(7), 859–869.
- Preisler, A., De Beer, D., Lichtschlag, A., Lavik, G., Boetius, A. and Jørgensen, B. B. (2007), 'Biological and chemical sulfide oxidation in a bebbiata inhabited marine sediment', *The ISME journal* **1**(4), 341–353.
- Rabalais, N. N. (2002), 'Nitrogen in aquatic ecosystems', *AMBIO: A Journal of the Human Environment* **31**(2), 102–112.
- Rao, A. M., McCarthy, M. J., Gardner, W. S. and Jahnke, R. A. (2007), 'Respiration and denitrification in permeable continental shelf deposits on the south atlantic bight: Rates of carbon and nitrogen cycling from sediment column experiments', *Continental Shelf Research* **27**(13), 1801–1819.
- Rao, A. M., McCarthy, M. J., Gardner, W. S. and Jahnke, R. A. (2008), 'Respiration and denitrification in permeable continental shelf deposits on the south atlantic bight: N 2: Ar and isotope pairing measurements in sediment column experiments', *Continental Shelf Research* **28**(4), 602–613.
- Revsbech, N. P. (1989), 'An oxygen microsensor with a guard cathode', *Limnology and Oceanography* **34**(2), 474–478.
- Rocha, C., Forster, S., Koning, E. and Epping, E. (2005), 'High-resolution permeability determination and two-dimensional porewater flow in sandy sediment', *Limnology and Oceanography: Methods* **3**(1), 10–23.
- Santoro, A. E. and Casciotti, K. L. (2011), 'Enrichment and characterization of ammonia-oxidizing archaea from the open ocean: phylogeny, physiology and stable isotope fractionation', *The ISME journal* **5**(11), 1796–1808.
- Santoro, A. E., Casciotti, K. L. and Francis, C. A. (2010), 'Activity, abundance and diversity of nitrifying archaea and bacteria in the central california current', *Environmental Microbiology* **12**(7), 1989–2006.
- Sharma, B. and Ahlert, R. (1977), 'Nitrification and nitrogen removal', *Water Research* **11**(10), 897–925.

- Sokoll, S., Holtappels, M., Lam, P., Collins, G., Schlüter, M., Lavik, G. and Kuypers, M. M. (2012), 'Benthic nitrogen loss in the arabian sea off pakistan', *The microbial nitrogen cycle* p. 33.
- Song, G., Liu, S., Marchant, H., Kuypers, M. and Lavik, G. (2013), 'Anammox, denitrification and dissimilatory nitrate reduction to ammonium in the east china sea sediment', *Biogeosciences* **10**(11), 6851–6864.
- Tait, D. R., Erler, D. V., Dakers, A., Davison, L. and Eyre, B. D. (2013), 'Nutrient processing in a novel on-site wastewater treatment system designed for permeable carbonate sand environments', *Ecological Engineering* **57**, 413–421.
- Thamdrup, B. and Canfield, D. E. (1996), 'Pathways of carbon oxidation in continental margin sediments off central chile', *Limnology and Oceanography* **41**(8), 1629–1650.
- Thamdrup, B. and Dalsgaard, T. (2002), 'Production of n₂ through anaerobic ammonium oxidation coupled to nitrate reduction in marine sediments', *Applied and environmental microbiology* **68**(3), 1312–1318.
- Thibodeaux, L. J. and Boyle, J. D. (1987), 'Bedform-generated convective transport in bottom sediment', *Nature* .
- Trimmer, M. and Nicholls, J. C. (2009), 'Production of nitrogen gas via anammox and denitrification in intact sediment cores along a continental shelf to slope transect in the north atlantic', *Limnology and Oceanography* **54**(2), 577–589.
- van Beusekom, J. E. (2005), 'A historic perspective on wadden sea eutrophication', *Helgoland Marine Research* **59**(1), 45–54.
- Ward, B. (2005), 'Temporal variability in nitrification rates and related biogeochemical factors in monterey bay, california, usa', *Marine Ecology Progress Series* **292**(97), 109.
- Ward, B. B. (2008), 'Nitrification in marine systems', *Nitrogen in the marine environment* **5**, 199–261.
- Warembourg, F. R. (1993), 'Nitrogen fixation in soil and plant systems', *Nitrogen isotope techniques* pp. 127–156.
- Yoo, H., Ahn, K.-H., Lee, H.-J., Lee, K.-H., Kwak, Y.-J. and Song, K.-G. (1999), 'Nitrogen removal from synthetic wastewater by simultaneous nitrification and denitrification (snd) via nitrite in an intermittently-aerated reactor', *Water research* **33**(1), 145–154.

6. Aerobic denitrification in sands

Denitrifying community in coastal sediments performs aerobic and anaerobic respiration simultaneously

Hannah K. Marchant

Max Planck Institute for Marine Microbiology, Bremen, Germany

Soeren Ahmerkamp, Gaute Lavik, Halina Tegetmeyer

Max Planck Institute for Marine Microbiology, Bremen, Germany

Jon Graf, Judith Klatt, Moritz Holtappels^{1,2}, Eva Walpersdorf

Max Planck Institute for Marine Microbiology, Bremen, Germany

Marcel MM Kuypers

Max Planck Institute for Marine Microbiology, Bremen, Germany

In preperation: ISME J.

Additional Affiliations:

¹*Alfred Wegener Institute - Helmholtz Centre for Polar and Marine Research, Bremerhaven, Germany*

²*MARUM Center for Marine Environmental Sciences, Bremen, Germany*

Abstract

Nitrogen inputs to the oceans have increased considerably due to anthropogenic activities, however most is removed before reaching the open ocean. Recently, it has been suggested that denitrifiers in coastal sandy sediments play a major role in removing N. These sandy, permeable sediments are dynamic environments, where concentrations of electron acceptors and donors fluctuate over short temporal and spatial scales. The responses of denitrifiers to these fluctuations are relatively unknown. We examined denitrification in the sediment under fluctuating oxygen concentrations, finding that it not only occurs at high O_2 concentrations but is stimulated by switches between oxic and anoxic conditions. Over a tidal cycle, concurrent expression of marker genes for aerobic respiration and denitrification was observed in a wide range of bacterial classes, regardless of O_2 . Combined, these results suggest that sandy sediments select for denitrifiers whose gene expression is not regulated by O_2 . This allows a rapid response to changing environmental conditions, but also means that denitrification is available as an auxiliary respiration pathway under aerobic conditions, when imbalances in electron donor and acceptor supply stimulate use of the denitrification pathway. While low in comparison to aerobic respiration, the rates of aerobic denitrification contributed significantly to overall N-loss.

Contributions to the manuscript:

SA performed analysis of the transport processes in the flow-through reactors to distinguish between transport processes and microbial reactions. The work included data analysis and the calculation of reaction rates and their representation. SA also discussed the data and helped write the manuscript.

6.1 Introduction

Worldwide, coastal seas receive large amounts of anthropogenic nitrogen (N) inputs through riverine run off and atmospheric deposition (48 and 8 Tg N yr⁻¹ respectively (Galloway et al., 2004). So far however, concurrent rises in N have not been observed in the open ocean. This is due to the activity of denitrifying microbes in coastal and continental shelf sediments which respire much of the fixed inorganic N to N₂, whereupon it is lost from the system (Gruber and Galloway 2008). This denitrification was assumed to primarily occur in cohesive muddy sediments. Recently however, extensive N-loss has been shown to occur in the permeable sands that cover 58-70% of the continental shelves (Gao et al., 2012; Gihring et al., 2010; Marchant et al., 2016).

Sandy sediments are characterized by advective porewater flow. Water movement above the rippled sediments forms pressure gradients leading to the advection of water rich in oxygen, nitrate and organic matter into the sediment (Huettel et al., 2003). These high fluxes, combined with a microbial biomass of 10⁸ – 10⁹ cell ml⁻¹ mean that sandy sediments act as biocatalytic filters, in which rates of respiration and organic matter turnover are high (de Beer et al., 2005; Rusch et al., 2001). The extent of advection changes dependent on current flow, sediment movement, and exposure of intertidal flats at low tide. This leads to frequent fluctuations in oxygen concentrations (Ahmerkamp et al., 2015; Billerbeck et al., 2006). Therefore, while sandy sediments provide high fluxes of electron donors and acceptors (Huettel et al., 2003), facultative anaerobes within them need to be able to rapidly adjust their respiratory strategy. A poorly understood consequence of this seems to be the occurrence of denitrification under oxic conditions, observations of which have been made in both intertidal and subtidal permeable sediments (Gao et al., 2010; Marchant et al., 2016; Rao et al., 2008).

All known marine denitrifiers are facultative anaerobes that can switch from aerobic respiration to anaerobic respiration. Their electron transport chain (ETC) is organized in such a way that the dissimilatory N-oxide reductases (nitrate, nitrite, nitric oxide and nitrous oxide reductase) are “plug-in” branches to the aerobic respiration pathway. These branched ETC's, which can also include multiple terminal oxidases, provide respiratory flexibility, as possession and differential expression of different terminal electron acceptors allows respiration to be adjusted to environmental conditions (Poole and Cook, 2000; Sharma et al., 2012). Canonically we assume that dissolved oxygen (O₂) needs to be depleted before facultative anaerobic organisms begin using nitrate (NO₃⁻) as an alternative terminal electron acceptor (Zumft, 1997). This is because physiological, bioenergetic and kinetic considerations all indicate that denitrification should not occur in the presence of

oxygen. Nevertheless, the simultaneous respiration of NO_3^- and O_2 has been demonstrated repeatedly in pure cultures (Kim et al., 2008; Patureau et al., 2000; Robertson and Kuenen, 1984; Robertson et al., 1995).

For aerobic denitrification to occur, the N-oxide reductases must be expressed under oxic conditions. This is rarely the case, as expression of the denitrification pathway is often repressed by O_2 (Bergaust et al., 2012). However, under fluctuating O_2 conditions such as those observed in permeable sediments, constitutive expression of the denitrification pathway would be advantageous, as continual rebuilding of the denitrification pathway in response to oxygen is costly (Bergaust et al., 2008; Robertson and Kuenen, 1990). The hypothesis that environmental settings with fluctuating O_2 concentrations select for aerobic denitrifiers is supported by previous observations of aerobic denitrification in permeable sediments and furthermore by the success that researchers have had in isolating aerobic denitrifiers from other environments where O_2 availability fluctuates. (Frette et al., 1997; Patureau et al., 1994, 2000). Until now most studies of aerobic denitrification have focused on biochemical and physiological characterization of the process using bacterial isolates (Ellington et al., 2002; Richardson and Ferguson, 1992; Sears et al., 1997). However, to the best of our knowledge no study has actually investigated whether significant constitutive expression of the N-oxide reductases occurs under oxic conditions in fluctuating marine environments. Nor has any study investigated which members of the microbial community might be responsible for co-respiration of oxygen and N-oxides in permeable sediments.

We investigated aerobic denitrification in permeable sediments of the Wadden Sea. These sandy sediments that fringe the North-West European coast are part of the world's largest tidal flat system and play a vital role in removing anthropogenic N-inputs from land before they reach the North Sea. The aim of our study was to determine the extent to which oxygen controls the expression and utilization of the denitrification pathway and to identify the microorganisms carrying out aerobic denitrification.

6.2 Methods

6.2.1 Sampling site

Sediment was sampled from the Janssand sand flat, in the back barrier area of Spiekeroog Island in the East Frisian Wadden Sea, Germany (see Billerbeck et al., 2006). The entire flat is inundated with ca. 2 m of seawater during high tide, before exposure to the air for 6 – 8 h during low tide in a semi diurnal cycle.

6.2.2 Sediment collection and experimental column set up

Sediment from the upper 5cm of the sand flat was collected at low tide in April 2012, November 2014 and February 2015, whereupon it was homogenized and returned to the lab. Less than 4 hours after collection sediment was packed into sediment columns (Marchant et al., 2014, 2016) and kept on a simulated tidal cycle consisting of repeated 6 hour “inundation” and “exposure” periods. During “inundation” seawater (collected from the sampling site) was pumped through the core in 30 minute on; 15 minute off cycles at a rate of 2.5 ml min^{-1} . During the 6 hour exposure period, no pumping occurred. In January 2016, sediment was cored without disturbing its structure and returned to laboratory where it was kept at 4°C , subsequently the core was percolated with aerated site seawater and oxygen consumption rates at 1.5 cm depth within the sediment were determined using a microsensors (as in Polerecky et al., 2005).

6.2.3 Incubation procedure

Oxygen consumption rates and denitrification rates within the sediment were determined over time (Sup Figure 1). Incubations were carried out by exchanging the entire volume of porewater within the sediment core 1.5 times with aerated, $^{15}\text{NO}_3^-$ amended seawater. The porewater within the core was subsequently sampled continuously from the inlet and pumped through a membrane inlet attached to a mass spectrometer (MIMS; GAM200, In Process Instruments). Membrane Inlet Mass Spectrometry (MIMS) was used to determine $^{28}\text{N}_2$, $^{29}\text{N}_2$, $^{30}\text{N}_2$, Ar and O_2 concentrations over the next 90 minutes. Data points were collected every 3-4 seconds. Rates of $^{29}\text{N}_2$ and $^{30}\text{N}_2$ production and O_2 consumption were then calculated using a second order central difference algorithm after smoothing using the Savitzky-Golay filter in Matlab ($n = 45$). Denitrification rates were calculated according to Nielsen (1992). In order to determine whether the multiple incubations changed the flow paths within the sediment, water saturated alternately with helium or argon was pumped through the core and breakthrough curves determined.

The alternation between oxic and anoxic conditions required repeated flushing of sediment cores with aerated, $^{15}\text{NO}_3^-$ amended water (see Figure S1). In tests using inert gases (helium and argon) very similar breakthrough curves obtained from multiple flushings indicated that the incubation method did not lead to the build-up of preferential flow paths within the sediment core. The break-through curves did indicate that the rapid changes in concentration within the sediment and funneling of water between the sediment and the small sampling port in the lid of water led to a smearing effect in observed concentrations of O_2 and N_2 . Briefly; when porewater from the edge of the core arrives at the lid, it has to travel towards the central port, therefore it reaches the port later than water from the

centre of the core. In effect, this means that water with a shorter residence time mixes with water that has had a longer residence time within the sediment (Figure S2). As such there is a smearing when reaction rates are changing rapidly. This methodological artifact can be observed when MIMS measurements are compared to those made with a microsensor placed directly in the sediment. Using the MIMS method, a rather low apparent half saturation constant (k_m) for O_2 is observed ($24 \mu\text{M}$), whereas with the microsensor method the observed k_m is $2 \mu\text{M}$ (Figure S3). Using the breakthrough curves, it was possible to determine the periods during incubations when mixing had the greatest effect on the observed concentration gradients (i.e. rates); allowing us to treat such data cautiously (grey bars, Figure 6.1 a).

6.2.4 Short term exposure experiments

For short term studies into denitrification and oxygen respiration, all cores were exposed to at least four flushing cycles which consisted of 18 minutes porewater exchange time and 90 minutes measurement time. In February 2015, flushing cycles were repeated until no change in rates was apparent. On the 5th cycle, one core was flushed for 50 minutes rather than 18 minutes, increasing the time the sediment was exposed to entirely oxic conditions. After 4 cycles, another core was kept attached to the MIMS for 3 hours, rather than 90 minutes, increasing the time that the sediment was exposed to anoxia before the incubation was repeated.

6.2.5 Long term exposure experiments

In February 2015 sediment cores were exposed to different oxygen regimes for 3 weeks. Six cores were supplied with North Sea seawater containing $20 \mu\text{M NO}_3^-$ and two cores were assigned to each of 3 conditions: a ‘tidal cycle’ condition as detailed above, an ‘anoxic’ condition during which the core was supplied with seawater degassed with N_2 during the inundation period and an ‘oxic’ condition, in which aerated seawater was constantly pumped through the sediment. After 21 days the sediment cores were removed from their respective conditions and the incubations described above were immediately carried out.

6.2.6 Metagenomics and in situ transcriptomics

Metagenomic and transcriptomic analyses focused specifically on the marker genes for terminal oxidases (A-class HCO, B-class HCO, C-class HCO and cyt bd-type oxidases) and the nitrate reductases (napA and narG), and nitrous oxide reductase (nosZ). Metagenomic libraries constructed were constructed with DNA from the upper 2 cm centimetres of the intertidal sand flat. Sediment was collected on October 24 2009 and March 23 2010. Two

of the three March samples were pooled, and the pool was divided into two samples, named March 1 and March 2. Sediment was stored at -20°C until DNA extraction, which was carried out according to Zhou et al. Sequencing was carried out in two GS FLX Titanium sequencing runs. The four sequence data sets were submitted to the sequence read archive (<http://trace.ncbi.nlm.nih.gov/Traces/sra/>) under the bioproject PRJNA174601 (Accession: SRP015924). The sample Accession numbers are SRS365699, SRS365698, SRS365700 and SRS365701. Sediment sampling for transcriptomics was carried out on March 21 2011 over a tidal cycle, sampling time points were 06:50 (low tide), 08:50 (late low tide), 10:50 (rising tide), 12:50 (high tide), 14:50 (falling tide) and 16:50 (early low tide). Sediment samples were immediately immersed in three volumes of RNA preservation solution (LifeGuardTM Soil Preservation Solution, MoBio), and stored at 4°C until RNA extraction (See supplementary methods). cDNA libraries generated from the RNA were sequenced on a HiSeq 1500 instrument, in a 1x250 bases single end run (Rapid v2 chemistry). 12 metatranscriptome libraries were generated from sediment sampled at six time points over a complete tidal cycle, each of these had between 1.2 and 8 million mRNA sequence reads with a mean length of 180 bp (Table S1). The largest metatranscriptome was from low tide, while the smallest was at high tide.

6.2.7 Data analysis - Metagenomics

The sequence data sets were pre-processed by removing identical reads with CD-hit (Li and Godzik, 2006) and translated into the correct protein sequences using PRODIGAL (Hyatt et al., 2010). The respective catalytic subunits for each of the four classes of terminal oxidases were identified using profile hidden markov models (HMM) and their identity validated following Sousa et al. (2011). Functional marker genes for the denitrification pathway were identified using a pipeline developed in house (See supplementary methods for details). To allow normalization between metagenomes and comparison to previous results, the abundance of 3 housekeeping genes (*rpoB*, *rpoC* and *recA*) was determined using model TIGRFAMs TIGR02027, TIGR02013, TIGR02386. The taxonomic identities of terminal oxidase genes were inferred using MEGAN 4 (Huson et al., 2011). Counts of terminal oxidase and N-oxide reductase gene transcripts were normalized to their respective gene lengths and to the normalized mean counts of housekeeping gene transcripts (*recA*, *rpoB* and *rpoC*).

6.2.8 Data analysis - Tidal cycle transcriptomics

The sequence data sets were pre-processed by Casava v1.8.4, and quality trimmed using Trimmomatic (Bolger et al., 2014). SortMeRNA v2.0 (Kopylova et al., 2012) was used to

filter out rRNA reads. From the resulting non-rRNA reads identical reads were removed using CD-hit (Li and Godzik, 2006) and translated into protein sequences using PRODIGAL (Hyatt et al., 2010). HMMs were generated for the following functional genes; *napA*, *narG* and *nosZ*, as well for the terminal oxidases and housekeeping genes. HMMs were used to identify transcripts within the sequence data (see supplementary methods) and the taxonomic identities of transcripts were inferred using MEGAN 4 (Huson et al., 2011). Counts of terminal oxidase and N-oxide reductase gene transcripts were normalized to their respective gene lengths and to the normalized mean counts of housekeeping gene transcripts.

6.3 Results

6.3.1 Sediment incubations

To gain insights into how and when N₂ production occurs in response to oxygen fluctuations within permeable sediments, we used an established method combining flow through sediment cores with online membrane inlet mass spectrometry (MIMS) (Marchant et al., 2014, 2016). This allows simultaneous and high resolution (< 4 s) measurements of O₂ and N₂ concentrations within the sediment. Within sediment cores, rapid changes in concentration within the sediment, combined with unavoidable funneling of water from the sediment to the sampling port cause a smearing effect in concentrations of both N₂ and O₂. As the smearing of the concentration gradients and rates are consistent between gases, the relative changes of N₂ and O₂ remain constant. Therefore, we focused on comparison of ¹⁵N-N₂ and O₂ concentrations at each time point (Figure 6.1 b).

6.3.2 Denitrification in sediment exposed to rapid fluctuations in oxygen availability

Exposure of the freshly collected sediment to rapid fluctuations in oxygen availability yielded the same results in each of the three seasons tested (Figure 6.1 and Figure S4). In the bottom centimeter of sediment in cores kept on a tidal cycle, we observed a rapid consumption of O₂ (maximum rate 6.8 and 5.5 μmol L⁻¹ min⁻¹ in November and February respectively) and the production of only small amount of N₂ under oxic conditions (< 0.25 μmol ¹⁵N L⁻¹ in all seasons). Denitrification rates rose rapidly when O₂ concentrations dropped below the apparent half saturation constant ($k_{m(O_2)}$) as determined by michaelis menten kinetics, stabilizing when sediment became fully anoxic (linear regressions of ¹⁵N-N₂ concentrations over time during anoxia had $r^2 > 0.99$). On average anoxic denitrification rates during anoxia reached 1.08 and 0.8 μmol N L⁻¹ min⁻¹ in November

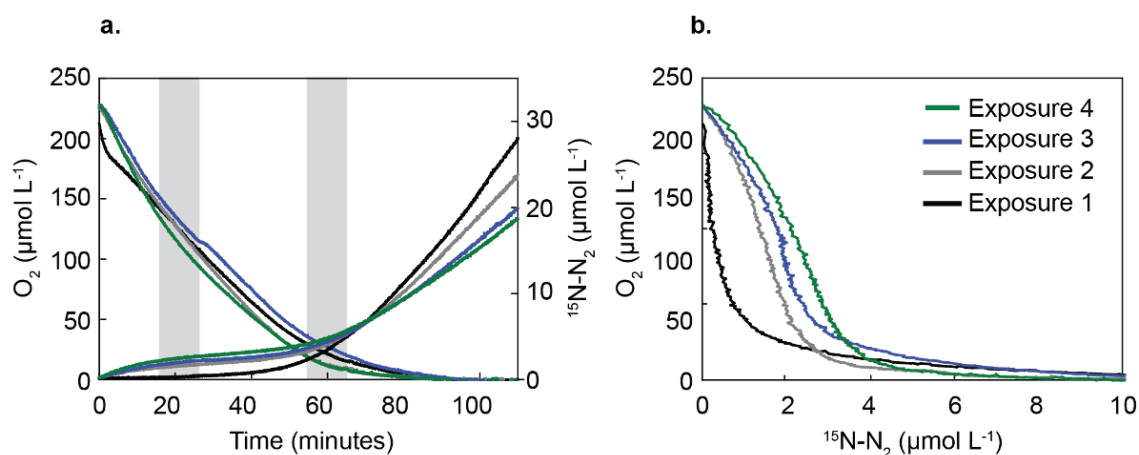


Figure 6.1: Oxygen and denitrification dynamics in sediment exposed to shifts between anoxic and oxic conditions. **a** Consumption of O₂ and production of ¹⁵N-N₂ in the December incubation, the grey bars indicate where mixing within the core lid might lead to over or underestimated concentrations **b** Comparison of O₂ concentrations and N₂ concentrations in the incubations.

and February respectively.

After the sediment had been anoxic for 90 minutes, air-saturated ¹⁵NO₃⁻ labeled seawater was reintroduced into the sediment. Such oxic-anoxic cycles were repeated up to 7 times on the same core. The production of ¹⁵N-N₂ at high O₂ concentrations increased with each subsequent incubation (Figure 6.1 **b**), eventually reaching a maximum after 4 cycles, by which time 3 μmol L⁻¹ ¹⁵N was produced at O₂ concentrations above 100 μmol L⁻¹, with maximal denitrification rates of 0.22 and 0.28 μmol N L⁻¹ min⁻¹ at O₂ > 100 μmol L⁻¹ (February and December respectively). After 4 oxic-anoxic cycles oxygen consumption rates (at O₂ concentrations above 100 μmol L⁻¹) in December increased 33% between the 1st and 4th incubation (from 3.7±0.6 SD to 4.9±0.9 SD μmol L⁻¹ min⁻¹). In February, no significant change in O₂ consumption rates was observed between incubations. Anoxic denitrification rates also varied as result of repeated incubations, decreasing by 44 % between the 1st and 4th incubation in December (from 1.08±0.03 SD to 0.6±0.03 SD μmol L⁻¹ N min⁻¹), and by 24 % between the 1st and 4th in February (0.8±0.01 SD to 0.62±0.01 SD μmol L⁻¹ N min⁻¹).

6.3.3 Denitrification rates in sediment exposed to long term oxic or anoxic.

Oxygen availabilities fluctuate within the sediment at the sand flat over a tidal cycle. In order to determine how these fluctuations have shaped the ability of the microbial community to denitrify, we compared the denitrification rates in sediment exposed different oxygen concentrations (i.e. entirely oxic, or entirely anoxic conditions) over longer

time periods. Sediment from the upper layer of the sand flat was kept under alternating oxic/anoxic, constantly oxic or constantly anoxic conditions for weeks. After this time, when aerated, $^{15}\text{NO}_3^-$ amended water was added to the sediment, oxygen consumption was observed in all three conditions (Figure 6.2). Denitrification also occurred in the sediment from all three conditions. No lag was observed between the onset of anoxia and denitrification in any of the conditions, in fact $^{15}\text{N-N}_2$ production began in all the sediments when O_2 concentrations were above $50 \mu\text{mol L}^{-1}$ (Figure 6.2).

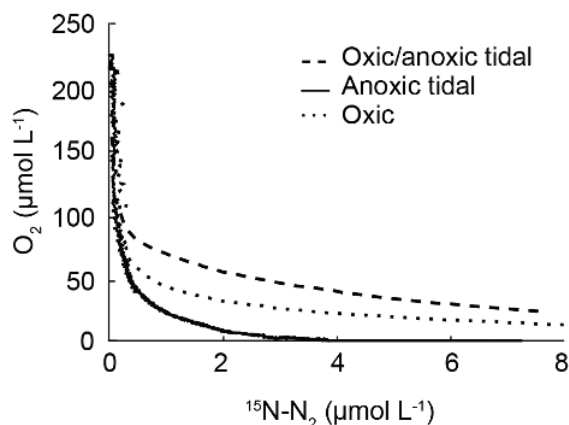


Figure 6.2: Consumption of O_2 and production of $^{15}\text{N-N}_2$ in sediment cores after exposure to different oxygen conditions for three weeks. Sediment was exposed to **a** constant porewater flushing with oxic water. **b** A simulated tidal cycle with anoxic water **c**. A simulated tidal cycle with fluctuating oxic and anoxic conditions.

6.3.4 Terminal oxidase classification in metagenomes

In order to determine how the frequent changes in oxygen conditions shape the respiratory strategies of the microbial within the sediment we focussed on both denitrification genes and terminal oxidases, which we classified as either high or low affinity. Both high affinity (B-class HCO's, C-class HCO's and cyt bd-type oxidases) and low affinity terminal oxidases (A class HCO's) were detected in the metagenomes. Significantly more high affinity terminal oxidases were detected per metagenome (1.73 ± 0.24) than low affinity terminal oxidases (1.17 ± 0.14) (Figure 6.3). Taxonomic assignment of the A-class HCO's revealed that between 7 and 20% were Eukaryota, mainly related to the Opisthokonta and Stramenopiles.

6.3.5 In situ expression of terminal oxidases and functional genes for denitrification across a tidal cycle

Transcriptomic analyses focused on the expression of marker genes for terminal oxidases and functional genes for denitrification over a 12 hour tidal cycle, during which the

sediment was sampled once every two hours. Low affinity terminal oxidases (A-class HCO's) were dominated by bacteria related reads in the metagenome, however in the transcriptomes, half of the total A-class HCO transcripts were most similar to eukaryotic sequences from the Stramenopile and the Opisthokonta. Eukaryote associated A-class HCO gene expression varied over a tidal cycle, with higher relative expression at late low tide, rising tide and high tide (Figure 6.4 b).

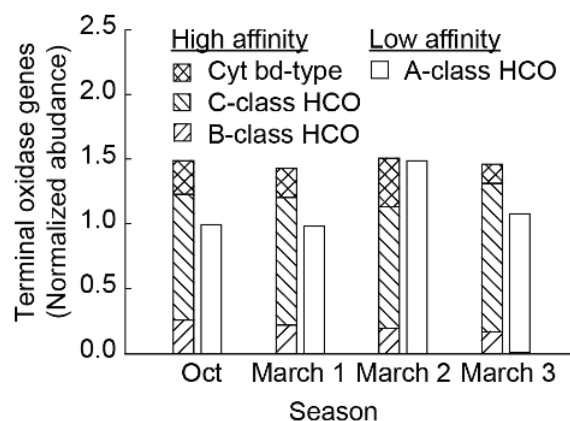


Figure 6.3: Abundance and distribution of terminal oxidase genes in 4 separate metagenomes. Counts were normalized by gene length and to the mean abundance of single copy housekeeping genes in the metagenome.

Of the bacteria associated A-class HCO transcripts, the most common taxonomic assignment was to Proteobacteria; specifically the class Gammaproteobacteria. As Gammaproteobacteria reads were so abundant (up to 1300 per metatranscriptome), further taxonomic assignment was carried out to the order level, where The majority of sequences fell into the orders Alteromonadales, Enterobacteriales, Oceanospirillales and Vibrionales, Over the tidal cycle, bacteria associated A-class HCO gene expression was inverse to that of the Eukaryotes and was relatively higher at falling tide, early low tide and low tide (Figure 6.4 c). The same trend was observed at class level, particularly in the Bacteroidetes and Gammaproteobacteria. At the order level, higher expression of A-class HCO transcripts was also visible at falling tide, early low tide and low tide in Alteromonadales and Vibrionales (Table S2a), however there was a different pattern in the Enterobacteriales; expression of A-class HCO's in this order was highest from rising tide to falling tide.

Of the high affinity terminal oxidase transcripts, Cyt bd-type oxidases were the most abundant, followed by C-class HCO's (Figure 6.4 d-f), only minor expression of B-class HCO's was observed. Expression of the high affinity terminal oxidases followed similar patterns to those of the low affinity terminal oxidases. Most transcripts were taxonomically assigned as Gammaproteobacteria (Figure 6.4 f), specifically to the classes

Alteromonadales and Vibrionales (Table S2). Furthermore, expression was higher at falling tide, early low tide and low tide. As such, when compared to the A-class HCO expression over the tidal cycle, there was a positive correlation between the high affinity terminal oxidases and the low affinity terminal oxidases, this correlation was especially strong for the A-class and C-Class HCO's of the Bacteroidetes, Alteromonadales and Vibrionales (Table S4), and between the A-class HCO's and cyt-BD type terminal oxidases of Actinobacteria, Enterobacteriales and Oceanospirales. Negative correlations between the expression of high and low affinity terminal oxidases were never observed

6.3.6 In situ expression of functional genes for denitrification across a tidal cycle

Transcriptomic analyses of denitrification marker genes focused on the expression of the nitrate and nitrous oxide reductases (*napA*, *narG* and *nosZ*). As the periplasmic nitrate reductase (*napA*) is normally associated with aerobic denitrification, differences in *napA* and *narG* expression might indicate whether specific taxonomic groups are responsible for aerobic denitrification, whereas nitrous oxide reductase is of particular as it mediates the last step in denitrification, whereby N_2 is formed and subsequently lost to the atmosphere. Denitrification genes were expressed within the sediment at all sampling points over the tidal cycle. The most common taxonomic assignment of transcripts for *napA* and *narG* was Proteobacteria; specifically the class Gammaproteobacteria (Figure 6.4 **g-h**) and Table S3 **a-b**). The majority of sequences fell into the orders Alteromonadales, Enterobacteriales, Oceanospirales, Pseudomonadales and Vibrionales. Other transcripts were commonly associated to the phyla Actinobacteria and Planctomycetes. *nosZ* transcripts were mostly assigned to the phyla Bacteroidetes (Figure 6.4 **i** and Table S3 **c**). When the sum of all *napA* transcripts were taken together, there was no clear trend over the tidal cycle (Figure 6.4 **g**). Neither was there a clear trend when the *napA* transcripts from individual Phyla, Class or Order were analyzed. Similar results were obtained for *narG* transcripts. Overall, *napA* transcripts were four times more abundant than *narG* transcripts (Figure 6.4 **g-h**). This was driven by high abundances of Alteromonadales and Vibrionales *napA* transcripts, however in the case of the Actinobacteria, Alphaproteobacteria and Enterobacteriales, *narG* transcripts were significantly more abundant (Table S4). *napA* and *narG* transcript abundance correlated positively within the phyla Bacteroidetes and the order Enterobacteriales (Pearson correlation, $p = < 0.001$ for both), no other correlations were observed. When the sum of all *nosZ* transcripts were taken together, there was a significant difference in transcript abundance over the tidal cycle, *nosZ* transcripts were less abundant at late low tide, rising tide and high tide compared to those from falling tide, early low tide and low tide (student t test $p = < 0.001$). This was mainly driven by changes

in the expression of Bacteroidetes associated *nosZ* (Figure 6.4 i).

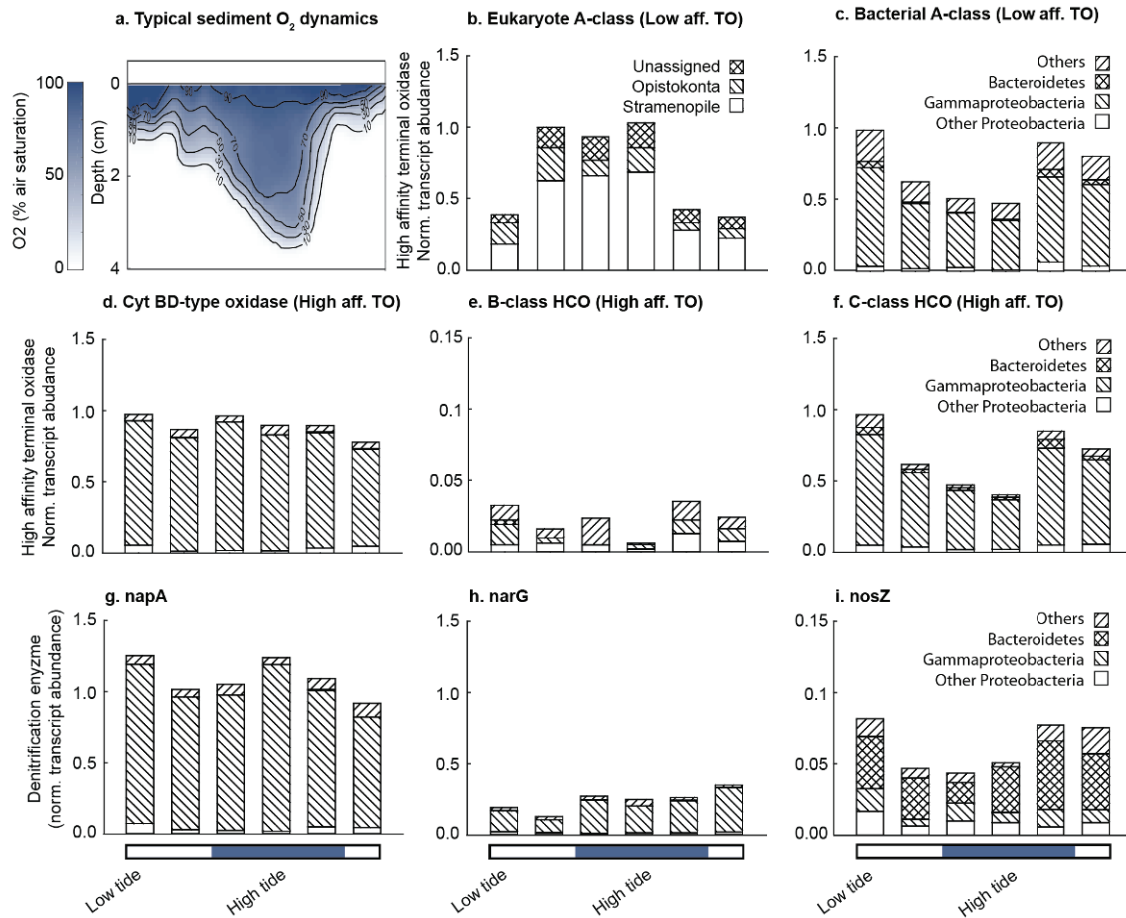


Figure 6.4: Normalized abundance of terminal oxidase and denitrification pathway transcripts in the top 2 cm of the sediment over a tidal cycle **a** Typical oxygen profile within the sediment over a tidal cycle **b – c** low affinity terminal oxidases **d – e** High affinity terminal oxidases **g** periplasmic nitrate reductase **h** membrane bound nitrate reductase **i** nitrous oxide reductase

6.3.7 Denitrification functional gene expression in comparison to terminal oxidase expression

In order to compare the expression patterns of *napA*, *narG* and *nosZ* with the expression patterns of terminal oxidases, the data for each gene pair from was compared on individual XY plots at Phyla, Class and Order level and Pearson Correlation values determined. There was only one case, the Alteromonadales, where expression of a denitrification functional genes (in this case *napA*) negatively correlated with the expression of terminal oxidases (Table S4). In contrast many, positive correlations were observed. Within the Bacteroidetes associated transcripts (which dominated the *nosZ* counts), *nosZ* expression always positively correlated with the expression of A-class HCO's, C-class HCO's and

cyt bd type HCO's (Figure 6.4 c,f,i). Similarly, Bacteroidetes napA and narG expression positively correlated with both A-class HCO and C-class HCO expression (but not cyt bd-type terminal oxidase expression)(Table S4). Positive correlations between napA, narG, and terminal oxidases were also common within the gammaproteobacterial classes (Table S4).

6.4 Discussion

High fluxes of electron acceptors and donors within permeable sandy sediments mean that they act as biocatalytic filters, mediating high rates of respiration. As such permeable sediments have been suggested to contribute extensively to marine N-loss. The extent of this N-loss might be further increased by denitrification occurring in the presence of oxygen. Here, we examined the expression and utilization of the denitrification pathway in natural sediment communities from an intertidal sand-flat where we hypothesize that fluctuating O₂ conditions lead to co-respiration of O₂ and N-oxides.

6.4.1 Simultaneous O₂ consumption and denitrification in permeable sediments

To study how the fluctuating oxygen concentrations in permeable sediments relate to the occurrence of aerobic denitrification within them, we collected sediment from an intertidal sandflat (Janssand) in the Wadden Sea. Over a tidal cycle the upper layer of sediment at the sand flat can generally be described as oxic while the tide is in, and anoxic while the tide is out (Billerbeck et al., 2006). To imitate this in the laboratory we simulated a tidal cycle for 36 – 48 h. This consisted of 12 hours of anoxia, and 12 hours in which we pumped aerated water through the sediment from the bottom of the core. This ensured that microbial community in the bottom centimetre of sediment within the core was exposed to oxygen for part of the day, whereas the rest of the core was anoxic the whole time due to the high O₂ consumption rates in the sediment (Figure S1). After 12 hours of pumping aerated water through the core, the pumping speed of water into the core was increased, exchanging the porewater throughout the sediment core with aerated ¹⁵NO₃⁻ amended water. After this exchange, O₂ consumption rates measured in the bottom of the core were high. Furthermore, a small amount of ¹⁵N₂ production was observed at O₂ concentrations above 100 μmol L⁻¹, indicating that denitrification was never fully inhibited by the presence of O₂(Figure 6.1). As oxygen was consumed, the production of N₂ by denitrification increased, this increase was highest when O₂ concentrations dropped below the calculated half saturation value (k_m) for aerobic respiration (as determined by fitting Michaelis-Menten kinetics, Figure A.6.7).

While the initial incubation imitated the large scale changes in O_2 concentrations over a tidal cycle (i.e. oxic or anoxic), it did not take into account the more complex oxygen dynamics that occur within the sediment when the tide is in. When the sand flat is inundated, advection of O_2 rich water depends on bottom water current velocities, which change over the tidal cycle (for Janssand the highest velocities occur during early rising tide and the lowest during high tide (Gao et al., 2012)). Furthermore, when velocities are high enough, rippled permeable sediments start to move, burying previously oxic sediment and exposing previously anoxic sediment to oxygen (Ahmerkamp et al., 2015). In order to simulate these rapid changes in oxygen concentrations, we repeatedly flushed the sediment with oxic water and then followed respiration rates within the bottom centimeter of sediment over the next 90 minutes (Figure A.6.5). When such repeated incubations were carried out on the same sediment core, the amount of $^{15}N-N_2$ produced at O_2 concentrations above $100 \mu\text{mol L}^{-1}$ increased by more than an order of magnitude, eventually reaching a maximum after 4 cycles. Such a large production of $^{15}N-N_2$ (more than $3 \mu\text{mol L}^{-1}$ was produced) is a clear indication that aerobic denitrification was occurring (see Sup. Material Figure A.6.9 for discussion concerning the low likelihood that denitrification was occurring solely in anoxic microniches). The production of μM concentrations of N_2 in the presence of high O_2 concentrations has not been shown before for marine environments. In fact, in oxygen minimum zones, the other main site of N-loss in the marine environment, denitrification is reversibly inhibited at O_2 concentrations above $2 \mu\text{mol L}^{-1}$ (Dalsgaard et al 2014). Furthermore, the stimulation of aerobic denitrification by repeated switches between oxia and anoxia has not been observed before in either culture or environmental samples.

The stimulation of aerobic denitrification in response to the switches in oxygen concentrations cannot be based on changes in gene expression due to the rapid timescales on which the incubations were carried out. Therefore they are more likely to be metabolic response to environmental conditions, such as changing substrate availabilities. We attribute the increase in aerobic denitrification upon repeated shifts between oxia and anoxia to increased electron donor supply resulting from aerobic breakdown of complex organic matter in the sediment upon re-oxygenation of parts of the core that were anoxic during the previous 36 h period (i.e. everything above the lower cm). As shown in the long term experiments, oxygen consumption rates drop in sediment over longer time periods when oxygen is constantly available, indicating that organic carbon (the electron donor) becomes limiting in the sediment. Therefore in the first incubation, carried out after a 12 h oxygenation period, electron donors rather than electron acceptors were more likely to be limiting respiration within the sediment. However, in subsequent incubations, electron

donor supply to the lower cm of the sediment would have increased as a consequence of reoxygenating the anoxic sediment immediately adjacent to the sediment layer. The products of remineralization that are formed in response to re-oxygenation after anoxia, as well as the less degraded OM from the previously anoxic sediment then percolate into the lower cm during the measurement period. The repeated incubations would push the system progressively into a state where electron donor supply is greater than electron acceptor supply. Imbalances in electron donor and electron acceptor supply, in particular the addition of more reduced carbon substrates have been shown to stimulate aerobic denitrification (Ellington et al., 2002; Sears et al., 1997). When electron donor supply becomes too great, electrons are hypothesized to overflow from the aerobic electron transport chain into the more poorly coupled denitrification enzymes in order to maintain redox homeostasis (Richardson, 2008). In pure cultures which respire nitrate to nitrite via the periplasmic nitrate reductase, electron overflow through the denitrification pathway is around 1% under oxic conditions when reduced carbon sources are supplied (Ellington et al., 2002; Sears et al., 1997). Here, electron flow through the denitrification pathway at O_2 concentrations above $150 \mu\text{mol L}^{-1}$ rose from $<1\%$ during the first incubation to 6% by the 4th and 5th incubation. Since we were measuring full denitrification, (NO_3^- to N_2), which represents the transfer of 2.5 more electrons than reduction of NO_3^- to NO_2^- , the increase in electron flow is in the same range as that seen in culture when reduced carbon substrates are used to stimulate aerobic denitrification.

In the environment, the imbalances in electron donor and electron acceptor supply that stimulate aerobic denitrification are likely to occur due both to the dynamic supply of oxygen into the sediment and the trapping of organic matter. While fluxes of oxygen, nitrate and organic carbon into the sediment are high, the depth to which organic carbon (in the form of particulate organic matter (POM)) penetrates is determined not just by the advective flow of water, but also by the trapping of POM in the sediment matrix (Ehrenhauss, Witte, Bühring and Huettel, 2004; Ehrenhauss, Witte, Janssen and Huettel, 2004). POM is rapidly filtered out in the upper centimeter of the sediment and remobilized when bottom water velocities increase to the extent that sediment starts to move. Such resuspension events expose previously buried POM to the sediment surface (Pilditch and Miller, 2006).

6.4.2 Adaptations in the microbial community leading to aerobic denitrification

It is evident that for aerobic denitrification to occur the entire denitrification pathway must be expressed in the presence of O_2 . After a three week exposure to constantly oxic conditions, denitrification still occurred within the sediment as soon as, or even before, the

sediment became anoxic (Figure 6.2). Therefore it seems that expression of denitrification genes must be constitutive within the sediment, as induction of the denitrification pathway upon anoxia takes hours rather than minutes (Baumann et al., 1996, 1997; Dalsgaard et al., 2014; Zumft, 1997). The rate of anaerobic denitrification that occurred in the sediment previously kept oxic was still a third of the rates measured in sediment that had been kept constantly anoxic or exposed to tidal cycle conditions. This indicates that the facultative denitrifiers persisted under fully oxic conditions, despite the significant maintenance costs associated with expressing an unneeded pathway. These costs are usually high enough that denitrification gene expression is regulated by oxygen concentrations in denitrifiers (Bakken et al., 2012; Bergaust et al., 2008, 2010). Yet, our results suggest that O₂ concentrations play a minor role in the day to day regulation of denitrification pathway expression in permeable sediments. Instead, the rapid fluctuations in O₂ concentrations that occur within these sediments may have shaped the community over longer time scales, reducing the regulatory role of oxygen. After all, in permeable sediments, where oxygen availability is variable, there are also costs associated with both the late induction of the denitrification pathway and with constantly rebuilding the denitrification pathway.

To gain further insights into how the frequent oscillations in O₂ within these sediments have shaped microbial respiration, we carried out metabolic profiling to examine the respiration pathways present and the expression of these pathways over a tidal cycle. We sampled sediment directly from the sand flat over an entire tidal cycle in order to capture the natural responses of the community respiratory gene expression to diurnal changes in in situ oxygen concentrations (Figure 6.4 a). Diverse terminal oxidase (which catalyze the terminal electron transfer in aerobic respiration) and denitrification pathway marker genes were present within DNA extracted from the upper layer of sediment (Figure 6.3). When normalized to single copy housekeeping genes, the abundance of the terminal oxidases was in the same range as that found in soils, but higher than the abundance observed in environments where O₂ concentrations are more stable (i.e. the open ocean or animal guts) (Morris and Schmidt, 2013). In such stable environments, which are either constantly oxic, or constantly anoxic, either low or high affinity terminal oxidases tend to dominate (Morris and Schmidt, 2013). In contrast, within the permeable sediments studied here there was a similar relative abundance of low affinity A-class haem-copper oxidases (HCO's) and high affinity C-class HCO's. The high abundance and even distribution of high and low affinity terminal oxidases indicate that the aerobes within the intertidal permeable sediment are more likely to possess multiple terminal oxidases than in stable environments. This would confer greater metabolic versatility and enable the microbial community to better exploit the fluctuating O₂ concentrations (Poole and Cook, 2000).

Microbes encoding multiple terminal oxidases are able to fine tune the expression of their high and low affinity terminal oxidases in response to O₂ concentrations (Vasil and Clark, 2011; Otten et al., 2001; Poole and Cook, 2000; Tseng et al., 1996). However, we could find no evidence for differential expression of high and low affinity bacterial terminal oxidases across a tidal cycle as O₂ concentrations changed (Figure 6.4 c-f). This contrasts with other environmental studies, where switches in expression of low and high affinity terminal oxidases have been observed over oxic-anoxic gradients. However in other studies, the changes in oxygen concentration occurred at time scales of weeks, or over spatial scales of metres (Eggleston et al., 2015; Hewson et al., 2014; Kalvelage et al., 2015; Schunck et al., 2013). In permeable sediments, changes in oxygen concentration happen over minutes and hours and at spatial scales of mm - cm.

In fact our evidence indicates that bacterial terminal oxidase expression is not correlated with changes in oxygen availability over a tidal cycle in Wadden Sea permeable sediments (Figure 6.3). Instead, bacterial low affinity terminal oxidase expression was strongly correlated to high affinity terminal oxidase expression at the class and order level, with expression of both dropping at late low tide, rising tide and high tide. These sampling points represent very different oxygen concentrations within the sediment, at late low tide oxygen availability is low within the sediment, having been consumed while the tide is out, whereas at rising tide and high tide oxygen availability increases rapidly as the sand flat is inundated with water and oxygen is supplied by advective forces.

Interestingly, the expression of eukaryote low affinity terminal oxidases also did not correlate well with O₂ concentrations, however, it was the inverse of the bacterial terminal oxidase expression. This could reflect differences in the energy demands of the bacteria and eukaryotes over the tidal cycle, and suggests that the respiratory apparatus of the eukaryotes in the sediment is regulated by different factors. These could be related to circadian rhythms or light, as most of the identified eukaryotes were Stramenopiles, and most likely diatoms, which are abundant in the surface layer of the sediment (Marchant et al., 2014; Stief et al., 2013). Repeated sampling during a period when high tide falls overnight could help to unravel this observation.

Genes for the entire denitrification pathway were also expressed at all time points across the tidal cycle regardless of the ambient oxygen concentration (Table S4). The expression of the marker gene for the periplasmic nitrate reductase (NapA) was almost 4 times greater than the expression of that for the membrane bound nitrate reductase (NarG). Predominance of Nap in certain marine systems has been attributed to its high affinity for nitrate (Dong et al., 2009; Smith et al., 2007; Vetriani et al., 2014). However, nitrate is rarely limiting in the permeable sediments of the Wadden Sea (Gao et al., 2012).

This suggests that the dominance of Nap is likely due to the physiological role that it plays during aerobic denitrification. Bacteria which carry out aerobic denitrification have frequently been shown to use Nap rather than Nar (Bell et al., 1990; Richardson and Ferguson, 1992), as its position in the periplasm and independence from cytochrome bc₁ means that it is poorly coupled to the ETC and can be used to maintain cellular redox balance.

Strikingly, there was no correlation between the expression pattern of napA, narG and nosZ and the diurnal changes in O₂ levels within the sediment. Instead, at the phyla, class and order level, expression of denitrification genes correlated with that of the high and low affinity terminal oxidases (Figure 6.3). A positive correlation between high affinity terminal oxidases and denitrification gene expression might not be unexpected, as both are known to be expressed under low O₂ conditions. However, the concurrent upregulation of low affinity terminal oxidase and denitrification gene expression strongly indicates that the broad changes in O₂ availability over a tidal cycle do not control expression of the respiratory pathways. Instead it seems that another factor must regulate expression of both terminal oxidases and alternate terminal electron acceptors i.e. for example redox balance between electron acceptor and donor supply (Iuchi and Lin, 1993; Otten et al., 1999; Taylor and Zhulin, 1999).

The distribution of Nap and Nar expression and the co-expression patterns observed between denitrification genes and terminal oxidases persisted even at the class and order level. This evidence, combined with the observations that a large proportion of the community appear to constitutively express the denitrification pathway, strongly suggests that no-one particular group of organisms is responsible for aerobic denitrification within these sediments, but rather the trait is selected for throughout the community.

6.5 Environmental implications and conclusions

Within the permeable sediments studied here, aerobic denitrification at high O₂ concentrations occurred due to a relaxed regulation by oxygen on expression of respiratory genes. Such a relaxation has likely occurred in order to allow microbes to exploit the large but periodic supply of electron acceptors that are supplied by advective porewater flux. Here, we have focused on intertidal sediments that are exposed to large fluctuations in O₂ availability over a daily cycle. However, even permanently inundated subtidal sandy sediments experience large fluctuations in O₂ depending on flow velocity and sediment redistribution (Ahmerkamp et al., 2015). We have observed denitrification occurring immediately when subtidal sediments kept oxic for a month were allowed to become anoxic (unpub. data).

Therefore, it is likely the same decrease in regulation by O₂ occurs in subtidal sediments, driving the aerobic denitrification that has reported previously (Marchant et al., 2016; Rao et al., 2007). While aerobic denitrification contributes little to the overall energy conservation by respiration in permeable sediments, in terms of N₂ production it can be substantial. Here we observed aerobic denitrification rates that were 60 % of the maximal anaerobic denitrification rate - rates which are amongst the highest measured in the marine environment (Gao et al., 2012; Gihring et al., 2010). Sandy sediments cover up to 58 -70 % of the continental shelves (Emery, 1968), and the growing consensus is that they are extremely important sites of N-loss (Devol, 2015; Huettel et al., 2014). It therefore appears that aerobic denitrification might not just be a fascinating process in regards to the kinetics and bioenergetics of branched respiratory pathways, but an important process in the marine nitrogen cycle.

Currently estimates of N-loss from permeable sediments are poorly constrained (Huettel et al., 2014), largely due to the difficulties of modeling biogeochemical transformations in such complex environments. However estimates of O₂ and N fluxes from permeable sediments are improving constantly due to the application of 2D reactive-transport models (Ahmerkamp et al., 2015; Cardenas et al., 2008). The occurrence of aerobic denitrification is currently not considered in these biogeochemical models, which rely on the kinetics of reaction rates for aerobic respiration and denitrification. We have shown that these rates are governed not only by kinetics but also by metabolic responses to changing electron donor and acceptor availability. If, as seems likely, the potential for aerobic denitrification is inherently selected for by the dynamic conditions that characterize permeable sands, then aerobic denitrification should be considered in permeable sediment models going forward.

6.6 Supplementary information

6.6.1 Addition methods

RNA extraction and sequencing

RNA was extracted using TRI Reagent solution (Ambion). Briefly, RNA preservation solution was removed after 10 min centrifugation, 5 volumes of TRI Reagent solution were added, and 1 volume sterile glass beads (0.1 mm diameter). Cells were lysed by bead beating for 45 sec at 6.5 m/s, followed by 5 min incubation at RT and 10 min centrifugation at 4500 x g and 4° C. From the supernatant, RNA was extracted by adding 200 µL Chloroform per 1 mL of added TRI reagent, vigorous shaking, incubation at RT for 10 min and centrifugation at 12000 x g and 4° C for 15 min. The upper phase was transferred to a fresh tube, and RNA was precipitated on ice for 15 min after adding 500 µL of ice cold isopropanol per 1 ml of TRI reagent. Pelleted RNA was washed twice with 75% Ethanol, the pellets were air dried and re-dissolved in TE buffer. rRNA was partially depleted with the MICROBExpressTM Bacterial mRNA Enrichment Kit (Ambion). Six random-primed, barcoded cDNA libraries were generated (by Vertis Biotechnologie AG, Freising, Germany) for illumina sequencing, one for each sampling time point. For each library enriched mRNA resulting from 2-3 ml sediment sample was used. Briefly, RNA was fragmented by sonication, random primed cDNA was generated, barcoded TruSeq sequencing adapters were ligated to the cDNA fragments, and the library was PCR amplified using a high fidelity DNA polymerase. For sequencing, library fragments of size range 300-550bp were eluted from a preparative agarose gel.

Metagenome data analysis

For terminal oxidases, reference gene sets from Morris et al 2013 and Sousa et al 2011 were aligned with ClustalW (Larkin et al. 2006) and used to construct profile HMM using the hmmbuild tool in the in the HMMER software package (Version 3.1b2; February 2015, <http://hmmer.org/>) The translated sequences were queried with the profile HMMs using hmmsearch. Matching sequences were manually validated via a blastp search against a local copy of the NCBI nr database (downloaded 31.08.2015 from <ftp://ftp.ncbi.nlm.nih.gov/blast/db/>). A sequence was considered as a terminal oxidase if there was a blastp hit of the expected terminal oxidase in the first 10 hits for each read.

For napA, narG and nosZ, a collection of selected protein sequences for each functional gene of interest was used for a tblastn search against the metagenomic reads (E-value cutoff 0.001). For an automated validation procedure of the reads with a hit in this tblastn search, a gene validation database was set up, by extracting protein sequences from all prokaryotic sequenced genomes available at NCBI (<FTP://ftp.ncbi.nlm.nih.gov/genomes/Bacteria>), file:

all.gbk.tar.gz, downloaded on: 08. Oct. 2010) and removing identical sequences using the uclust software (Edgar 2010) (version 3.0). Additionally, available (putative) protein sequences of the functional genes of interest from uncultured prokaryotes were retrieved from Uniprot and from FunGene (<http://www.uniprot.org>, <http://fungene.cme.msu.edu/index.spr>, download on: 24. Feb. 2011). To decrease redundancy, the retrieved sequences were clustered at 90% identity using the uclust software (Edgar 2010), and only the seed sequences of the resulting clusters were marked as environmental and added to the gene validation database. All of the protein sequences used for the initial tblastn search of the metagenomes that were hit by a metagenomic sequence, were tagged as functional protein of interest and temporarily added to the validation database. The reads with a hit in the initial tblastn search were validated by translating them into the respective amino acid sequences and performing a blastp search (no E-value cutoff) against the validation database including the tagged sequences. Based on prior manual evaluation, a read was considered as validated if in this blastp search a hit with a tagged sequence (of the expected functional gene) was among the first 50 hits for this read. Additionally, reads retrieved in the functional genes search of the MG-RAST analysis platform (Meyer et al. 2008) (<http://metagenomics.anl.gov/> search reference database: M5NR) that were not detected by the automated validation, were added to the collection of the automatically validated reads. All reads in this collection were then manually curated to remove false positives of the automatic validation procedure and the MG-RAST analysis. The automated validation procedure yielded reads that were not detected by the search via MG-RAST, and vice versa.

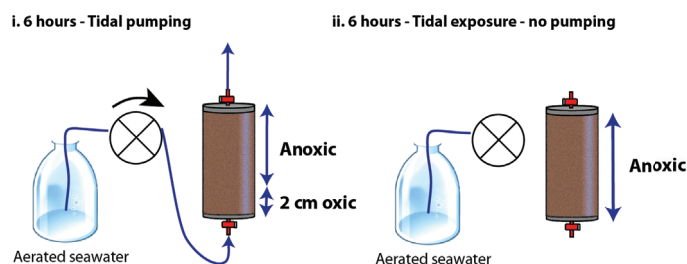
6.6.2 Metatranscriptome data analysis

Identification of functional genes was carried out after reviewed sequences for each gene of interest were retrieved from the UniProtKB database (<http://www.uniprot.org>) in August 2015. A seed alignment was generated with ClustalW (Larkin), further sequences retrieved from the metagenomes were subsequently added to the seed alignment. Profile HMMs were then generated and searched against the translated sequence data sets. Subsequently, validation was carried out after a blastp search as above. The same protocol was followed for housekeeping genes.

6.6.3 Additional figures

Supplementary tables are available upon request.

1. 24-36 hour acclimatization of sediment simulating large scale tidal dynamics



2. Incubations simulating fine scale sediment dynamics

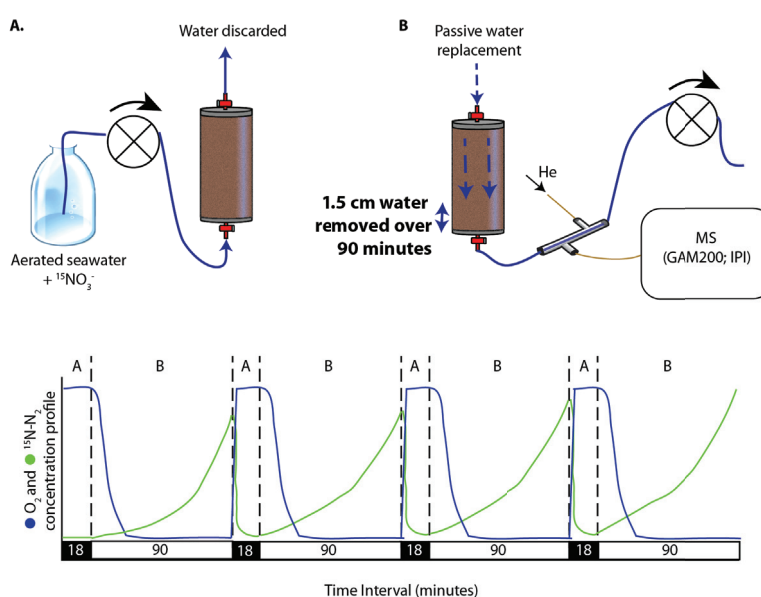


Figure A.6.5: Schematic of the incubation set-up. 1) Sediment was packed into sediment cores and then kept in the laboratory for 24 - 36 hours before the incubation was started. During this time it was exposed to a simulated tidal cycle, consisting of 6 hours in which aerated seawater was pumped into the core, causing the bottom 2 cm to be oxic, during the subsequent 6 hour period no pumping occurred and the entire core rapidly became anoxic. 2) At the beginning of incubations, aerated seawater was amended with $^{15}\text{NO}_3^-$ and then pumped through the core from the bottom until all of the porewater in the core was exchanged with the ^{15}N -labelled, aerated seawater (18 minutes). B) Porewater was then pumped out of the bottom of the core (at a rate of $400 \mu\text{L min}^{-1}$) by a peristaltic pump which was placed downstream of a membrane inlet attached to a quadrupole mass spectrometer (MIMS) set to measure the masses of 28, 29, 30, 32 and 40 (N_2 , O_2 and Ar) once every 4 seconds. After 90 minutes, the core was removed from the MIMS and porewater was again exchanged with ^{15}N -labelled, aerated seawater. Concurrently, the MIMS was recalibrated with aerated seawater.

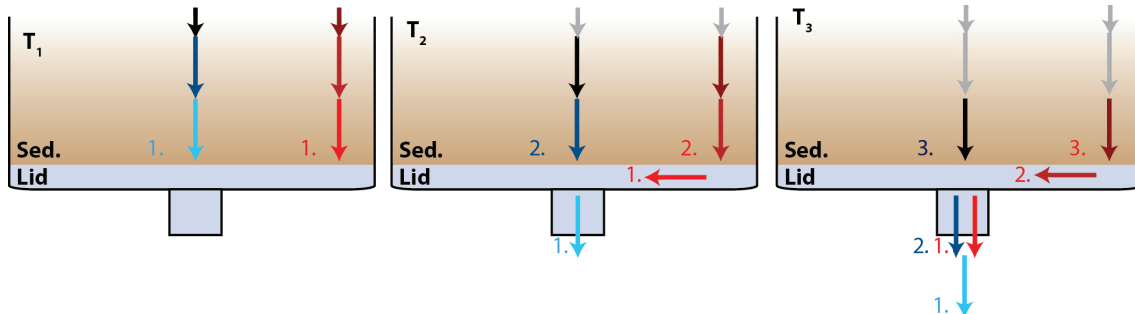


Figure A.6.6: Mixing and dispersion effects within the lid of the sediment core that lead to “smearing” effects within the data. Lines indicate the flow of water, while numbers indicate age of water within the sediment.

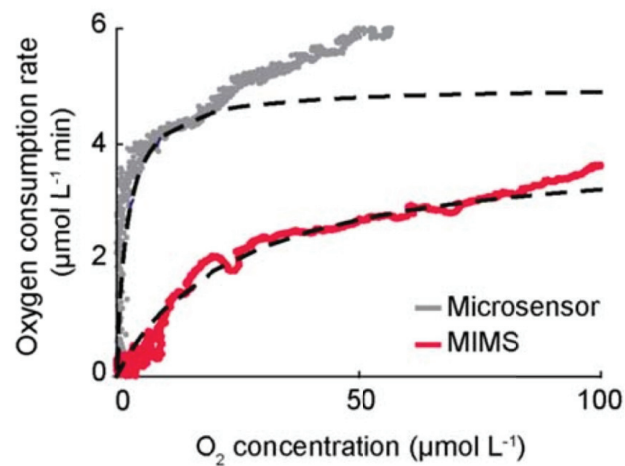


Figure A.6.7: Oxygen consumption kinetics in sediment measured in a flow through sediment core with the MIMS setup or with a microsensor placed at one spot in a percolated sediment core. Dashed lines show the Michaelis-Menten fit used to calculate K_m values for the lower part of the curve.

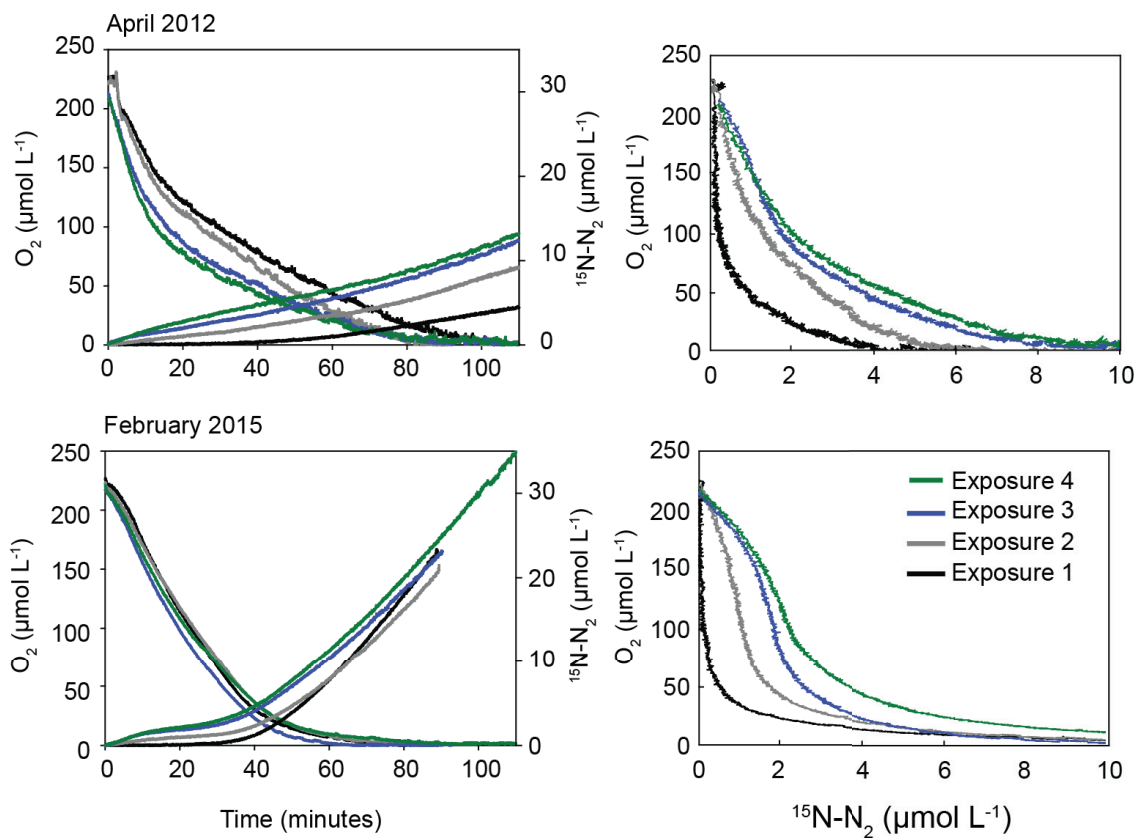


Figure A.6.8: Seasonal replicates of oxygen and denitrification dynamics in sediment exposed to shifts between anoxic and oxic conditions. Left panels: Consumption of O_2 and production of $^{15}N-N_2$ in the December incubation. Right panels: Comparison of O_2 concentrations and N_2 concentrations in the incubations.

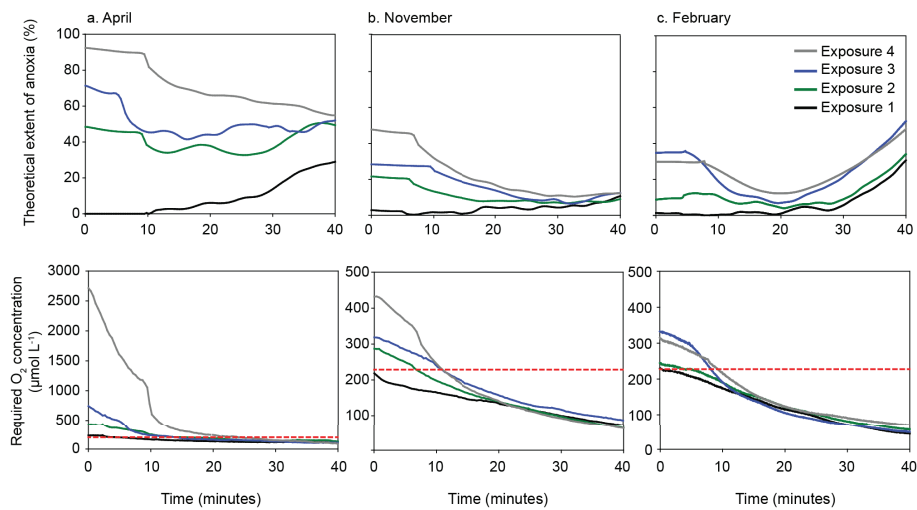


Figure A.6.9: Comparison of bulk oxygen concentrations in the porewater of the sediment against the denitrification rates obtained under anoxia and oxia indicated that the denitrification observed at high oxygen concentrations could not have occurred solely in anoxic microsites. Especially during the 2nd - 4th exposures to oxic conditions, denitrification rates at high oxygen concentrations were very high - between 50 and 90 % of the maximal denitrification rate observed during anoxia. Therefore, were these rates occurring in anoxic parts of the core, between 50 and 90 % of the sediment would have to be anoxic. If the volume of anoxic microsites were so large, then oxygen would have had to be super-saturated (in respect to air equilibration values) in the rest of the porewater for the bulk measured O_2 concentration to be possible. Upper panels: Theoretical extent of anoxia within the sediment if anoxic microsites were wholly responsible for the denitrification rates calculated from the incubations. Lower panels: Oxygen concentration required in the remainder of the core to give the bulk O_2 concentrations observed. The dashed red line in the lower panels represents oxygen saturation values for seawater at the measured temperature and salinity.

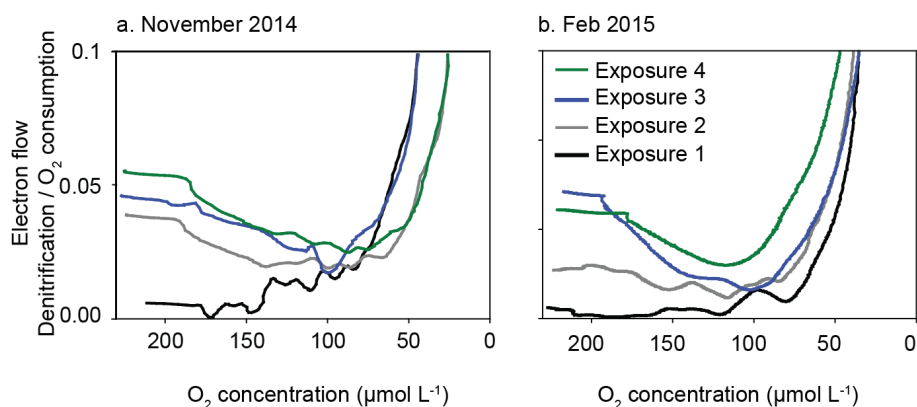


Figure A.6.10: Ratio of electrons flowing through the denitrification pathway compared to the oxygen respiration pathway

Bibliography

- Ahmerkamp, S., Winter, C., Janssen, F., Kuypers, M. M. and Holtappels, M. (2015), 'The impact of bedform migration on benthic oxygen fluxes', *Journal of Geophysical Research: Biogeosciences* **120**(11), 2229–2242.
- Bakken, L. R., Bergaust, L., Liu, B. and Frostegård, Å. (2012), 'Regulation of denitrification at the cellular level: a clue to the understanding of n₂o emissions from soils', *Phil. Trans. R. Soc. B* **367**(1593), 1226–1234.
- Baumann, B., Snozzi, M., Zehnder, A. and Van Der Meer, J. R. (1996), 'Dynamics of denitrification activity of paracoccus denitrificans in continuous culture during aerobic-anaerobic changes.', *Journal of Bacteriology* **178**(15), 4367–4374.
- Baumann, B., van der Meer, J. R., Snozzi, M. and Zehnder, A. J. (1997), 'Inhibition of denitrification activity but not of mrna induction in paracoccus denitrificans by nitrite at a suboptimal ph', *Antonie van Leeuwenhoek* **72**(3), 183–189.
- Bell, L. C., Richardson, D. J. and Ferguson, S. J. (1990), 'Periplasmic and membrane-bound respiratory nitrate reductases in thiosphaera pantotropha', *FEBS letters* **265**(1-2), 85–87.
- Bergaust, L., Mao, Y., Bakken, L. R. and Frostegård, Å. (2010), 'Denitrification response patterns during the transition to anoxic respiration and posttranscriptional effects of suboptimal ph on nitrogen oxide reductase in paracoccus denitrificans', *Applied and environmental microbiology* **76**(19), 6387–6396.
- Bergaust, L., Shapleigh, J., Frostegård, Å. and Bakken, L. (2008), 'Transcription and activities of nox reductases in agrobacterium tumefaciens: the influence of nitrate, nitrite and oxygen availability', *Environmental microbiology* **10**(11), 3070–3081.
- Bergaust, L., van Spanning, R. J., Frostegård, Å. and Bakken, L. R. (2012), 'Expression of nitrous oxide reductase in paracoccus denitrificans is regulated by oxygen and nitric oxide through fnrp and nnr', *Microbiology* **158**(3), 826–834.
- Billerbeck, M., Werner, U., Polerecky, L., Walpersdorf, E., DeBeer, D., Huettel, M. et al. (2006), 'Surficial and deep pore water circulation governs spatial and temporal scales of nutrient recycling in intertidal sand flat sediment', *Marine Ecology Progress Series* **326**, 61–76.
- Bolger, A. M., Lohse, M. and Usadel, B. (2014), 'Trimmomatic: a flexible trimmer for illumina sequence data', *Bioinformatics* p. btu170.

- Cardenas, M. B., Cook, P. L., Jiang, H. and Traykovski, P. (2008), 'Constraining denitrification in permeable wave-influenced marine sediment using linked hydrodynamic and biogeochemical modeling', *Earth and Planetary Science Letters* **275**(1), 127–137.
- Dalsgaard, T., Stewart, F. J., Thamdrup, B., De Brabandere, L., Revsbech, N. P., Ulloa, O., Canfield, D. E. and DeLong, E. F. (2014), 'Oxygen at nanomolar levels reversibly suppresses process rates and gene expression in anammox and denitrification in the oxygen minimum zone off northern chile', *MBio* **5**(6), e01966–14.
- de Beer, D., Wenzhöfer, F., Ferdelman, T. G., Boehme, S. E., Huettel, M., van Beusekom, J. E., Böttcher, M. E., Musat, N. and Dubilier, N. (2005), 'Transport and mineralization rates in north sea sandy intertidal sediments, sylvt-rømø basin, wadden sea', *Limnology and Oceanography* **50**(1), 113–127.
- Devol, A. H. (2015), 'Denitrification, anammox, and n₂ production in marine sediments', *Annual review of marine science* **7**, 403–423.
- Dong, L. F., Smith, C. J., Papaspyrou, S., Stott, A., Osborn, A. M. and Nedwell, D. B. (2009), 'Changes in benthic denitrification, nitrate ammonification, and anammox process rates and nitrate and nitrite reductase gene abundances along an estuarine nutrient gradient (the colne estuary, united kingdom)', *Applied and environmental microbiology* **75**(10), 3171–3179.
- Eggleston, E. M., Lee, D. Y., Owens, M. S., Cornwell, J. C., Crump, B. C. and Hewson, I. (2015), 'Key respiratory genes elucidate bacterial community respiration in a seasonally anoxic estuary', *Environmental microbiology* **17**(7), 2306–2318.
- Ehrenhauss, S., Witte, U., Bühring, S. I. and Huettel, M. (2004), 'Effect of advective pore water transport on distribution and degradation of diatoms in permeable north sea sediments', *Marine ecology. Progress series* **271**, 99–111.
- Ehrenhauss, S., Witte, U., Janssen, F. and Huettel, M. (2004), 'Decomposition of diatoms and nutrient dynamics in permeable north sea sediments', *Continental Shelf Research* **24**(6), 721–737.
- Ellington, M., Bhakoo, K., Sawers, G., Richardson, D. and Ferguson, S. (2002), 'Hierarchy of carbon source selection in paracoccus pantotrophus: strict correlation between reduction state of the carbon substrate and aerobic expression of the nap operon', *Journal of bacteriology* **184**(17), 4767–4774.

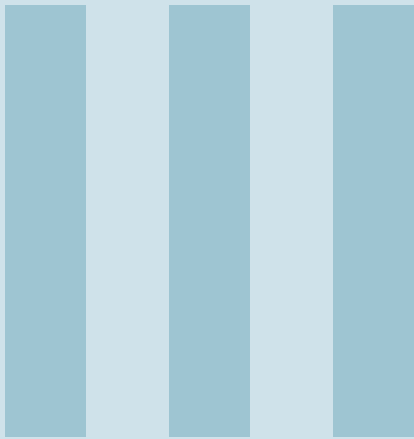
- Emery, K. (1968), 'Relict sediments on continental shelves of world', *AAPG Bulletin* **52**(3), 445–464.
- Frette, L., Gejlsbjerg, B. and Westermann, P. (1997), 'Aerobic denitrifiers isolated from an alternating activated sludge system', *FEMS Microbiology Ecology* **24**(4), 363–370.
- Galloway, J. N., Dentener, F. J., Capone, D. G., Boyer, E. W., Howarth, R. W., Seitzinger, S. P., Asner, G. P., Cleveland, C., Green, P., Holland, E. et al. (2004), 'Nitrogen cycles: past, present, and future', *Biogeochemistry* **70**(2), 153–226.
- Gao, H., Matyka, M., Liu, B., Khalili, A., Kostka, J. E., Collins, G., Jansen, S., Holtappels, M., Jensen, M. M., Badewien, T. H. et al. (2012), 'Intensive and extensive nitrogen loss from intertidal permeable sediments of the wadden sea', *Limnology and Oceanography* **57**(1), 185.
- Gao, H., Schreiber, F., Collins, G., Jensen, M. M., Kostka, J. E., Lavik, G., de Beer, D., Zhou, H.-y. and Kuypers, M. M. (2010), 'Aerobic denitrification in permeable wadden sea sediments', *The ISME journal* **4**(3), 417–426.
- Gihring, T. M., Canion, A., Riggs, A., Huettel, M. and Kostka, J. E. (2010), 'Denitrification in shallow, sublittoral gulf of mexico permeable sediments', *Limnology and Oceanography* **55**(1), 43–54.
- Hewson, I., Eggleston, E. M., Doherty, M., Lee, D. Y., Owens, M., Shapleigh, J. P., Cornwell, J. C. and Crump, B. C. (2014), 'Metatranscriptomic analyses of plankton communities inhabiting surface and subpycnocline waters of the chesapeake bay during oxic-anoxic-oxic transitions', *Applied and environmental microbiology* **80**(1), 328–338.
- Huettel, M., Berg, P. and Kostka, J. E. (2014), 'Benthic exchange and biogeochemical cycling in permeable sediments', *Marine Science* **6**.
- Huettel, M., Røy, H., Precht, E. and Ehrenhauss, S. (2003), Hydrodynamical impact on biogeochemical processes in aquatic sediments, in 'The Interactions between Sediments and Water', Springer, pp. 231–236.
- Huson, D. H., Mitra, S., Ruscheweyh, H.-J., Weber, N. and Schuster, S. C. (2011), 'Integrative analysis of environmental sequences using megan4', *Genome research* **21**(9), 1552–1560.

- Hyatt, D., Chen, G.-L., LoCascio, P. F., Land, M. L., Larimer, F. W. and Hauser, L. J. (2010), 'Prodigal: prokaryotic gene recognition and translation initiation site identification', *BMC bioinformatics* **11**(1), 1.
- Iuchi, S. and Lin, E. (1993), 'Adaptation of escherichia coli to redox environments by gene expression', *Molecular microbiology* **9**(1), 9–15.
- Kalvelage, T., Lavik, G., Jensen, M. M., Revsbech, N. P., Löscher, C., Schunck, H., Desai, D. K., Hauss, H., Kiko, R., Holtappels, M. et al. (2015), 'Aerobic microbial respiration in oceanic oxygen minimum zones', *PloS one* **10**(7), e0133526.
- Kim, M., Jeong, S.-Y., Yoon, S. J., Cho, S. J., Kim, Y. H., Kim, M. J., Ryu, E. Y. and Lee, S.-J. (2008), 'Aerobic denitrification of pseudomonas putida ad-21 at different c/n ratios', *Journal of bioscience and bioengineering* **106**(5), 498–502.
- Kopylova, E., Noé, L. and Touzet, H. (2012), 'Sortmerna: fast and accurate filtering of ribosomal rnas in metatranscriptomic data', *Bioinformatics* **28**(24), 3211–3217.
- Li, W. and Godzik, A. (2006), 'Cd-hit: a fast program for clustering and comparing large sets of protein or nucleotide sequences', *Bioinformatics* **22**(13), 1658–1659.
- Marchant, H. K., Holtappels, M., Lavik, G., Ahmerkamp, S., Winter, C. and Kuypers, M. M. (2016), 'Coupled nitrification–denitrification leads to extensive n loss in subtidal permeable sediments', *Limnology and Oceanography* .
- Marchant, H. K., Lavik, G., Holtappels, M. and Kuypers, M. M. (2014), 'The fate of nitrate in intertidal permeable sediments', *PloS one* **9**(8), e104517.
- Morris, R. L. and Schmidt, T. M. (2013), 'Shallow breathing: bacterial life at low o₂', *Nature Reviews Microbiology* **11**(3), 205–212.
- Otten, M. F., Reijnders, W. N., Bedaux, J. J., Westerhoff, H. V., Krab, K. and Van Spanning, R. J. (1999), 'The reduction state of the q-pool regulates the electron flux through the branched respiratory network of paracoccus denitrificans', *European Journal of Biochemistry* **261**(3), 767–774.
- Otten, M. F., Stork, D. M., Reijnders, W. N., Westerhoff, H. V. and Van Spanning, R. J. (2001), 'Regulation of expression of terminal oxidases in paracoccus denitrificans', *European Journal of Biochemistry* **268**(8), 2486–2497.

- Patureau, D., Davison, J., Bernet, N. and Moletta, R. (1994), 'Denitrification under various aeration conditions in *comamonas* sp., strain sgly2', *FEMS Microbiology Ecology* **14**(1), 71–78.
- Patureau, D., Zumstein, E., Delgenes, J. and Moletta, R. (2000), 'Aerobic denitrifiers isolated from diverse natural and managed ecosystems', *Microbial ecology* **39**(2), 145–152.
- Pilditch, C. A. and Miller, D. C. (2006), 'Phytoplankton deposition to permeable sediments under oscillatory flow: Effects of ripple geometry and resuspension', *Continental shelf research* **26**(15), 1806–1825.
- Polerecky, L., Franke, U., Werner, U., Grunwald, B. and de Beer, D. (2005), 'High spatial resolution measurement of oxygen consumption rates in permeable sediments', *Limnol. Oceanogr. Methods* **3**, 75–85.
- Poole, R. K. and Cook, G. M. (2000), 'Redundancy of aerobic respiratory chains in bacteria? routes, reasons and regulation', *Advances in microbial physiology* **43**, 165–224.
- Rao, A. M., McCarthy, M. J., Gardner, W. S. and Jahnke, R. A. (2007), 'Respiration and denitrification in permeable continental shelf deposits on the south atlantic bight: Rates of carbon and nitrogen cycling from sediment column experiments', *Continental Shelf Research* **27**(13), 1801–1819.
- Rao, A. M., McCarthy, M. J., Gardner, W. S. and Jahnke, R. A. (2008), 'Respiration and denitrification in permeable continental shelf deposits on the south atlantic bight: N 2: Ar and isotope pairing measurements in sediment column experiments', *Continental Shelf Research* **28**(4), 602–613.
- Richardson, D. J. (2008), Structural and functional flexibility of bacterial respiromes, in 'Bacterial Physiology', Springer, pp. 97–128.
- Richardson, D. J. and Ferguson, S. J. (1992), 'The influence of carbon substrate on the activity of the periplasmic nitrate reductase in aerobically grown *thiosphaera pantotropha*', *Archives of microbiology* **157**(6), 535–537.
- Robertson, L. A., Dalsgaard, T., Revsbech, N.-P. and Kuenen, J. G. (1995), 'Confirmation of 'aerobic denitrification' in batch cultures, using gas chromatography and ¹⁵n mass spectrometry', *FEMS Microbiology Ecology* **18**(2), 113–120.

- Robertson, L. A. and Kuenen, J. G. (1990), 'Combined heterotrophic nitrification and aerobic denitrification in thiosphaera pantotropha and other bacteria', *Antonie van Leeuwenhoek* **57**(3), 139–152.
- Robertson, L. and Kuenen, J. (1984), 'Aerobic denitrification—old wine in new bottles?', *Antonie van Leeuwenhoek* **50**(5-6), 525–544.
- Rusch, A., Forster, S. and Huettel, M. (2001), 'Bacteria, diatoms and detritus in an intertidal sandflat subject to advective transport across the water-sediment interface', *Biogeochemistry* **55**(1), 1–27.
- Schunck, H., Lavik, G., Desai, D. K., Großkopf, T., Kalvelage, T., Löscher, C. R., Paulmier, A., Contreras, S., Siegel, H., Holtappels, M. et al. (2013), 'Giant hydrogen sulfide plume in the oxygen minimum zone off peru supports chemolithoautotrophy', *PLoS One* **8**(8), e68661.
- Sears, H. J., Spiro, S. and Richardson, D. J. (1997), 'Effect of carbon substrate and aeration on nitrate reduction and expression of the periplasmic and membrane-bound nitrate reductases in carbon-limited continuous cultures of paracoccus denitrificans pd1222', *Microbiology* **143**(12), 3767–3774.
- Sharma, P., Hellingwerf, K. J., de Mattos, M. J. T. and Bekker, M. (2012), 'Uncoupling of substrate-level phosphorylation in escherichia coli during glucose-limited growth', *Applied and environmental microbiology* **78**(19), 6908–6913.
- Smith, C. J., Nedwell, D. B., Dong, L. F. and Osborn, A. M. (2007), 'Diversity and abundance of nitrate reductase genes (narg and napa), nitrite reductase genes (nirs and nrfa), and their transcripts in estuarine sediments', *Applied and Environmental Microbiology* **73**(11), 3612–3622.
- Sousa, F. L., Alves, R. J., Pereira-Leal, J. B., Teixeira, M. and Pereira, M. M. (2011), 'A bioinformatics classifier and database for heme-copper oxygen reductases', *PLoS One* **6**(4), e19117.
- Stief, P., Kamp, A. and de Beer, D. (2013), 'Role of diatoms in the spatial-temporal distribution of intracellular nitrate in intertidal sediment', *PloS one* **8**(9), e73257.
- Taylor, B. L. and Zhulin, I. B. (1999), 'Pas domains: internal sensors of oxygen, redox potential, and light', *Microbiology and Molecular Biology Reviews* **63**(2), 479–506.

- Tseng, C.-P., Albrecht, J. and Gunsalus, R. P. (1996), 'Effect of microaerophilic cell growth conditions on expression of the aerobic (cyoabcde and cydab) and anaerobic (narghji, frdabcd, and dmsabc) respiratory pathway genes in escherichia coli.', *Journal of bacteriology* **178**(4), 1094–1098.
- Vasil, M. L. and Clark, V. (2011), 'Regulation and function of versatile aerobic and anaerobic respiratory metabolism in pseudomonas aeruginosa', *Pseudomonas Aeruginosa, Biology, Genetics, and Host-pathogen Interactions* p. 36.
- Vetriani, C., Voordeckers, J. W., Crespo-Medina, M., O'Brien, C. E., Giovannelli, D. and Lutz, R. A. (2014), 'Deep-sea hydrothermal vent epsilonproteobacteria encode a conserved and widespread nitrate reduction pathway (nap)', *The ISME journal* **8**(7), 1510–1521.
- Zumft, W. G. (1997), 'Cell biology and molecular basis of denitrification.', *Microbiology and molecular biology reviews* **61**(4), 533–616.



Implications for the Environment

| | | |
|----------|---|------------|
| 7 | Implications for the Environment | 221 |
| 7.1 | Discussion & Outlook | |
| 7.2 | Quantification | |
| 7.3 | Bibliography | |
| 8 | Acknowledgements | 233 |

7. Implications for the Environment

7.1 Discussion & Outlook

The important role played by sandy sediments in global biogeochemical cycling was only identified the last quarter-century. It was shown that the porewater advection induced by the interaction of bottom water currents and bedforms leads to an accelerated exchange of particles and solutes through the sediment-water interface stimulating benthic metabolism (Huettel et al., 2014). Most studies have attempted to explain mechanisms underlying biogeochemical cycling in sandy sediments using numerical models or laboratory investigations. Generally, only a limited number of bottom water velocities were considered. No study has resolved the high spatial and temporal gradients of reactive solutes present in the subtidal of continental shelves. As a consequence, little is known about the impact of changing bottom water velocities and bedform migration on porewater advection and reaction rates, thus complicating quantification and prediction of benthic carbon remineralization and nutrient turnover.

The aim of this thesis was to assess how the temporal dynamics of currents and sediment transport influence biogeochemical cycling in permeable sediments. To understand mechanisms regulating interfacial solute and particle fluxes, we examined both transport processes as well as the microbial reaction rates. An integrated approach combining numerical models with in situ measurements and ex situ laboratory experiments was used here. The results and findings can be divided into three parts where the first two parts are based on the numerical model. Part (i) is intended to outline the processes that occur within stationary bedforms when bottom water velocities are constant. In part (ii), this model is extended to migrating bedforms under constant bottom water velocities. In part (iii) the processes occurring under in situ conditions are summarized and discussed. The combination of the three parts allows for in-depth insights into transport processes which allow for the quantification of benthic remineralization and nitrogen-loss within the German Bight as presented in the subsequent chapter.

(i) The main findings derived from the manuscripts under stationary forcing are depicted in Figure 7.1 a-c. The most studied case is a stationary bedform under a constant bottom water velocity (Figure 7.1 a) (e.g. Ziebis et al., 1996; Huettel et al., 2003; Precht et al., 2004). The bedform interacts with the bottom water currents creating a pressure gradient at the sediment-water interface that drives the porewater advection (Thibodeaux and Boyle, 1987). Thus, the transport rate of solutes and particles into and out of the sediments depends on the hydrodynamic forcing and sediment characteristics (Manuscript I). We showed that the penetration depth of a reactive solute such as oxygen depends on the strength of the reaction rate relative to the transport rate. This proportion is summarized by the Damköhler number (Manuscript I, Equation 2.12). Based on the Damköhler number, a previously described scaling law could be extended allowing for the estimation of reactive solute fluxes in sandy sediments (Manuscript I, Equation A.2.40). To reduce the numbers of variables in the model, we found that all physical sediment properties (permeability, bedform dimensions) can be well described by empirical relations based on the characteristic grain size (Manuscript II). In other words, solute fluxes are mainly a function of the grain size, bottom water velocity, solute concentration and bulk respiration rate of the bacterial community.

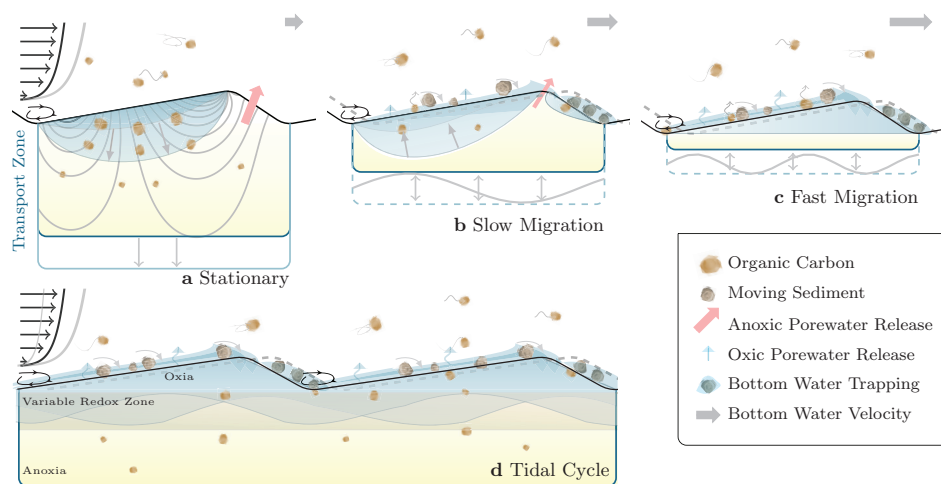


Figure 7.1: Schematic illustration of the oxygen dynamics in permeable sediments for **a** stationary bedforms, **b** slowly migrating bedforms and **c** fast migrating bedforms (see also Manuscript I). In **d** the oxygen distribution is schematically shown for conditions as present in a tidal cycle (derived from Manuscript II). The blue shaded region indicates the oxygenated zone, while yellow indicates anoxia.

(ii) When the bottom water velocity reaches the critical bed shear stress, sediment starts to move and the migration of bedforms is initialized (Figure 7.1 b) (Yalin, 1972). The combined effect of sediment erosion at the stoss side, and sediment deposition at the

lee side of the bedform, was found to influence interfacial solute fluxes (Precht and Huettel, 2003). These findings were limited to a flume study with arbitrary wave settings. In a model study, it was shown, that bedform migration reduces the penetration depth of a non-reactive solute (Elliott and Brooks, 1997; Bottacin-Busolin and Marion, 2010). To investigate the impact of bedform migration on a reactive solute (oxygen), we introduced bedform migration to the transport-reaction equations. In the first study (Manuscript I), we directly coupled bedform migration and advective porewater flow to the bottom water velocity. We found that interfacial oxygen fluxes change significantly as soon as the sediment divides into an upper mobile layer (migrating bedform) and an underlying stationary layer. The bedform is increasingly flushed with oxic bottom water and meanwhile porewater flow begins to oscillate at increasing frequencies beneath the bedform (Figure 7.1 **b, c**). This suppresses net porewater displacement and reduces the oxygen penetration depth. As a result, the overall oxygen uptake decreases dramatically with bedform migration although bottom water velocities increase. As soon as bedform migration dominates, the turnover of bottom water on the lee side flushes the whole bedform (Figure 7.1 **c**). Indications of bedform flushing were observed in flume experiments and in this context Precht et al. (2004) coined the term 'redox seal', as reduced substances that diffuse upwards are oxidized within the bedform. The oscillation frequency of water parcels below the bedform increases with increasing bedform migration. Dispersion thereby substantially contributes to the solute fluxes between the migrating bedform and the stagnant sediment underneath (Manuscript I).

(iii) The model results raise the question to what extent the described processes occur under in situ conditions. Within a tidal cycle the strong current velocities in the southern North Sea are highly variable, changing on a semi-diurnal basis both in direction and magnitude. Regular wave events additionally contribute to current velocities which leads to an high energy environment reflected in the sea floor morphodynamics (Kösters and Winter, 2014). Bedforms are ubiquitous in this environment, and within a tidal cycle bedforms start migrating, change direction and stop again (Traykovski, 2007). Therefore, the above-described transport processes under stationary forcing conditions co-occur in an intricate way which leads to variable spatial and temporal solute distributions with unknown implications for the benthic biogeochemistry. With the development of the benthic observatory 'LanceALot' it was possible to resolve these solute distributions in the subtidal sediments of the German Bight. For the first time, high-resolution benthic oxygen distributions were presented covering the large variety of bottom water velocities and sediment characteristics as found in the North Sea (Manuscript II). This includes oxygen distributions underneath migrating and stationary bedforms.

In the German Bight, bedform migration was mostly limited to the tidal peak times and was found to have a versatile feedback on solute fluxes (Figure 7.1 d). First, bedform migration maintains the advective porewater flow as with the erosion of sediments, organic particles from the pore space are exposed to the sediment surface where they are resuspended (Manuscript II). This diminishes clogging of the pore space and preserves the permeability. In essence, sandy sediments can be seen as a biocatalytic filter and bedform migration represents the flushing of this filter. Reworked and resuspended the organic particles might fuel high rates of remineralization in bottom waters.

However, rates of bedform migration might be reduced due to stabilization by extra-cellular polymeric substances excreted by microbes (Malarkey et al., 2015; Underwood and Paterson, 1993). Evidence for biological sediment stabilization was obtained in the summer 2014 deployments under good light conditions when oxygen profiles indicated high benthic primary production. During deployments, rates of bedform migration were much lower, despite hydrodynamic conditions similar to autumn deployments. The microphytobenthos responsible for benthic primary production excrete large amounts of extra-cellular polymeric substances (MacIntyre et al., 1996; Hoagland et al., 1993) which might clog the pore space and reduce the permeability (Zetsche et al., 2012). As soon as strong hydrodynamic forcings, such as storm events, re-mobilize the sediments this effect might be reversed. We hypothesize that the extra-cellular polymeric substances excreted by microbenthos affect the benthic biogeochemical cycling by reducing porewater advection and preventing the maintaining function of bedform migration. In this context the application of hyperspectral cameras could reveal the distribution of microphytobenthos in the shallow subtidal (Chennu et al., 2013) and their potential impact on benthic biogeochemistry.

During a tidal cycle the migrating bedform and with it the pressure gradient typically moves a few bedform wavelengths (Manuscript II). Further, the transient bottom water currents vary in magnitude and change direction causing a variable strength of porewater advection and also a variation of the inflow and outflow zones along the bedform. The concomitant changes of oxic and anoxic lead to the formation of a variable redox zone (Manuscript II, see also Figure 7.1 d). This variable redox zone implies rapid fluctuations of electron acceptors and electron donors, therefore, sand provides a challenging environment with variable limitations for the benthic microbial community as discussed below. Above the variable redox zone sediment layers were typically oxic and no 'chimney'-like structures bursting through the sediment-water interface were observed.

Under stationary conditions it was shown (Manuscript I) that bedform migration reduces porewater advection and thus solute fluxes. Bedform migration, further, impacted

respiration rates through the release of organic particles (Manuscript II) and mechanical abrasion (Miller, 1989; Nickels et al., 1981). It is the mechanical abrasion that leads to the specific microbial colonization of sand grains as it forces the microbes into cracks and depressions (Manuscript III, Figure 4.2). Chemical conditions in these semi-isolated microenvironments can be vastly different from the bulk sediment especially when the bulk conditions fluctuate rapidly and equilibration via diffusion is slow.

We showed that bacterial cells colonize sand grains at constant areal densities, and thus, the respiration rate becomes a function of the sediment surface area. But, the total bacterial uptake also depends on the supply of electron donor and electron acceptor. This became apparent within the experiments in flow-through reactors, where increasing pore-water advection stimulated aerobic respiration (Manuscript III). The limitation of electron acceptors could be excluded making the limitation of the electron donor likely. During the expeditions the volumetric reaction rates were highly variable and did not correlate to particulate organic carbon (Manuscript II). In combination, this strongly indicates that the supply of labile compounds of organic matter have a strong influence on the microbial reaction rates. However, under in situ conditions the supply of electron acceptors and electron donors is highly variable (Manuscript II), therefore, the limitation of one specific compound can not be generalized. Further, while the macroscale transport could be well described within this thesis, the microscale transport remains largely unknown. On a microscale the limitation of specific substrates could be largely different from bulk measurements (Manuscript III). Therefore, it is an important future-task to investigate the microscale transport of solutes to the microbial community colonizing sand grains. For this purpose, microfluidic systems (Ahmed et al., 2010) in combination with models could be an appropriate method.

Classically, the sediment and water column have been seen as two separated systems where sediment processes are only marginally coupled to those in the water column. This picture has altered as our understanding has grown of advective porewater flow, which transports particles and solutes into sandy sediments enhancing the benthic-pelagic coupling. My thesis adds to this picture by showing that the surface sediment layer represents a transition zone between water column and sediment with a strong coupling, in both directions. This leads to a microbial realm characterized by large variations in chemical gradients and fluctuations in the availability of electron donor and electron acceptor.

Microbes in the upper layer of sandy sediments encode functional genes for a diverse range of metabolisms (Gobet et al., 2012). Few studies have investigated how these organisms thrive in such variable redox environments, but it may be that redox processes in sandy

sediments may not occur strictly in the order predicted by the redox tower. In incubations with intertidal sediments, denitrification was observed under aerobic conditions (Gao et al., 2010). The mechanism behind these observations is debated. To address the mechanism, experiments in flow-through reactors were conducted and it was concluded that denitrification is occurring in oxic sediments (Manuscript V). It was shown, that microbes constantly express denitrification genes within the sediment and that use of these genes under aerobic conditions is promoted by regular changes between oxic and anoxic conditions. This increases the potential for nitrogen-loss from permeable sediments, especially when oxygen penetration depths are high, as seen in the German Bight (Manuscript II). Thus, subtidal sandy sediments are a major sink for anthropogenically fixed nitrogen. Despite these findings, it remains largely unclear how the hydrodynamics and morphodynamics on continental shelves interact with the nitrogen-cycle. A recent modelling study describes a negligible impact of bedform migration on denitrification (Kessler et al., 2015). In Manuscript I this was shown to be an effect of limited parametrization. Therefore, it is an important future-task to include the nitrogen-cycle into the presented transport-reaction equations and investigate coupled - nitrification and denitrification (aerobically and anaerobically) under transient conditions.

In conclusion, this thesis elucidates the important role of sandy sediments in biogeochemical cycling on continental shelves. The interaction of microbial reaction rates with advective porewater flow and bedform migration leads to an environment with highly variable redox conditions that differs strongly from cohesive sediments. The modelling study laid the foundation allowing for the quantification of solute fluxes as a function of advective porewater flow and migration of bedforms. On that basis, the in situ processes were studied by developing a benthic observatory. The observatory allowed for visualization of oxygen distributions and the correlation to the surface topography. Bedform migration was found to play a key role for benthic biogeochemical cycling by reducing respiration rates and penetration depths of reactive solutes but also in maintaining the advective porewater flow by flushing the sediment and enhance the benthic-pelagic coupling. The current dynamics on continental shelves were found to lead to the formation of a variable redox zone in which the conditions of oxic and anoxic are highly variable. The redox seal, which was previously discussed as a feature for migrating bedforms, was always present as a result of the current- and morphodynamics.

Despite the inherent complexity and co-occurrence of transport processes a relatively simple scaling law based on the Damköhler number and derived from the advective porewater flow along bedforms is sufficient to explain most of the observed variability of oxygen fluxes within continental shelf sediments (Manuscript I, Manuscript II and

Manuscript IV). Therefore, the model could be used in future studies to quantify carbon remineralization and determine potential nitrogen-loss within sandy sediments. As an outlook, the calculations are performed for the German Bight.

7.2 Quantification

In a first attempt, oxic remineralization and nitrogen-loss in the German Bight was quantified. Based on empirical relations the input parameters were reduced to median grain size, bottom water velocity, respiration rates and reactive solute concentration - as described above. The median grain size was determined by reexamination of a dataset including over 20000 grain size distributions measured in the German Bight (*Geopotential Deutsche Nordsee*, <http://gpdn.de>). The bottom water velocity was extracted from a high resolution circulation model focusing on sediment transport in the German Bight (Kösters and Winter, 2014). The measured reaction rates from Manuscript II were temporally averaged and interpolated in between sampling stations. The reaction rates for denitrification and nitrification were scaled by assuming the Redfield ratio ($O_2 : N = 138 : 16$, Manuscript III, see also Santos et al., 2012). For nitrogen-loss the focus is on nitrification and denitrification which have been shown to contribute strongly to nitrogen-loss in the German Bight (Manuscript IV). Aerobic denitrification is not included, as measurements are limited. However, by considering the few measured rates (Manuscript IV) a range of potential contributions can be provided.

The results are presented in Figure 7.2. The average carbon flux in sandy sediments of the German Bight was predicted to be $3.5 \text{ mol m}^{-2} \text{ yr}^{-1}$. In comparison to the $31 \text{ mol m}^2 \text{ yr}^{-1}$ primary production estimated (Wollast, 1998) this is approximately 11% of the total carbon fixation. Our findings correspond well to pelagic remineralization measurements in the North Sea where approximately 90% of carbon were remineralized in the water column (Heip et al., 1995). Despite some uncertainties (Manuscript II) this indicates a complete remineralization of the fixed carbon within the water column and, finally, in the sediment. In this thesis, we have shown that benthic and pelagic processes are strongly coupled and high remineralization rates in the water-column might, therefore, be a result of the benthic transport processes such as resuspension events of organic matter.

The nitrogen runoff from the major rivers Rhine, Elbe, Meusel and Weser equals 300 kt yr^{-1} of which approximately 37% is potentially reduced to dinitrogen gas within the German Bight. In combination with the high potential nitrogen-loss rates within intertidal systems (30%, Gao et al., 2012) this budget calculation reveals the strong buffer role of sandy sediments which might be further enhanced by aerobic denitrification

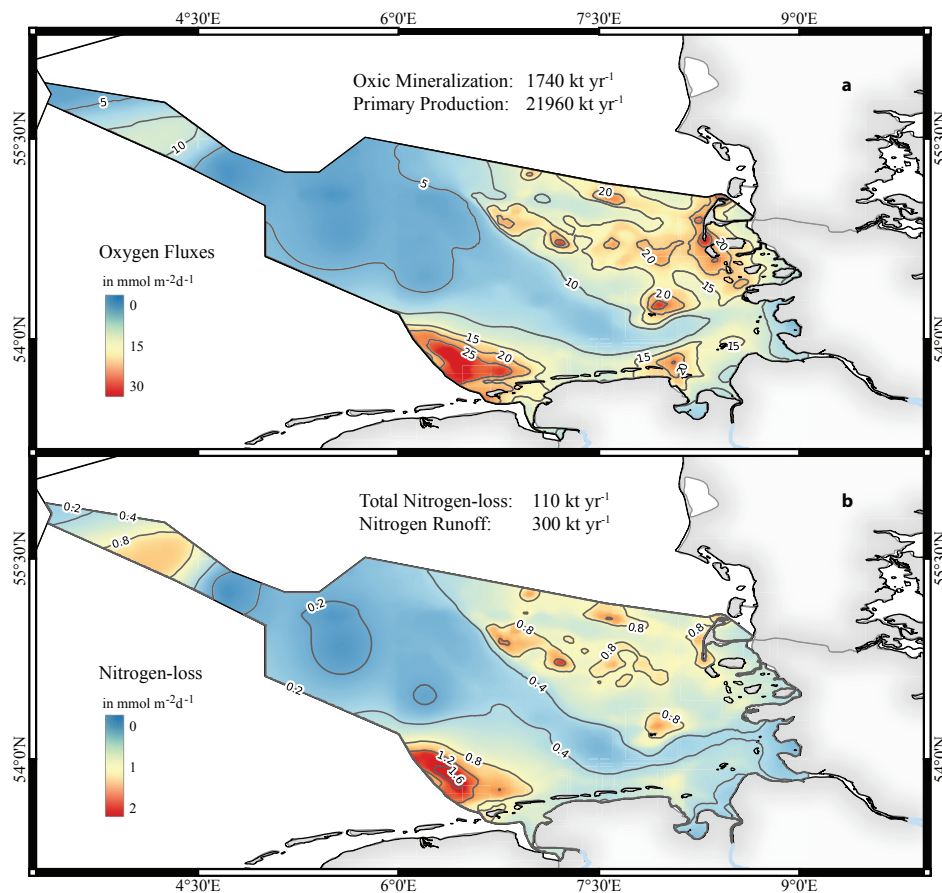


Figure 7.2: Modelled total and spatial resolved benthic **a** oxidic mineralization and **b** nitrogen-loss in permeable sediments of the German Bight. The model is based on the findings of the five Manuscripts (see text for further information). Primary production is based on the average chlorophyll concentrations of 2013-2016 (Nasa, Modis Aqua) and nitrogen runoff is based on the average of various investigations (Ducrottoy et al., 2000; Radach and Pätsch, 2007; Johannsen et al., 2008).

(Manuscript IV, Manuscript V). By considering the limited measured aerobic denitrification rates (Manuscript IV), the potential additional nitrogen-loss within the German Bight could be estimated to range between 30 – 100 kt yr⁻¹.

Our first attempt to quantify benthic remineralization and nitrogen-loss in the German Bight reveals that we have largely resolved the transport processes in sandy sediments within this thesis. However, the parameterization of the volumetric remineralization rates remains a challenging task. Manuscript III showed that the sediment surface area controls the bacterial cell numbers. Therefore, the sediment surface area presents a basis from where the magnitude of the respiration rate depends on the supply of the limiting substrate. In future studies, the limitation of electron acceptors and electron donors should be further disentangled to allow for a better parameterization in model studies.

7.3 Bibliography

- Ahmed, T., Shimizu, T. S. and Stocker, R. (2010), 'Microfluidics for bacterial chemotaxis', *Integrative Biology* **2**(11-12), 604–629.
- Bottacin-Busolin, A. and Marion, A. (2010), 'Combined role of advective pumping and mechanical dispersion on time scales of bed form–induced hyporheic exchange', *Water Resources Research* **46**(8).
- Chennu, A., Färber, P., Volkenborn, N., Al-Najjar, M. A., Janssen, F., De Beer, D. and Polerecky, L. (2013), 'Hyperspectral imaging of the microscale distribution and dynamics of microphytobenthos in intertidal sediments', *Limnology and Oceanography: Methods* **11**(10), 511–528.
- Ducrotoy, J.-P., Elliott, M. and de Jonge, V. N. (2000), 'The north sea', *Marine Pollution Bulletin* **41**(1), 5–23.
- Elliott, A. H. and Brooks, N. H. (1997), 'Transfer of nonsorbing solutes to a streambed with bed forms: Theory', *Water Resources Research* **33**(1), 123–136.
- Gao, H., Matyka, M., Liu, B., Khalili, A., Kostka, J. E., Collins, G., Jansen, S., Holtappels, M., Jensen, M. M. and Badewien, T. H. (2012), 'Intensive and extensive nitrogen loss from intertidal permeable sediments of the wadden sea', *Limnology and Oceanography* **57**(1), 185.
- Gao, H., Schreiber, F., Collins, G., Jensen, M. M., Kostka, J. E., Lavik, G., de Beer, D., Zhou, H.-y. and Kuypers, M. M. (2010), 'Aerobic denitrification in permeable wadden sea sediments', *The ISME journal* **4**(3), 417–426.
- Gobet, A., Böer, S. I., Huse, S. M., van Beusekom, J. E., Quince, C., Sogin, M. L., Boetius, A. and Ramette, A. (2012), 'Diversity and dynamics of rare and of resident bacterial populations in coastal sands', *The ISME journal* **6**(3), 542–553.
- Heip, C. H., Goosen, N., Herman, P., Kromkamp, J., Middelburg, J. and Soetaert, K. (1995), 'Production and consumption of biological particles in temperate tidal estuaries', *Oceanography and Marine Biology-an Annual Review* **33**.
- Hoagland, K. D., Rosowski, J. R., Gretz, M. R. and Roemer, S. C. (1993), 'Diatom extracellular polymeric substances: function, fine structure, chemistry, and physiology', *Journal of Phycology* **29**(5), 537–566.

- Huettel, M., Berg, P. and Kostka, J. E. (2014), 'Benthic exchange and biogeochemical cycling in permeable sediments', *Marine Science* **6**.
- Huettel, M., Røy, H., Precht, E. and Ehrenhauss, S. (2003), Hydrodynamical impact on biogeochemical processes in aquatic sediments, in 'The Interactions between Sediments and Water', Springer, pp. 231–236.
- Johannsen, A., Dähnke, K. and Emeis, K. (2008), 'Isotopic composition of nitrate in five german rivers discharging into the north sea', *Organic Geochemistry* **39**(12), 1678–1689.
- Kessler, A. J., Cardenas, M. B. and Cook, P. L. (2015), 'The negligible effect of bed form migration on denitrification in hyporheic zones of permeable sediments', *Journal of Geophysical Research: Biogeosciences* .
- Kösters, F. and Winter, C. (2014), 'Exploring german bight coastal morphodynamics based on modelled bed shear stress', *Geo-Marine Letters* **34**(1), 21–36.
- MacIntyre, H. L., Geider, R. J. and Miller, D. C. (1996), 'Microphytobenthos: the ecological role of the "secret garden" of unvegetated, shallow-water marine habitats. i. distribution, abundance and primary production', *Estuaries* **19**(2), 186–201.
- Malarkey, J., Baas, J. H., Hope, J. A., Aspden, R. J., Parsons, D. R., Peakall, J., Paterson, D. M., Schindler, R. J., Ye, L. and Lichtman, I. D. (2015), 'The pervasive role of biological cohesion in bedform development', *Nature communications* **6**.
- Miller, D. (1989), 'Abrasion effects on microbes in sandy sediments.', *Marine ecology progress series. Oldendorf* **55**(1), 73–82.
- Nickels, J. S., Bobbie, R. J., Martz, R. F., Smith, G. A., White, D. C. and Richards, N. L. (1981), 'Effect of silicate grain shape, structure, and location on the biomass and community structure of colonizing marine microbiota', *Applied and environmental microbiology* **41**(5), 1262–1268.
- Precht, E., Franke, U., Polerecky, L. and Huettel, M. (2004), 'Oxygen dynamics in permeable sediments with wave-driven pore water exchange', *Limnology and Oceanography* **49**(3), 693–705.
- Precht, E. and Huettel, M. (2003), 'Advective pore-water exchange driven by surface gravity waves and its ecological implications', *Limnology and Oceanography* **48**(4), 1674–1684.

- Radach, G. and Pätsch, J. (2007), 'Variability of continental riverine freshwater and nutrient inputs into the north sea for the years 1977–2000 and its consequences for the assessment of eutrophication', *Estuaries and Coasts* **30**(1), 66–81.
- Santos, I. R., Eyre, B. D. and Glud, R. N. (2012), 'Influence of porewater advection on denitrification in carbonate sands: Evidence from repacked sediment column experiments', *Geochimica et Cosmochimica Acta* **96**, 247 – 258.
- Thibodeaux, L. J. and Boyle, J. D. (1987), 'Bedform-generated convective transport in bottom sediment'.
- Traykovski, P. (2007), 'Observations of wave orbital scale ripples and a nonequilibrium time-dependent model', *Journal of Geophysical Research: Oceans (1978–2012)* **112**(C6).
- Underwood, G. J. and Paterson, D. M. (1993), 'Seasonal changes in diatom biomass, sediment stability and biogenic stabilization in the severn estuary', *Journal of the Marine Biological Association of the United Kingdom* **73**(04), 871–887.
- Wollast, R. (1998), 'Evaluation and comparison of the global carbon cycle in the coastal zone and in the open ocean', *The sea* **10**, 213–252.
- Yalin, M. (1972), *Mechanics of Sediment Transport*, Vol. 1, Pergamon Press.
- Zetsche, E., Bulling, M. T. and Witte, U. (2012), 'Permeability of intertidal sandflats: Impact of temporal variability on sediment metabolism', *Continental Shelf Research* **42**, 41–50.
- Ziebis, W., Huettel, M. and Forster, S. (1996), 'Impact of biogenic sediment topography on oxygen fluxes in permeable seabeds', *Marine Ecology Progress Series* **140**, 227–237.

8. Acknowledgements

To begin with, I want to thank Marcel Kuypers for giving me the opportunity to work in this great research environment. Thank you for supporting my work with your immense scientific knowledge and in encouraging discussions. Your innovative ideas and inspiration make science so thrilling. Further, I want to thank Dirk de Beer who gave me the chance to also be part of the microsensor group. Thank you for sharing all the experience and expertise with me.

I am most grateful to Moritz Holtappels who always supported me as a supervisor, a mentor, and a friend. I am incredibly thankful for all the time we spend next to rivers, on research vessels, in telephone conferences, in workshops, and in the office together. During our long discussions, Moritz shared his broad knowledge and expertise on basically everything with me. His passion for science empowered me and made this work possible. It was a privilege to be supervised by you, Moritz, thank you.

In particular, I also want to thank Christian Winter for allowing me to be part of his group 'coastal morphodynamics' and for all the help during cruises, for long helpful discussions, for organizing social events, or simply for his positive feedbacks - and also for tolerating my inability of multitasking. Further, I want to thank Felix Janssen for supporting my work since the very first day as a PhD Student when introducing me to 'LanceALot'. Special thanks also go to Arzhang Khalili, Kolja Kindler and Bo Liu for giving me first insights into the world of environmental fluid dynamics.

I would further like to thank all the people in the Biogeochemistry Department who made my last years so pleasant. Being among all these experts and nice people was such a great and unique experience for me. I want to thank especially Gabriele Klockgether for all the conversations during lunch time. My thanks also go to Sten Littmann, Daniela Tienken, Kirsten Imhoff and Swantje Lilienthal for all the technical help and ideas. Further, I thank Tim Ferdelman for his support with coordination; Ulrike Tietjen and Tomas Wilkop for their organizational assistance; Christiane Glöckner and Anita Tingberg as the Marmic

organizers. Finally, I want to thank the great public relations team Naomi Halbach, Fanni Aspetsberger and Manfred Schlösser.

My work would not have been possible without the help and support of the technicians at the Max-Planck-Institute and Marum. In particular, I thank Paul Färber and Volker Meyer, who spend so much time in supporting me with technical advice. Further I thank Gabriel Herbst, Eberhard Kopiske, Georg Herz, Axel Nordhausen, and Volker Asendorf for their advice on many technical aspects. Carsten John is thanked for the IT-support and for sharing his Unix skills with me.

My interdisciplinary work was only possible because of a close collaboration among different marine institutes in Northern Germany. Herewith, I thank all members of the Marum, HZG Geesthacht, Alfred Wegener Institute and Senckenberg Institute am Meer who supported my work. In particular, I want to thank Jana Friedrich, Ulrike Schückel, Celine Naderipour, Andreas Neumann, and Justus van Beusekom for sharing all the expertise and making the cruises so pleasant. Further, I thank the captains and crew of the RV *Heincke* and RV *Senckenberg*.

Many thanks go to my friends who made my last years such a marvelous time. In particular, Emmo Hamann and Oliver Bleich thank you for being my friends and for skill-sharing since the very first day at university. Nadine Lehnen and Julien Dekaezemacker - thank you for making my life in Bremen so wonderful. Further, I thank my friends Jasmine Berg and David Probandt for all the scientific support, help with writing, help with keeping plants alive,... but also the fun at work, after work and during cruises. Knut Krämer, thank you for spending endless hours on the telephone to discuss sediment transport and qgis, and all the people who made my social life and MPI life so amazing: Philipp Hach, Jon Graf, Andi Krupke, Jessika Füssel, Cameron Callbeck, Clara Martinez Perez, Katharina Kitzinger, Wiebke Mohr, Jana Milucka, Julia Dürschlag the MPI soccer team and so many others. Special thank goes to all the office mates I had over the years, with whom I shared the best gossip and had great fun: Niels Schoffelen, Alexander Khachikyan, Sarah Sokoll, Phylis Lam and Caroline Buckner and also Hannah Marchant and Morten Iversen for all the scientific discussions and fun time after work.

All this would not be possible without the great support of my family and friends to whom I dedicate this thesis: Liebe Mama, lieber Papa, danke, dass ihr mich stets unterstützt und diesen Weg ermöglicht habt. Liebe Katharina, Liebe Lilli, Lieber Jan, danke, dass ihr immer für mich da gewesen und so großartige Geschwister seid. Ich bin all meinen Freunden dankbar, die endlose Stunden mit mir auf und im Wasser verbracht haben. Ohne euch wäre diese Arbeit nicht möglich gewesen.

IV

Appendix

Wave Transformation and Wave-Driven Flow across a Steep Coral Reef

Stephen G. Monismith and Liv M.M. Herdman

Environmental Fluid Mechanics Laboratory, Stanford University, Stanford, California

Soeren Ahmerkamp

Max Planck Institute for Marine Microbiology, Bremen, Germany

James L. Hench

*Environmental Fluid Mechanics Laboratory, Stanford University, Stanford, California, and
Nicholas School of the Environment Marine Laboratory, Duke University, Beaufort, North
Carolina*

doi: 10.1175/JPO-D-12-0164.1

Abstract

Observations of waves, setup, and wave-driven mean flows were made on a steep coral forereef and its associated lagoonal system on the north shore of Moorea, French Polynesia. Despite the steep and complex geometry of the forereef, and wave amplitudes that are nearly equal to the mean water depth, linear wave theory showed very good agreement with data. Measurements across the reef illustrate the importance of including both wave transport (owing to Stokes drift), as well as the Eulerian mean transport when computing the fluxes over the reef. Finally, the observed setup closely follows the theoretical relationship derived from classic radiation stress theory, although the two parameters that appear in the model—one reflecting wave breaking, the other the effective depth over the reef crest—must be chosen to match theory to data.

A laboratory model of marine snow: Preparation and characterization of porous fiber particles

Anna L. Doergens

Max Planck Institute for Marine Microbiology, Bremen, Germany

Department for Biomimetics, University of Applied Sciences Bremen, Bremen, Germany

Soeren Ahmerkamp

Max Planck Institute for Marine Microbiology, Bremen, Germany

Jörg Müssig

Department for Biomimetics, University of Applied Sciences Bremen, Bremen, Germany

Roman Stocker

Department of Civil and Environmental Engineering, Massachusetts Institute of Technology, Cambridge, Massachusetts

Marcel Kuypers, Arzhang Khalili, Kolja Kindler

Max Planck Institute for Marine Microbiology, Bremen, Germany

doi: 10.1002/lom3.10056

Abstract

A method is described to prepare laboratory models of marine snow flocks using textile fibers to facilitate settling and mass transfer experiments under hydrodynamically well-defined conditions. A simple and effective roll-agglomeration process is introduced to fabricate macro-scale (up to centimeter-size) fiber particles, with predefined porosity, permeability, and excess density. Hydrodynamic similarity with natural marine snow aggregates was confirmed by measurements of porosity, permeability and settling velocity measurements. The assessment is completed by an analysis of the performance of the fabrication method. The fiber particles generated via this method can be used to advance our understanding of the hydrodynamics underlying settling dynamics and the associated mass transfer.

Gas seep-induced solute transport into submerged sediments**Mohammad Reza Morad***Department of Aerospace Engineering, Sharif University of Technology, Tehran, Iran*

Reza Malek Mohammadi, Soeren Ahmerkamp

Max Planck Institute for Marine Microbiology, Bremen, Germany

Arzhang Khalili

Max Planck Institute for Marine Microbiology, Bremen, Germany and Earth & Space Sciences Program, Jacobs University, Bremen, Germany

doi: -

Abstract

We studied the downward migration of solutes mediated by air bubbles rising through a bed of sediment. The porous bed was composed of three samples of fire-dried quartz sands with coarse, medium and fine grains. In the experimental setup a rectangular container filled with a saturated sediment column was overlaid by a dyed water layer. Air was injected centrally from the bottom of the container. Quantification of the total dye uptake inside the sediment layer was carried out digitally using image processing. The spread of dye from the overlying water into the sediment layer showed two distinct patterns, i.e. a conically developing shape for fine sand and horizontal front propagation for the medium and coarse sands. Based on the physical processes involved we introduce appropriate pressure boundary conditions for numerical simulation of solute uptake within sediment that reproduced our experimental observations. Furthermore, we obtained two empirical relations for the total solute uptake as well as the dye propagation area as a function of the injected air. This finding is a significant factor to consider in the quantitative estimation of the downward flux of electron acceptors and electron donors fueling microbial activity.

**Syntrophic linkages between the anaerobic predatory flagellate
Carpediemonas frisia sp. nov. and specific prokaryotic populations**

Emmo Hamann

Max Planck Institute for Marine Microbiology

Halina E. Tegetmeyer, Dietmar Riedel, Sten Littmann, Soeren Ahmerkamp

Max Planck Institute for Marine Microbiology, Bremen, Germany

Jianwei Chen and Marc Strous

Energy Bioengineering Group, University of Calgary, Canada

doi: -

Abstract

The anoxic areas of marine sediments are populated by diverse communities of microbial eukaryotes. Most known anaerobic eukaryotes are small heterotrophs (< 50 μm) that prey on prokaryotic species. Despite the ubiquity of predatory eukaryotes in anoxic habitats it has rarely been investigated how they interact in mutually beneficial interactions with prokaryotes. We assessed such interactions by cultivating the anaerobic marine flagellate, *Carpediemonas frisia* sp. nov. (supergroup *Excavata*), with parts of its naturally associated microbiota. This microbiota consisted of members of the *Deltaproteobacteria*, *Bacteroidetes*, *Firmicutes*, *Verrucomicrobia* and so far uncultivated relatives of the Nanoarchaeota. Using interspecies metabolic network modeling informed by genomics and transcriptomics, we showed that *C. frisia* stimulated prokaryotic growth through the release of hydrogen, acetate, amino acids and pre-digested macromolecular organic material. A specific involvement of Bacteroidetes in the hydrolysis of macromolecular material was indicated by high transcriptional activities of genes encoding biopolymer degrading enzymes, as well as oligopeptide and lipid transporters. Complementary to that, *Firmicutes* and *Nanoarchaeota* appeared to be involved in the fermentation of sugar monomers and amino acids. Physiological experiments also showed that the fitness of *C. frisia* was directly determined by the hydrogen oxidizing activity of sulfate reducing *Deltaproteobacteria*. In conclusion, our results demonstrate that anaerobic predatory protists engage in mutually beneficial syntrophic interactions with specific bacterial and archaeal populations.

